The Application of Fibre Bragg Grating Networks As Strain Sensors and As Phased Array Antenna True Time Delay Elements

Anna Molony

Doctor of Philosophy

1996

THE UNIVERSITY OF ASTON IN BIRMINGHAM

November 1996

'The University of Aston in Birmingham'

THE APPLICATION OF FIBRE BRAGG GRATING NETWORKS AS STRAIN SENSORS AND AS PHASED ARRAY ANTENNA TRUE TIME DELAY ELEMENTS

Anna Molony

Doctor of Philosophy

1996

THESIS SUMMARY

The fabrication of in-fibre Bragg gratings, and the application of arrays of such gratings as strain sensors and as true time delay elements for the control of phased array antennas is reported. Chirped period Bragg gratings were produced using the fibre deformation fabrication technique, with chirps of between 2.9nm and 17.3nm achieved. Arrays of 5mm and 2mm long uniform period Bragg gratings were fabricated using the dissimilar wavefronts inscription method, for use as true time delay elements, and their spectral characteristics recorded. The uniform period grating arrays were used to create minimum time delays of 9.09ps, 19.02ps and 31ps; making them suitable for controlling phased array antennas operating at RF frequencies of up to 3GHz, with 10° phase resolution. Four 4mm long chirped gratings were produced using the dissimilar wavefronts fabrication method, having chirps of 7nm, 12nm, 20nm and 30nm, and were used to create time delays of between 0.3ps and 59ps. Hence they are suitable for controlling phased array antennas at RF frequencies of up to 48GHz. The application of in fibre Bragg gratings as strain sensors within smart structure materials was investigated, with their sensitivity to applied strain and compression measured for both embedded and surface mounted uniform period and fibre Fabry-Perot filter gratings. A fibre Bragg grating sensor demultiplexing scheme based on a liquid crystal filled Fabry-Perot etalon tuneable transmission filter was proposed, successfully constructed and fully characterised. Three characteristics of the LCFP etalon were found to pose operational limitations to its application in a Bragg grating sensor system; most significantly, the resonance peak wavelength was highly (-2.77nm/°C) temperature dependent. Several methods for minimising this temperature sensitivity were investigated, but enjoyed only limited success. It was therefore concluded that this type (E7 filled) of LCFP etalon is unsuitable for use as a Bragg grating sensor demultiplexing element.

Key words: smart structures, optical fibre, microwave and millimeter-wave photonics, in-fibre Bragg gratings, strain sensors

To my parents and my friends, particularly Sarah, Sarah, Paul and Kate. You kept me sane and never stopped believing that I could do it, even when I had my doubts. Thankyou.

ACKNOWLEDGEMENTS

I must acknowledge the help of my supervisor Ian Bennion for his support throughout this work, and I would like to thank Cathy Ragdale and Colin Edge for their many helpful discussions.

Acknowledgement is also due to Lin Zhang, Kate Sugden, John Williams, Colin Edge, Julian Fells and Richard Fallon for the work which was carried out in collaboration with them, especially the work on grating fabrication using the fibre deformation fabrication technique and that concerning true time delay control of phased array antennas. Thanks must be expressed to Lin Zhang, Kate Sugden, John Williams and Julian Fells for their help and support, particularly in the lab. I would also like to acknowledge the support of GEC Marconi Materials Technology for supporting my work and for providing the liquid crystal Fabry-Perot etalons.

Lastly, thanks to everyone else in the research group, particularly Bert Biggs, who has helped me at one time or another over the last three years.

1. Introduction

1.1 Prologue

The work which forms the basis of this thesis is concerned with the applications of arrays of in-fibre Bragg gratings. Specifically, with their use as strain sensors and as control elements for phased array antennas. In this introduction to the thesis it is assumed that the reader is more familiar with in-fibre Bragg grating technology than with phased array antennas, and so more detail will be given on the latter in order to prepare the reader for the following chapters.

1.2 In-fibre Bragg gratings

In-fibre Bragg gratings can be written in optical fibre by producing a periodic variation in the refractive index of the core over a short length of fibre, Figure 1.1. For wavelengths equal to twice the spacing of the periodic index perturbation, Λ, the gratings couple fibre modes into their counter propagating modes. *Hill et al*[1] first observed the formation of these gratings in germania-doped optical fibre when the core of the fibre was exposed to a standing wave, interference pattern produced by counter propagating beams of 488nm argon laser radiation within the core. The interference pattern induced permanent, localised changes in the refractive index of the fibre core, causing a Bragg type grating to be formed by the periodic refractive index variation. These 'Hill' gratings can be up to 1m in length, with extremely narrow reflection profiles, of the order of 1.5×10^{-4}nm. One disadvantage of these gratings is that their reflection wavelength is fixed at that of the writing beams, making their application rather restricted.

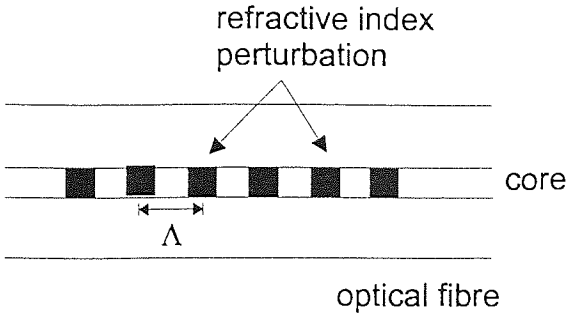

Figure 1.1 Basic representation of an in-fibre Bragg grating: a periodic variation in the refractive index of the fibre core

Although there was much interest in the Hill gratings it was not until 1989 that the fabrication of Bragg gratings was pursued further, *Meltz et al*[2,3] demonstrated that Bragg gratings can be formed in optical fibre by exposing the core, through the side of the fibre, to an interference pattern of overlapping coherent beams of UV radiation. The Bragg gratings used in the work described herein were fabricated using this transverse holographic exposure technique; the theory behind these gratings will be discussed in 2.1.1. and the experimental arrangement used to fabricate them will be described in 3.1.1. More recently, *Hill et al*[4] have developed another method of directly writing photorefractive gratings which uses a phase mask to create the interference pattern; the plus and minus first order diffracted beams produced by the phase mask interfere in the near field, and it is here that the fibre core is positioned; this fabrication method will be discussed further in Chapter 3.

Before the direct write holographic fabrication method was developed periodic in-fibre filters were written using photoresists and surface relief etching[5,6]. The fibre was mounted in a glass block and the cladding lapped and polished tangentially to the fibre, to within a few tenths of a micron of the core. Photoresist was then deposited on the polished surface, and a two beam interference pattern exposed onto the resist, following which the grating was etched into the fibre. Gratings with a reflectivity of >90% can be fabricated in this way, with reflection profiles similar to those of photorefractive gratings,

but they suffer low wavelength loss in transmission due to modal outcoupling. The advantages of the direct write holographic fabrication procedure are that it overcomes the reflection wavelength inflexibility of the Hill gratings, and the time consuming, multiple stage process of the surface relief etching approach.

The maximum grating reflectivity that could be achieved using the holographic side-writing fabrication procedure was initially limited, to values below that available for surface etched gratings, by the photosensitivity of the fibres that were available at that time. This was overcome in 1993 by the development of boron-germania codoped optical fibre[7] and the high pressure hydrogen loading[8] of optical fibre, which were shown to increase a fibre's photosensitivity by a factor of ten and several orders of magnitude respectively.

In 1992 the fabrication of the first chirped in-fibre gratings was reported by *Farries et al*[9], using the surface relief etching technique. The fabrication of chirped gratings in waveguide structures for integrated optics was first reported[10] in 1977, but it was only with the development of highly photosensitive optical fibres that photorefractive chirped gratings could be fabricated in optical fibre. The first holographically written chirped grating was reported by *Byron et al*[11], written in a tapered length of optical fibre. Several other methods of fabricating chirped gratings have also been reported including the use of phase masks[12], and various interferometric techniques[13,14] based on the interference of beams of different curvature, which will be discussed further in 2.1.2 and 3.3.

Chirped gratings can also be produced by applying a linearly varying strain to a length of fibre containing a uniform period grating either during fabrication of the grating, or post exposure; this can be achieved by attaching two different weights to either end of the fibre[15] or by mounting the grating on a tapered cantilever[16] and bending it. Additionally, chirped gratings can be fabricated by writing uniform period gratings in lengths of fibre which have undergone

graded pre-exposure to UV light, use of the intensity shading in half-gaussian beams, and by writing uniform period gratings in curved fibre; this last technique is known as fibre deformation and work carried out using this fabrication method will be presented in 3.3.

1.3 Optical true time delay controlled phased array antennas

The use of fibre optics for the control and distribution of signals within microwave phased array antenna systems has been investigated for many years[17,18]. Numerous potential advantages are envisaged in implementing compact optical fibre transmission line beamforming networks in place of the bulky microwave waveguides used in conventional RF systems, particularly in airborne systems where weight is at a premium.

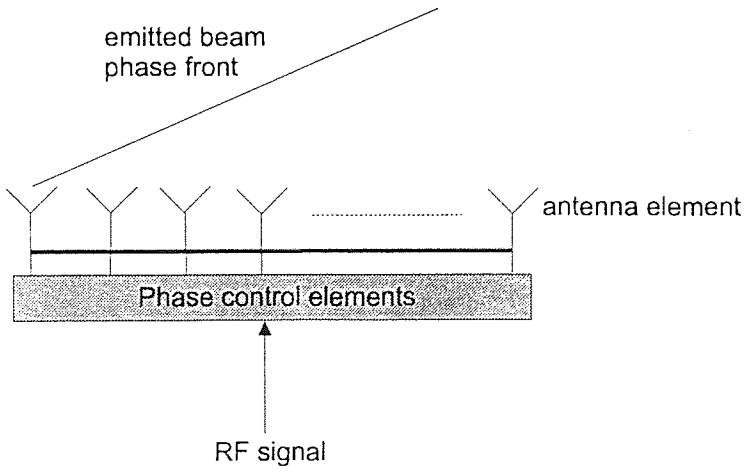

Figure 1.2 A phased array antenna; the phases of the RF signal sent to the individual antenna elements are controlled to steer the emitted beam

A phased array antenna is a directive microwave (RF) antenna composed of a group of individual radiating elements which are distributed in a linear or two-dimensional spatial configuration, Figure 1.2. The amplitude and phase of the signal emitted by each radiator can be individually controlled to produce a

radiated beam of any desired shape. The position of the beam in space is controlled electronically by adjusting the phase of the RF excitation signals emitted at the individual radiators. Hence, the beam direction can be scanned while the antenna aperture remains fixed in space: no mechanical movement is involved in the scanning process, making it inertialess scanning, and thus very fast.

Phased array antennas offer many operational advantages over mechanically steered arrays, including extremely accurate beam pointing, inertialess and highly flexible beam scanning in two dimensions, low weight and power consumption, and the ability to produce a beam with low power spatial side lobes, so that most of the power is concentrated in the main beam. Modern phased array radar systems are expected to work over large beam scan angles, of up to $+/-45^{0}$, at signal frequencies anywhere from the UHF to the X-band, with instantaneous RF bandwidths of the order of hundreds of megahertz, and to produce up to five simultaneous, independently controlled beams. In order to satisfy the required wide bandwidth and rapid beam pointing, true time delay (TTD) antenna array control techniques must be implemented to obtain efficient signal distribution to the radiating elements, independent of the RF signal frequency.

Applications of phased array antennas include radar and telecommunications systems, where rapid, and accurate scanning of the microwave beam direction is called for. Accurate beam scanning in a microsecond time frame allows radar systems to perform multiple functions either simultaneously or through the use of time division multiplexing; for example, a phased array radar is able to simultaneously track large numbers of targets, and illuminate some of those targets with RF energy to allow missile guidance toward them. In communications systems phased array antennas can be used to accurately point high power beams towards distant receivers and transmitters, and to enable contact to be maintained between a base station and rapidly moving

receivers, or between two rapidly moving receivers, in, for example, vehicles or aircraft.

In conventional phased array antenna systems the phases of the RF excitation signals emitted by the individual radiators are controlled directly by passing the signals through microwave phaseshifter waveguides. However, if the RF frequency changes, the apparent length of the microwave waveguide changes and, as a consequence, the phases of the signals emitted by the antenna elements are altered. This results in a change in the beam's spatial position, a phenomenon known as beam 'squint', which will be discussed further in 2.2.2. In order for a radar system to be capable of gathering large amounts of information about its target(s) it must employ a wide instantaneous RF signal bandwidth; of the order of a few hundred megahertz. Hence a wide range of RF frequencies are transmitted along each phaseshifter waveguide, and the resulting beam squint suffered by the extreme RF frequencies means that some of the signal power does not strike the target, and the information that the higher RF frequencies would collect is lost.

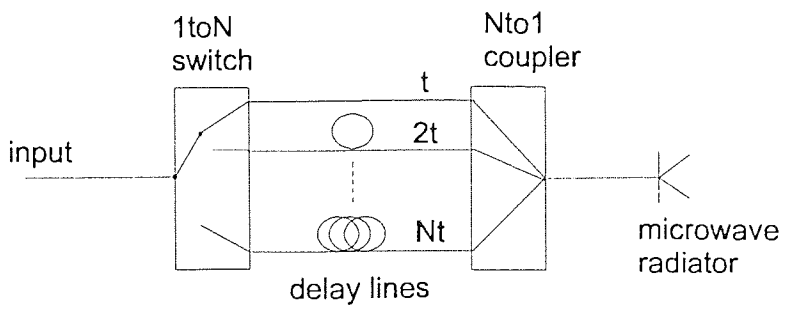

Figure 1.3 Switched lengths of delay line (electrical waveguide or cable, or optical fibre) in a TTD control device; time delay increments in steps of t

In order to prevent the occurrence of beam squint in systems which require a wide RF signal bandwidth, TTD control of the RF signal phases is used instead of the simple phase shift technique. This can implemented by replacing the

phaseshifter waveguides with switched lengths of electrical waveguide or cable, or lengths of optical fibre, Figure 1.3. Electrical waveguide TTD control devices suffer several disadvantages: they tend to be bulky; sustain high loss at high RF frequencies; and are susceptible to electrical crosstalk and temperature-induced time delay changes. The feed system for an array of, say, one thousand elements, comprising thousands of metres of heavily shielded electrical cable, and power splitters, is so heavy, bulky, inflexible and expensive that the application of electrical waveguide TTD control to large phased array antennas is impractical in many applications. In contrast, optical fibre is lightweight, compact, immune to electromagnetic interference and cross-talk, and has significantly lower transmission loss and higher signal bandwidth capacity. Optical TTD control can therefore overcome many of the problems associated with electrical TTD control networks, and has the potential to become a low cost alternative to them.

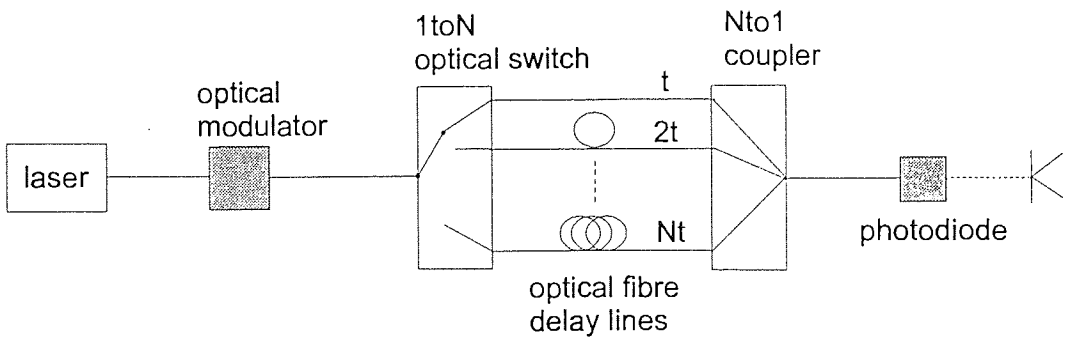

Figure 1.4 Switched optical TTD control device; switch between different lengths of optical fibre; time delay increments in steps of t

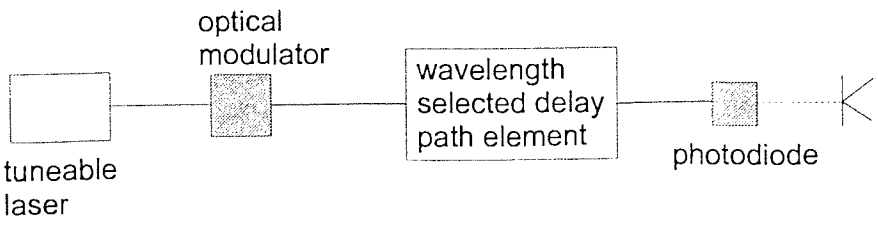

Figure 1.5 Wavelength 'switched' TTD control element; tuning optical carrier wavelength varies optical path length

To implement an optical RF link the chosen electrical RF excitation signal is impressed on an optical carrier as an intensity modulation, and the optical carrier distributed to the antenna elements via optical fibres. In optical TTD systems the required time delay is achieved by switching the optical signal through an appropriate length of optical fibre. This can be done physically, by switching the optical signal into different lengths of optical fibre, Figure 1.4, or through wavelength switching, Figure 1.5, where changing the wavelength of the optical carrier changes the length of optical fibre that the signal travels through.

To date, switched optical TTD has been dominated by two approaches: systems dependent on optical switches to directly alter the length of optical fibre that the optical carrier traverses on its route to the antenna element, Figure 1.4; and those which select the length of optical fibre by switching between many different laser sources, each of which feeds a different optical path. *Goutzoulis et al*[19] have reported a binary fibre optic delay line in which 2x2 optical switches are used to select the optical carrier path length; the time delay units within the system provided delays which incremented according to the binary number system, allowing any delay from ΔT to $2^{M-1}\Delta T$ to be created (M is the number of switches). An RF frequency of 1GHz was used and the delay line produced a maximum delay of 5μs, with a resolution of 39ns. Designs for an all optical binary fibre optic delay line based architecture[20], and for a hybrid delay line architecture[21], containing both electrical waveguides and binary fibre optic delay lines, have also been reported by *Goutzoulis et al.* A similar approach which has been demonstrated[22] used 2x2 optical switches to route the optical carrier through dispersive elements, such as dispersive fibre, fibre gratings, or WDM delay lines, with the available time delays again incrementing in binary steps.

A 3-bit optical true time delay unit based on laser selection has been reported by *Ng et al*[23] in which the desired delay increment is selected by switching on the bias to the semiconductor laser diode pigtailed to the appropriate length of dispersive optical fibre. This time delay unit was used to create a minimum time delay of ~88ps, with a maximum delay of 7 times this value, for RF frequencies in the range 1GHz to 11GHz. Four of these delay elements have been built into a network[24], and used to steer a dual-band (2GHz and 9GHz) phased array antenna[25] over an angular range of -28° to +28°, and used to demonstrate that the beam direction was unaffected on changing the RF frequency from the L-band to the X-band[26,27,28]. A 5-bit optical TTD element has also been reported[29] which used 12 delay lines connected to a 4x8 coupler to create 32 different delay paths. Laser switching was used to select one of the four input delay lines to the 4x8 coupler, and the delay line on the output side of the coupler was selected by switching on the photodiode connected to the chosen delay line; all eight photodiodes were connected to a single antenna. A total delay of 7.75ns was reported, with a resolution of 0.25ns, for an L-band (850-1400MHz) RF signal. Control of a 96 element conformal array using a combination of electrical waveguide TTD delay and the 5-bit optical TTD unit has also been demonstrated[30], and was used to scan the antenna beam across an angular range of -60° to +60°.

Wavelength switched optical TTD has been dominated, until recently, by systems which use high dispersion optical fibre in conjunction with a tuneable wavelength laser[31,32]. By tuning the optical carrier wavelength the signal can be made to acquire varying amounts of time delay; 5ns of delay has been reported[32] for 1km of fibre with a dispersion of -98ps/km.nm. Either a single length of fibre can be used[32] or many lengths of fibre can be constructed into a 'fibre-optic prism', Figure 1.6, as reported by *Esman et al*[33]. Here N equal lengths of optical fibre, each with a different net dispersion, are connected, at opposite ends, to the output of a 1xN coupler and N matching photodetectors respectively; each photodetector feeds a single radiating element. For a given optical carrier wavelength the array will radiate an RF beam in a fixed direction;

changing the optical carrier wavelength alters the time delay acquired by each of the N signals and hence changes the radiated beam direction. The fibre-optic prism TTD unit has been used to control a sparsely populated phased array containing 8 active radiating elements, over an RF frequency range of 2GHz to 12GHz[34,35], and in a 2 element sparsely populated array operating over 2GHz to 18GHz[36]. Good agreement between the measured and calculated beam patterns was reported.

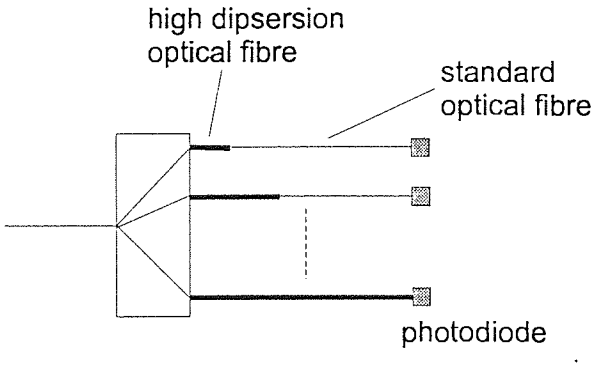

Figure 1.6 'Fibre optic prism'; N equal lengths of optical fibre each of different net dispersion; each provides different amount of delay, and delay can be varied by tuning optical carrier wavelength

Other, non-fibre based, methods of creating optical TTD which have been reported include a delay unit constructed using birefringent crystal segments[37]. Light polarized along one of the principle birefringence axes of the crystal passes through many crystal segments, separated by polarisation rotators, as it travels from the optical source to the receiver at the array element. The time delay is varied by switching the polarization of the light between the two crystal axes, so that it accrues a different time delay in each segment of crystal. Semiconductor integrated photonic waveguide circuits have also been used, on GaAs/AlGaAs [38] and on Lithium Niobate[39] substructures, creating a 3-bit delay line with a maximum delay of 8ps, and a beam steering sensitivity of 1.5° per volt of applied bias voltage, respectively.

While the switched optical TTD approaches described above offer significant advantages over electrical waveguide/cable based systems, their requirement of many optical switches, semiconductor lasers, and 1 to many optical couplers makes them somewhat expensive. Their use of these bulk optic devices also compromises the compact nature of the optical fibre delay lines which they use, and introduces loss into the system. Dispersive fibre based optical TTD is more compact and uses fewer lossy bulk optic elements, but it is not an ideal solution as it uses very long lengths of optical fibre and still requires expensive 1 to many couplers.

A simpler, cheaper, and more compact approach to wavelength switching accesses the inherent advantage of wavelength-selected time delays through the use of a series of Bragg gratings[40]. An array of gratings of different central wavelengths, are fabricated along a single length of optical fibre, with the individual gratings addressed by wavelength tuning the optical source. The total length of fibre traversed by the optical signal is thereby selected and the desired time delay to be acquired by the optical signal chosen. The principles of operation of this type of optical TTD system are described further in 2.2.3 and 5.1. The initial demonstration and subsequent development of an in-fibre Bragg grating based optical TTD element suitable for controlling phased array antennas operating at RF frequencies of up to several gigahertz, forms the driving force behind the work to be reported in Chapter 5.

1.4 In-Fibre Bragg grating sensors

1.4.1 Introduction

Much work has been reported on the use of optical fibre as a sensing element, and it has been used to detect a wide range of measurands, including temperature[41], strain[41,42], electric[43] and magnetic[44] fields, pressure[45] and chemical species[46]. These sensor systems use long lengths of optical fibre as the sensing

element and interferometric detection to determine the effect of the measurand.

Soon after the direct write, holographic method of fabricating in-fibre Bragg gratings was reported, described in 1.2, their potential use as sensors was demonstrated[47,48,49] and sensor multiplexing discussed[49,50]. Placing a fibre Bragg grating under strain or subjecting it to a change in temperature causes its reflection wavelength to change, and by determining the change in wavelength the strain or temperature to which the grating is being subjected may be found; this will be discussed in more detail in 2.3. Fibre Bragg grating sensors are inherently wavelength encoded devices, which offer several advantages over intensity based, sensing schemes. Most notably, the reflection wavelength is an absolute parameter, and therefore it is not affected by losses within the sensor system, due to environmental changes for example, or by variations in the source power level. Uniform period fibre Bragg grating sensors easily lend themselves to multiplexing, where each grating in the sensor arrangement is written with a different wavelength of maximum reflectivity, and a narrow reflection bandwidth, <0.5nm. Wavelength division multiplexing can therefore be used to separate the signals from the different sensors at the receiving end of the system. This can be achieved using an optical spectrum analyser or a scanning spectrometer, but for a real sensor array, in which cost, bulk and weight must be minimised, a more compact wavelength interrogation device is called for. Much interest has been shown in developing such a sensor demultiplexing scheme, and a brief overview of the work reported to date is given below.

1.4.2 Wavelength demultiplexing fibre Bragg grating sensors

The interferometric wavelength measurement techniques used with the optical fibre sensors mentioned in 1.4.1 have also been applied to the demultiplexing of arrays of Bragg grating sensors. *Kersey and Berkoff*[51] have reported a Bragg grating interrogation scheme based on an unbalanced Mach-Zehnder

interferometer which has been used to measure strain, with a resolution of ~0.6nε/Hz$^{1/2}$. The measurement capabilities of the system were restricted by low frequency drift in the interferometer arms, hence it could only measure strains which varied periodically at frequencies of greater than 100Hz. Time division demultiplexing was then applied to this arrangement[52,53] increasing the number of sensors that it could interrogate from 1 to 4, and then to 8. A system using a fibre Fourier transform spectrometer has also been reported[54,55] for the demultiplexing of fibre Bragg gratings. A Michelson interferometer was used to create an interferogram, from which the Fourier transform was computed to obtain the source spectra. Three gratings were multiplexed and a Bragg wavelength sensitivity of ~0.015nm was recorded in the 1550nm region.

In addition to wavelength division multiplexing and time division multiplexing, spatial division multiplexing has also been applied to the interrogation of Bragg grating sensor systems[56,57] A bulk optic transmitting Michelson interferometer[58] has been used as a wavelength discriminator, to interrogate 4 identical gratings in an arrangement capable of multiplexing up to 32 identical gratings. All of the gratings in the sensor array were illuminated simultaneously, with the sensor of interest selected by switching on its associated detector; a strain resolution of 2με and a temperature resolution of ~0.2°C were achieved. The transmitting Michelson interferometer has also been used in series with a Fabry-Perot transmission filter: the Fabry-Perot filter, with a resonance peak bandwidth of ~0.65nm, was used to select the grating of interest, and the Michelson interferometer, free spectral range ~0.98nm, was used to measure the grating wavelength. The spectral characteristics of the filters restricted the absolute wavelength measurement range of each fibre Bragg grating to ~0.65nm, equivalent to a strain measurement range of 650με.

A further bulk optic based Bragg grating sensor interrogation technique uses ratiometric wavelength measurement, first reported by *Melle et al*[59,60]. The system splits the light reflected from the Bragg grating into two beams, one of

which passes through a filter with a wavelength dependent transmission function, while the other is used as a reference signal to compensate for any signal intensity fluctuations; a strain sensitivity of 0.65pm/με was achieved. Since the filter is not wavelength discriminating, each filter can interrogate only one sensor grating, unless time division multiplexing is applied. All optical fibre based ratiometric wavelength determination has also been reported[61] using a wavelength division coupler designed to display a monotonic dependence of splitting ratio on wavelength. A strain measurement resolution of 3με was demonstrated, but again only one grating can be interrogated by each coupler. A highly overcoupled coupler, which also exhibits wavelength dependent coupling, has been used to implement ratiometric Bragg grating sensor interrogation[62], with a strain measurement resolution of 10με, as has a biconical fibre filter[63], which had a dynamic strain resolution of $1.5\mu\varepsilon/Hz^{1/2}$.

Another all fibre based grating interrogation system which has been reported is based on the use of fibre lasers whose lasing wavelength is determined by the central wavelength of the sensor grating: a laser cavity is constructed in a length of rare-earth doped optical fibre using two wavelength matched Bragg gratings, one of which is used as the sensor element and hence determines the operational wavelength of the laser. Fibre-laser sensor systems have been reported which can interrogate single gratings and multiple gratings[64,65], through the application of mode-locking. An alternative approach to the fibre-laser sensor has been reported in which a much smaller laser cavity is used, and the whole laser cavity is the sensing element[66,67,68]; interferometric wavelength detection was used to interrogate these sensors. Fibre lasers may also be used as tuneable wavelength sources for interrogating Bragg grating sensors[69]; the laser wavelength is tuned through the wavelengths of the grating sensors, and the wavelengths which return the maximum signal intensity correspond to the grating central wavelengths. This arrangement achieved a wavelength measurement resolution of ~2.3pm.

Acousto-optic tuneable transmission filters can be used to interrogate an array of fibre Bragg grating sensors illuminated by a broadband source, with the filter output detected by a broadband receiver. This was first reported by *Xu et al*[70], to track the central wavelength of a single grating sensor exposed to temperature variations, and then developed to interrogate multiple strain sensors[71,72], giving a strain sensitivity of 0.4με; a simple linear model which describes the grating wavelength tracking has also been presented[73]. A similar system was reported by *Coroy et al*[74] which achieved a strain resolution of 2.24με.

All optical fibre grating sensor demultiplexing can also be achieved by using an arrangement of matched gratings. In this approach each sensor grating has a twin receiving grating, which is tuned to match the sensor grating wavelength, thus reflecting light into a photodetector, or spectrum analyser. The array of receiver gratings can either be tuned all together[75] or individually[76], by fixing the gratings to piezo-electric transducers and applying strain to them; the photodetector output is used in a feedback loop to maximise the reflected signal and hence match the sensor and receiver grating wavelengths. Other all optical sensor demultiplexing schemes include a feedback loop controlled in-fibre Fabry-Perot tuneable filter[77], which gave a strain measurement resolution of 3με for an array of 4 gratings, and strain-tuned phase-shifted Bragg gratings which comprise single or multiple pass bands within a wide stop band grating; the application of this type of filter to sensor grating interrogation will be discussed further in Chapter 4.

These sensor demultiplexing schemes are based upon wavelength measurement devices which are capable of interrogating, at best, a few Bragg grating sensors, and rely on time and spatial division multiplexing to increase their capacity towards the needs of a real sensor system. In order to simplify the demultiplexing scheme architectures required for a real Bragg grating sensor system, comprising hundreds of sensing elements, a wavelength measurement device capable of interrogating tens of gratings is called for. One such potential

device is a liquid crystal filled Fabry-Perot etalon tuneable transmission filter. This has previously been used as a wavelength selection device in optical communication systems[78,79], and its reported transmission characteristics suggest that it is suitable for use as a sensor demultiplexing element. The application of one particular form of this type of wavelength selective filter to the interrogation of Bragg grating sensor forms a large part of the work which was carried out on in-fibre Bragg grating strain sensor systems, and will be reported in detail in chapter 4.

1.4.3 In-Fibre Bragg grating sensors in smart structures

A smart structure is one which senses its surrounding environment, or its own condition, interprets the sensory data, makes a decision and then responds to any changes that it has detected. For example, a smart structure designed to operate at a specific temperature will detect any temperature changes, determine the sense of the change, and implement action to return its temperature to the correct value, by, say, turning on some peltier devices mounted on its surface. Aircraft incorporating smart structure technology could monitor their flight loads, structural health and airworthiness, and reduce their vibration. They could also implement real-time, in-flight corrective action in response to any mechanical failure and schedule their maintenance programmes, which would result in lower operational costs and increased safety standards. Further in the future these structures could be designed to be 'intelligent', using neural networks to improve their decision making[80].

Smart structures consist of a sensor, or a network of sensors, which convert environmental parameters into electrical or optical signals for processing, a processor, and actuators to maintain the smart structure in its desired state. Although the sensors in a smart structure measure temperature or strain, the measurand may be one of a wide variety of variables, including deformation, shape, force, vibration, damage, pressure, magnetic or electric field strength, and chemical concentration; all of which can be converted to temperature or

strain by an appropriate sensor. Most of the sensors used to date in smart structures[81] have been electrical, such as metal-foil resistive-strain gauges and piezoelectric ceramic strain gauges. Both of these sensor types require a pair of electrical wires to monitor them, and suffer from transverse strain sensitivity error. Fibre optic sensors[82] offer the advantages of being extremely small and light, immune to electromagnetic interference (EMI), and corrosion and fatigue resistant. In addition, they are compatible with composite materials, and do not cause severe weakening of the structure in which they are embedded[83].

As aerospace platforms become more advanced they will be required to perform to increasingly tight specifications which will necessitate the use of materials which are of lighter weight, greater strength, and have the ability to change their parameters, such as shape, stiffness, and electrical and mechanical properties, as demanded. In aerospace applications one of the most important design considerations is the minimisation of the weight of the craft, and fibre optic sensors can offer many advantages over conventional sensors in this area[84]. Since they are EMI immune, fibre optic sensors do not require the costly, heavy shielding that is used to support electrical sensors. The ability to multiplex many sensors on a single optical fibre line offers further weight reductions, and minimises the number of points of ingress into the structure. Problems with routing other electrically conductive paths and lightening strikes are also simplified due to the passive dielectric nature of optical fibre.

A technique based on the differential sensitivities of dual mode and polarimetric sensing systems has been reported[85] which can simultaneously resolve temperature and strain variations experienced by a structure. An 80cm length of optical fibre was used as the sensing medium, and strain and temperature resolutions of 20με and 1K were achieved, over measurement ranges of 2με and 45K respectively. The successful embedding of polyimide coated Bragg gratings in glass-fibre reinforced polyester has been achieved[86], and the gratings used to measure strain with a sensitivity of 0.65nm/1000με.

Damage assessment using optical fibre sensors has also been reported[83], in which the application of a large force on the structure causes the sensor to fail. Optical fibre based sensing has also been applied to aircraft wing leading edge damage assessment[83], in which the fibres undergo a special etching process to preset their damage sensitivity.

Smart structure systems which utilise Bragg gratings as the sensor elements have also been reported, most notably the embedding of 15 gratings within the precast concrete deck support girders of a two span road bridge has been reported by *Measures et al*[87]. The bridge, constructed near the city of Calgary in Canada, was the first in the world to test the use of carbon composite tendons as a replacement for steel tendons. It was demonstrated that the sensors were capable of measuring both the strain relief experienced by the steel and carbon composite tendons within the concrete girders, as the concrete set, and the internal strain within the girders associated with static and dynamic loading of the bridge with a truck. The sensor demultiplexing system which was used comprised four independent erbium doped fibre lasers, pumped from a single 980nm semiconductor laser diode, the wavelengths of which were determined by their respective remote Bragg gratings. A strain measurement resolution of a few $\mu\varepsilon$ was recorded for a measurement range of 5000$\mu\varepsilon$.

The development of in-fibre Bragg grating sensor demultiplexing systems is vital to the future of optical fibre sensor based smart structures. Systems capable of interrogating hundreds, or even thousands, of sensor signals will be required to monitor, for example, entire aerospace or aircraft bodies, buildings and bridges. The liquid crystal Fabry-Perot filled etalon based demultiplexing scheme mentioned in 1.4.2 can, in principle, offer a compact, lightweight demultiplexing architecture suitable for use with smart structures, particularly those in spacecraft and aircraft, where weight and size must be minimised. Strong, lightweight composite materials are being developed for use in these structures and both the sensors and the demultiplexing system must

complement their properties. The initial part of the work to be reported on Bragg grating strain sensors was concerned with the performance of grating sensors embedded within a carbon composite material, and will be discussed in chapter 4.

1.5 Overview and aims

This thesis is concerned with two distinct applications of in-fibre Bragg grating arrays, and as such there are two main objectives. The first is to investigate the application of in-fibre Bragg gratings as strain sensors in a composite material smart structure, and to develop a compact, lightweight and potentially low cost method of demultiplexing many sensors, which can then be applied, by combining it with spatial and time division multiplexing, to the interrogation of hundreds of sensors in a real smart structure system. The second goal is to explore the utilisation of arrays of Bragg gratings as true-time delay control elements for phased array antennas. In addition to these, the Bragg gratings which are to be used in these applications must be successfully fabricated.

Much work has been reported on various approaches for interrogating Bragg grating sensor arrays, but there is still a requirement for a wavelength demultiplexing element which can be used to measure the wavelengths of tens of sensors. No previous work has been reported on the use of fibre Bragg grating arrays as true time delay elements, although the principle has been discussed[40], hence a practical demonstration of the concept is needed, followed by some development of this type of time delay element.

This chapter has given an introduction to the relevant areas of research, so that the reader may view the work which will be reported in the following chapters in the context of the current state of the fields. Chapter 2 will be concerned with discussing the appropriate theory which supports these subject areas,

allowing the reader to follow the results presented in the subsequent chapters. In chapter 3 the fabrication processes used to produce the gratings used in the work which will be reported in chapters 4 and 5 will be described, and results relating to the fabrication and characterisation of these gratings will be presented. Results pertaining to the investigation of the use of Bragg gratings as embedded strain sensors, in a carbon composite board, will be reported in chapter 4, followed by the presentation and discussion of results concerning the development of a compact, lightweight, and potentially low cost sensor demultiplexing system. Chapter 5 will cover the initial investigation and subsequent development of fibre Bragg grating array based true-time delay elements for the control of phased array antennas. Discussions of the results presented will be offered at the end of each chapter, and an overall conclusion of the work reported herein will be given in chapter 6, including the discussion of relevant results reported by other authors since the conclusion of this work, and further developments which could be implemented to carry this work forward.

2. Background

2.1 In-fibre Bragg gratings

2.1.1 Basic grating theory

A Bragg grating is photoinscribed in the core of an optical fibre as a spatial modulation of the refractive index through exposure to a pattern of ultra-violet (UV) interference fringes. Light travelling down the fibre will be reflected by this periodic index modulation if its wavelength matches the Bragg resonance condition, given by

$$\lambda_B = 2n_{eff}\Lambda$$

Equation 2-1

where λ_B is the Bragg resonance wavelength of the grating, n_{eff} is the effective refractive index of the fibre core, and Λ is the period of the refractive index modulation, related to the wavelength of the UV writing beams, λ_{UV}, and the angle between them, θ, Figure 2.1, by

$$\Lambda = \frac{\lambda_{UV}}{2\sin\theta/2}$$

Equation 2-2

The grating can be described as a uniform sinusoidal modulation of the refractive index throughout the core, given by[88]

$$n(z) = n_{core} + \Delta n\left[1 + \cos\left(\frac{2\pi z}{\Lambda}\right)\right]$$

Equation 2-3

where n_{core} is the refractive index of the unexposed core and Δn is the amplitude of the photoinduced refractive index change.

The interaction of guided waves with a uniform-period grating can be modelled using coupled mode theory in which a pair of first-order differential equations are used to describe the amplitudes of the forward and backward travelling waves. The grating provides a coupling mechanism between the two modes, enabling energy to be transferred between them.

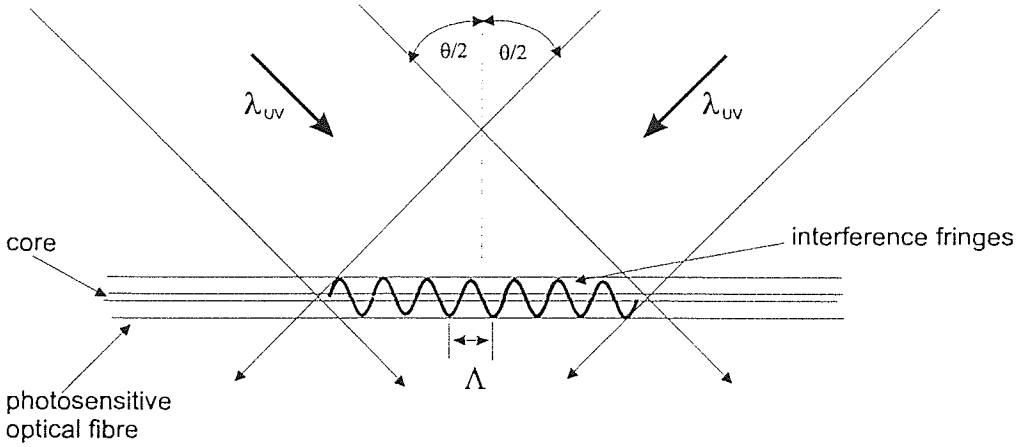

Figure 2.1 Fabrication of a Bragg grating in optical fibre core by interfering two UV beams of wavelength λ_{UV}

The formation and solution of these equations is well known[89,90] and gives the reflectivity of the grating, R, as

$$R = \frac{\kappa^2 \sinh^2(SL)}{\delta\beta^2 \sinh^2(SL) + S^2 \cosh^2(SL)} \quad for \kappa^2 > \delta\beta^2$$

Equation 2-4

and

$$R = \frac{\kappa^2 \sin^2(QL)}{\delta\beta^2 - \kappa^2 \cos^2(QL)} \; for \kappa^2 < \delta\beta^2$$

Equation 2-5

where L is the grating length, κ is the coupling coefficient and $\delta\beta = \beta - \beta_g$ is a measure of the detuning of the incident light from exact Bragg resonance. The mode propagation constant, β, is given by

$$\beta = \frac{2\pi n_{eff}}{\lambda}$$

Equation 2-6

where λ is the free-space wavelength, and n_{eff} is the mode effective index; the grating wavenumber, β_g, is expressed as

$$\beta_g = \frac{m\pi}{\Lambda}$$

Equation 2-7

where m is an integer. Variables S and Q are given respectively by

$$S = \left(\kappa^2 - \delta\beta^2\right)^{1/2}$$

Equation 2-8

and

$$Q = \left(\delta\beta^2 - \kappa^2\right)^{1/2} = iS$$

Equation 2-9

Assuming no loss, the normalised transmission of the grating is described by $T = 1\text{-}R$.

Maximum reflectivity for a uniform grating occurs when $\delta\beta=0$ *i.e.* when the Bragg condition is met such that

$$p\lambda = 2n_{eff}\Lambda \equiv \lambda_B$$

Equation 2-10

where λ_B is the Bragg wavelength of order p. The strongest interaction occurs for the fundamental Bragg order, when p=1. For $\delta\beta$=0, Equation 2-4 simplifies to give a maximum reflectivity of[88]

$$R_{max} = \tanh^2(\kappa L)$$

Equation 2-11

The Equation 2-11 indicates that for increasing κL the peak reflectivity of the grating rises to unity, accompanied by an increase in the amplitude of the sidelobes and a broadening of the spectral bandwidth; illustrated in Figure 2.2.

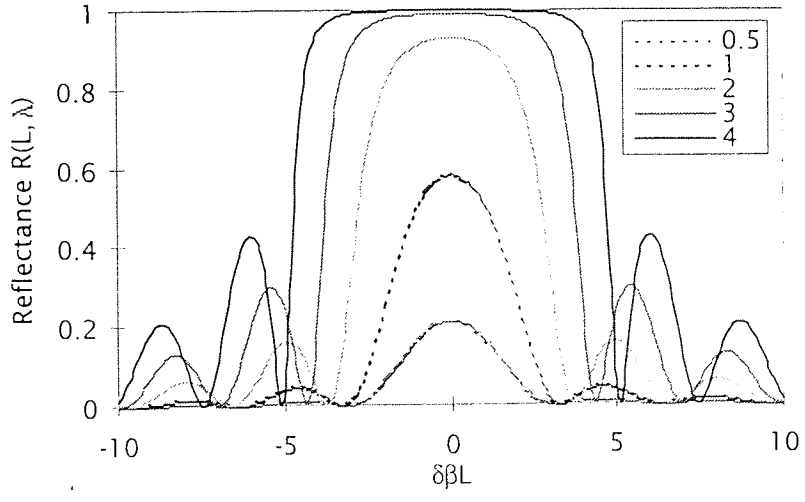

Figure 2.2 Reflectance R(L,λ) as a function of δβL for a periodic grating with κL values of 0.5, 1, 2, 3, and 4

From Equation 2-4 the full grating bandwidth, $\Delta\lambda$, measured between the zeros on either side of R_{max} is given by[88]

$$\Delta\lambda = \frac{\lambda_B^2}{\pi n_{eff} L}\left[(\kappa L)^2 + \pi^2\right]^{1/2}$$

Equation 2-12

For a uniform sinusoidal refractive index modulation in the core the coupling coefficient, κ, may be described by[88]

$$\kappa = \frac{\pi \delta n}{\lambda_B}\eta$$

Equation 2-13

where η is the fraction of the normalised mode power that exists within the fibre core, and which can therefore interact with the grating; assuming that the grating is written uniformly throughout the core. η may be approximated by

$$\eta \approx \frac{1}{V^2}$$

Equation 2-14

where V is the V-value of the fibre.

This model is suitable for many cases, but it does have limitations in that it deals with a simplified version of the experimental situation and cannot be applied to gratings in which the period or coupling coefficient varies with length. A more general approach appropriate for tackling such gratings solves the coupled mode equations by a process of numerical iterations[91,92], or by reducing them to a single Riccati differential equation[93]. Another method for

modelling aperiodic gratings uses the transfer matrix formalism, which will be discussed further in section 5.8.2.2.

2.1.2 Fabrication principles

Morey et al[94,95] demonstrated that Bragg gratings can be formed in optical fibre by exposing the core to an interference pattern of overlapping coherent beams of UV radiation through the side of the fibre; the gratings used in this work were fabricated using this transverse holographic exposure technique (the experimental arrangement will be discussed further in section 3.1.1). The UV radiation is split into two equal intensity beams and then recombined to produce an interference pattern within the core, normal to the fibre axis. The intensity of the pattern can be increased by focusing the beams on the fibre with a pair of cylindrical lenses. The UV interference pattern produces a permanent periodic variation in the refractive index of the fibre core, see 2.1.3, forming a phase grating which acts like a band rejection filter. Wavelengths which are not in resonance with the grating are passed, while those which satisfy the Bragg condition are strongly reflected. The central wavelength of the grating is sensitive to changes in temperature and axial strain; see 2.3.1and 2.3.2.

The transverse holographic fabrication technique enables easy selection of Bragg wavelength and allows the gratings to be formed at localised points along the fibre, hence a large number of gratings can easily be written along a single length of fibre[96]. From Equation 2-1 and Equation 2-2, the wavelength reflected by a uniform-period grating can be described by

$$\lambda_B = \frac{n_{eff}\,\lambda_{UV}}{2\sin\theta/2}$$

Equation 2-15

The Bragg wavelength can therefore be controlled by varying either the angle, the UV wavelength, or both. As the grating grows there is a shift in the Bragg wavelength due to an increase in the effective refractive index of the core during exposure[97].

The grating reflectivity, at the central wavelength, is given by Equation 2-11. The fractional index change ($\Delta n/n$) produced in the fibre core is of the order of 3×10^{-5}. The strength of the index perturbation is not constant along the length of the fibre, but decreases from the centre to the edges due to the gaussian intensity profile of the writing beams. Evidence of the taper in the depth of the index perturbation is apparent in the spectral line shapes of the grating reflections which exhibit very low side lobes[98].

Gratings in which the period varies linearly with distance can be fabricated by recording the interference pattern created between a collimated laser beam and a converging one[99,100]. The fibre is located in the z=0 plane, Figure 2.3, the collimated beam is incident on the fibre at an angle $\theta/2$ to the normal to this plane, and the angle subtended by the collimated beam and the bisector of the converging beam is θ. The interference pattern produced where the two beams overlap in space, arranged to be within the fibre core, is recorded over a length s of fibre.

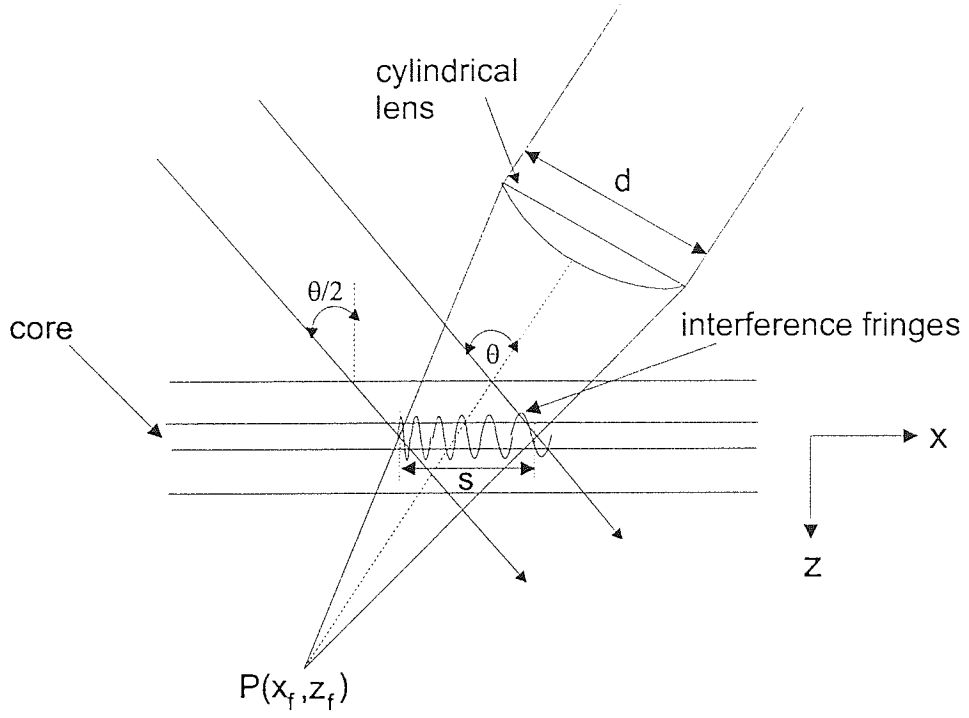

Figure 2.3 Fabrication of a chirped Bragg grating using method of dissimilar wavefronts

The output of a 244nm laser is 50:50 power split to produce the two writing beams, and the converging beam passed through a cylindrical lens of focal length *f*, width *d*, whose focus is located at the point $P(x_f, z_f)$. Simple geometry then relates the focal line co-ordinates (position of the focal plane) to *f*, *s*, *d*, and θ [99]:

$$z_f = \tfrac{1}{8} s \frac{\cos\theta + \cos(2\phi)}{\sin(2\phi)}$$

Equation 2-16

$$x_f = -z_f \tan\left(\tfrac{1}{2}\theta\right)$$

Equation 2-17

where

$$\phi = \tan^{-1}\left(\frac{\frac{1}{2}d}{f}\right)$$

Equation 2-18

The electric field in the fibre core (z=0) is the sum of the collimated and converging waves, given by[99]

$$E(x, z=0) = A\exp\left[-jkx\sin\left(\tfrac{1}{2}\theta\right)\right] + a\exp\left[jk\left\{\left(x-x_f\right)^2 + z_f^2\right\}^{1/2}\right]$$

Equation 2-19

where k=2π/λ is the wave number for the incident fields, and A and a are the amplitudes of the collimated and converging beams respectively. The period of the grating is given by[99]

$$\Lambda(x) = \frac{\lambda}{\sin\left(\frac{1}{2}\theta\right) + \left(x-x_f\right)\Big/\sqrt{\left(x-x_f\right)^2 + z_f^2}}$$

Equation 2-20

2.1.3 Photosensitivity and hydrogenation

The dominant source of photosensitivity in optical fibre is defects associated with oxygen deficiencies in the GeO_2-SiO_2 glass matrix. A mechanism for the induced refractive index change in the fibre has been suggested by *Hand and Russell*[97] in which Ge-Si bond breakage, driven by two-photon-absorption at 488nm, yields positively charged Si^+ sites (Ge-E' centres) and a free electron. The Si^+ ion is held in the matrix while the electron has enough energy to escape and subsequently become trapped at neighbouring defect sites, creating Ge(1) and Ge(2) colour centres. Formation of colour centres in the glass alters its UV absorption spectrum, producing a change in refractive index through the

Kramers-Kronig principle[97]. The colour centre photosensitivity model is supported by many experimental observations[101,102,103,104,105], including those reported by *Malo et al*[106] that the photosensitivity of standard germanosilicate optical fibre can be irreversibly removed by annealing the fibre in air at a temperature of 1200°C. However, it has not been able to explain all experimental findings[107,108,109], and this has lead to the proposal of a second model[110,111] based on glass densification induced by the photoionisation of the GeO defects. There is also some discussion about whether photoionisation is a one-photon process[112,113] or a two photon process[114,115,116]. It is currently believed that more than one process is occurring within the fibre during grating fabrication, with the type of fibre, writing power and writing wavelength involved in determining the relative importance of each process.

Optical fibre in which the core is co-doped with boron and GeO_2 is more photosensitive than fibres containing the same amount of GeO_2 but no boron[117], and the UV exposure time required to saturate the refractive index change is greatly reduced. The presence of boron in germanosilicate optical fibre causes stress within the glass matrix, which is believed to increase the number of GeO defect sites and hence raise the photosensitivity of the glass. The reduction in UV exposure time required to saturate the refractive index change in boron-germania codoped fibre supports the densification model of refractive index change[110,111].

The photosensitivity of optical fibres containing germania may be increased through the use of a high-pressure hydrogen-loading technique[118,119], where the fibre is soaked in H_2 at a pressure in the range 20-750 atmospheres and at a temperature of between 20°C and 75°C, for a period of several days; typical values are 150atm and room temperature. The presence of dissolved molecular hydrogen allows the photoinduced reaction which produces the refractive index change to occur at all Ge sites, not just at GeO defects, however its presence alone does not produce any discernible increase in absorption near 240nm. The UV light used to write the gratings appears to produce dissociation of the H_2

molecules, forming Si-OH and/or Ge-OH groups in the glass matrix, oxygen-deficient Ge defects, and a large permanent refractive index change. The photoinduced refractive index change in hydrogenated fibres is permanent, and typically two orders of magnitude greater than that achieved for non-hydrogen-loaded fibre of the same type[120]. A side-effect of hydrogen loading is the appearance of loss at 1.39μm due to absorption by the OH groups; this can be overcome by loading the fibre with deuterium instead of hydrogen[121]. The presence of molecular hydrogen in the optical fibre core can change the effective refractive index seen by guided optical modes by as much as 0.05%[122].

The hydrogen starts to diffuse out of the fibre immediately it is removed from the pressure vessel, so grating fabrication must be carried out reasonably quickly. It has been observed that the wavelength of a grating written in hydrogenated fibre initially increases in wavelength, over a period of a few hours, and then decreases to a central wavelength shorter than the value measured immediately after inscription[122]. As described above, exposure to UV illumination causes the dissolved H_2 molecules to dissociate, and Ge-OH bonds to form. H_2 dissociation occurs throughout the fibre, but the Ge-OH bond forming reaction occurs only in the core; the dissociated molecules in the cladding most likely recombine. Immediately after UV exposure the fibre core is virtually emptied of dissolved hydrogen, but the cladding is still fully loaded and these H_2 molecules undergo isotropic dispersion. For the first 5 hours after exposure this has the effect of partially refilling the fibre core with H_2, increasing its refractive index and causing the central wavelength of the Bragg grating to increase. Over a longer time period, however, all of the hydrogen disperses out of the fibre, and the refractive index returns to its original 'empty' value. This slow Bragg grating wavelength drift can be removed by annealing the fibre after the grating has been written[123]. The effect on grating wavelength of post-exposure diffusion of hydrogen was characterised for the various types of fibre used in this work, and will be discussed in detail in 3.2.3.

Dissolved hydrogen in fused silica is an example of both physical and chemical solubility of a polyatomic molecule[124]; physical solubility is solution without molecular dissociation, involving relatively weak van der Waals bonding of the dissociated species with the glass, and chemical solubility infers molecular dissociation, and hence relatively strong chemical bonding of the dissociated species with the glass. The solution of gases in a glass solid is generally restricted to smaller molecular species which can interstitially diffuse through the glass matrix, when the glass is a rigid solid.

2.1.4 Grating stability

Practical use of fibre Bragg gratings in sensor networks or as time delay elements requires that the properties of the gratings remain stable over the lifetime of the system. Accelerated ageing tests have shown that the drift in central wavelength observed in gratings fabricated in hydrogenated fibre, due to the out-diffusion of unreacted H_2, can be removed by a post-exposure annealing step[123], giving the grating a lifetime of ~25 years. It has also been observed that when a grating is heated to temperatures in the range 80°C to 425°C and then allowed to return to its initial temperature, the Bragg central wavelength undergoes a permanent shift to shorter wavelengths[125]. The magnitude of the shift depends upon the type of fibre and the exposure conditions during fabrication. The size of this effect can be significantly reduced by annealing the grating at a temperature in excess of its anticipated maximum operating temperature[125].

Bragg gratings written in non-hydrogenated germanosilicate optical fibres exhibit a temperature dependent decay of the UV-induced refractive index change, Δn, with time. *Erdogan et al*[126] have shown that the decay can be described by a 'power-law' function of time with a small exponent ($<<1$), which results in an initial rapid decay of Δn with time, followed by a decreasing rate of decay as time progresses. The decay is also highly temperature dependent, with a reduction in the index change of several percent over a period of a few years

at room temperature. A simple model of the physical mechanism which causes this thermal decay has been proposed[123] in which the carriers excited during UV exposure are trapped in a continuous distribution of energy states, and the rate of thermal depopulation is dependent on the applied temperature and the depth of the trap states. For a given temperature approximately all of the electrons in traps of up to a certain depth will be liberated by the decay process over a sufficiently long period of time. Therefore the decay history of a grating must be taken into account when predicting its subsequent decay behaviour on the application of a given set of conditions. This characteristic of the decay can also be utilised to preanneal a grating for applications which require stable grating properties over long times, erasing the portion of the UV-induced refractive index excursion that would decay over the working lifetime, and leaving only the very stable portion of the index change.

One of the attractions of optical fibre based sensing is its potential use in hostile environments, such as those subject to ionising radiation. *Niay et al*[127] have demonstrated that no significant change in the spectral characteristics of Bragg gratings is produced under exposure of the gratings to γ–radiation at dose rates of between 14Gy/h and 122Gy/h. A dose rate of 10Gy/h is comparable to that found in the vicinity of the reactor chamber in nuclear facilities under normal operating conditions.

2.2 Phased array antennas

2.2.1 Beam formation

2.2.1.1 Huygen's wavelets

In order to explain the bending of light when it is diffracted Huygens[128] proposed that *each point on a wave front may be regarded as a new source of waves.* Assuming that the secondary wavelets radiated by each point on the original wavefront all have the same phase, the new wavefront, plane of

constant phase, will be the same shape as the original one: a plane wavefront will produce a plane wavefront, and a circular wavefront will produce a second circular wavefront, centred upon the same point. If the secondary wavelets do not all radiate in phase, the new wavefront will be described by a plane which passes through points of equal phase on the secondary wavelets.

Huygen's principle may be applied to a planar RF antenna array, in order to determine the shape and direction of the beam produced by it. Treating the antenna array as the original wavefront, and the individual radiators as the sources of the secondary wavelets, Huygen's principle describes, for zero phase shift between the radiators, the production of a plane wavefront whose propagation axis lies along the array normal. Similarly, plane wavefronts propagating at an angle to the array normal, or non-planar wavefronts, can be produced by implementing various values of phase shift between the individual radiators

2.2.1.2 Mathematical description of phased array antenna beam formation

A simple description of phased arrays may be obtained by considering an array of isotropic radiating elements equally spaced along a straight line and only allowing continuous wave signals; the reciprocity principle is applied, in which the array far field pattern appears the same from both transmitting and receiving viewpoints. A more detailed theory of linear arrays is given by *Schelkunoff*[129]

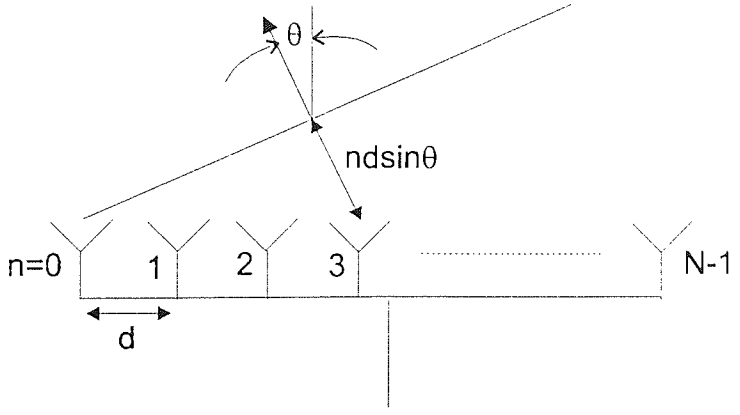

Figure 2.4 Basic linear array comprising N isotropic resonators

Consider an elementary linear array comprising N isotropic resonators, equally spaced by a distance *d*, Figure 2.4. In receive mode, a plane wave incident on the array, from a direction θ to the array normal, will produce a current, i_n, in the *nth* array element of[130]

$$i_n = Ae^{jnkd\sin\theta}$$

Equation 2-21

where A is a complex constant, known as the array factor, related to the instantaneous amplitude and phase of the plane wave and k is the wave number:

$$k = \frac{2\pi f}{c} = \frac{2\pi}{\lambda}$$

Equation 2-22

in which f is the RF signal frequency and c is the free space velocity of light.

From Equation 2-21 it follows that the phase of the current in the *nth* element leads that of the current in the *(n+1)th* element by[131]

$$\Delta\psi = kd\sin\theta$$

Equation 2-23

This corresponds to a difference in time of arrival of the plane wave at the two elements of

$$\tau = \frac{d\sin\theta}{c}$$

Equation 2-24

If a control element is placed behind each array element, with a transfer coefficient for the *nth* element of[130]

$$\frac{i_n'}{i_n} = a_n e^{j\psi_n}$$

Equation 2-25

where a_n and ψ_n are the real current gain and phase shift of the control element, then the sum of the currents from all *N* elements in the array is given by

$$E_a(\theta) = \sum_{n=0}^{N-1} a_n e^{j(\psi_n + nkd\sin\theta)}$$

Equation 2-26

neglecting the constant *A* from Equation 2-21. This is the response of the array to a signal arriving from direction θ to the array normal, given as a set of real currents a_n, the array-amplitude taper, and real phase shifts ψ_n, the phase taper.

In order to produce a maximum output current from the receiving array, for an RF signal incident at an angle θ_0 to the array normal, the signals from all of the array elements must be combined in phase. The set of ψ_n's in Equation 2-26 will therefore be given by

$$\psi_n = -nkd \sin\theta_0$$

Equation 2-27

indicating that a linear phase taper is required across the array: a constant phase difference should be applied between adjacent elements. In transmit mode, applying the reciprocity principle, a main beam will be produced in direction θ_0 when the phases of the signals emitted by the individual radiating elements in the array are set to the phase taper given by Equation 2-27.

2.2.2 Beam steering and beam 'squint'

In order to carry information, an RF beam must contain a bandwidth of frequencies, of the order of a few hundred MHz. The central RF frequency is chosen in conjunction with the antenna aperture dimensions to produce the required beam diameter, at the 3dB intensity point, for operation over the chosen range.

The bandwidth available to a phased array antenna is determined by the characteristics of the components within the antenna, such as the radiating elements, phase-shifters and the feed network. The radiating elements used in phased array antennas have been designed to operate over a wide range of frequencies, and, in practice, do not produce any bandwidth limiting effects. To distribute the RF signal to the radiating elements in an array either a corporate (equal-line-length parallel feed) or space feed network[131] can be used. Phased array antennas generally use corporate feeds, which do not exhibit any bandwidth limiting effects since all signals travel an equal distance from the RF

signal source to the antenna elements. This leaves the phase shifters as the components most likely to limit the antenna bandwidth.

Taking the first derivative of Equation 2-27 indicates that for a fixed phase taper, a fixed set of ψ_n's, the antenna beam will shift from its original direction by an amount[130]

$$\Delta\theta_0 = -\tan\theta_0\left(\frac{\Delta\omega_m}{\omega_m}\right)$$

Equation 2-28

if the microwave frequency undergoes an instantaneous change, $\Delta\omega_m$. This effect, known as 'beam squint', causes the beam pattern to scan with frequency, and results in reduced antenna beam power in the designed direction, θ_0. From Equation 2-28 it follows that an RF signal comprising a wide range of frequencies will produce a transmitted beam in which each frequency component propagates in a different direction, hence only a small RF signal bandwidth can be used if most of the beam power is to reach the designated target. In order to overcome the bandwidth limiting nature of beam squint, arrays requiring wide instantaneous signal bandwidth use true time delay units instead of microwave phase shifters to steer the antenna beam; for example, *R.J.Mailloux*[132] reported that when the RF frequency was switched from 1.9GHz to 9.0GHz in an antenna controlled by true time delay, the spatial position of main beam changed by only 0.5^0, compared to a beam squint of the order 12.5^0 under non-true-time delay control.

2.2.3 True time delay control of phased arrays

In true-time-delay control of phased array antennas beam squint is removed by compensating for the path difference to the phase front between adjacent radiating elements: the delay line to the radiator with the shorter path to the

microwave phase front is lengthened. For a particular beam angle θ_0 a fixed set of delay lines is designed to compensate, at all frequencies, for the differences in path length to the radiating elements[132]. The RF signal radiated by the *(n+1)th* element in the array must travel through a delay line of length $nL(\theta_0)$, where

$$L(\theta_0) = \frac{v_m d \sin\theta_0}{c}$$

Equation 2-29

for a microwave group velocity in the delay line of v_m. This corresponds to a time delay of

$$t_n(\theta_0) = \frac{nd \sin\theta_0}{c}$$

Equation 2-30

The phase taper required to produce a maximum array output in the direction θ_0, for all RF signal frequencies, ω_m, is therefore given by

$$\psi_n = -\omega_m t_n(\theta_0)$$

Equation 2-31

True time delay control of phased array antennas can be implemented using two different types of delay line: electrical waveguide and optical fibre. Electrical waveguide based true time delay control faces the problem of weight and expense of the feed networks. The advantages offered by optical time delay lines[133] include: the size and weight of the feed network are orders of magnitude less than microwave or millimetre wave feeds; the low loss and wideband characteristics of the optical components mean no restrictions on the RF frequency, and bandwidth, which can be used; and there is no signal leakage.

2.3 Fibre Bragg grating sensors

2.3.1 Temperature sensitivity

A variation in the temperature applied to an in-fibre grating will induce a shift in Bragg wavelength through a change in the grating spacing caused by thermal expansion of the fibre, and a change in the core refractive index due to the thermo-optic effect. The fractional change in the Bragg wavelength, λ_B, for an applied temperature change of ΔT, is given by[94]

$$\frac{\Delta\lambda_B}{\lambda_B} = (a + \xi)\Delta T$$

Equation 2-32

where a is the thermal expansion coefficient for the fibre, 0.55×10^{-6} for fused silica, and ξ is the thermooptic coefficient, 8.3×10^{-6} for the germania-doped silica core[134]. The change in the refractive index due to the thermo-optic effect is the dominant cause of the wavelength shift. A grating wavelength tuning sensitivity of 9pm/°C has been achieved[135] in the 1550nm wavelength region.

2.3.2 Strain sensitivity

Application of axial strain to a Bragg grating produces a shift in the central wavelength through a change in the grating spacing, and through a photoelastic induced variation in the core refractive index. The fractional change in the Bragg wavelength, λ_B, is given by[94]

$$\frac{\Delta\lambda_B}{\lambda_B} = (1 - p_e)\varepsilon$$

Equation 2-33

where ε is the axial strain, and p_e is the effective photoelastic constant, equal to 0.22 for germanosilicate glass[136]. A strain sensitivity of 1.20pm/με has been

reported[137] in the 1550nm wavelength regime, which is in good agreement with Equation 2-33.

The maximum axial tensile strain that can be measured using Bragg gratings is limited by fibre strength. Young's modulus of fused silica fibre[138] is ~7x10^{10}Pa. A maximum strain of ~1% can be applied to fibre that has been proof tested at 690x10^{6}Pa before the fibre strength begins to degrade, and the fibre eventually breaks, limiting the wavelength tuning range to the order of 10nm. Silica is 23 times stronger under compression than under tension, and wavelength tuning of a single-frequency, erbium-doped, Bragg grating fibre laser over a 32nm range in the erbium fluorescence bandwidth has been achieved through compression tuning of a Bragg grating[139].

Measurement of the strain applied to a grating may also be used as an indirect measure of other quantities by applying various special coatings to the optical fibre; the coating converts the effect of the chosen measurand into a strain on the coated section of fibre. Polymer materials with large thermal expansion coefficients, such as Nylon-6 and PTFE, have been used to measure temperature in this manner, enabling a temperature sensitivity of 0.15nm/°C at 1550nm to be recorded[140]. Pressure sensing can be achieved by housing the grating in a glass bubble[141] which converts pressure induced changes in the bubble diameter into strain on the grating; producing a pressure sensitivity of 27.6pm/MPa at 1300nm. Other coatings that may be used include nickel for the measurement of magnetic fields, and PVF_2 for electric fields.

2.3.3 Simultaneous measurement of temperature and strain

Wavelength stability over a range of operating temperatures is vital for many applications of fibre Bragg gratings including strain-based sensing systems, true-time-delay elements, and wavelength-division-multiplexed optical

communication systems. A grating mounting system which compensates for the temperature dependence of the grating wavelength has been reported[142] in which temperature variations induce an opposite sense strain in the fibre to offset the temperature induced wavelength change. Temperature independent strain sensing has been performed using a chirped Bragg grating fabricated in a length of tapered optical fibre[143]. A chirped grating was inscribed in tapered fibre with a taper profile such that when tension is applied to the fibre a strain gradient is created along the grating, inducing a linear chirp in the grating spectral profile. A temperature independent strain measurement resolution of 1% was reported. A method of simultaneous measurement of temperature and strain has also been reported by *Xu et al*[144] which used two, superimposed, Bragg gratings of different wavelength (850nm and 1300nm). As the photoelastic and thermo-optic coefficients of fused silica are wavelength dependent this means that each grating will experience a different wavelength change when subjected to the same level of strain, allowing the temperature and strain to be measured concurrently.

Bragg grating sensor applications such as smart materials require the simultaneous measurement of temperature and strain at a single point in the system. A method using a fibre Bragg grating and a fibre polarisation-rocking filter[145,146] has been reported[147] which allows the simultaneous measurement of strain and temperature to an accuracy of 165με and 1.5°C respectively. The two filters are written at the same point on the fibre and the measurements rely on the different dependencies of the fibre refractive index and birefringence on temperature and strain. *Xu et al*[148] have reported a method using two Bragg gratings, of central wavelengths 850nm and 1300nm, written at the same point on the sensing fibre. The photoelastic and thermo-optic coefficients of the fibre are wavelength dependent, hence the wavelength shift experienced by each grating will be different for the same applied strain and temperature. The change in Bragg wavelength of the grating, λ_B, due to both temperature, T, and strain, ε, effects can be expressed by

$$\Delta\lambda_B(\varepsilon,T) = K_\varepsilon \Delta\varepsilon + K_T \Delta T$$

Equation 2-34

where K_ε and K_T are the photoelastic and thermo-optic coefficients respectively.

2.4 Grating array multiplexing architectures

As discussed in 1.4, fibre Bragg gratings readily lend themselves to wavelength division multiplexing[47] (WDM). However, the bandwidth of the optical source in Bragg grating sensor systems is finite, and although the problem can be overcome by multiplexing optical sources of different wavelength range, this approach will only cover slices of wavelength space, since suitable optical sources are not available at all wavelengths. Alternative methods of increasing the number of grating sensors which can be included in a single sensing scheme must therefore be applied.

Many of the Bragg grating sensor demultiplexing arrangements discussed in 1.4.2. are suitable for the application of time division multiplexing (TDM) to increase the number of sensors in the system, including those based on ratiometric filters[61], acousto-optic modulators[72], and interferometric wavelength measurement systems[52,53]. TDM can be implemented through the use of a pulsed optical source, and time gated electronics associated with the system's photodetector. The grating arrangement can take the form of a single array of wavelength identical gratings, or of a spatially division multiplexed arrangement of several such arrays.

Spatial division multiplexing (SDM) has also be demonstrated using identical single Bragg gratings at the end of each sensor arm[56]. In this approach the gratings are easily replaceable, should any of them fail, and the failure of one sensor will not affect the operation of any others. However, it does require a

large number of optical power splitters which results in it being less hardware compressive than systems which comprise linear arrays of gratings at each sensor arm. Another system of SDM which has been reported[37] combines its advantages with those of WDM schemes, using a tuneable transmission filter, directly after the broadband optical source, to determine the grating sensor wavelengths, and 1x8 fibre splitters to route the optical signal to the various sensors; nine gratings were multiplexed in this way and a strain measurement resolution of ~1.8με recorded. A scheme which combines WDM, SDM and TDM has also been reported[73] in which spatially multiplexed identical arrays of gratings of different wavelength are illuminated with a pulsed optical source and interrogated with an array of matched gratings; a strain measurement resolution of 4.12με was demonstrated.

Multiplexing of true time delay control elements in phased array antenna architectures, to feed the radiating elements, is predominantly SDM based, and is well documented[26,149]. The individual time delay elements may use SDM or WDM to create the different delays, as discussed in 1.3. RF beam multiplexing has been reported[36], using multiple RF frequencies to simultaneously modulate the optical carrier, and hence create multiple RF beams. This can also be implemented through the use of multiple optical source signals, of different wavelength, to produce multiple antenna beams either by utilising different groups of radiating elements to create each beam, or by using a pulsed optical source which is sent to all of the radiators; different beams are made to point in different directions by varying the optical source wavelength.

3. Grating Fabrication

3.1 Introduction

This chapter is concerned with the fabrication of uniform period and chirped period Bragg gratings. Results will be presented on the fabrication of both types of grating using the method of dissimilar wavefronts and the, novel, method of fibre deformation. The successful fabrication of uniform period gratings, both singly and in arrays, and of chirped gratings, was a prerequisite for the work on the application of fibre Bragg gratings as sensors and as true time delay elements, which will be reported in chapters 4 and 5 respectively. The post-exposure evolution, due to hydrogen out-diffusion, of the central wavelength of gratings written in hydrogen loaded fibres was characterised for each of the different types of fibre in which gratings were fabricated, and will be discussed in the context of long term grating wavelength stability.

3.2 Uniform period gratings

3.2.1 Fabrication method

The experimental arrangement used to fabricate uniform period gratings is shown in Figure 3.1. The output from a frequency-doubled argon-ion laser, wavelength 244nm, is intensity split with a 50:50 beamsplitter and the resulting beams form the two arms of a kite-shaped interferometer. The beams meet and interfere at the tip of the kite, producing interference fringes parallel to the kite bisector. The photosensitive fibre is placed at this point and the light focused onto the fibre core, in the vertical plane, by the cylindrical lens. The induced core refractive index modulation has the same periodicity as the interference pattern. The frequency-doubled argon-ion laser comprised a standard Spectra Physics 12W argon-ion laser with the front reflector removed and secondary optical cavity, containing a BBO crystal and guiding optics, coupled on to it. The laser produced an optimised power output at 244nm of up to 200mW. In

addition, ~300mW of unconverted blue/green light at 488nm was delivered, which was used as the pump for an erbium-doped-fibre fluorescence source for in-situ monitoring of the gratings during fabrication.

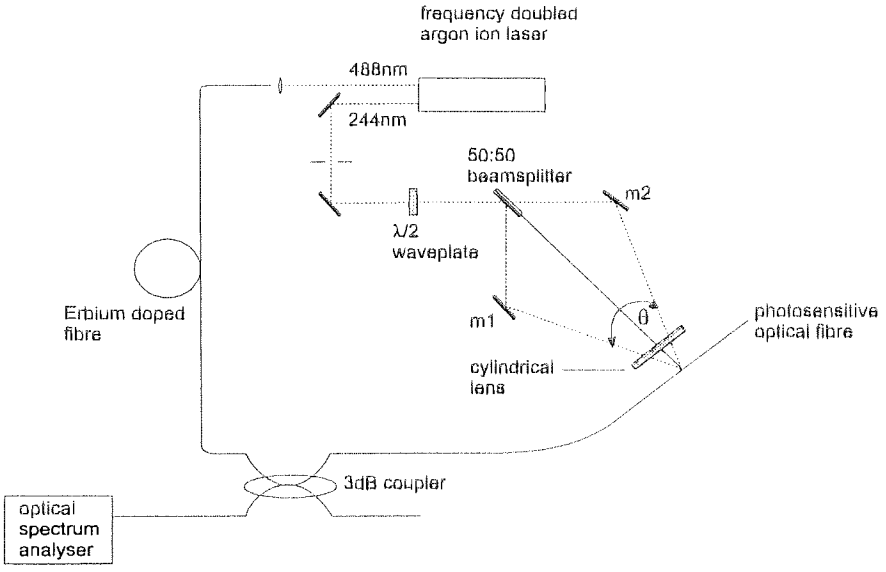

Figure 3.1 Uniform period grating fabrication experimental arrangement

The Bragg wavelength at which the grating will be fabricated is selected by altering the angle between the UV writing beams in the kite interferometer. This can be done by varying the distance between each mirror, m1 and m2, and the beamsplitter, to create large changes in the grating wavelength. Or, for small wavelength changes, the position of the fibre can be moved backwards or forwards along the kite bisector, and the mirrors rotated to maximise the beam overlap area on the fibre; the fibre is mounted on a translation stage.

The optical path lengths of the interferometer arms must be equal to ensure good fringe visibility and to avoid the production of any wavelength chirp in the grating spectrum due to the beams having different divergence. Good fringe visibility in the interference pattern is essential to maximise the strength of the grating; a decrease in the visibility gives rise to a reduction in the maximum

refractive index modulation achievable. The Gaussian intensity profile of the UV laser beam creates a shading effect in the interference pattern which tapers the refractive index modulation profile of the grating towards the edges. This causes a slight wavelength chirp to be formed across the 'uniform' grating which has the effect of suppressing the grating sidebands.

The polarisation of the laser beam was rotated, using a half-wave plate, to give vertically polarised light. An aperture was inserted into the beam path during the fabrication of some gratings to select the central portion of the beam, in order to produce shorter length gratings. However, this minimises the intensity variation across the interference pattern, which decreases the amount of shading applied to the refractive index modulation, and thus increases the amplitude of the grating sidebands.

The gratings used in the fibre Bragg grating sensor work were fabricated with a large separation between them, of the order of tens of centimetres of optical fibre, using the apparatus described above. The uniform period gratings used in the true time delay work were fabricated with very small separations between adjacent gratings in the array, which required some modifications to be made to the basic fabrication rig.

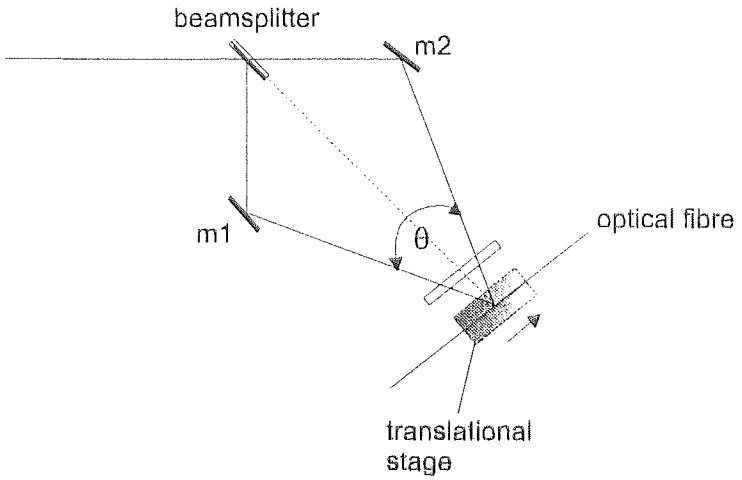

Figure 3.2 True time delay array fabrication arrangement

3.2.2 True time delay grating arrays

The time delay acquired by the optical carrier in a true time delay control system is determined by the distance separating adjacent gratings in the grating array. Therefore the array must be fabricated with some attention paid to the accurate positioning of the gratings. The fabrication rig described in 3.2.1 was modified to include a second linear translation stage which would allow the fibre to be advanced along the normal to the kite bisector, Figure 3.2. This allowed subsequent gratings in the array to be positioned accurately.

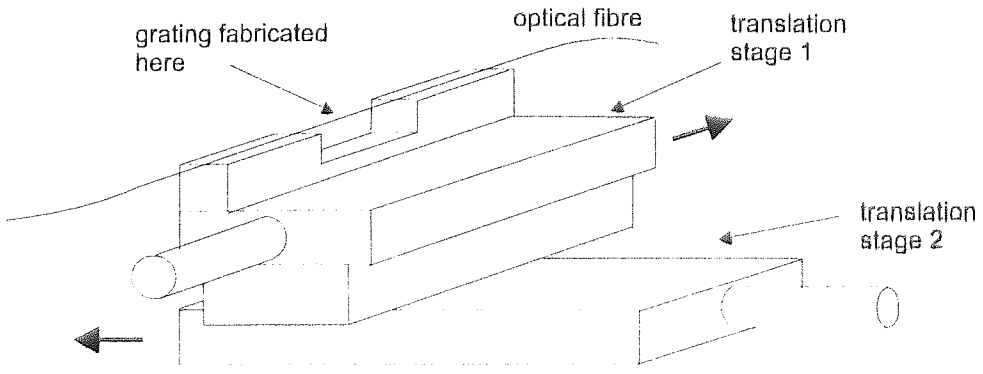

Figure 3.3 True time delay array fabrication fibre mount

After the first grating in the array had been fabricated the fibre was advanced by the required amount along the normal to the kite bisector, of the order of a few millimetres, using translation stage 1, Figure 3.3. To change the fabrication wavelength for the next grating the second translation stage was used to move the position of the fibre in the kite, along the bisector, hence changing the angle between the UV writing beams. Translating the fibre position along the kite bisector resulted in the interferometer becoming slightly mis-aligned. To re-optimise the interference fringe pattern the region of overlap of the UV beams on the fibre was re-maximised by slightly rotating the mirrors m1 and m2, Figure 3.2. However, in rotating the mirrors to maximise the beam overlap, the central position of the interference pattern on the fibre may move away from the desired location for the next grating, and as the previous grating could not be detected by eye it was very difficult to judge whether, and to what degree, any misalignment had occurred. It was this realignment procedure which formed the main source of error in the positioning of the gratings. The problem was partially overcome by placing a marker next to the fabrication rig, fixed to the optical bench, and aligning one end of the beam overlap region with this during the fabrication of each grating.

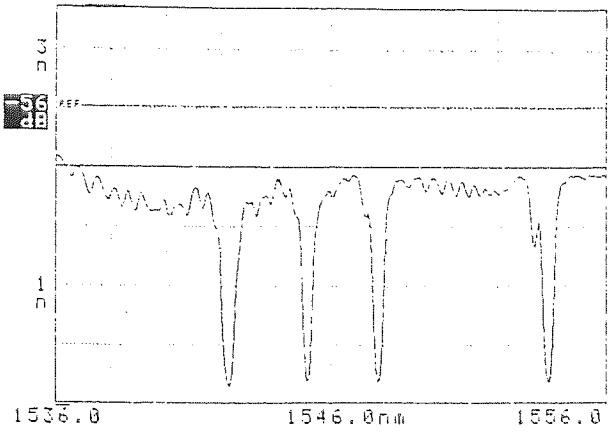

Figure 3.4 Optical spectrum of TTD grating array of 5mm long gratings, with 5mm centre-to-centre separation

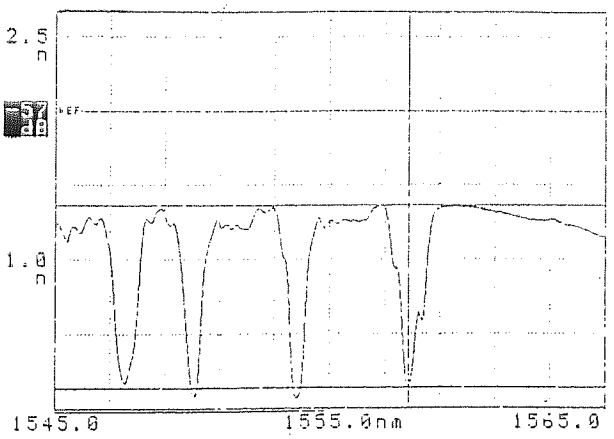

Figure 3.5 Optical spectrum of TTD grating array of 5mm long gratings, with 2.5mm separation

Four uniform period Bragg grating arrays were fabricated for use as TTD control elements; several versions of each array were produced in order to achieve the best possible combination of physical separation, wavelength separation, and grating reflectivity. Two of the grating arrays were produced in hydrogenated, standard Corning single-mode fibre, and contained four 5mm long gratings, of ~0.5nm full-width half-maximum (FWHM) bandwidth and ~90% peak reflectivity, with centre-to-centre separations between adjacent gratings of 5mm and 2.5mm respectively. Two further arrays were fabricated in hydrogenated, boron-germania single-mode fibre and comprised eight 2mm long gratings, with FWHM bandwidths of ~0.5nm and peak reflectivities of ~60%, with grating separations of 2mm and 1mm.

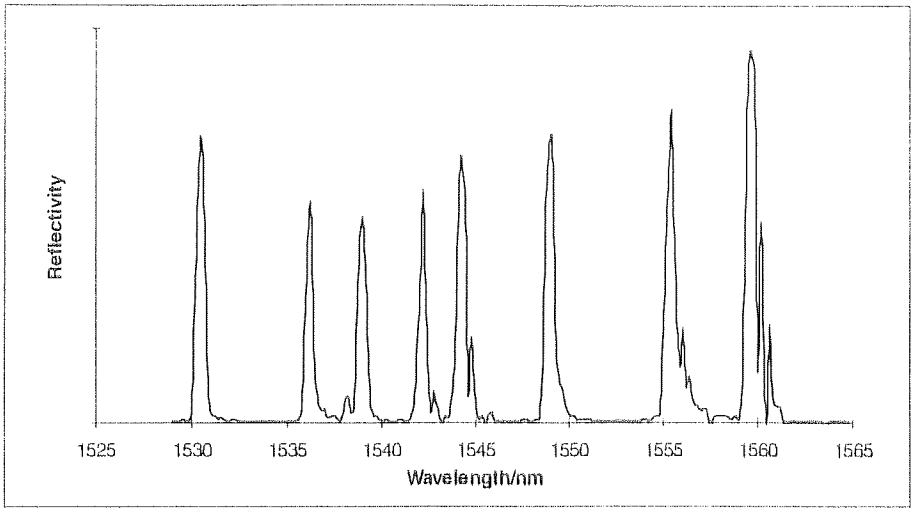

Figure 3.6 Optical spectrum of the TTD grating array of 2mm gratings, with a 2mm inter-grating separation; grating wavelengths 1530.80nm, 1536.55nm, 1539.35nm, 1542.55nm, 1544.55nm, 1549.30nm, 1555.70nm and 1560.00nm

The optical spectrum of the array of 5mm long gratings with a 5mm grating separation is displayed in Figure 3.4, and that of the 2.5mm grating separation array is shown in Figure 3.5; spectra measured using Ando AQ-6310C optical spectrum analyser, resolution 0.1nm. Figure 3.6 and Figure 3.7 contain the wavelength spectra of the 2mm and 1mm inter-grating separation, 2mm gratings arrays respectively; spectra measured using the 1GHz TTD experimental arrangement which will be described fully in 5.3.2. The secondary resonance peaks displayed by the 1mm grating separation array will be investigated further in 5.8.

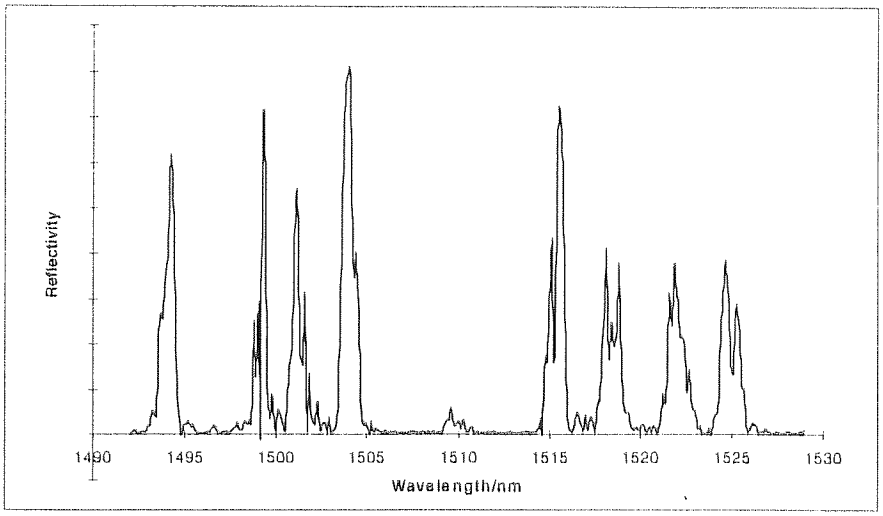

Figure 3.7 Optical spectrum of TTD array of 2mm long gratings, with 1mm grating separation; grating wavelengths 1494.10nm, 1498.75nm, 1501.05nm, 1503.75nm, 1515.05nm, 1518.05nm, 1521.85nm, 1524.65nm

The fabrication of the true time delay linear grating arrays was carried out in collaboration with Dr. Lin Zhang of the Photonics Research Group, Aston University.

3.2.3 Effect of hydrogenation on post-exposure grating wavelength

As described in 2.1.3, any unreacted hydrogen remaining in the fibre after UV exposure undergoes isotropic diffusion. During the initial hours following fabrication this results in some of the hydrogen which is present in the fibre cladding diffusing into the core, with the effect of raising the core refractive index and causing the grating wavelength to shift to a higher value. Over a longer period of time, of the order of several weeks, all of the hydrogen escapes from the fibre, the core refractive index is decreased and the Bragg wavelength of the grating undergoes a corresponding down shift. The magnitude of the wavelength shift is determined by the amount of unreacted hydrogen remaining in the fibre after grating fabrication.

The short term and long term post-exposure wavelength evolution was recorded, at room temperature, for both saturated and non-saturated gratings written in standard telecommunications fibre, germania doped fibre (CA2114) and boron-germania codoped fibre; saturated gratings are defined here as those in which the fibre has been exposed to the UV fringe pattern until the grating reflectivity has reached its maximum value i.e. all of the available photosensitivity has been utilised; unsaturated gratings are those which have been UV exposed until the grating reflectivity has reached a specified value, of less than the achievable maximum. The gratings were written within 2 hours of being removed from the hydrogen high pressure vessel.

Figure 3.8 shows the evolution of the Bragg wavelengths of the various gratings over the initial 6 hours following fabrication: Figure 3.8(a) and Figure 3.8(b) show the wavelength variation of the non-saturated and saturated gratings written in standard fibre respectively; Figure 3.8(c) and Figure 3.8(d) show the wavelength evolution of the non-saturated and saturated gratings fabricated in germania doped fibre; and Figure 3.8(e) and Figure 3.8(f) show the shift in Bragg wavelength experienced by the non-saturated and saturated gratings written in boron-germania codoped fibre. The maximum wavelength increase undergone by the saturated gratings was greater than that experienced by the non-saturated gratings for all of the types of fibre. In addition, the increase in Bragg wavelength observed in the saturated grating fabricated in boron-germania codoped fibre was significantly larger than that seen in the other fibres.

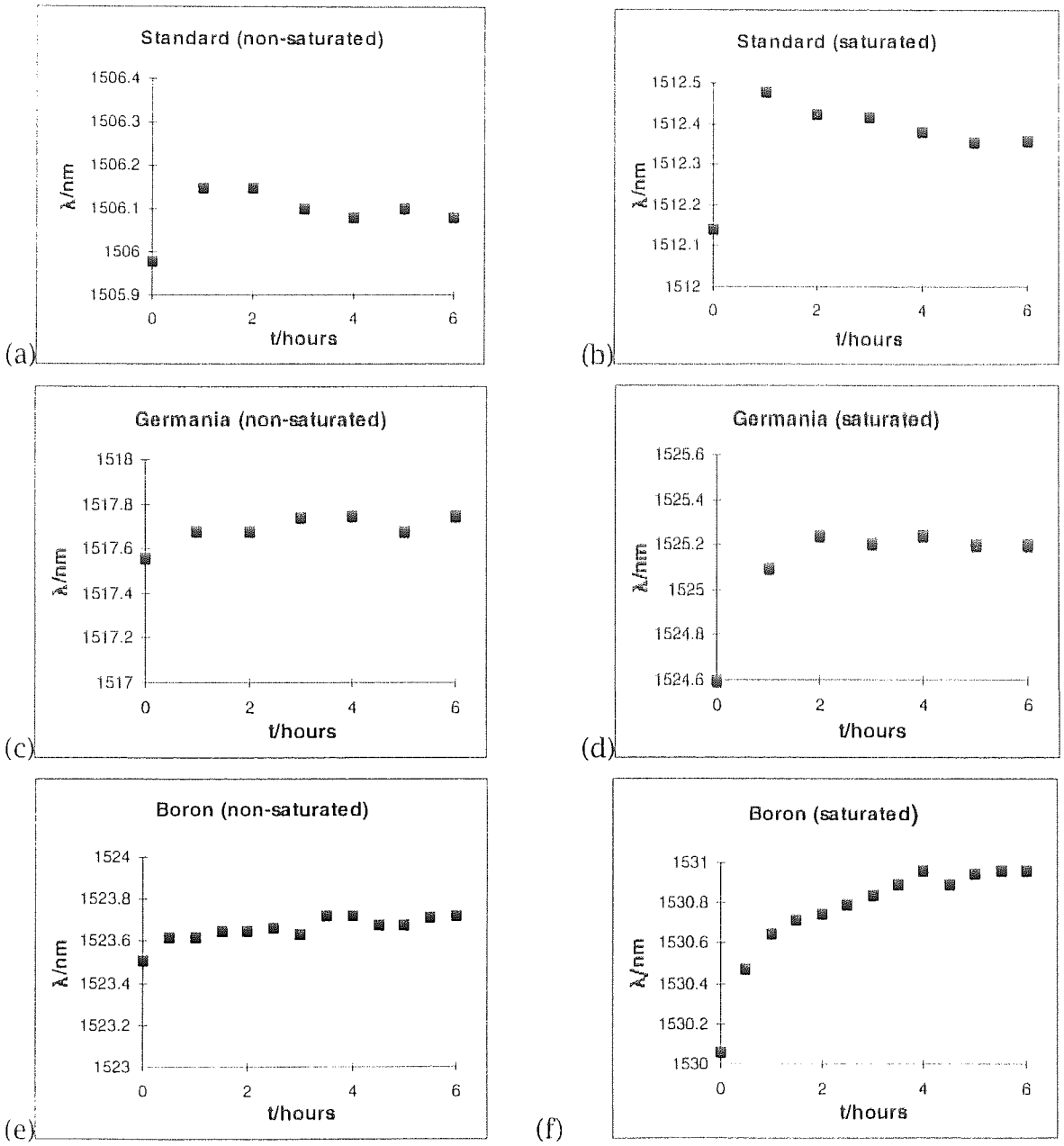

Figure 3.8 Short term post-exposure wavelength evolution of saturated and non-saturated gratings written in standard, germania doped and boron-germania codoped fibres

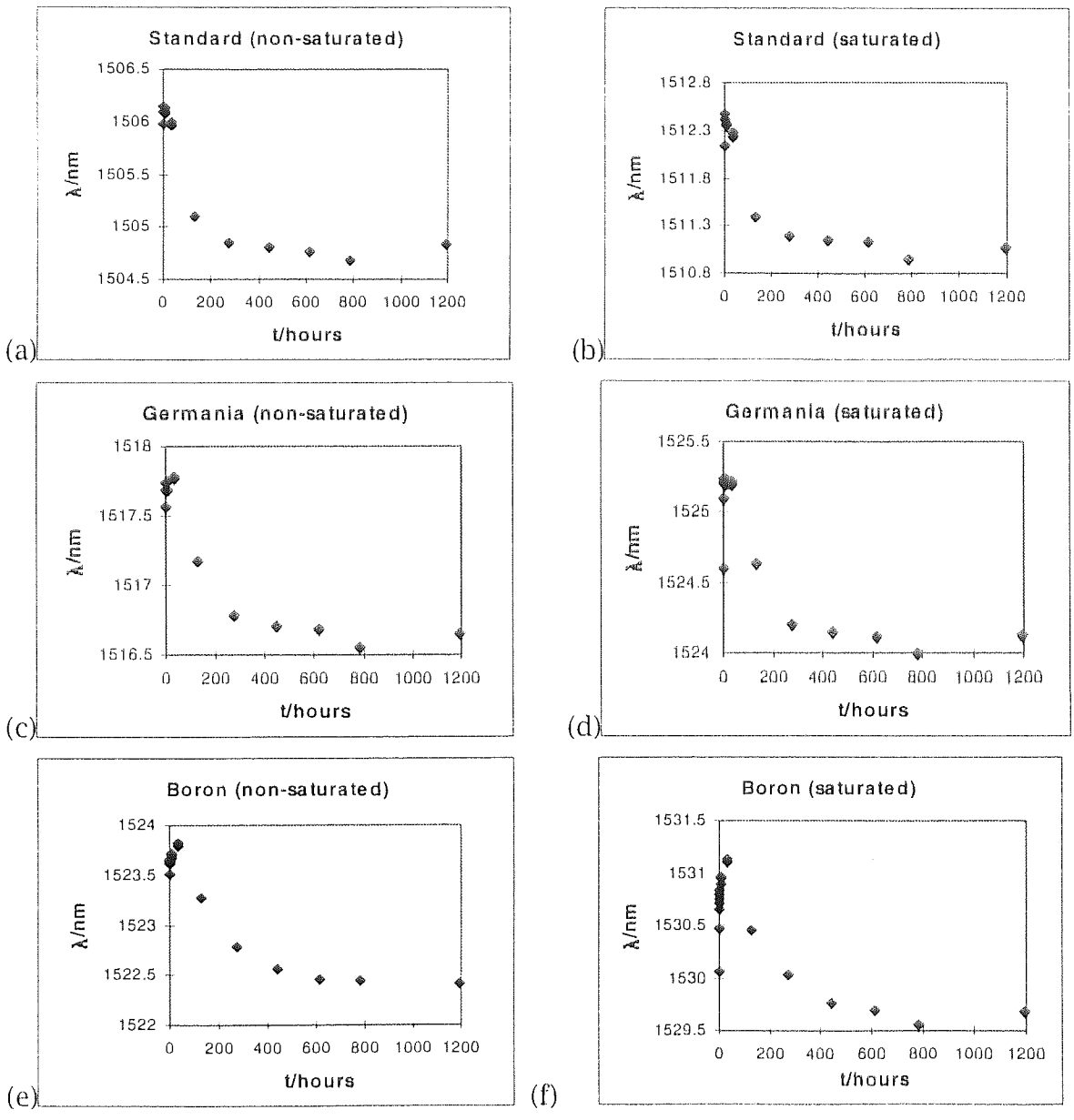

Figure 3.9 Long term post-exposure wavelength evolution of saturated and non-saturated gratings written in standard, germania doped and boron-germania codoped fibres

Figure 3.9 shows the long term evolution, over 7 weeks, of the Bragg wavelength of the gratings; Figure 3.9(a) and Figure 3.9(b) show respectively the wavelength shift undergone by the non-saturated and saturated gratings written in standard fibre; Figure 3.9(c) and Figure 3.9(d) show the evolution of the Bragg wavelengths of the non-saturated and saturated gratings fabricated in

germania doped fibre; and Figure 3.9(e) and Figure 3.9(f) show the variation in wavelength experienced by the non-saturated and saturated gratings written in boron-germania codoped fibre. In all of the fibres the final wavelength reached by the saturated gratings was shorter than their wavelengths immediately after exposure by a greater amount than for the non-saturated gratings; the saturated standard fibre grating showed the largest reduction in wavelength.

		maximum wavelength increase/nm	maximum wavelength decrease/nm
Standard fibre	saturated grating	0.34	1.18
	non-saturated grating	0.17	1.3
Germania-doped fibre	saturated grating	0.64	0.6
	non-saturated grating	0.19	1.01
Boron-Germania codoped fibre	saturated grating	0.9	0.51
	non-saturated grating	0.21	1.05

Figure 3.10 Maximum and minimum post-exposure wavelength shift experienced by saturated and non-saturated gratings written in standard telecommunications fibre, germania doped fibre and boron-germania codoped fibre

These results are consistent with the isotropic diffusion process described above. The fabrication of the saturated gratings requires all of the available photosensitivity in the fibre core, and hence uses the maximum amount of dissolved hydrogen. Thus, there is a greater difference in the hydrogen concentration between the core and the cladding in the saturated gratings than in the non-saturated gratings, allowing a larger volume of hydrogen to diffuse into the core of the saturated gratings. The result being the greater Bragg wavelength increase observed in the saturated gratings during the first hours after UV exposure, Figure 3.10. In addition, the greater usage of hydrogen during saturated grating fabrication results in there being less unreacted

hydrogen to diffuse out of the core than in the case of the non-saturated gratings, and hence the maximum downward shift of the saturated grating wavelength, once all of the hydrogen has out-diffused, is smaller than that experienced by the non-saturated gratings, as observed in Figure 3.10.

The use of gratings both in sensor applications and as elements in true time delay units requires their fabrication to exacting wavelength specifications. It is therefore important to characterise the effect of hydrogen out-diffusion on the grating final wavelength. The results obtained suggest that in order to produce gratings at precisely defined wavelengths one should fabricate absolutely saturated gratings, in which all of the dissolved hydrogen is used in the inscription process, in germania doped fibres. In such gratings the Bragg wavelength would undergo the characteristic increase during the first few hours after fabrication, and then return to the wavelength it was fabricated at, suffering no further decrease in wavelength. The diffusion process is temperature dependent so removal of any unreacted hydrogen from gratings which are not absolutely saturated can be accelerated[123] to produce very long wavelength stable lifetimes.

3.3 Chirped grating fabrication techniques

3.3.1 Fibre deformation

A straightforward method for fabricating chirped gratings is that of fibre-deformation, in which the chirp is created through the physical deformation of the fibre during exposure to a uniform interference fringe pattern. A length of photosensitive optical fibre is curved in an approximately circular arc and placed in a uniform fringe pattern, of periodicity Λ, produced by two beam interference, Figure 3.11. The period, $\Lambda(x)$, of the grating varies as

$$\frac{\Lambda}{\cos\theta(x)}$$

Equation 3-1

where θ(x) is the angle between the fibre and the normal to the interference fringes at a position x along the fibre. This produces a chirped grating in which the period varies from Λ, at x=0, to Λ/cosθ(L), at x=L. The grating fringes formed in the fibre core increasingly tilt away from the normal to the fibre axis with distance x, but providing θ(L) remains small enough coupling to the fibre radiation modes will be minimal.

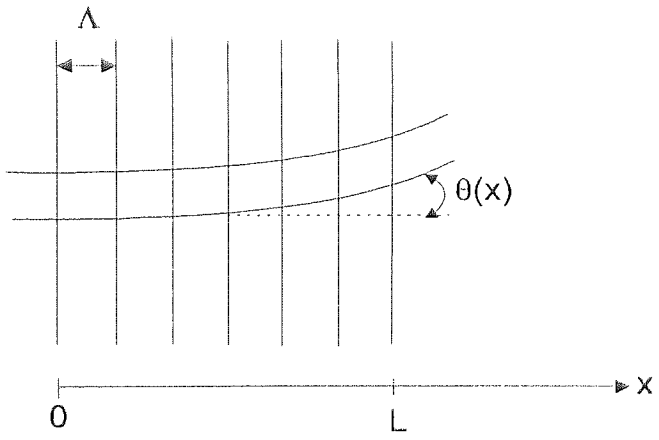

Figure 3.11 Fibre deformation method for the fabrication of chirped gratings

This grating fabrication technique was used to write several gratings of differing chirp in boron-germania codoped optical fibre; the work was carried out in collaboration with Dr. Kate Sugden of the Photonics Research Group, Aston University.

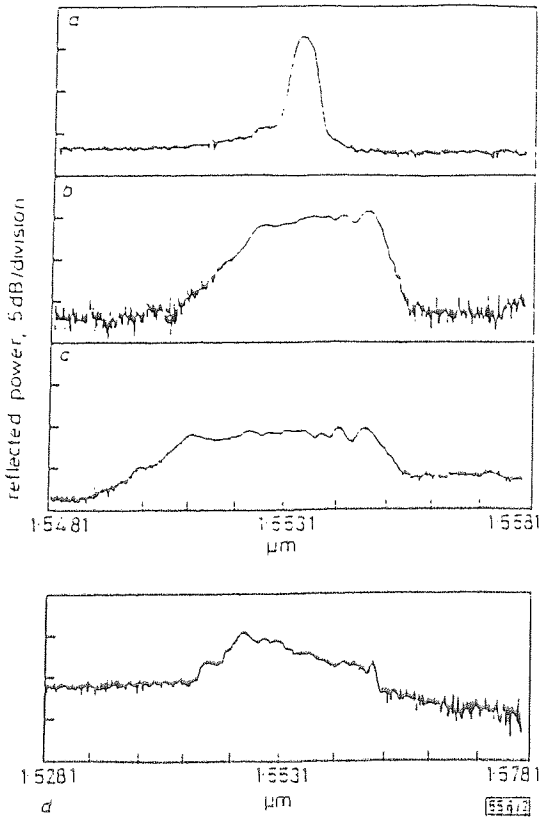

Figure 3.12 Reflection spectra for a series of gratings, length L=5mm, written in boron-germania codoped fibre; fibre curvature increases from (a) to (d)

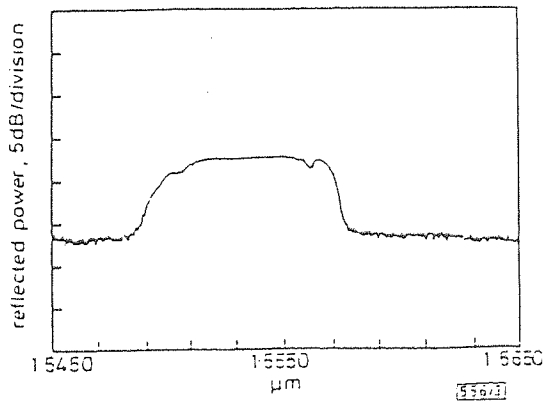

Figure 3.13 Reflection spectrum of chirped grating fabricated using the fibre deformation technique in hydrogenated germania doped fibre

A series of four gratings of length L = 5mm were fabricated in fibres of increasing curvature, producing gratings with the reflection spectra[150] shown in Figure 3.12. The grating displayed in Figure 3.12(a) was written in a straight section of fibre resulting in an unchirped grating with a Bragg wavelength of 1553.3nm, a peak reflectivity of 88% and a FWHM bandwidth of 0.4nm. Figure

3.12(b) indicates how the introduction of a small amount of curvature into the fibre significantly increased the reflection bandwidth of the grating to 2.9nm and resulted in a reduction in the maximum reflectivity to 40%. A further increase in the fibre curvature produced further broadening of the grating bandwidth to 4.4nm, with a corresponding fall in the peak reflectivity to 13%, Figure 3.12(c). A final increase in the fibre curvature, to θ(5mm) ~8°, gave the grating spectrum shown in Figure 3.12(d), with a bandwidth of 17.3nm and a maximum reflectivity of >4%. The estimated curvatures for gratings (b) and (c) were θ(5mm) ~3.5° and θ(5mm) ~4.3°.

In order to counteract the fall in maximum reflectivity as the grating bandwidth increased, hydrogenated germanosilicate fibre was used in the fabrication of a further grating, Figure 3.13. The grating, L = 5mm, has a FWHM bandwidth of 7.5nm and a peak reflectivity of ~99%; greater than 90% reflectivity is available over a 5nm spectral range.

Fabricating gratings by this method requires some degree of care to be practised in setting the degree of curvature of the fibre in order to achieve the desired wavelength chirp in the spectral profile of the grating. Although a range of chirps can be produced, several iterative stages may be needed to attain the desired value. Since completing this work on the fibre deformation fabrication method, new techniques for writing chirped Bragg gratings have been developed which allow greater control of the spectral characteristics of the gratings, enabling the production of both highly linear and quadratic chirps, and complex grating filters. These are the dissimilar wavefront fabrication method, and techniques based on phase masks, which will be discussed in more detail below.

These fabrication methods have the added benefit of producing gratings with significantly lower optical loss characteristics than could be achieved with the fibre deformation technique. This is most probably due to the removal of the

fringe tilt associated with gratings fabricated by the fibre deformation technique, which, although small, is significant in comparison with the loss characteristics of gratings produced using the dissimilar wavefront and phase-mask methods.

The chirped gratings produced using the fibre deformation fabrication method represented a significant improvement in the size of chirp and grating reflectivity at the time of publication. However, the improvements in loss characteristics and spectral profile control offered by the dissimilar wavefront technique prompted a move to using it for all of the subsequent grating fabrication carried out during this work. Indeed, these advances in grating fabrication technology facilitated much of the work on true-time delay control of phased array antennas, which will be reported in chapter 5, and are necessary for the advanced demultiplexing techniques which will be proposed in 4.9.

3.3.2 Dissimilar wavefronts

As discussed in 2.1.2, chirped gratings may also be fabricated by a method of dissimilar wavefronts. There are three lens arrangements which may be used in this writing method: a single cylindrical lens in one interferometer arm and no lens in the other[99,100]; a single cylindrical lens, of different focal length, in each arm[151]; and a two-lens telescope arrangement in one arm and no lens in the other[152].

The chirped gratings used in this work were fabricated, by Dr. Lin Zhang, using the telescopic lens fabrication arrangement. In this method of writing Bragg gratings two cylindrical lenses of equal focal length, f, are mounted vertically at a separation d, equal to twice their focal length, to form a telescope in one arm of the kite interferometer, Figure 3.14. The lenses are initially aligned to produce a collimated beam, which results in the formation of a uniform fringe

pattern on interference with the second writing beam. The telescope is then slightly detuned by moving lens *L1*, mounted on a translation stage, a small distance Δd towards or away from *L2*, along the path of the interferometer arm. This produces a slowly converging or diverging beam, and hence introduces a small, controllable linear chirp into the interference pattern.

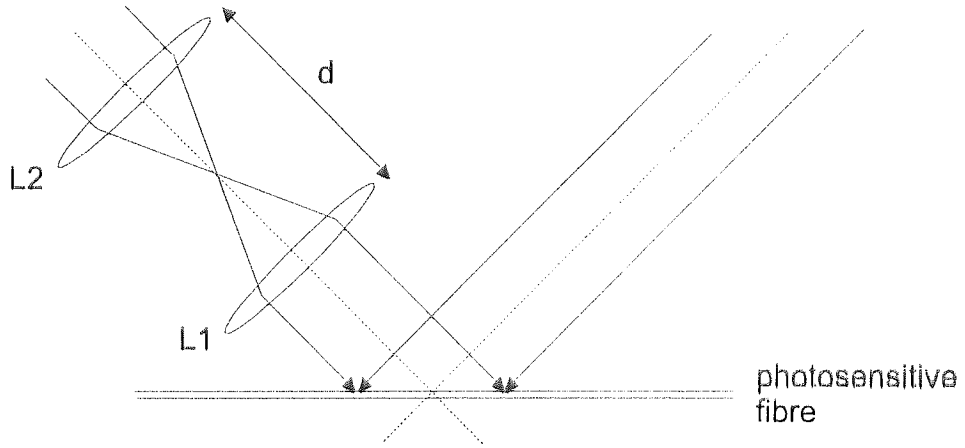

Figure 3.14 Telescopic lens interferometric chirped grating fabrication arrangement

The effective focal point of the lens system can be calculated using the paraxial lens theory[153]. Where the lenses are of equal focal length the image distance, s_{i2}, from lens *L2* is given by

$$s_{i2} = \frac{(d - s_{i1})f}{d - s_{i1} - f}$$

Equation 3-2

where $d = (2f + \Delta d)$, and s_{i1} is the lens *L1* image distance. For $d > s_{i1}$ a diverging beam is formed, and for $d < s_{i1}$ a converging beam is formed. The new focal line coordinates, x_f and z_f, can then be substituted into Equation 2.19 to calculate the grating period as a function of distance, x.

Four chirped gratings were fabricated, in boron-germania codoped fibre, for use as true-time delay control elements, each of length 4mm and reflectivity ~60%. Grating full width half maximum bandwidths of 7nm, 12nm, 20nm and 30nm were selected, at random, from a range of regularly fabricated chirp bandwidths. A physical length of 4mm was used as it was the maximum grating size available using the grating fabrication arrangement in existence at the time that the work was carried out, while a grating reflectivity of ~60% was chosen as a convenient, and easily fabricated value. The optical spectra of the 7nm, 12nm, 20nm and 30nm chirped gratings can be seen in Figure 3.15, Figure 3.16, Figure 3.17 and Figure 3.18 respectively; recorded using the 1GHz TTD experimental arrangement given in 5.3.2, and normalised to remove the transmission response of the optical coupler within the system.

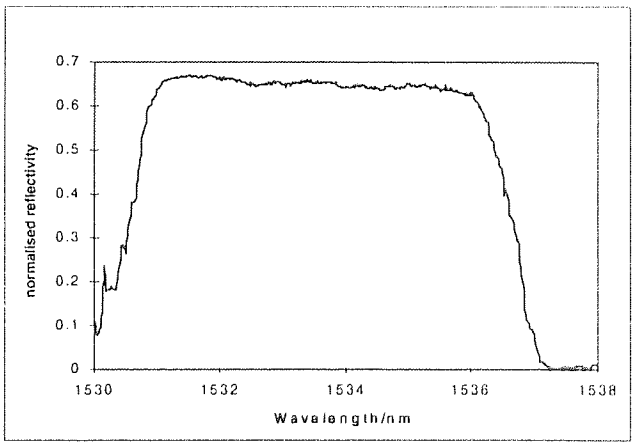

Figure 3.15 7nm chirped Bragg grating for TTD control of phased array antennas

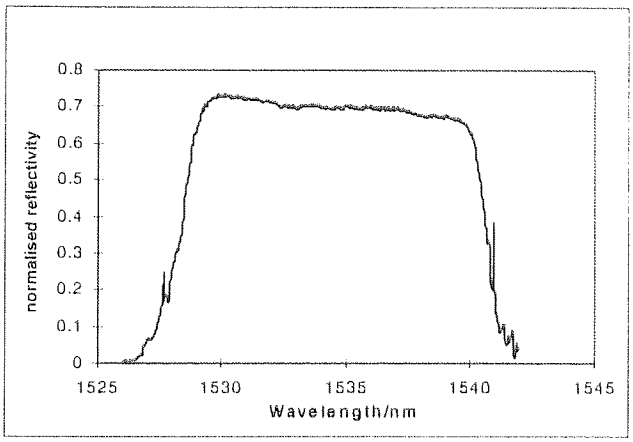

Figure 3.16 12nm chirped Bragg grating for TTD control of phased array antennas

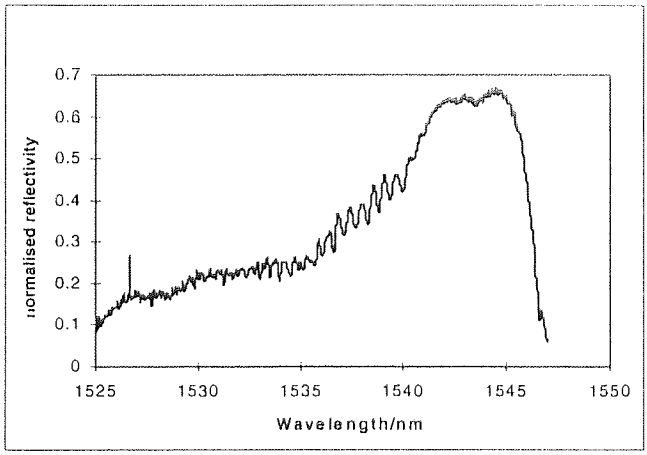

Figure 3.17 20nm chirped Bragg grating for optical TTD control of phased array antennas

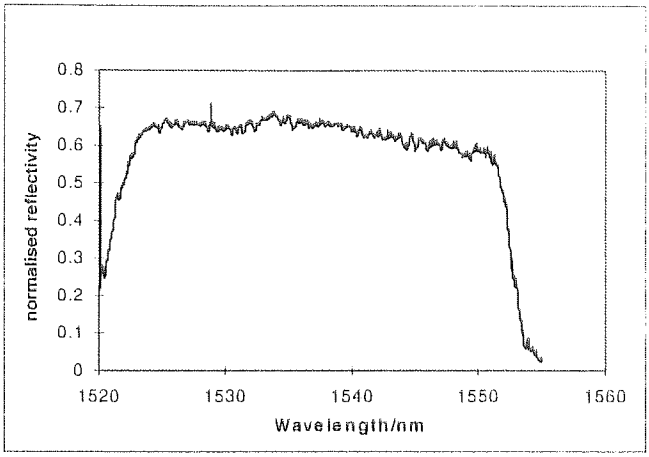

Figure 3.18 30nm chirped Bragg grating for TTD control of phased array antennas

3.3.3 Phase mask

Hill et al[154] first reported the use of a phase mask based method of fabricating in-fibre Bragg gratings, in which the phase mask acts as a diffractive element, splitting an incident UV beam into various diffracted orders which interfere to produce a fringe pattern within the fibre core, Figure 3.19. A phase mask consists of a high quality fused silica flat on which a one-dimensional periodic structure, approximately square wave in profile, has been surface relief etched to a depth, d, given by

$$d = \frac{\lambda_{UV}}{2\left(n_{UV} - 1\right)}$$

Equation 3-3

where λ_{UV} is the wavelength of the laser fabrication beam and n_{UV} is the refractive index of fused silica at that wavelength. This depth was chosen in order to produce maximum suppression of the zero order for a beam incident normally on the phase mask, and to maximise the power in the plus and minus first orders. The phase mask is placed in contact, or near contact, with the optical fibre, with its periodic structure oriented normal to the fibre axis. The diffracted plus and minus first order interfere in the near field, producing a pattern of fringes which photoimprints a corresponding refractive index

modulation in the fibre core, with the period of the fringes, Λ, and hence the grating, equal to half that of the phase mask, Λ_{mask}.

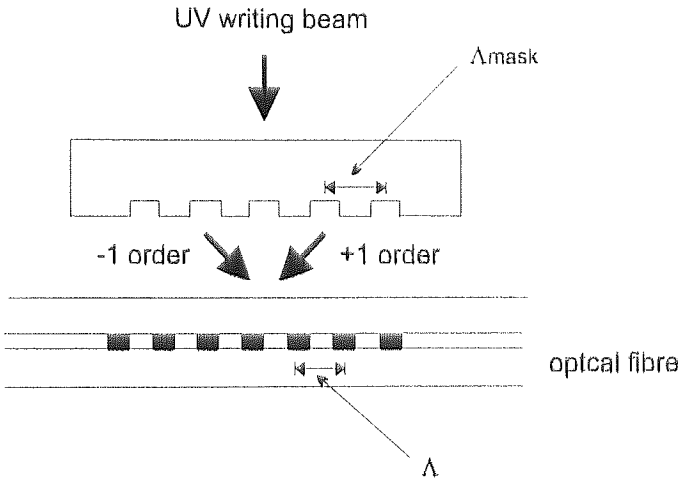

Figure 3.19 Phase mask grating fabrication arrangement

An alternative phase mask arrangement has been used in which a silica block is placed between the phase mask and the fibre[155], guiding the diffracted beams and combining them at the fibre core; this avoids the need to place the mask in contact with the fibre and hence any risk of damage to it is minimised. Phase masks can also be used to fabricate long Bragg gratings by translating either the mask[156] or the UV writing beam[157] along the fibre, and have been used to write gratings of 50mm and 150mm respectively.

3.3.4 Fabry-Perot grating resonators

The chirped grating fabrication procedures described in 3.3.2 and 3.3.3 can be applied to the production of in-fibre Fabry-Perot filters[158,159], which can be used as Bragg grating sensor demultiplexing elements, see 4.9. A chirped Fabry-Perot grating resonator is produced by fabricating two linearly chirped gratings, ideally of equal strength, at a separation D along the fibre, Figure 3.20. The wavelength range of the resonator is determined by the bandwidths of the two

gratings, and, as for a bulk optic Fabry-Perot etalon, the free spectral range is set by the grating, mirror, separation; if there are no internal losses the finesse of the filter can be determined from the grating reflectivities. In-fibre Fabry-Perot resonators have been reported[158] with operational ranges of up to 200nm, and with resonance peak separations of between 0.09nm and 11.27nm, with FWHM bandwidths of the order of 0.02nm.

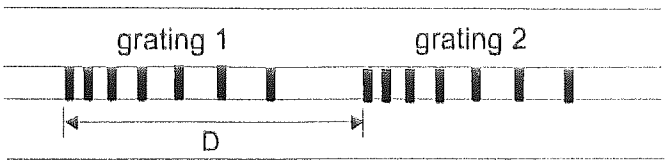

Figure 3.20 Arrangement of linearly chirped gratings for the fabrication of in-fibre Fabry-Perot resonators

3.4 Fabrication considerations for arrays of gratings

There are several characteristics which gratings intended for use in sensor applications and in true time delay elements must have. Uniform period gratings for use as sensors must have a high maximum reflectivity in order to reflect as much of the low power, broadband light source as possible. They should be physically short in length, as they are intended for use as point sensors in many applications, and the grating linewidth should be kept small to allow dense packing of sensors into the available wavelength range. These two requirements are in conflict with one another, as detailed in equation 2.12, and a compromise must be reached between the grating length and bandwidth requirements in each sensor system.

The wavelength spacing between gratings adjacent in wavelength should be greater than the expected maximum measurand induced wavelength change; a strain of 1000με will produce a wavelength increase of 1nm, so a system which will experience a maximum strain of 3000με will require a grating wavelength

separation of greater than 3nm. The separation must be increased if the system is to be exposed to compression also. The width of a grating, in sensor systems in which the grating sidebands are not suppressed, is taken to be $3\Delta\lambda$, where $\Delta\lambda$ is the full grating bandwidth, given by Equation 2.11. This is to ensure that the sidebands of adjacent gratings do not interfere and cause measurement error. Ideally, the grating refractive index modulation profile should be shaded or apodised in order to suppress the sidebands, allowing closer packing of gratings in wavelength space.

The requirements for uniform gratings fabricated in true time delay elements are slightly different than those for sensor gratings. The absolute reflectivity value is not required to be as high, since the optical carrier is a tuneable laser, but the all of the gratings in the system must have the same reflectivity. This is because the magnitude of the optical carrier amplitude modulation determines the magnitude of the RF signal produced by the individual microwave emitters in the phased array antenna, and these must all have the same amplitude in order to produce the correct beam shape. The positioning accuracy of the gratings in each array is critical to ensure that the specified time delays are produced. In addition, the fabrication system must be capable of reproducing identical gratings in many different time delay elements. The chirped gratings used as time delay elements must have a linear wavelength chirp in order to produce a linearly increasing time delay across the bandwidth of the grating, and, similarly to the uniform period gratings, the reflectivity must be constant across the working wavelength range. These requirements will be discussed further in Chapter 5.

3.5 Conclusion

The fabrication of uniform period gratings both individually and in arrays of up to eight gratings has been successfully achieved, and the spectra of the arrays have been recorded. The effect of hydrogenation on the post-exposure

evolution of the Bragg wavelength of the gratings has been characterised for three types of fibre.

Chirped gratings with bandwidths of up to 7.5nm have been fabricated using the fibre deformation writing technique in both hydrogenated and non-hydrogenated optical fibre. At the time that the results for the fabrication of chirped gratings using the fibre deformation technique were first reported we believed that it produced linearly chirped Bragg gratings. Subsequent work on this method of chirped grating formation has been reported by *Zhang et al*[160], in which they have demonstrated that the expression given to describe the grating periodicity in the fibre deformation approach used here, Equation 3-1, in fact describes a quadratic wavelength chirp.

Four chirped gratings have been fabricated using the method of dissimilar wavefronts, for use as true time delay elements in the control of phased array antennas, and their spectral characteristics recorded. Each grating was of length 4mm, and reflectivity ~60%, with chirps of 7nm, 12nm, 20nm and 30nm selected from a range of values regularly produced

4. In-fibre Bragg grating strain sensor systems

4.1 Introduction

As discussed in chapter 1, much work has been reported on the use of in-fibre Bragg gratings as both strain and temperature sensors, including several demultiplexing methods. One of the most significant potential applications of in-fibre Bragg grating sensors is as smart structure sensing elements. Although much work has been done on the strain and temperature response of fibre Bragg gratings, little work has been reported[87] on their performance when embedded within a structure. In this chapter the first report, of which I am aware, of the strain response of fibre Bragg gratings embedded within a carbon-composite material, for potential use in avionics and aerospace craft, will be discussed.

Many different approaches for demultiplexing the optical signal returned from an array of Bragg grating sensors have been reported, see Chapter 1, but most use bulky, bench-top equipment. Hence there is still the need for a compact, lightweight, low cost system capable of demultiplexing an array of many gratings, which will complement the compact, lightweight nature of the in-fibre Bragg grating sensor array. This chapter reports the construction and testing of such a Bragg grating sensor demultiplexing system based on a liquid-crystal filled Fabry-Perot etalon transmission filter.

4.2 In-fibre Bragg gratings as smart structure strain sensors

4.2.1 Introduction

In-fibre Bragg gratings have great potential use as sensors embedded within smart structures where they can be used to monitor the internal temperature and strain experienced by structural components. This will enable real-time

structural monitoring to be implemented, permitting maintenance to be carried out as and when faults develop, and allowing the 'health' of the structure to be continually assessed. Another application of real-time strain monitoring involves damping structural vibrations by applying equal magnitude, opposite sense, vibrations to the structure through piezo-electric transducers embedded within it. This has applications in aerospace and aviation craft, where reducing the amount of vibration in the aircraft wings and body greatly enhances its aerodynamics, and hence its fuel efficiency and flying lifetime.

4.2.2 Carbon composite board

A composite board constructed from carbon (graphite), epoxy resin and glass plies, containing several embedded fibre Bragg gratings, was fabricated by GEC-Marconi Materials Technology (San Diego, C.A., U.S.A.), Figure 4.1. The board was of length 251mm, and thickness 1.73mm. It was constructed from four graphite/epoxy plies, with glass/epoxy plies in between; the gratings were laid down after the first graphite/epoxy ply (thickness ~350μm), and were therefore closer to the surface without the flanges, as indicated in Figure 4.1. The optical fibres were laid parallel to the glass fibres in the glass/epoxy layer.

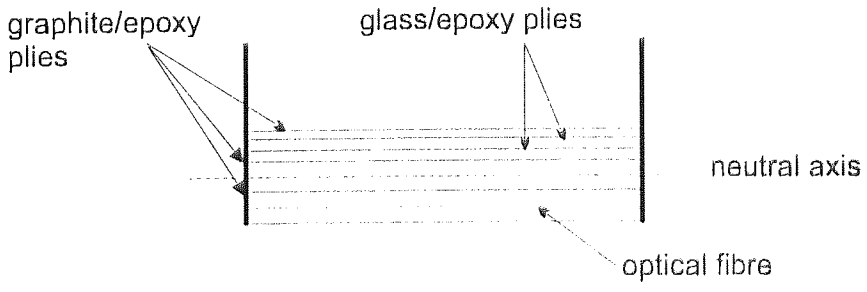

Figure 4.1 Carbon composite board construction

4.2.3 Embedded gratings

4.2.3.1 Theory

The strain experienced by a thin sheet of solid material upon bending is related to the bend induced deflection of the sheet away from its initial horizontal position, Figure 4.2. A solid sheet of length l, measured from the bending axis, Figure 4.3, width w and thickness t, will undergo a deflection Z, at a point a distance x from the bending axis, given by[161]

$$Z = \frac{V}{D}\left(\frac{lx^2}{2} - \frac{x^3}{6}\right)$$

Equation 4-1

where V is the applied force and the stiffness of the sheet, D, is

$$D = \frac{Yt^3 w}{12\left(1-\mu^2\right)}$$

Equation 4-2

in which Y is the Young's modulus of the material and μ ~1/3 is Poisson's ratio. For $l >> t$ no shear will occur within the board.

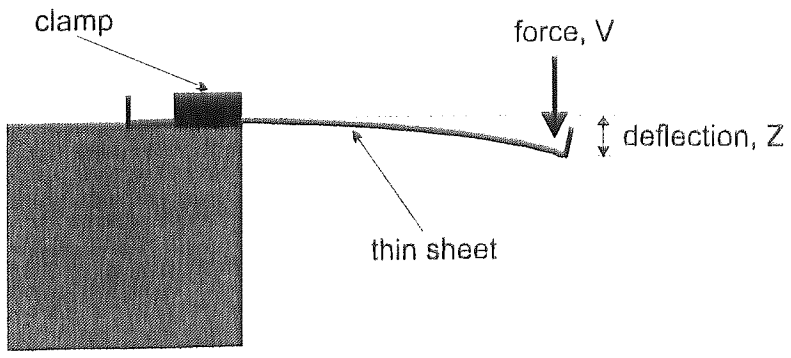

Figure 4.2 Bend induced deflection from horizontal plane in thin sheet, on application of downwards force

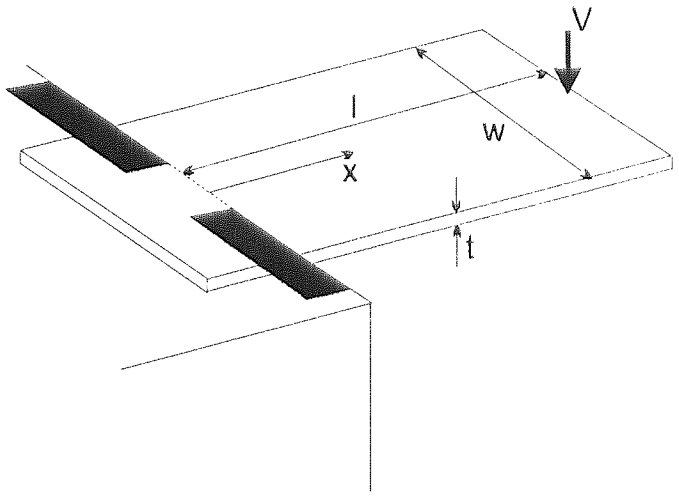

Figure 4.3 Bending a thin sheet; length l, *width* w, *thickness* t

The strain experienced by the upward facing surface of the sheet, for a force applied downwards onto this surface, is given by

$$\frac{\Delta l}{l} = \frac{t}{2}\left(\frac{d^2 Z}{dx^2}\right) = \frac{t}{2}\left(\frac{V}{D}\right)(l - x)$$

Equation 4-3

For x=*l*,

$$Z_l = \frac{V}{D}\left(\frac{l^3}{3}\right)$$

Equation 4-4

Hence the strain on the top surface can be written as

$$\frac{\Delta l}{l} = \frac{t}{2}(l - x)\left(\frac{3Z_l}{l^3}\right)$$

Equation 4-5

The plane in the middle of the sheet, a distance $t/2$ from either surface, is known as the neutral axis and experiences no strain. The magnitude of the strain increases linearly with distance from the neutral axis to the upper surface, and, similarly, the amount of compression increments linearly from the neutral axis to the lower surface. The gratings were embedded within the board at a distance of ~515μm from the neutral axis, and hence experienced 59.54% of the strain or compression felt at the surface of the sheet:

$$\frac{\Delta l}{l} = 0.5954\left(\frac{t}{2}\right)(l-x)\frac{3Z_l}{l^3}$$

Equation 4-6

4.2.3.2 Measurement systems and grating spectra

The experimental arrangement used to interrogate the in-fibre Bragg gratings is shown in Figure 4.4. The broadband optical source, which covered the erbium fluorescence spectral range (~1525nm to ~1560nm), comprised a length of erbium-doped-core optical fibre pumped by a 980nm solid state laser diode. A 3dB fibre coupler was used to couple light into the embedded fibre, and to separate out the optical signal reflected by the grating. The reflected signal was monitored using an optical spectrum analyser (HP7004A); wavelength resolution 0.2nm; ten scan averaging applied.

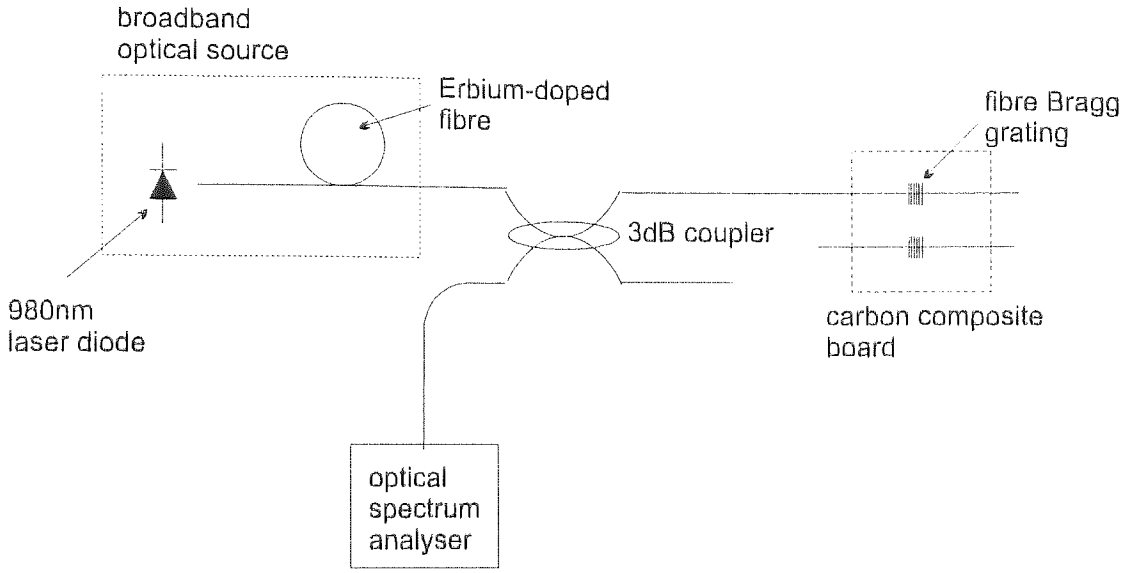

Figure 4.4 Experimental configuration used to interrogate embedded Bragg gratings

Four optical fibres containing a single uniform period grating[162] and one fibre containing an array of four uniform period gratings[163] were embedded in the carbon composite board. Of these, three optical fibres survived the embedding process, and subsequent shipping, with enough fibre extruding from the board to facilitate measurement of the grating. On investigation, one of these fibres did not return a signal from the grating, indicating that it was broken within the board itself. The reflection spectra of the two remaining gratings are shown in Figure 4.5; grating (a) has a central wavelength of 1541.84nm and grating (b) has a central wavelength of 1549.06nm; the reflectivity of both gratings was within the range 50% to 60%. Grating (b) was used in the following measurements.

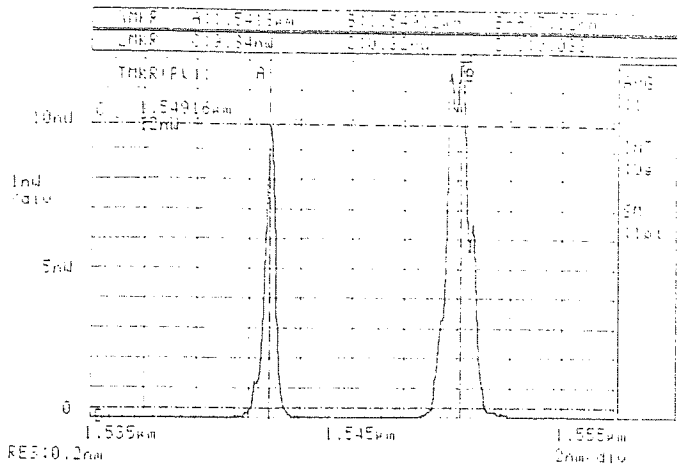

Figure 4.5 Embedded fibre grating spectra: (a) λ=1541.84nm; (b) λ=1549.06nm

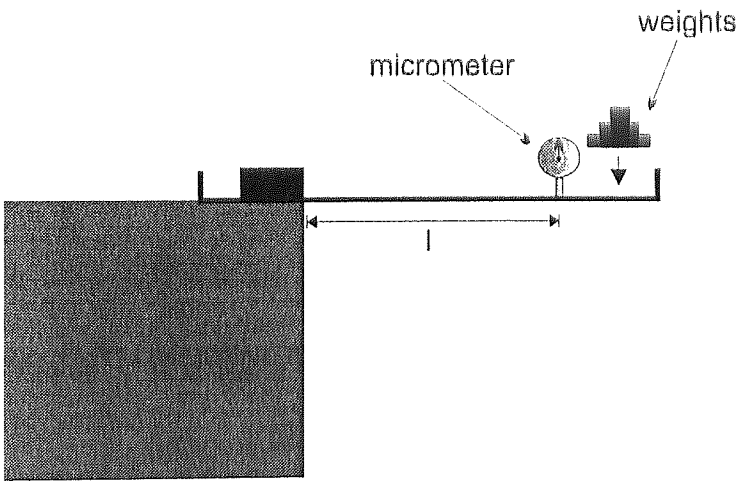

Figure 4.6 Experimental arrangement used to exert strain on embedded fibre grating

The carbon composite board was clamped to the edge of an optical bench, Figure 4.3, and force applied in both the upwards and downwards directions in order to strain and compress the grating respectively. The experimental arrangement used to exert strain on the embedded grating is shown in Figure 4.6. The board was clamped to the optical bench at a distance of 65mm from one edge, leaving 186mm of board available for use. Force was applied to the board by placing weights on it at the opposite, unclamped, edge. The deflection was measured using a micrometer fixed at a point 23.5mm from the unclamped end, aligned along the normal to the unstrained board, resulting in an effective

board length, l=162.5mm. The gratings were located at a distance x=6mm from the bending axis. The grating was compressed using the arrangement shown in Figure 4.7; the effective board length and the grating position remained the same. Here force was applied to the board in the upwards direction by placing a variable height stage underneath the unclamped edge and incrementally increasing the height; as the stage is raised the board is deflected upwards. The deflection was measured using the fixed point micrometer set up as before.

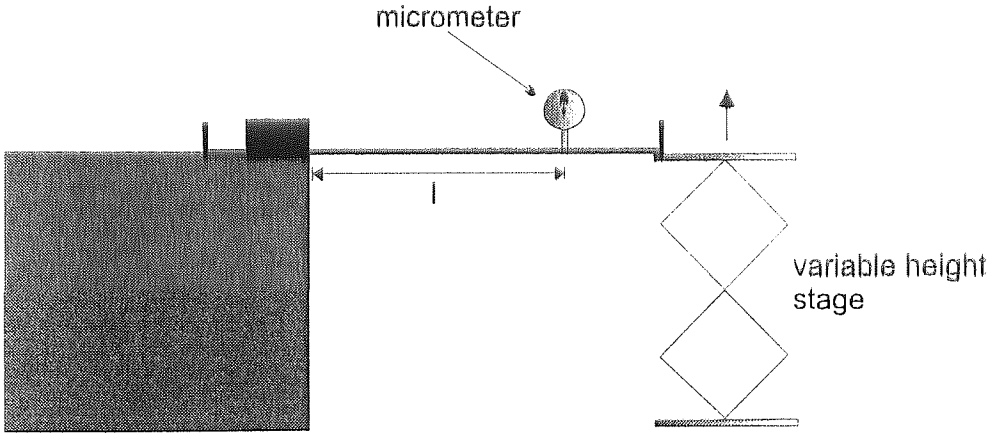

Figure 4.7 Experimental arrangement used to compress embedded fibre grating

4.2.3.3 Strain and compression measurement results

Figure 4.8 shows the experimental and theoretical dependence of wavelength change, $\Delta\lambda$, on deflection, for strain applied to the grating. The theoretical values of the Bragg wavelength change were calculated using Equation 4-6, assuming a grating wavelength strain sensitivity[137] of 1.15pm/nm. Least-squares straight-line fitting statistics were applied to both sets of data. The experimental points lie on a $\Delta\lambda$/deflection dependence of -0.029nm/mm, and the theoretical points lie on a $\Delta\lambda$/deflection dependence of -0.065nm/mm. The experimental and theoretical variation of wavelength shift with deflection, for the grating under compression, are shown in Figure 4.9. The straight-line fits to the experimental and theoretical data points have gradients of 0.023nm/mm and 0.065nm/mm respectively.

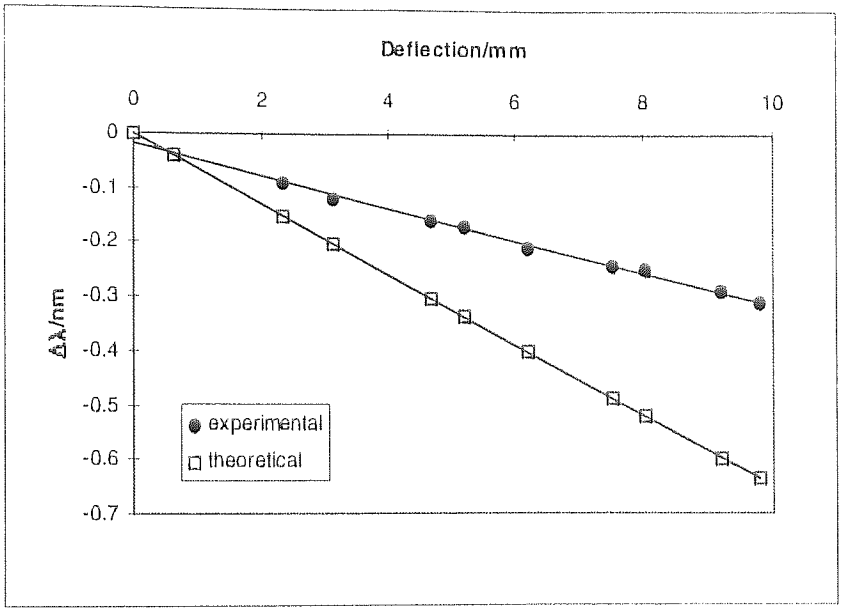

Figure 4.8 Embedded grating under strain: wavelength change as a function of deflection

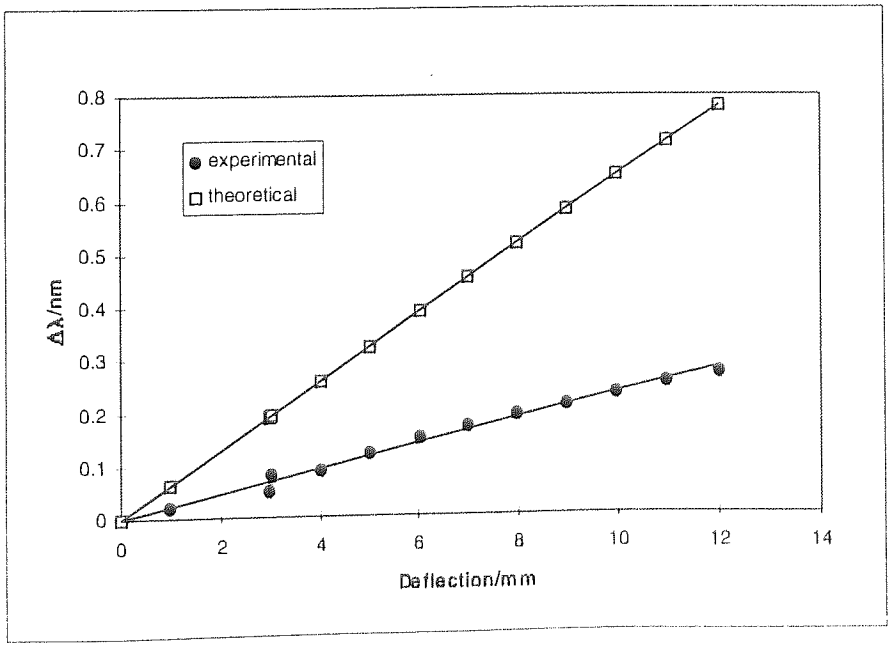

Figure 4.9 Embedded grating in compression: wavelength change as a function of deflection

4.2.3.4 *Discussion of results*

The experimental results show a clearly linear dependence of the grating wavelength on the applied deflection. The change in Bragg wavelength experienced by a grating is known to be linearly related to the strain[137], or compression, applied to it. The difference in the gradients of the straight-line fits to the experimental and theoretical data values suggests that incomplete transfer of strain from the board to the optical fibre is occurring. This could be caused by the fibre slipping inside the board due to poor bonding between the fibre and the epoxy resin. An alternative explanation for the poor agreement between the experimental and theoretical data straight-line fit gradients is that the presence of the glass plies in the composite may move the bending axis[164], in which case the theory which has been applied is inappropriate for this type of composite board.

4.2.4 Surface mounted gratings

4.2.4.1 *Introduction*

In order to test the validity of the theory used for the embedded gratings, and as a comparison to the results obtained from them, a uniform period grating and a Fabry-Perot filter grating were mounted on the surface of the board, and the strain and compression measurements repeated. If the glass plies are affecting the position of the bending axis within the board there should be significant disagreement between the experimental and theoretical values of $\Delta\lambda$ for these measurements also.

4.2.4.2 *Measurement systems and grating spectra*

The gratings were glued, using cyanoacrylate adhesive, after removing the protective jacket from the length of fibre containing the grating, onto the upper surface of the carbon composite board; they were therefore on the opposite side of the neutral axis with respect to the embedded gratings. The board was fixed to the optical bench in a similar arrangement to that used for the embedded

fibre grating measurements: the board was clamped to the optical bench at a distance of 68mm from one edge, leaving 183mm of board available for use. The deflection was measured using a micrometer at a point 30.5mm from the unclamped end, resulting in an effective board length, l =152.5mm. The gratings were located at a distance x=83mm from the bending axis. The gratings were strained and compressed using the experimental arrangements of Figure 4.6 and Figure 4.7 respectively.

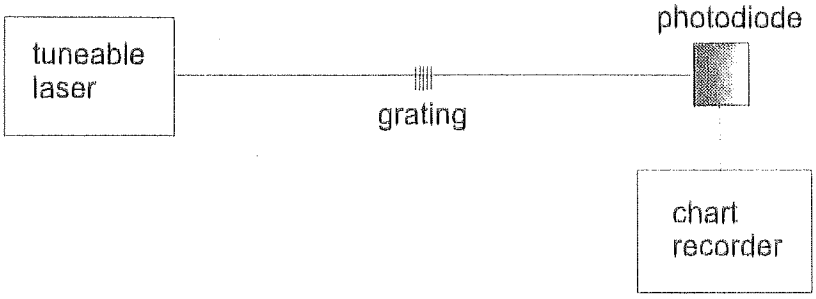

Figure 4.10 Experimental arrangement used to record transmission spectra of surface mounted uniform period grating and fibre Fabry-Perot filter

The grating spectra were interrogated using the experimental arrangement shown in Figure 4.10. An external cavity grating-tuned semiconductor laser (Photonetics Tunics 1550) was wavelength tuned across the grating bandwidth. The transmitted optical signal was detected using a photodiode, and the resulting voltage plotted on a chart recorder, set to a suitable scan speed. Figure 4.11 shows the transmission response of the uniform period grating; central wavelength 1540.02nm. Figure 4.12 shows the fibre Fabry-Perot filter transmission spectrum; FWHM bandwidth ~4.64nm; stopband peak wavelength 1543.93nm; and stopband FWHM linewidth ~0.17nm.

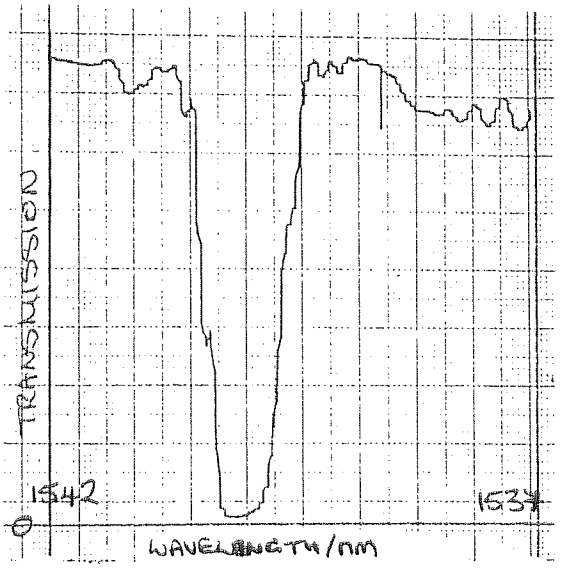

Figure 4.11 Surface mounted uniform period grating transmission spectrum

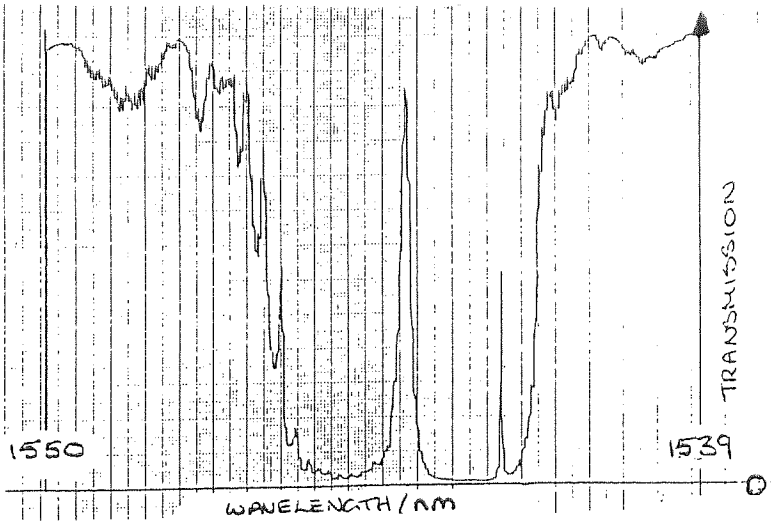

Figure 4.12 Surface mounted fibre Fabry-Perot filter transmission spectrum

4.2.4.3 *Strain measurement results*

Figure 4.13 shows the experimental and theoretical change in Bragg wavelength of the fibre Fabry-Perot filter passband as a function of the deflection experienced by the board, under the application of strain to the fibre. Application of least-squares straight-line-fit statistics to the experimental and theoretical data points gave $\Delta\lambda$/deflection dependencies of 0.069nm/mm and 0.070nm/mm respectively.

The experimental and theoretical dependence of Bragg wavelength change on deflection, for strain applied to the uniform period grating, is shown in Figure 4.14. Straight-line fits to the data returned $\Delta\lambda$/deflection dependencies of 0.079nm/mm for the experimental values and 0.070nm/mm for the theoretical values.

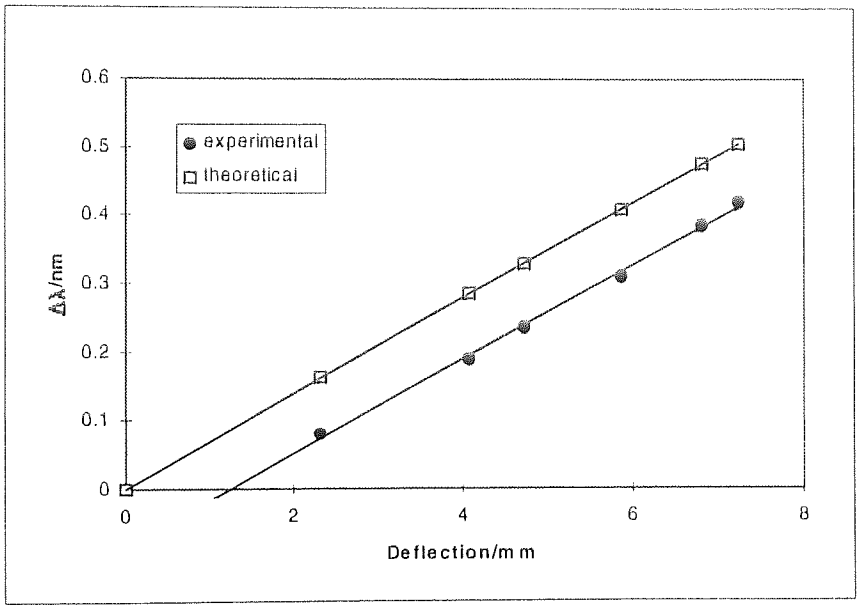

Figure 4.13 Surface mounted fibre Fabry-Perot filter under strain: experimental and theoretical wavelength change as a function of deflection

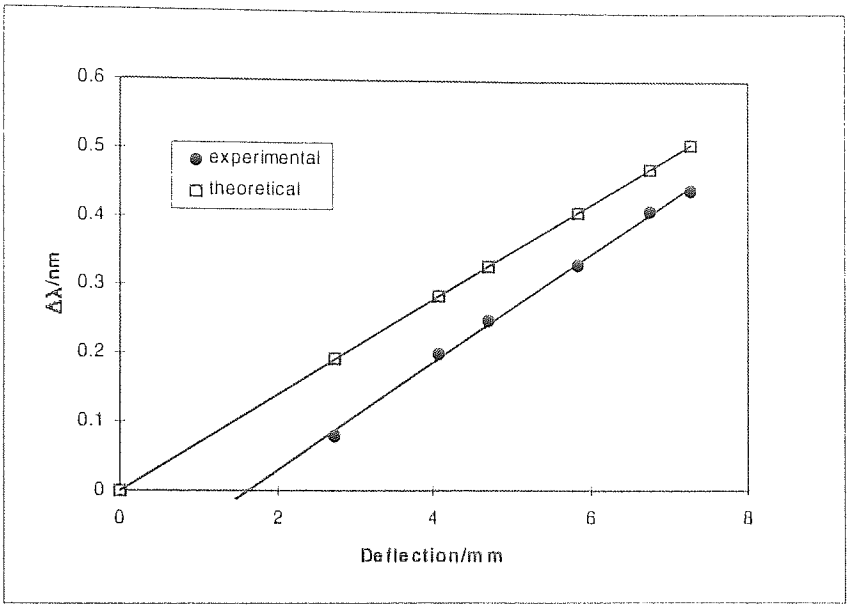

Figure 4.14 Surface mounted uniform period grating under strain: experimental and theoretical wavelength change as a function of deflection

4.2.4.4 Compression measurement results

Figure 4.15 shows the experimental and theoretical $\Delta\lambda$/deflection dependencies for the fibre Fabry-Perot filter in compression. Applying straight-line-fit statistics, the experimental dependence was -0.063nm/mm, and the theoretical dependence -0.070nm/mm.

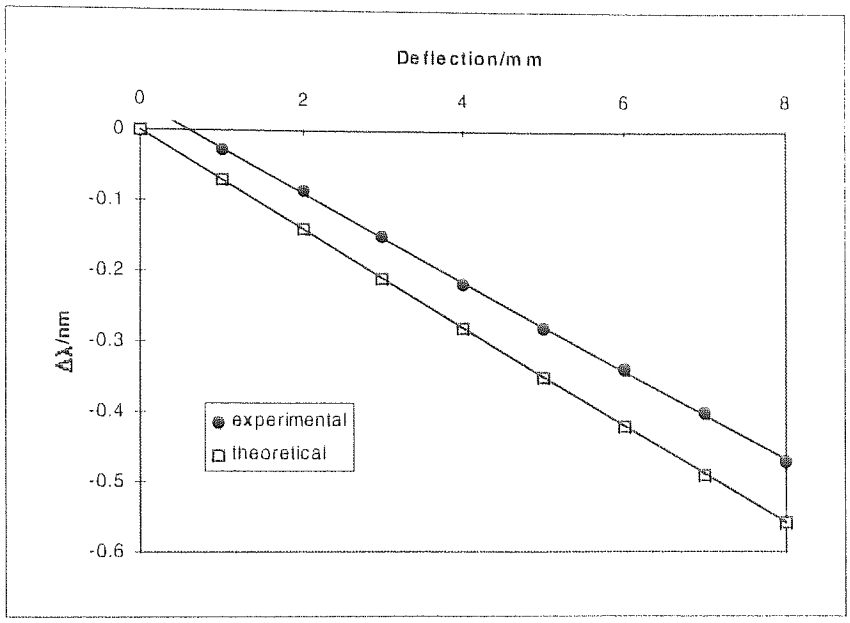

Figure 4.15 Surface mounted fibre Fabry-Perot filter in compression: experimental and theoretical wavelength change as a function of deflection

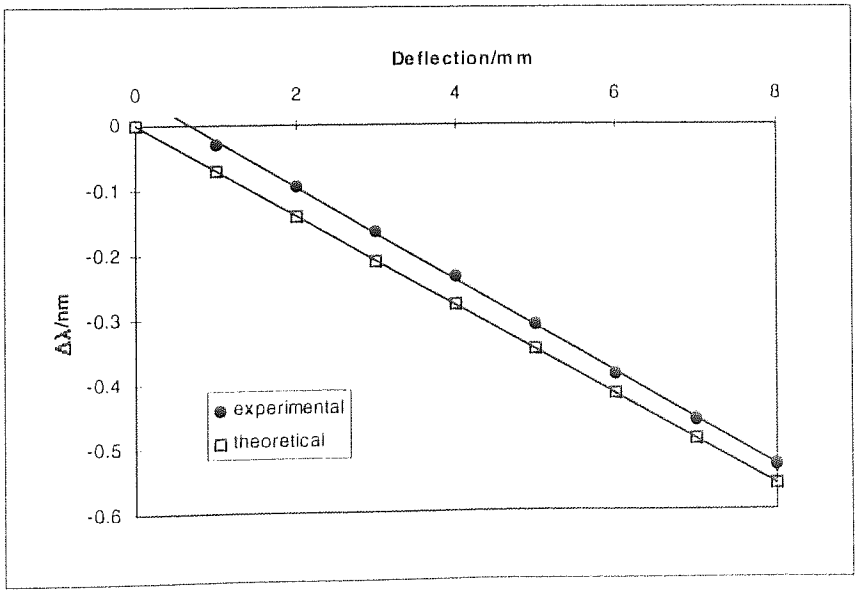

Figure 4.16 Surface mounted uniform period grating in compression: experimental and theoretical wavelength change as a function of deflection

Compressing the uniform period grating gave the experimental and theoretical dependence of Bragg wavelength on deflection shown in Figure 4.16. The

gradients of the experimental and theoretical straight-line-fits were -0.072nm/mm and 0.070nm/mm respectively.

4.2.4.5 *Discussion of results*

The two gratings were glued to the board at the same point in time, and the order in which the results are presented above is the order in which the measurements were made; it is important that this is kept in mind while discussing the results. All of the experimental results display a clear linear dependence of Bragg wavelength change on applied deflection. The displacement of the experimental data from the corresponding theoretical values indicated that some initial slippage was being experienced by the lengths of optical fibre containing the gratings. This can be accounted for by the grating slipping in the glue due to incomplete bonding or through take up of slack in the fibre during the initial loading of the board.

There is very good agreement between the experimentally recorded and theoretically predicted $\Delta\lambda$/deflection dependencies for the Fabry-Perot filter strain measurements. Better than 98% of the strain felt on the surface of the board, as predicted by Equation 4-5, is detected by the fibre grating. Closer agreement might be achieved by taking into account the distance from the surface of the board to the fibre axis. Equation 4-5 can therefore be said to be a good model of the dependence of the surface strain experienced by this type of composite board on the deflection applied to it.

The uniform period grating experimental strain results agree less well with the calculated values than the Fabry-Perot filter results, in fact they show more strain being experienced by the grating than the theory predicted. This may be due to the presence of additional strain in the fibre, although the source of this extra strain is unclear.

Under compression, the experimentally measured values of the wavelength change experienced by the fibre Fabry-Perot filter passband are in poorer agreement with their corresponding predicted values than was observed for the filter under strain. It appears that this fibre may be experiencing some additional strain here also, which must be cancelled out before compression can occur. Hence a smaller wavelength change than expected was observed.

The three sets of measurements discussed above were carried out consecutively within the space of one day. The dependence of Bragg wavelength change on deflection for the uniform period grating under compression was made the following day, allowing the board to relax back towards its unstrained state. The experimental results show that the fibre is experiencing more compression than the theory predicted, although the mismatch is less severe than in the two preceding measurements. The source of the additional compression is again unclear

4.2.5 Discussion

The results obtained for the application of strain to the surface mounted fibre Fabry-Perot filter support the model of strain experienced by a thin sheet, given by Equation 4-5. From this it may be concluded that the presence of the glass plies within the carbon composite board structure do not significantly affect the position of the bending axis, as suggested in 4.2.3.4. Therefore, the cause of the observed mismatch between the experimental and theoretical values for the embedded gratings must be slippage of the fibre within the board. The most probable causes of this are insufficient bonding between the uncoated length of fibre containing the grating and the epoxy resin, and slippage of the fibre within its coated sections.

The observation that the carbon composite board required a long time to relax back to its unstrained state highlights the need to consider the elasticity of any materials being proposed for the fabrication of smart structures. The type of carbon composite board used here is most suited for structures which would experience small amounts of strain over long periods of time. It is obviously unsuitable for smart structures which would be repeatedly exposed to large strains over short time periods.

This work forms the first report, of which I am aware, of the utilisation of in-fibre Bragg gratings as strain sensing elements within composite material smart structures. For commercial reasons further investigation of the performance of the smart board could not be carried out, and the work was not publically reported. The subject has since been further investigated by *Rao et al*[165] and the government sponsored Link Photonics Programme project 'Maritime Applications of Smart Structures Technology' (MAST).

4.3 Requirements for a Bragg grating sensor demultiplexing system

An ideal demultiplexing system should be able to remotely interrogate many tens of sensors, and must be low cost, stable and, in the case of avionics and aerospace applications, lightweight and compact. In addition, it should be suitable for serially examining each grating in the sensor system and for tracking a single grating in real-time. Both periodically variable and static strain and compression must be detectable, and the system should be either temperature independent or able to measure this also.

A realistic measurable strain range is of the order 100με to a few 1000με. One suggested application[166], to provide quasi-distributed strain monitoring, requires 100 sensors to be equally spaced across an 8m span bridge, each with

a measurement range of 100με to 1000με. This strain is equivalent to a wavelength change of 0.15nm to 1.15nm; assuming a strain sensitivity[137] of 1.15pm/nm, on gratings with an average FWHM linewidth of ~0.3nm.

Few of the fibre Bragg grating sensor demultiplexing systems described in chapter 1 are suitable for interrogating more than one sensor with a single detection unit, and use expensive laboratory equipment to measure the wavelength change incurred by a grating. The sensor demultiplexing solution offered in this work is based upon a Fabry-Perot etalon tuneable filter in which the etalon cavity is filled with a liquid crystal, and has the potential to meet all of the above requirements.

4.4 Liquid Crystal Fabry-Perot etalon tuneable filter

4.4.1 Introduction

Use of a liquid crystal filled Fabry-Perot etalon (LCFP) as a wavelength tuneable transmission filter was first reported by *Gunning et al*[167], for operation in the visible and infrared (3-5μm) wavelength ranges. LCFP filters have since been developed for wavelength-division-multiplexing in optical communications systems, and high performance, including low loss, narrow transmission peak linewidth and wide tuning range, has been achieved[168,169,170].

The results reported on the use of LCFP filters for wavelength selection in optical transmission systems[78,79] suggest that these devices could be readily applied to the demultiplexing of fibre Bragg grating sensors. Transmission peak linewidths from 0.07nm to 3.4nm have been reported[170,171], with tuning ranges of >9nm and 127nm respectively.

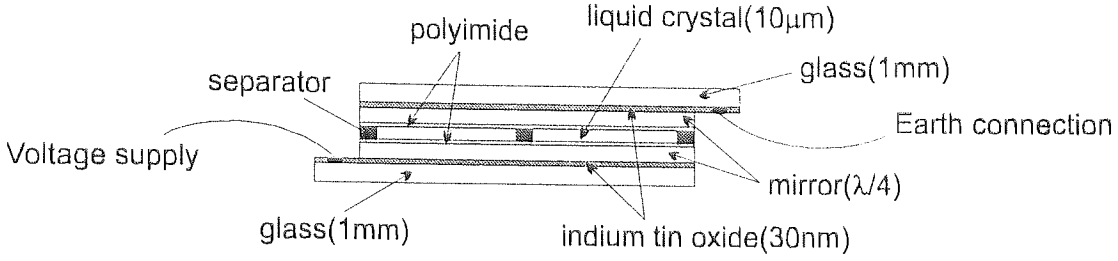

Figure 4.17 Liquid crystal Fabry-Perot etalon construction

4.4.2 Construction and theory of operation

The LCFP filter is a Fabry-Perot interferometer with a homogeneously aligned, nematic liquid crystal (Merck[172] Licrilite® E7) filled cavity. The liquid crystal layer is sandwiched between two glass substrates, containing alignment films, indium tin oxide (ITO) electrodes and dielectric mirrors, Figure 4.17. The ITO electrodes must be placed outside the etalon cavity since the transmittance of ITO is less than 100% at 1.5μm; the ITO electrodes reduce the etalon transmittance[79] by ~5%. The dielectric mirrors have a reflectivity of between 95% and 99%. The purpose of the polyimide alignment layer is to control the initial orientation of the liquid crystal molecules, when no voltage is applied to it, so that they lie parallel to the glass substrates, Figure 4.18(a). When voltage is applied to the liquid crystal the molecules become realigned, Figure 4.18(b), and the refractive index changes from n_e to n_o as the voltage increases, for light polarised parallel to the molecules. This alters the optical length of the etalon cavity and produces a shift in the resonance wavelength; the resonance wavelength decreases as the amplitude of the applied voltage increases. The resonance wavelength of the cavity is given by[79]

$$\lambda_m = \frac{2nL}{m}$$

Equation 4-7

where n is the refractive index of the liquid crystal, L is the cavity length, and m is an integer, and shifts from $2n_eL/m$ to $2n_oL/m$ with increasing applied voltage. For light polarised orthogonally to the liquid crystals, the refractive index does not change and no variation in the resonance wavelength is observed. Only a.c. voltages, with frequencies of the order of kilohertz, should be applied to the liquid crystal; use of d.c voltages leads to degradation of the liquid crystal.

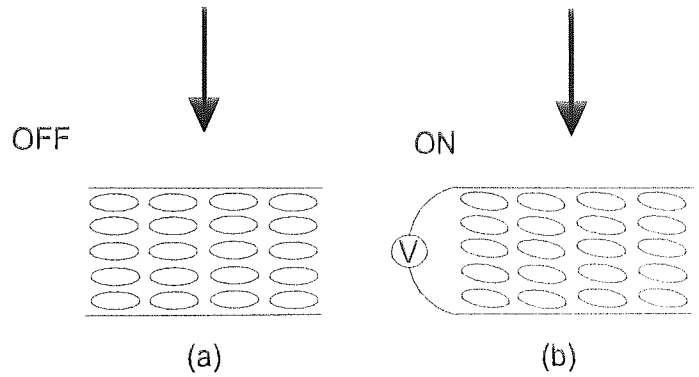

Figure 4.18 Liquid crystal molecule alignment: (a) when no voltage is applied the molecules are aligned parallel to the etalon faces, and the transmitted light polarisation; (b) when voltage is applied they become realigned

The Fabry-Perot etalon transmission spectrum, as a function of wavelength, λ, can be described by[79]

$$T = \frac{T_{\max}}{1+\left(4/\pi^2\right)F^2 \sin\left(2\pi nL/\lambda\right)}$$

Equation 4-8

where T_{max} is the maximum transmittance at the resonance wavelength, and F is the total finesse of the Fabry-Perot interferometer, determined by the mirror reflectivity and loss, the absorption coefficient of the liquid crystal, the curvature, waviness and roughness of the glass substrates, and the parallelism of the two substrates.

The resonance peaks are separated in wavelength by the free spectral range (FSR),

$$FSR = \frac{\lambda_m}{m+1}$$

Equation 4-9

and the tuning range of the resonance peaks is

$$\Delta\lambda = \frac{\lambda_m \Delta n}{n}$$

Equation 4-10

The time required for a LCFP filter to tune across a specified wavelength range depends upon the magnitude of the tuning range, the length of the etalon cavity and the type of liquid crystal. The response time of the liquid crystal increases with increasing cavity length and tuning bandwidth, and it takes a greater length of time to tune the resonance wavelength to a longer value than to a shorter value because the turn-off time of a liquid crystal is longer than its turn-on time: the length of time required for the molecules to relax is greater than the length of time it takes for them to align when voltage is applied to the liquid crystal.

The refractive index of a liquid crystal is strongly temperature dependent, and the glass substrates can also distort when the temperature changes[79], which results in a corresponding temperature dependence of the etalon resonance wavelength; a wavelength temperature dependence of -0.2nm/°C has been reported for an LCFP etalon filled with the liquid crystal ZLI-3103[172,79].

4.5 Initial LCFP characterisation measurements

Initial investigations of the transmission characteristics of the LCFP etalon were carried out using the experimental arrangement shown in Figure 4.19. A 980nm solid state laser was used to pump a length of erbium-doped-core optical fibre to provide a broadband optical source. As described above, the LCFP etalon resonance peak wavelength is determined by the voltage applied to the liquid crystal. Therefore, the resonance wavelength can be tuned by applying a voltage of varying amplitude. A function generator (HP 3311A), with an in-built amplitude ramp, was used to provide a 1kHz square-wave voltage to the liquid crystal; the voltage amplitude was monitored with an oscilloscope, voltage measurement resolution 0.1V. The LCFP etalon transmission spectrum was recorded using an optical spectrum analyser (Ando AQ-6310C).

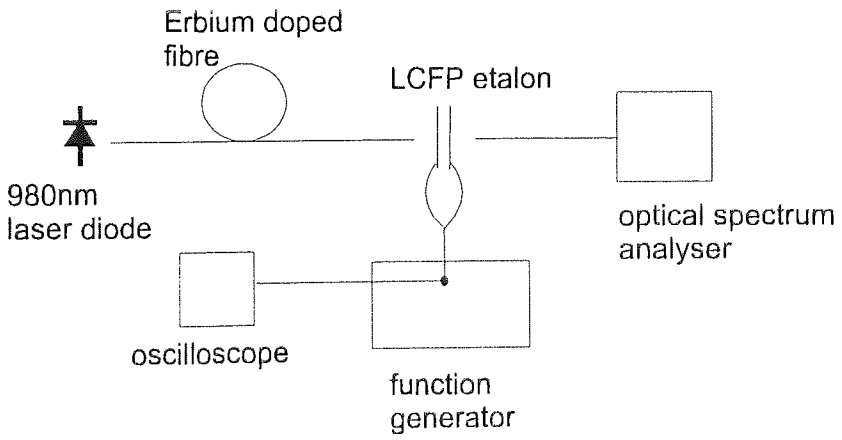

Figure 4.19 Experimental arrangement used to carry out initial characterisation of LCFP etalon

Figure 4.20 shows the LCFP etalon optical transmission spectrum, optical spectrum analyser resolution bandwidth 0.2nm. The resonance peaks at 1572nm and 1500nm were observed to scan towards shorter wavelengths with increasing voltage amplitude, while the peaks at 1605nm, 1540nm and 1490nm did not wavelength tune; the latter three peaks correspond to light which is polarised orthogonally to the liquid. This polarisation sensitive transmission

characteristic is currently the subject of a PhD research project at University College London[173]. The free spectral range of the etalon was measured to be 71.7nm. The variation of resonance peak wavelength with applied voltage amplitude is shown in Figure 4.21; optical spectrum analyser resolution bandwidth 2nm. For voltage amplitudes greater than ~2.5V the resonance wavelength was observed to vary linearly with voltage.

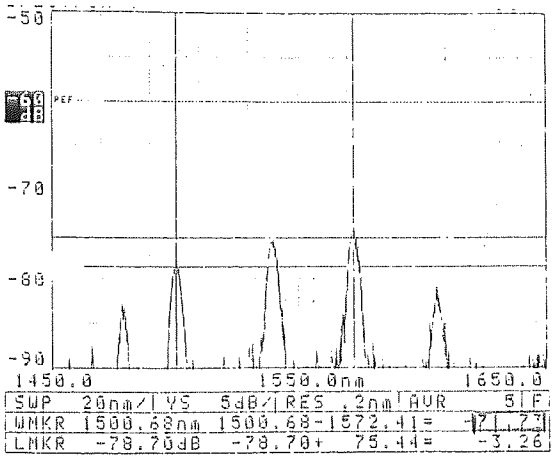

Figure 4.20 LCFP etalon transmission spectrum

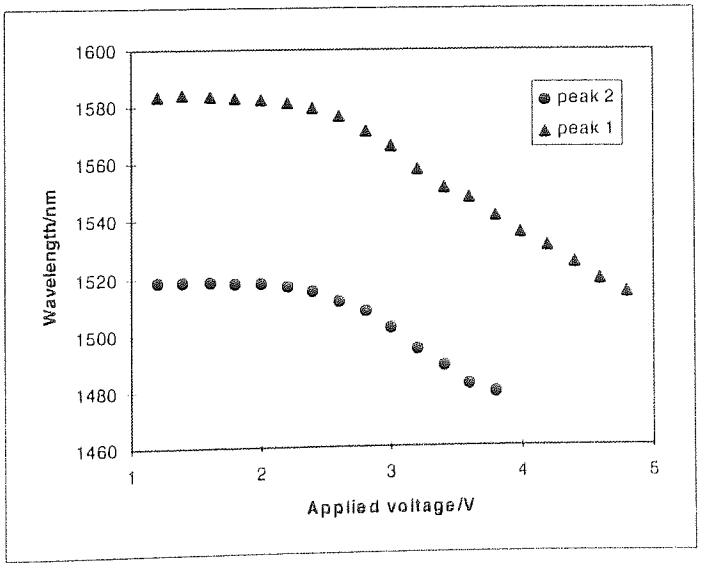

Figure 4.21 Resonance peak wavelength tuning as a function of applied voltage

Figure 4.23 shows the experimental arrangement used for the initial detection of fibre Bragg gratings using the LCFP tuneable filter. The LCFP voltage was controlled as above, and the optical spectrum analyser (HP70004A) scan was triggered by the function generator. After some effort, the optical spectrum analyser was successfully set to scan synchronously with the voltage amplitude ramp, and Figure 4.22 shows a typical recorded wavelength scan: gratings at 1545.28nm, 1547.58nm, 1556.61nm and 1557.93nm.

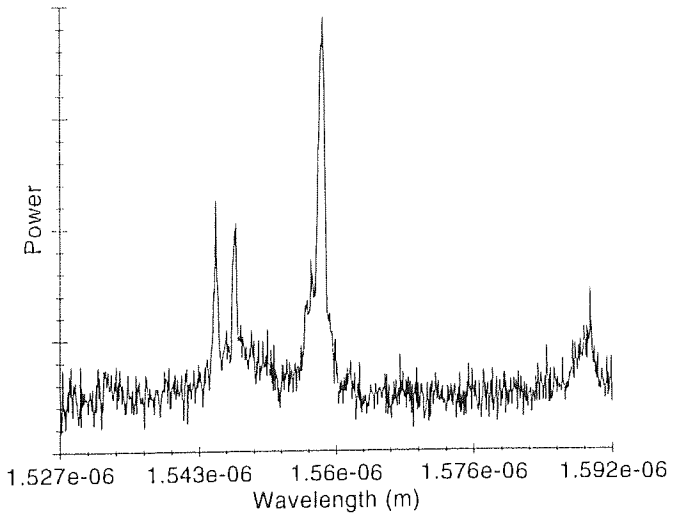

Figure 4.22 Typical wavelength scan of LCFP etalon recorded on optical spectrum analyser and displaying signal peaks corresponding to Bragg gratings at at 1545.28nm, 1547.58nm, 1556.61nm and 1557.93nm.

Although the gratings were successfully detected, the measurement was not easily repeatable or controllable due to difficulties in setting the voltage amplitude ramp range, caused by the poor voltage measurement resolution, and matching this to an appropriate optical spectrum analyser wavelength scan width. This experimental arrangement was therefore unsuitable for accurately characterising the LCFP etalon, and did not offer sufficient controllability of the LCFP etalon for it to be used as the demultiplexing element in a Bragg grating sensor system.

In order to move towards the application of the LCFP etalon as a Bragg grating sensor demultiplexing element a precisely controllable voltage source is required to drive the etalon, operating in conjunction with a wavelength measurement system of significantly higher resolution. The design and development of such a control and measurement system comprises the major part of this work on LCFP etalon tuneable transmission filters, and will be reported in the following sections.

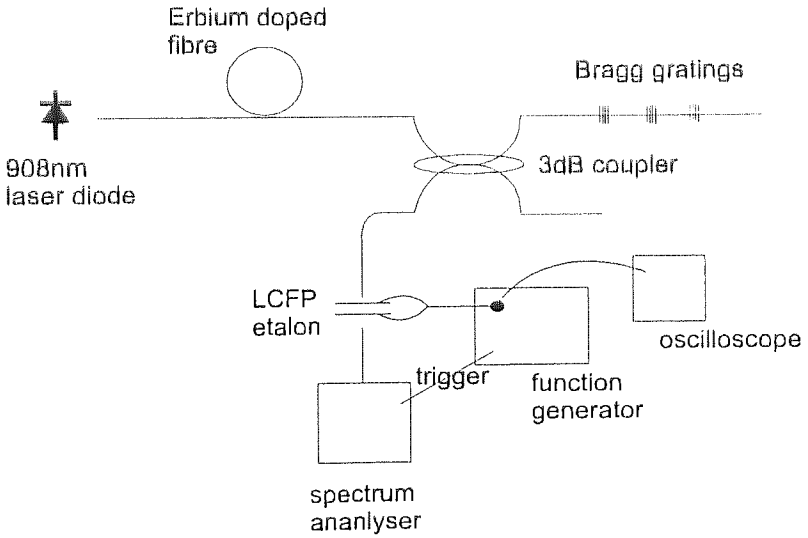

Figure 4.23 Experimental arrangement used for initial detection of fibre Bragg gratings using LCFP tuneable filter

4.6 Experimental LCFP tuneable filter demultiplexing system

4.6.1 Experimental arrangement

Several developmental stages were progressed through in order to develop the LCFP control system from the prototype, described in 4.5, into the final, computer controlled arrangement suitable for calibration and system testing

measurements. Only the final experimental arrangement will be discussed in detail as it includes all of its predecessors.

Figure 4.24 shows the generalised experimental arrangement used to characterise the LCFP etalon and test its application as a Bragg grating sensor system demultiplexing element. A broadband optical source was constructed by reverse pumping ~20.5m of erbium-doped-core optical fibre with a 1480nm, fibre pigtailed, semiconductor laser diode (AT&T M255D) (~30mW output power); a 1480nm optical isolator was placed between the laser diode and the erbium-doped fibre. Two chirped fibre Bragg gratings, central wavelength ~1480nm, bandwidth ~17nm, were included at either end of the erbium-doped fibre to maximise the available pump power and to remove any residual 1480nm radiation from the measurement system. The erbium fluorescence was coupled into the sensor arm, containing the Bragg gratings, via a 3dB optical coupler, which also separated the reflected optical signals from the incoming broadband illumination. During some of the LCFP characterisation measurements the broadband source was turned off, and an external-grating tuned semiconductor laser (HP8168B) was used in place of the fibre Bragg gratings, as a narrow linewidth source of accurately known wavelength, to be detected by the LCFP etalon.

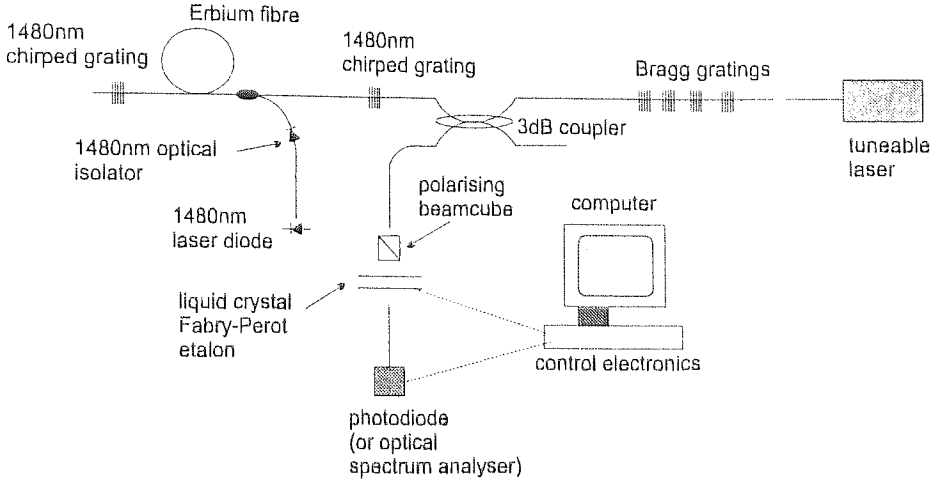

Figure 4.24 Generalised experimental arrangement used to characterise the LCFP etalon and test its application as a Bragg grating sensor system demultiplexing element

A polarising beamcube was used to remove light polarised orthogonally to the liquid-crystal molecules, eliminating the non-tuneable resonance peaks from the LCFP etalon spectrum; this is necessary when the detector used is a photodiode as any background illumination will reduce the system's measurement accuracy. The detector was either an optical spectrum analyser (HP70004A) or a photodiode (Nortel DRP2-43T2). The voltage applied to the LCFP etalon was provided by a specially constructed electronic circuit, described in detail in 4.6.2, where the amplitude was controlled by computer through an analogue input/analogue output (AIAO), analogue to digital conversion board (NIDAQ Lab PC+), interfaced to the control program described in 4.6.3.

When the LCFP etalon resonance wavelength matches that of a Bragg grating in the sensor system the light reflected by the grating will be transmitted by the etalon, and a peak will appear in its transmitted optical spectrum.

4.6.2 LCFP square-wave drive voltage generation circuit

The initial characterisation measurements performed on the LCFP etalon showed that the etalon resonance peaks wavelength tuned for applied voltage amplitudes in the range 2-5V. Since the AIAO board in the computer had an output range of 0-10V some method of converting this into 2-5V was required in order to make full use of the board's output resolution.

The circuit used to convert the 0-10V d.c. voltage output from the AIAO board in the computer into the 2-5V 1kHz square-wave required to drive the LCFP etalon is shown in Figure 4.25. The input voltage (0V to 10V) from the computer is inverted by the first semiconductor amplifier (UA741CP) (-10V to 0V), and then divided by three (-3V to 0V) by the voltage divider resistor arrangement. The second inverting amplifier performs two functions: -2V is added to the voltage (-5V to -2V) and the voltage is inverted again (2V to 5V). The 1kHz square-wave is generated using a semiconductor IC timer chip (NE555), running at 2kHz, to drive a J-K flip-flop IC (4027B) which produces an output signal frequency of 1kHz. The 1kHz signal and the d.c. voltage are input into a single-pole double-throw analogue switch IC (DG303ACJ) to create a square-wave whose amplitude is determined by the voltage produced by the computer. This electronic circuit was successfully constructed and tested, and accurately performed the required voltage conversion.

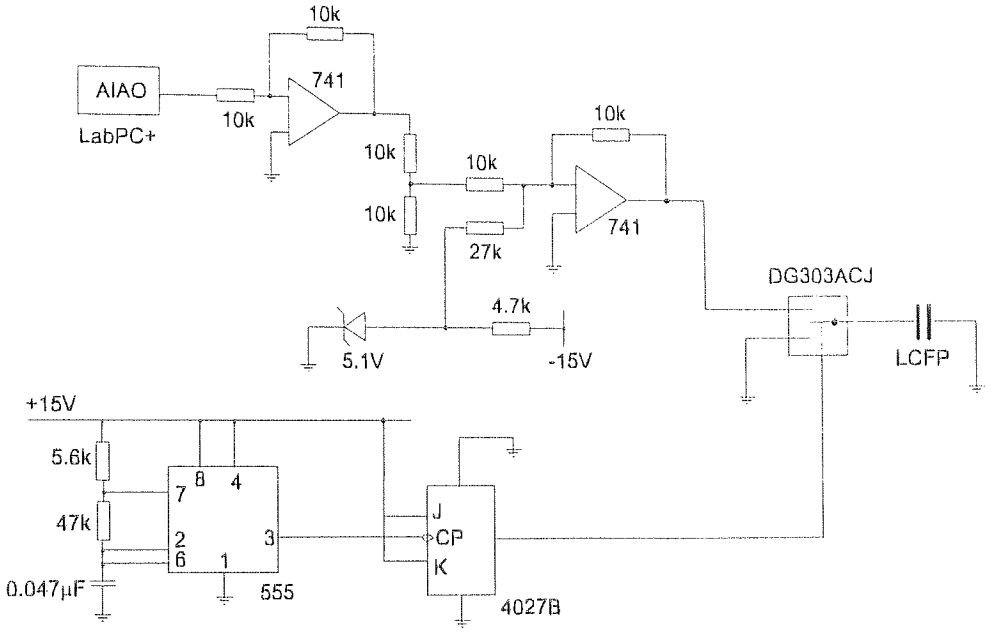

Figure 4.25 Electronic circuit used to convert the 0-10V d.c. voltage output from the AIAO board in the computer into the 2-5V 1kHz square-wave required to drive the LCFP etalon

4.6.3 LCFP measurement control program

In order to allow the system user to define the limits of the square-wave voltage amplitude scan a user interface program was written in the Visual Basic programming environment through which the voltage applied to the LCFP etalon was controlled, and which had the facility to record the output signal from the photodetector. The desired voltage amplitude range for the LCFP etalon is entered on screen by the user and when the 'start' button is selected, this voltage scan is converted into the values which the computer will output to the electronic circuit given above; in order to make use of the full output range of the AIAO board, and hence achieve the maximum voltage resolution, a 2V to 5V user defined range is converted for output as 0V to 9V. The output voltage is then incremented through these values in a user defined step size; see Appendix B1 for program code.

When the photodiode is being used as the transmitted optical signal detector the computer reads in the voltage from the photodiode at each step in the voltage scan, storing both the LCFP voltage and photodiode voltage values in an array. On completion of the voltage scan the program contains an option which converts the photodiode voltages into their equivalent wavelength values, Appendix B2, and normalises them, Appendix B3, to remove the effect of any optical power/wavelength dependencies of other optical elements within the system. The values are then processed by the peak searching code, Appendix B3, in order to find any peaks in the photodiode measurements, in either voltage or wavelength form, which represent the Bragg gratings. The wavelength, or voltage, peak values are then displayed on screen.

The computer control program evolved through several developmental stages, and many changes to the code were implemented before the final version was reached. The program successfully scanned the LCFP drive voltage for any user defined range and step size, and recorded and processed the output voltage signals from the photodiode.

4.6.4 Discussion

An improved LCFP etalon control and measurement system was designed and constructed. Use of a higher power, fibre-pigtailed semiconductor laser diode to pump a longer length of erbium-doped optical fibre produced a significantly higher power broadband optical source for interrogating the LCFP etalon and the fibre Bragg gratings. Coupled with the use of more sensitive optical measurement devices, this dramatically raised the resolution available for measuring the optical signal transmitted by the LCFP etalon.

The construction of a computer program to control the voltage applied to the LCFP etalon, and to measure the signal produced by the detector photodiode, allowed the LCFP voltage to be accurately controlled, and the LCFP etalon

transmitted optical spectrum to be recorded in detail. These improvements produced a measurement system which offered a 10mV LCFP voltage resolution; equivalent to 0.09nm resolution. In addition, it enabled the use of a highly accurate wavelength source in place of the Bragg grating sensor element array for the investigation of the wavelength dependent characteristics of the LCFP etalon. The LCFP etalon can therefore be fully characterised and its suitability for use as a demultiplexing element investigated further.

4.7 LCFP tuneable filter characterisation

4.7.1 Optical spectrum

The optical transmission spectrum of the LCFP filter was analysed using the experimental arrangement shown in Figure 4.24, using the broadband erbium-fluorescence source to illuminate the filter and the optical spectrum analyser to record the transmission spectrum; wavelength resolution bandwidth 0.1nm. The polarising beamcube was removed initially, in order to view all of the resonance peaks, and then replaced when the effect of applying voltage to the liquid crystal was to be investigated.

The LCFP etalon optical transmission spectrum, with no voltage applied to the liquid crystal, is shown in Figure 4.26; both polarisations of light are present. Resonance peaks are clearly visible at 1487.3nm, 1528.2nm, 1560.6nm and 1592.7nm, and the optical profile of the spectrum clearly follows the shape of the erbium fluorescence spectrum.

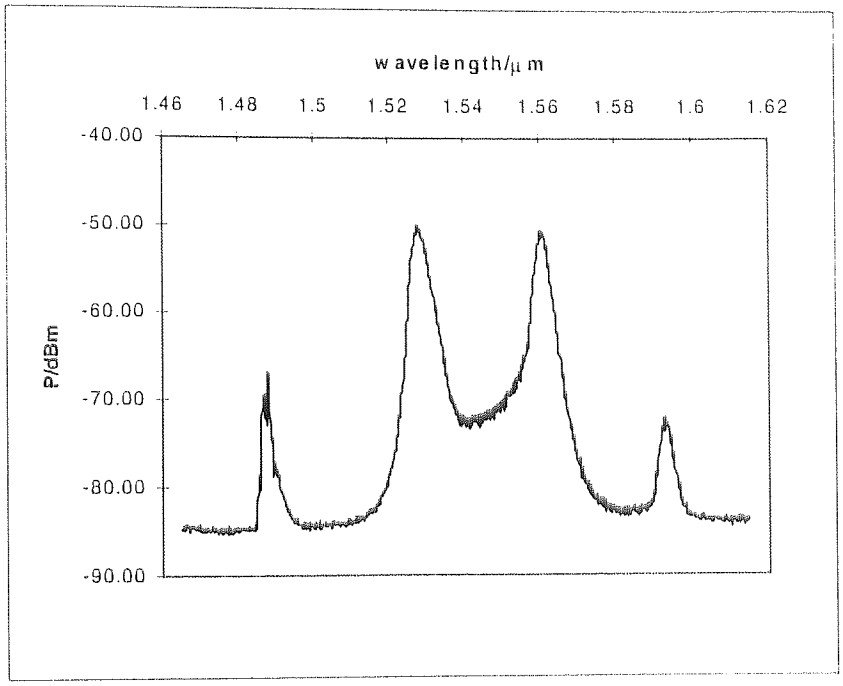

Figure 4.26 LCFP etalon transmission spectrum: both polarisations of light present; no voltage applied to the liquid crystal

Inserting the polarising beamcube and applying 0V and 2V, from the computer (equal to 2V and 2.67V after the square-wave generation circuit) to the liquid crystal, gave the transmission spectra shown in Figure 4.27. The 0V spectrum displays peaks at 1596.4nm and 1531.9nm while the 2V spectrum peaks are at 1591.2nm and 1528.2nm, indicating that applying increasing voltages shifts the resonance wavelengths to shorter values, as predicted. The different wavelengths displayed by corresponding resonance peaks in Figure 4.26 and Figure 4.27(0V) are produced by both the different applied voltage and a change in ambient temperature, which will be discussed further in 4.7.5.

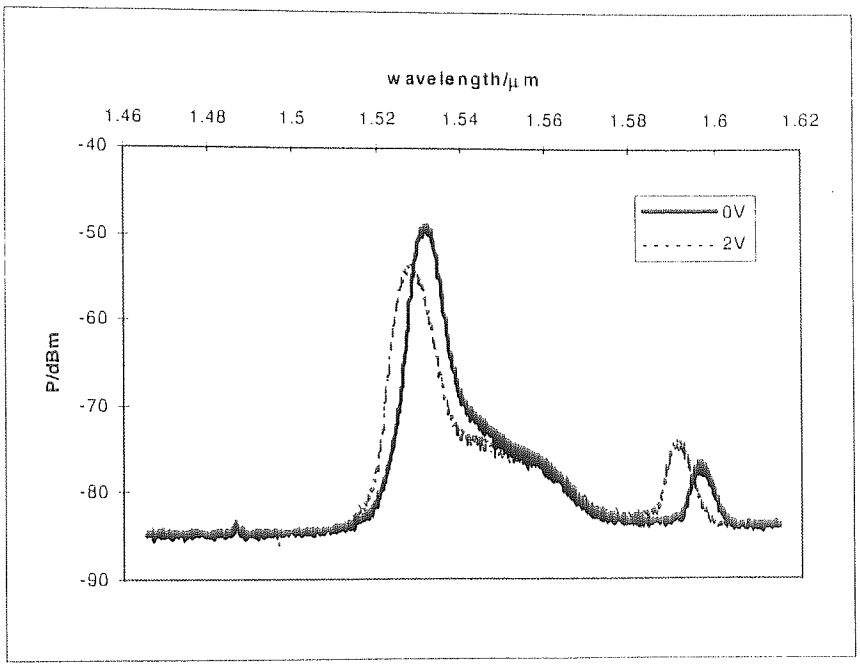

Figure 4.27 LCFP transmission spectrum: only light polarised parallel to the liquid crystal molecules is present; computer voltages of 0V and 2V applied

4.7.2 Capacitance

In order to select the correct J-K flip-flop semiconductor IC, in Figure 4.25, the input impedance of the LCFP etalon must be known, and was found by measuring its capacitance using the experimental arrangement shown in Figure 4.28. A 1kHz sine wave, V_{rms}=1.075V, was applied to the effective RC circuit, and its phase before and after the LCFP filter compared using an oscilloscope; this gave the phase difference between the voltage at the resistor and the voltage at the 'capacitor'. A phase shift, θ, of 21.6° was measured between the two voltages, which was converted to the equivalent impedance, X_C, and capacitance, C, using the following theory; where V_R and V_C are the voltages across the resistor, resistance R, and capacitor respectively; ω (=$2\pi f$) is the sine wave frequency; and Z is the reactance of the capacitor.

$$V = V_R + V_C$$
$$V_R = V_{R,0}\sin(\omega t + \vartheta)$$
$$V_C = V_{C,0}\sin(\omega t + \vartheta + \theta)$$

Equation 4-11

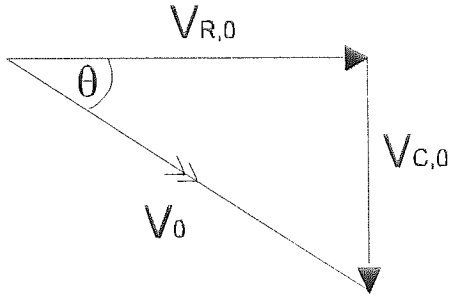

$$V_0 = \sqrt{V_{R,0}^2 + V_{C,0}^2}$$
$$\frac{V_0}{I_0} = Z = \sqrt{R^2 + X_C^2}$$
$$\Rightarrow X_C = \sqrt{Z^2 - R^2} = \frac{1}{\omega C}$$
$$\Rightarrow C = \frac{1}{\omega X_C}$$

Equation 4-12

For a resistance of 10kΩ and $I_{R,0}$=0.028mA, this gave an impedance of 3.96kΩ and a capacitance of 40.2nF.

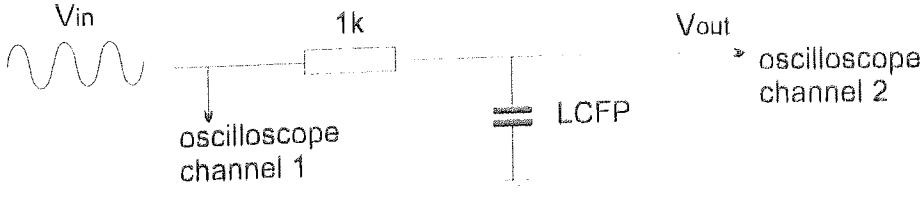

Figure 4.28 Electrical circuit for measurement of LCFP etalon capacitance

4.7.3 Resonance peak wavelength / Applied voltage

As described in 4.4.2, the wavelength at which the LCFP etalon resonance conditions are met can be changed by altering the refractive index of the liquid crystal, through varying the amplitude of the square-wave voltage applied to the liquid crystal. There are four resonance peaks which are visible during a full computer voltage scan of 0V to 9V, three are visible initially, as seen in Figure 4.27(0V), and a further peak appears at the high wavelength end of the spectrum when the voltage reaches ~6V. The variation of wavelength with applied voltage was measured (at T=19.55°C) for each resonance peak, using the experimental arrangement of Figure 4.24, employing the broadband optical source and the optical spectrum analyser, and is shown in Figure 4.29. A straight-line fit to the linear section of Figure 4.29(peak2), voltage range 2V to 9V, gives a resonance-peak-wavelength/applied voltage dependence of

$$\lambda = -10.642V_{computer} + 1619.39$$

Equation 4-13

In the voltage range 0V to 4V three peaks are present in the transmission spectrum, this is reduced to two peaks for a voltage of ~4V to ~6V, and returns to three peaks for the ~6V to 9V range. The existence of multiple resonance peaks at any one voltage value presents a problem for the photodiode detection based demultiplexing system. If the computer voltage is set at, say, 5V, there will be two wavelengths at which the LCFP etalon can transmit: 1500nm and 1564nm. Should the sensor system contain Bragg gratings at both of these wavelengths, the system will be unable to discriminate between them, since the photodiode can only measure total optical power. This reduces the operational wavelength tuning range from the full 81-85nm experienced by each resonance peak, as the voltage is tuned from 0V to 9V, to between 61nm and 65nm. One LCFP etalon can therefore be used to demultiplex gratings within only one of

the ranges 1610-1545nm and 1545-1464nm, as indicated by the shaded areas in Figure 4.29, requiring a computer generated voltage range of 0V to ~7V.

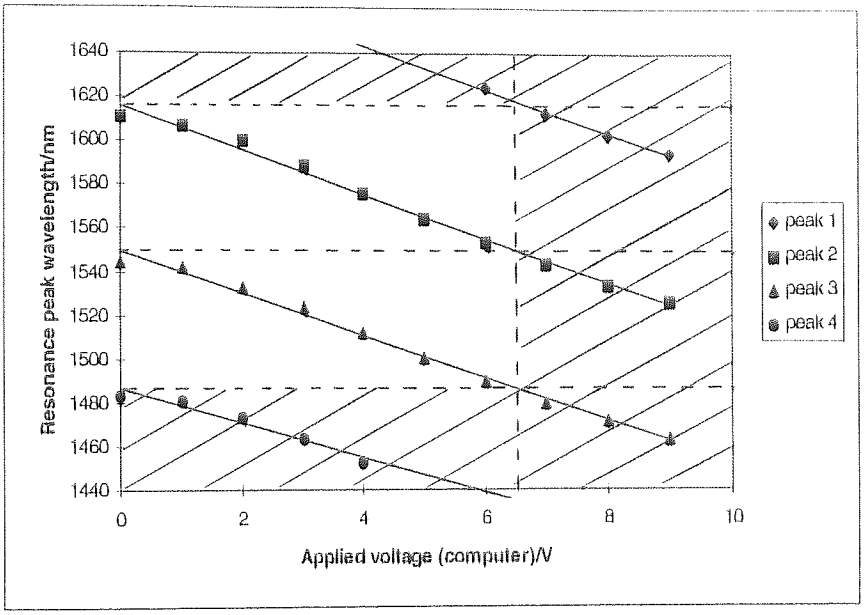

Figure 4.29 Applied voltage dependence of the wavelength of the four resonance peaks present in the LCFP spectrum over the full voltage range, ambient temperature 19.55°C; initial peak wavelengths: (1) 1624.2nm; (2) 1611nm; (3) 1544.5nm; and (4) 1483.5

4.7.4 Transmitted optical power/Applied voltage

The optical power transmitted by the LCFP etalon as a function of applied voltage was measured (at T=25.6°C) with the experimental arrangement of Figure 4.24, using the broadband optical source and the photodiode detector. The results, shown in Figure 4.30 display a pronounced fall in the transmitted optical power level, to approximately one quarter of the maximum transmitted power, between applied voltages of 3V and 6.5V.

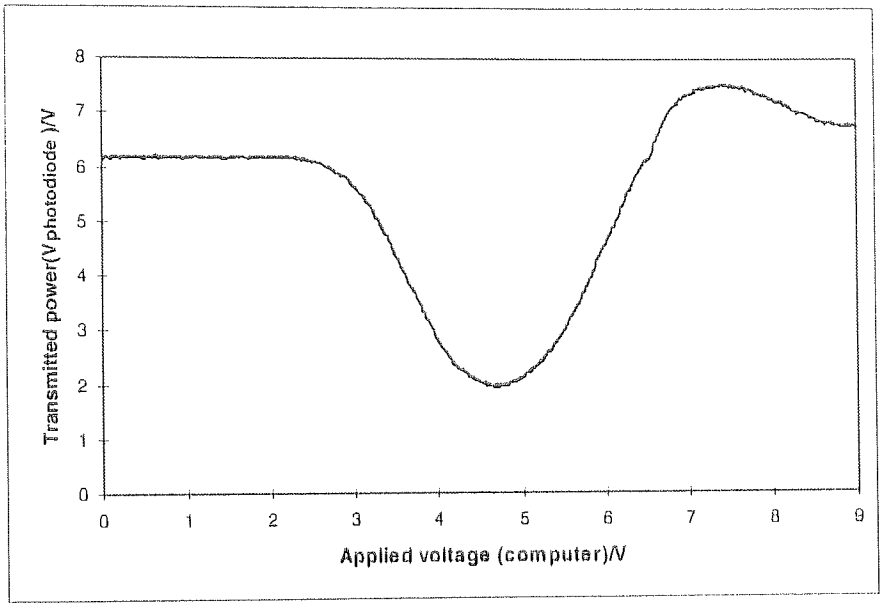

Figure 4.30 LCFP transmitted optical power as a function of applied voltage

The shape of the curve can be related to the wavelengths of the two central resonance peaks (peaks 2 and 3 of Figure 4.29) and the erbium fluorescence source spectral profile. Over the voltage range 0V to 3V peak 3 tunes from ~1544.5nm to ~1524nm, traversing the spectral region in which the erbium fluorescence optical power is at its maximum, while peak 2 tunes from ~1611nm to ~1588nm, where the erbium fluorescence is very low power. The voltage range 3V to 6.5V finds resonance peak 3 in the spectral region ~1524nm to ~1485nm, while peak 2 tunes from ~1588nm to ~1559nm. Hence neither resonance peak enters the main erbium fluorescence bandwidth of ~1525nm to ~1560nm, and the total available optical power is very low. For the voltages 6.5V to 9V peak 2 tunes across the spectral range ~1559nm to ~1526nm, accessing the full erbium fluorescence optical power, and the total transmitted optical power rises again.

These results indicate that the erbium fluorescence bandwidth does not cover the full tuning range of the filter, resulting in approximately one third of the voltage range being unusable. This limitation can be overcome by using an

optical source with a larger spectral bandwidth. However, such a device was not available for this work.

The fraction of incident optical power transmitted by the LCFP etalon was measured, using the experimental arrangement of Figure 4.24, in which a power meter (Antritsu ML910A & MA9301A) replaced the photodiode. Three values of voltage (at computer) applied to the etalon (0V, 4.4V and 6V), which was illuminated with 0.6μW of 1530nm radiation from the tuneable laser. The LCFP etalon transmitted 5.2nW, 35nW and 1.6nW, 0.9%, 5.8% and 0.3% respectively, of the optical power at these voltages; the maximum fractional transmission recorded corresponds to transmission at a resonance peak. The extremely low optical power transmission of the LCFP etalon means that the vast majority of the reflected optical signal power is lost, and therefore a relatively high power source is required. 28.3mW of 1480nm radiation was used to pump ~20.5m of Erbium-doped fibre to produce ~640μW of Erbium fluorescence, of which 50% is lost at the 3dB coupler, ~99% is lost at the gratings (assuming 40nm fluorescence bandwidth and 0.5nm grating linewidth), a further 50% is lost returning through the 3dB coupler, 50% is lost at the polarising beamcube and ~65% is lost coupling the light from fibre to fibre to allow it to pass through the bulk optic LCFP etalon. Hence the poor transmission characteristics of the LCFP etalon were compounded by an already low optical power budget. The loss could be reduced by replacing the 3dB coupler with an optical circulator, and by using a single polarisation optical source, however neither of these devices were available for this work.

4.7.5 Resonance peak wavelength/Temperature

The resonance peak wavelength temperature dependence was investigated using the experimental arrangement shown in Figure 4.24, in which the tuneable laser was used as the narrow linewidth signal source, λ=1550nm, and the transmitted optical signal was detected with the photodiode. The temperature of the LCFP etalon was measured using a platinum-film

temperature detector (conforming to BS 1904 Grade II) which was fixed to the front face of the etalon, on which the light is incident, with thermal heat-sink compound. The platinum film detector was connected to a lineariser module (RS 158-418) containing electronic circuitry designed to produce a linearised 1mV output per degree centigrade within the range -100°C to +500°C, with a long term stability of better than 0.1°C per annum; the lineariser output was displayed on a digital power meter. The temperature values were the room temperatures that the laboratory experienced over a period of several days. At each temperature point the control program scanned the applied voltage over the range 4.5V to 9V, and the transmitted optical signal detected by the photodiode was recorded at every voltage step; a 4.5V to 9V range was selected in order that only one resonance peak was being used and to ensure that a measurable optical signal power level was transmitted by the LCFP etalon. The stored V(computer) and V(photodiode) values were then processed to find V(computer) at the maximum V(photodiode) value, which corresponded to λ=1550nm; the results are displayed in Figure 4.31, and lie on a straight-line fit given by

$$V_{computer} = 0.2601T(^{o}C) + 0.616$$

Equation 4-14

From the resonance peak wavelength/voltage dependence of Equation 4-13, the temperature dependence of the LCFP etalon resonance peak wavelength is therefore -2.77nm/°C.

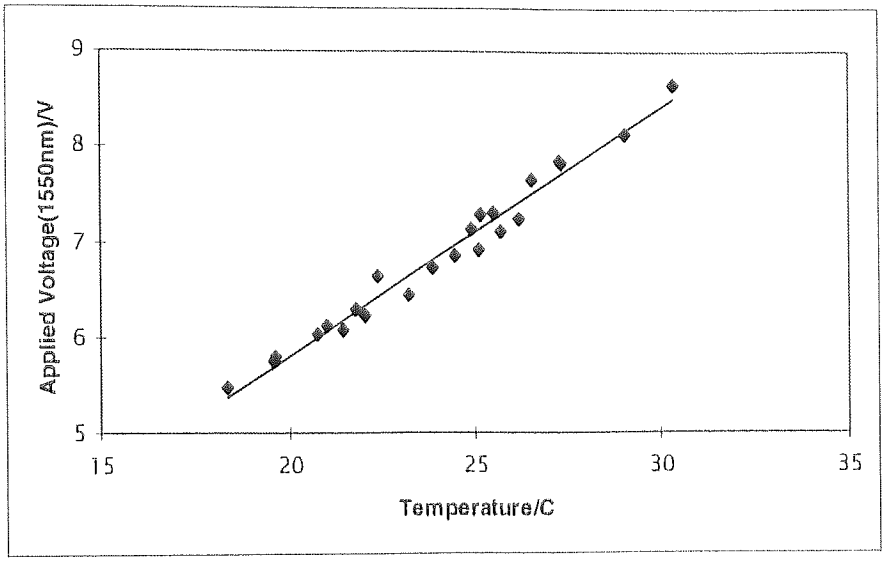

Figure 4.31 Peak applied voltage as a function of LCFP temperature; detecting a 1550nm signal

4.7.6 Discussion

The optical transmission spectrum of the liquid crystal Fabry-Perot etalon was recorded, and exhibited resonance peaks at wavelengths of 1487.3nm, 1528.2nm, 1560.6nm and 1592.7nm, when illuminated by light polarised both parallel and orthogonally to the liquid-crystal molecules. For parallel polarised light the application of a 1kHz square-wave, of 2.67V peak-to-peak amplitude, two resonance peaks were observed to tune from 1596.4nm to 1591.2nm, and from 1531.9nm to 1528.2nm respectively.

A clear dependence of the LCFP etalon transmission spectrum on the erbium fluorescence spectrum was observed, with the resonance peaks rising and falling in magnitude as they tuned across the erbium spectral bandwidth. This was also reflected in the dependence of the power transmitted by the etalon on the amplitude of the voltage applied to it. The transmitted power level was not constant, falling to approximately one quarter of its maximum value over the computer voltage range 3V to 6.5V. For the signal power levels available here this resulted in the loss of more than one third of the voltage tuning range,

since the transmitted optical signal fell below the detection threshold. This limitation can be overcome by using a higher power erbium fluorescence source, however any signals from Bragg grating sensors within the wavelength range covered by these voltages, from ~1485nm to ~1524nm, and from ~1559nm to ~1588nm, will be of significantly lower power, necessitating the normalisation of all experimental data before a peak search can be performed.

The impedance and capacitance of the LCFP etalon were measured in order to facilitate construction of the square-wave voltage drive signal electronics: values of 3.96kΩ and 40.2nF were recorded respectively.

The characterisation of the voltage dependence of the resonance peak wavelengths gave a wavelength tuning range for each resonance peak of approximately 85nm. It was also observed that for certain applied voltages the LCFP etalon transmitted at more than one wavelength. In order to achieve measurement clarity it was therefore necessary to restrict the resonance peak tuning range to ~85nm, requiring a computer voltage range of 0V to 7V, so that only one wavelength was passed by the etalon at each voltage setting. This reduced the available wavelength tuning capacity to two distinct ranges: 1545nm to 1610nm, and 1464nm to 1545nm.

The temperature dependence of the resonance peak wavelength was found to be -2.77nm/°C, which is more than an order of magnitude larger than the -0.2nm/°C previously reported by *Hirabayashi*[9] for the liquid-crystal type ZLI-3103. Hirabayashi reported that the temperature variation experienced by the LCFP etalon must be kept to less than 0.25°C in order to achieve better than 0.1nm stability of the resonance wavelength. To be able to produce this level of wavelength stability for the LCFP etalon reported here, the temperature must be held constant to better than 0.04°C.

The transmitted power characteristics of the etalon and the presence of multiple resonance peaks at certain applied voltages impose restrictions on the number of Bragg grating sensor signals that a single LCFP etalon can demultiplex. Assuming a 65nm tuning range for a single LCFP etalon resonance peak, one can in principle wavelength division multiplex 18 Bragg grating strain sensors, of 1nm linewidth (to the zeros on either side of the first secondary resonance peaks), each with a 3000με measurement range.

The number of sensors which can be interrogated by a single LCFP filter may be increased through the use of a wavelength selective switch, which can be set to transmit wavelengths which fall within the tuning bandwidth of the chosen etalon resonance peak. Such a filter can be constructed using an optical switch and two chirped gratings, arranged to act as transmission filters[174,175,176]. The chirped gratings should each have a bandwidth of 65nm, to match the tuning ranges of the resonance peaks; reflectivities of up to 80% are available[177,178,179] over this size of bandwidth. The working wavelength range of the LCFP etalon tuneable filter can then be chosen by activating the optical switch, preferably a 2x2 single-mode fibre routing switch[180], thus swapping from one Bragg grating transmission filter to the other, Figure 4.32. The optical switch is activated through the application of an acoustic wave to the fused, tapered-fibre pair, generated by a piezo-electric device and focused through a horn onto the optical fibre. The application of this switch arrangement would overcome the restriction imposed on the available tuning range of the LCFP filter by the presence of multiple transmission peaks at certain values of applied voltage. However, the most significant restriction on the use of the LCFP etalon as a tuneable wavelength selective filter is presented by the temperature dependence of the resonance peak wavelength; this must be surmounted if the LCFP etalon is to be applied as a demultiplexing element in Bragg grating sensor systems.

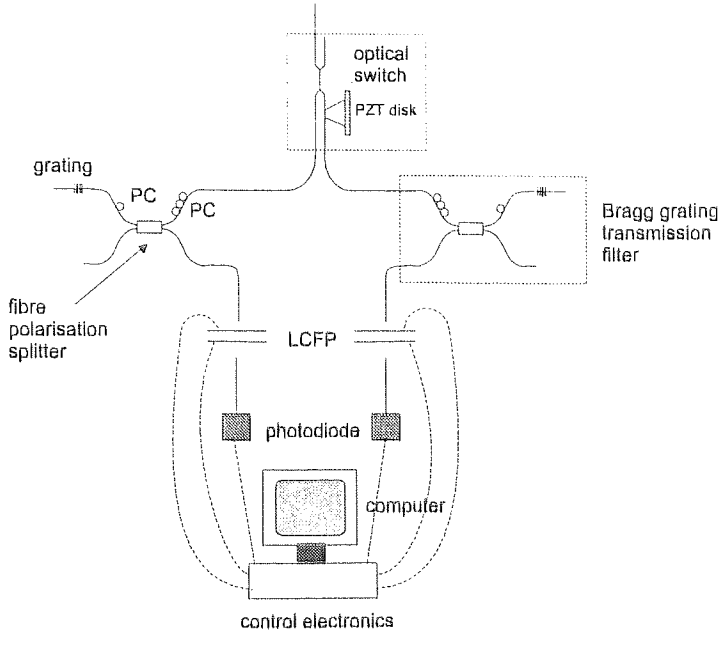

Figure 4.32 Switch to select LCFP filters in sensor demultiplexing system; an all fibre routing switch is used to select which of the Bragg grating transmission filters the optical signal is sent to

4.8 LCFP temperature compensation / control

4.8.1 Introduction

As evidenced in 4.7.5, the room temperature in the laboratory was not stable, due to a lack of air conditioning and to the presence of several people, and much electrical equipment. The high temperature sensitivity of the LCFP resonance wavelength required that either the room temperature or the LCFP etalon temperature must be stabilised, or that its temperature sensitivity must be compensated for. Controlling the room temperature was impractical, hence the other two options were investigated.

4.8.2 Temperature compensation

4.8.2.1 Introduction

In order to compensate for the temperature dependence of the LCFP etalon its temperature must be measured during each voltage scan. This was achieved by reading the voltage signal output by the platinum film temperature sensor into the computer at each step in the LCFP voltage scan. The temperature sensor output was of the order of millivolts, while the AIAO board required voltages of greater than 1V, hence an electronic circuit was constructed which amplified the signal; the gain of the circuit was ~100, but not exactly 100, due to the nature of the circuit components. Once the LCFP voltages have been converted into wavelength, the wavelength values can be scaled to those at the characterisation temperature (19.55°C) (Appendix B2), normalised (Appendix B3), and the peak search performed.

4.8.2.2 Temperature averaged over whole voltage scan

In the initial measurement procedure the temperature of the LCFP etalon was recorded at every voltage scan step, and averaged to give the temperature to be used in the conversion equations: Equation 4-13 and Equation 4-14. In order to compensate for the non-perfect gain in the electronic circuit used to amplify the electrical signal from the platinum film temperature sensor, slight changes to the conversion equations were implemented.

The measurement accuracy of the system was tested using the experimental arrangement of Figure 4.24, with the tuneable laser acting as a precisely known signal source for the system to detect. Using this arrangement, with the tuneable laser output set at 1540nm, the LCFP/computer system measured the wavelength to be 1540.97nm; the temperature of the LCFP etalon was stable to within 0.01°C over the scan, and the voltages representing the temperature at the output of the temperature detector and at the computer, after amplification, both gave a value of 19.80°C.

Temperature at platinum film sensor/°C	Temperature at computer/°C	Wavelength measured by computer/nm
17.99	17.93	1539.88
18.11	18.06	1531.83
18.16	18.11	1531.83
18.16	18.14	1531.83
18.19	18.15	1532.17
18.20	18.18	1532.05
18.27	18.26	1531.00
18.36	18.37	1542.32
18.38	18.37	1542.47
18.41	18.40	1535.07
18.46	18.44	1530.45
18.52	18.54	1530.45
18.55	18.54	1528.51

Figure 4.33 Wavelength measured by computer at various values of LCFP temperature, recorded at the platinum film temperature sensor and at the computer; source signal wavelength 1530nm.

However, when the temperature of the LCFP etalon was not stable over the period of a voltage scan, as was generally the case, the system measured the wavelength incorrectly, by up to 10nm. Figure 4.33 shows a typical series of wavelength measurements made using the experimental arrangement of Figure 4.24, with the tuneable laser output set at 1530nm, as the LCFP etalon temperature increased. The temperature of the LCFP etalon was observed to fluctuate by several tenths of a degree during a complete scan, hence the

average value may not have been the actual temperature at the moment that the signal peak was detected.

4.8.2.3 *Temperature found at time grating peak measured*

In order to overcome this mismatch in temperature values, the data processing technique was changed so that the temperature at the time that the signal was detected was known exactly. The photodiode and temperature sensor outputs were recorded by the computer at every voltage scan step, and a peak search on the photodiode voltage readings performed. From this the temperature at the grating peak was found by looking-up the corresponding temperature reading in the data stored by the computer. The LCFP etalon applied voltage values were then scaled to the appropriate temperature, and the peak search on the photodiode voltage readings repeated in order to find the LCFP voltage at the maximum photodiode value, which was then converted to the corresponding wavelength.

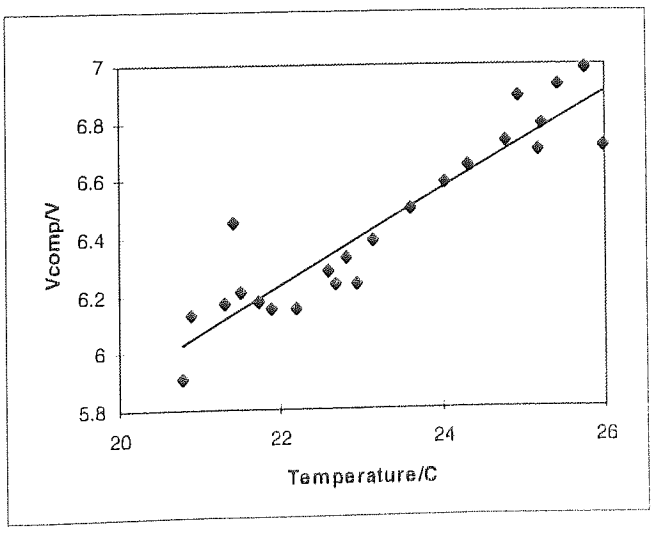

Figure 4.34 Peak applied voltage as a function of LCFP temperature; detecting a 1550nm signal; temperature measured at computer

In parallel, the temperature calibration was repeated using the temperature values recorded at the computer in order to remove the need to build in compensation factors to the conversion equations; the same measurement procedure as that used in 4.7.5 was applied. The recalibrated temperature dependence of the peak applied voltage, detecting a 1550nm source signal, is shown in Figure 4.34. The results lie on a straight-line given by

$$V_{computer} = 0.168T(^{o}C) + 2.541$$

Equation 4-15

4.8.2.4 Measuring temperature and strain applied to a Bragg grating

This processing system was tested using the experimental arrangement of Figure 4.24, with the broadband source used to illuminate a single Bragg grating; peak wavelength 1557.01nm. Both temperature and strain were applied, independently, to the grating and the LCFP control programme used to measure the wavelength of the Bragg reflection. The grating was heated by mounting it on a peltier device, with the temperature controlled through use of a thermistor based feedback loop. Strain was applied to the grating using the experimental arrangement shown in Figure 4.35; the length of fibre containing the grating was fixed at one end, with the other end clamped to a displacement stage, and the distance between them increased incrementally. Both the temperature and strain were applied using a computer control system, connected to the computer via a GPIB board (IEE488). These measurements were carried out in collaboration with Dr. Lin Zhang and Richard Fallon of the Photonics Research Group, Aston University.

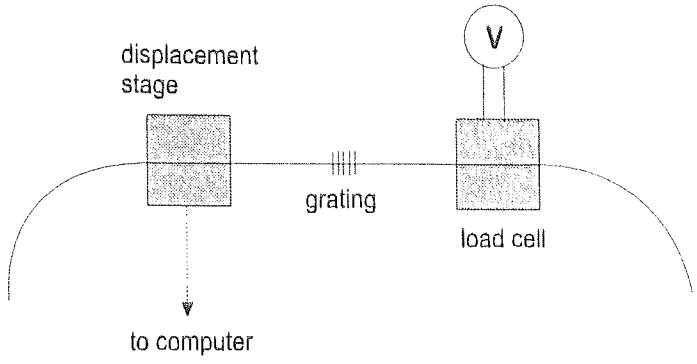

Figure 4.35 Experimental arrangement for applying strain to Bragg grating

The measured grating wavelength at each applied temperature and strain is shown, with the corresponding theoretically predicted value[137], in Figure 4.36. and Figure 4.37 respectively. The LCFP temperature used in the wavelength calculation was averaged over 10 points either side of the peak voltage to allow for any response time of the liquid crystal refractive index to temperature changes. At applied temperatures of 20°C and 40°C the measured value of the grating peak wavelength and the predicted value agree to within the experimental error caused by the fluctuation in the LCFP temperature during a voltage scan. However, at the other applied temperatures and the applied strains, the measured peak wavelength of the grating is not in agreement with the predicted values.

T(grating)/ °C	grating peak wavelength/nm	wavelength error/nm	theoretical wavelength/nm
10	1545.04	0.75	1557.10
20	1555.78	1.61	1557.19
30	1554.15	0.82	1557.28
40	1556.07	1.39	1557.37
50	1547.35	0.64	1557.46
60	1550.46	1.04	1557.55
70	1548.96	0.38	1557.64

Figure 4.36 Experimental and theoretical grating wavelength for application of temperature to grating

strain/με	grating peak wavelength/nm	wavelength error/nm	theoretical wavelength/nm
0	1544.49	0	1557.01
666	1548.73	0.43	1557.81
1333	1548.33	0.52	1558.61
3333	1535.75	0.82	1561.01

Figure 4.37 Experimental and theoretical grating wavelength for application of strain to grating

There are two probable causes of this disagreement between the experimentally measured peak wavelengths and their corresponding predicted values. Firstly, the LCFP etalon has a significant thermal mass, therefore the temperature measured by the platinum film temperature sensor mounted on the front face could, in principle, be different to that at the point on the etalon through which the optical signal passes. Secondly, the peak search method may contain some

error due to the method of determining the voltage at the peak transmitted signal, since the shape of the transmitted signal peak is determined by both the Bragg grating spectral profile and the LCFP etalon resonance peak profile. The data processing code searches for the maximum value of V(photodiode), and records the corresponding V(computer) as the voltage at the grating peak. However, this may not correspond to the central wavelength of the grating in all cases, and an improvement would be to implement a peak searching mechanism that removes the effect of the LCFP resonance peak profile from the recorded transmission profile and then performs a peak search based on finding the centre of mass of the spectrum.

4.8.2.5 Temperature control

Temperature control of the LCFP etalon was attempted using a peltier device with a central, circular aperture, fixed to the front face of the etalon, and a thermistor based feedback loop was used to control the temperature. Various sizes of heat sink were applied, several different thermistor beads used, and their position altered, and the feedback loop gain altered, however the temperature of the etalon did not stabilise, but rapidly increased. A possible cause of this is that the liquid crystal type (E7) has a long thermal response time, hence the temperature measured at the etalon face is not the same as that of the liquid crystal. This would result in the temperature measured by the thermistor cyclically heating and cooling. After the peltier device has applied heat to the etalon for a short period it stops and waits to see how the thermistor reading changes, but due to the large thermal mass and slow response of the liquid crystal no noticeable change is detected, so the peltier device applies more heat, again little increase in the etalon temperature is recorded and the peltier applies heat again, and so the temperature of the peltier device spirals upwards, which is what was observed to happen. The large thermal mass of the LCFP etalon therefore makes it unsuitable for direct temperature control in this manner.

An alternative approach involves mounting the LCFP etalon inside a box constructed from a material of high thermal mass, in an attempt to reduce the variation in the temperature of its surrounding environment. A box was constructed from brass for this purpose and the temperature variation inside it was compared to that of the room temperature over a period of several hours; the temperatures were measured using two separate platinum film temperature sensor/linearisers arrangements, identical to that described in 4.7.5.

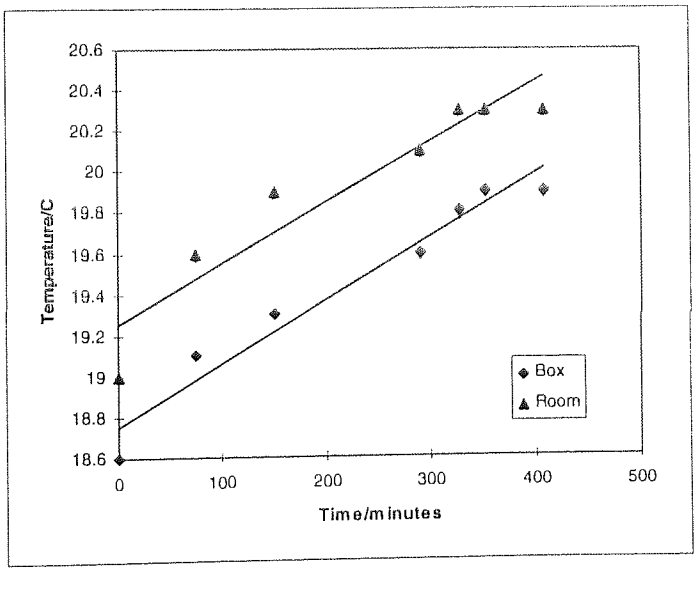

Figure 4.38 Variation of room temperature and temperature in brass box as room heated slowly

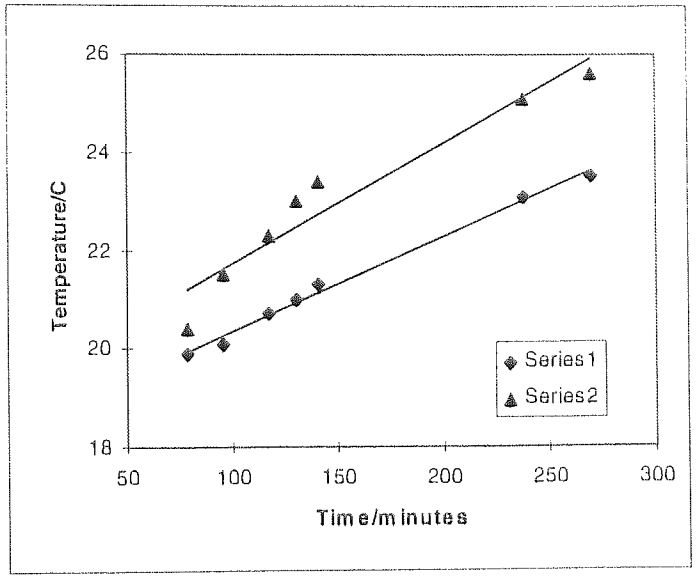

Figure 4.39 Variation of room temperature and temperature in brass box as room heated rapidly

The variation of the room temperature and the temperature inside the box, as the room was allowed to heat up naturally, are shown in Figure 4.38. The results lie on straight lines of gradient 0.00296°C/minute and 0.00307°C/minute respectively, indicating that the box offered no improvement to the temperature stability of the LCFP environment. Figure 4.39 shows the variation of the two temperatures as the room was rapidly, actively heated. Straight line fits to the data give a gradient of 0.0193°C/minute for the temperature within the brass box, while a gradient of 0.0246°C/minute was recorded for the room temperature. The temperature within the box is clearly more stable than that of the room when the room temperature rises quickly, but it still does not offer the level of stability required to practically implement the LCFP etalon as a tuneable transmission filter for demultiplexing Bragg grating sensor signals.

4.8.2.6 Comments

The approaches to temperature compensation which have been attempted enjoyed limited success, and further developments to improve them have been suggested. It has been demonstrated, in 4.8.2.2, that if the temperature of the LCFP etalon can be kept stable to better than 0.1°C over the duration of a voltage scan then its use as a Bragg grating sensor demultiplexing element becomes feasible; however, temperature control to better than 0.04°C is required to obtain the wavelength measurement accuracy (0.1nm) needed for a real Bragg grating sensor system. Placing the etalon inside a brass box offered some degree of protection from room temperature variations if the temperature increased rapidly, but no beneficial effect was observed when the room heated up slowly.

The temperature sensitivity of a liquid crystal is greatest at temperatures approaching its nematic to isotropic phase transition. The liquid crystal E7 has a transition temperature of ~68°C, while other liquid crystals are available which have significantly higher transition temperatures, of the order of 100°C. Using these liquid crystals in the LCFP etalon will increase the separation of the operating temperature and the transition temperature, and hence reduce the temperature sensitivity of the etalon. Unfortunately all of the LCFP etalons manufactured by GEC Marconi Materials Technology[181] were filled with E7, therefore the temperature sensitivity of LCFP etalons filled with other liquid crystal materials could not be investigated.

The temperature sensitivity of the resonance peak wavelength significantly compromised the performance of the LCFP etalon. For implementation of this device as a wavelength demultiplexing element it is vital that the temperature instability be greatly reduced. The LCFP etalon is unsuitable for this task in its current form, even with the application of temperature control and compensation techniques. A move to a liquid crystal with a higher transition temperature and hence a reduced temperature sensitivity, could, in principle,

make it a viable alternative to existing demultiplexing techniques if used in conjunction with the temperature control and compensation methods detailed in 4.8.2.

4.9 Further system developments

4.9.1 Introduction

Assuming that the temperature dependence of the LCFP etalon resonance peak wavelength has been minimised, by changing the liquid-crystal to a type with a significantly smaller refractive index temperature dependence, and through the application of one or more of the above temperature compensation and control techniques, the resolution of the demultiplexing system can be enhanced through the use of a second stage filter. The LCFP etalon can be used to select a 1nm band of wavelength space, containing the grating sensor of interest, with a second stage filter, of narrower resonance peak linewidth, then tuned across this 1nm in order to more accurately determine the peak wavelength of the grating reflection response. Two such secondary filters are a narrow linewidth LCFP, and a fibre Fabry-Perot; demultiplexing systems using these tuneable transmission filters will be discussed further in sections 4.9.2 and 4.9.3 respectively.

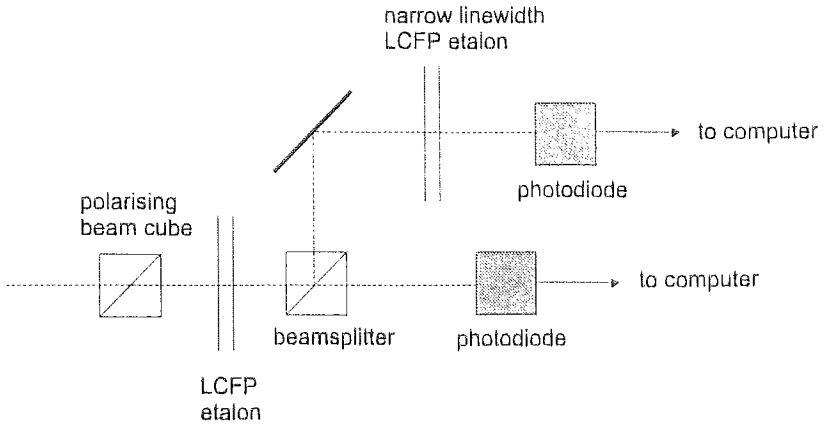

Figure 4.40 Experimental arrangement for an LCFP demultiplexing system based on two etalons of different linewidth

4.9.2 Concatenate two LCFP etalons of different resonance peak linewidth

The experimental arrangement for a two stage LCFP etalon filter demultiplexing system is shown in Figure 4.40. The first stage filter is operated as described in section 4.6, and selects the grating to be interrogated by the second stage filter. Once the signal peak has been found the control system can be set to follow this peak, thus maintaining the signal power transmitted to the secondary filter at its maximum level. The optical signal transmitted by the first stage filter is intensity split in the ratio 90:10, where 10% of the signal power is routed to the photodetector used to control the first stage filter, and 90% continues on to the secondary LCFP etalon. The narrow linewidth LCFP etalon was filled with the same liquid crystal as before, and thus suffered from the same temperature based instability of the resonance peak wavelength. The spectral profile of the secondary etalon was measured, Figure 4.41, and it displayed a resonance peak FWHM linewidth of ~0.1nm and a free spectral range of 1.1nm. The necessary optical mounts and detectors were constructed, however the temperature dependence of both etalons prevented the system from reaching the testing stage. The secondary filter would be controlled identically to the first stage filter, with the computer voltage tuning range selected to produce a resonance peak wavelength scan of 1nm. Use of the narrow linewidth LCFP etalon would,

in principle, allow the grating resonance peak to be measured to better than 0.1nm, the spectral resolution required to detect the minimum expected strain of 100με.

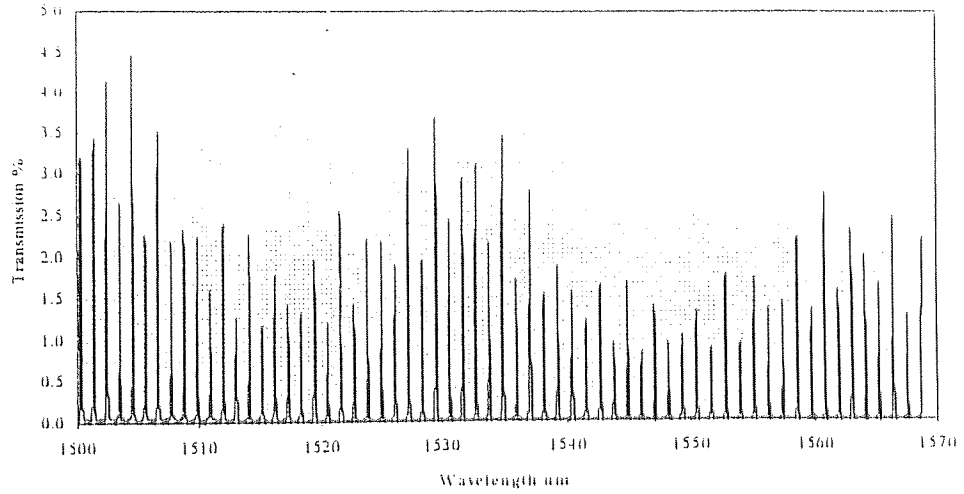

Figure 4.41 Optical transmission spectrum of narrow linewidth LCFP etalon

4.9.3 LCFP etalon combined with a Fibre Fabry-Perot filter

Rather than using a second bulk optic wavelength filter, an in-fibre Fabry-Perot (FFP) transmission filter can be used, such as those shown Figure 4.42 and Figure 4.43. The first stage LCFP filter is controlled as described in 4.6, and the transmitted optical signal is then split using an optical fibre coupler, Figure 4.44, with part of the signal used to control the first stage filter, and the rest coupled into the FFP filter.

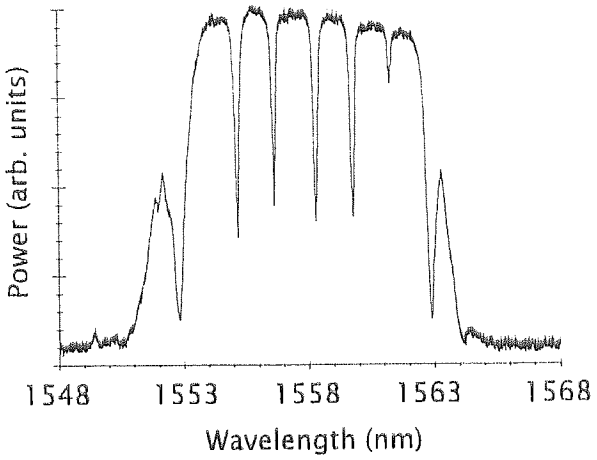

Figure 4.42 Optical transmission spectrum of Fibre-Fabry Perot filter; bandwidth ~12nm; free spectral range 1.43nm

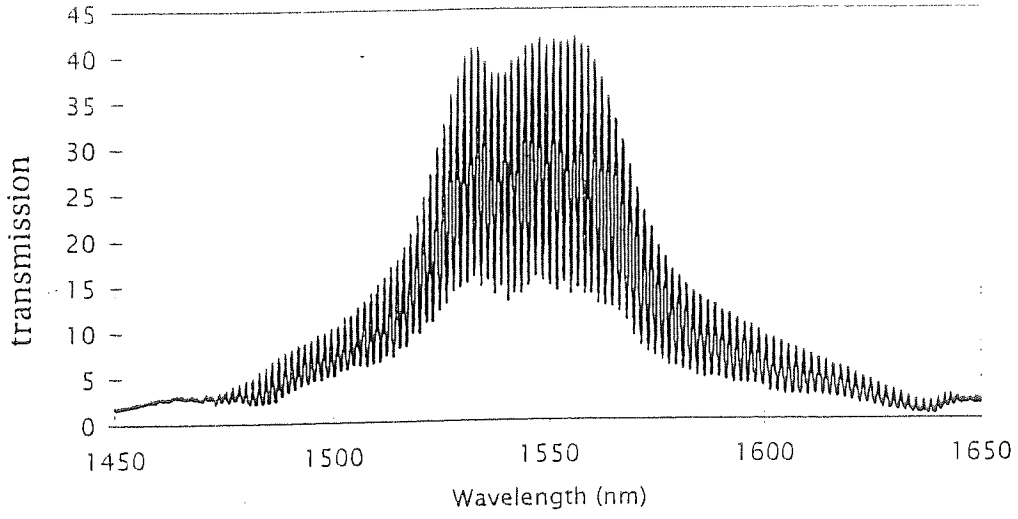

Figure 4.43 Optical transmission spectrum of Fibre Fabry-Perot filter; bandwidth ~150nm; free spectral range ~1.5nm

Wavelength tuning of the FFP resonance peak wavelength is achieved by straining, or compressing, the section of fibre containing the filter, as described in 4.2. Instead of fixing the FFP filter onto a solid sheet and bending it, the fibre can be axially strained by applying force along the fibre axis in order to stretch or compress it. To integrate this filter with the LCFP etalon control system, the FFP filter tuning can be computer controlled through the use of the mount shown in Figure 4.45, which is based on a piezo-electric containing micrometer positioner (PI piezomike® M-311.80 and P-853.00). The micrometer has a 6mm

manual travel range and a 30μm piezoelectric travel range, achieved by applying 120V. For a 4mm long grating (standard fabrication length using holographic two beam interferometry), mounted such that 10mm of fibre will be strained, this can produce a 3nm resonance peak tuning range. Hence 1nm wavelength tuning can be achieved by applying 40V to the piezoelectric device. This filter would, in principle, be capable of determining the sensor grating peak wavelength to better than 0.17nm. The FFP filter tuning mount was successfully constructed and the electronic control circuit designed. The FFP transmission peak wavelength was shown to vary linearly with applied strain in 4.2.4.3, Figure 4.13. However, the demultiplexing scheme could not be implemented due to the temperature sensitivity of the LCFP etalon.

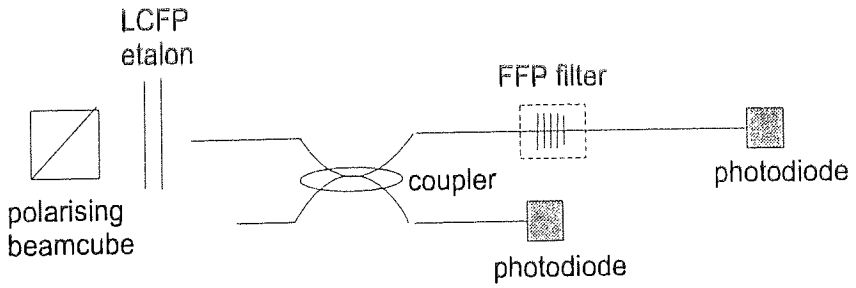

Figure 4.44 Experimental arrangement of demultiplexing system based on combination of LCFP etalon and fibre Fabry-Perot (FFP) filter

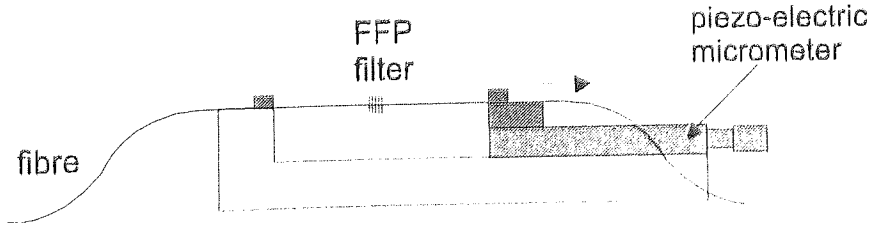

Figure 4.45 Fibre Fabry-Perot filter tuning mount; fibre is strained by displacing micrometer stage through activation of piezoelectric element

4.10 Conclusion

The employment of in-fibre Bragg gratings as smart structure strain sensors was investigated, using gratings embedded in, and mounted on the surface of, a sheet of carbon composite material. The shift in central wavelength of the embedded grating was measured under the application of strain and compression. Incomplete transfer of the strain experienced by the composite board to the fibre grating was observed, which can be explained by slippage of the fibre within the board due to poor bonding between the fibre and the composite material. In order to verify the bending theory applied in the embedded grating measurements, the response, to strain and compression, of a uniform period grating and a fibre Fabry-Perot (FFP) filter, mounted on the surface of the sheet, were measured. Excellent agreement was achieved between the theory and the experimental results for the FFP filter under strain, supporting the theory which was applied to both the embedded and surface mounted grating measurements. This work was the first, of which I am aware, on the investigation of in-fibre Bragg grating strain sensors embedded in composite materials. For commercial reasons the work did not continue, but it has since been taken up be *Rao et al*[165], of the University of Kent at Canterbury, and through the Link Photonics Programme MAST project.

A discussion of the requirements for a demultiplexing element for a Bragg grating sensor system was offered, and a scheme based on the use of a liquid crystal filled Fabry-Perot etalon tuneable transmission filter proposed. Previous reports of the use of such a device for wavelength selection in optical transmission systems suggested that it could be readily applied to grating sensor demultiplexing. Initial characterisation of the LCFP etalon was followed by the design, construction and testing of a computer controlled demultiplexing scheme. The characterisation of the LCFP etalon highlighted some operational limitations of the tuneable filter.

The available tuning range of the LCFP etalon resonance peaks was reduced from the full tuning range of ~85nm, as the applied voltage is tuned from 0V to 9V, to between 61nm and 65nm due to the presence of more than one transmitting wavelength at certain applied voltages. The transmitted power level was not constant across the full voltage scan, which led to the loss of one third of the voltage tuning range, since the optical power level fell below the photodiode detection threshold; although this can be overcome through the use of a broader band width source or a higher power source, neither option was available here.

The resonance peak wavelength was highly temperature dependent due to the temperature sensitivity of the liquid crystal refractive index.; a wavelength/temperature dependence of -2.77nm/°C was recorded, more than an order of magnitude larger than that previously reported by *Hirabayashi*[79]. In order to produce the 0.1nm wavelength measurement accuracy required to detect a minimum strain of 100με the temperature of the LCFP etalon must be held constant to better than 0.04°C.

Schemes to compensate for, and control, the LCFP temperature sensitivity were investigated. The temperature compensation approach enjoyed limited success when the temperature was averaged over the whole voltage scan; when the temperature of the LCFP etalon remained constant to within 0.1°C over the duration of the scan, the signal wavelength was measured to within 1nm of the actual value. The compensation system which averaged the temperature over a smaller number of points about the actual signal peak was used to measure the wavelength of a Bragg grating under the application of temperature and strain. This was also partially successful, with the experimentally measured wavelength agreeing with the theoretically predicted value, to within the measurement error, for two readings. Two probable causes for the generally poor agreement between the experimental and theoretical wavelength values

were offered, based on the bulk thermal properties of the LCFP etalon and the method of determining the position of the peak in the recorded photodiode voltage values, which represent the wavelength of the etalon resonance peaks.

The operational limitations associated with the non-constant optical power transmission characteristic and the presence of multiple resonance peaks at certain values of the applied voltage amplitude can be overcome by applying some straightforward changes to the experimental arrangement, as described in 4.7.6. However, the temperature dependent nature of the etalon resonance peak wavelength presents a more serious limitation to the use of the LCFP etalon as a tuneable wavelength filter. Although limited success was achieved by applying the temperature control and compensation schemes of 4.8, it must be concluded that LCFP etalons filled with this particular liquid crystal (E7) are not suitable for use as wavelength demultiplexing filters in a Bragg grating sensor system.

The future of this demultiplexing approach is ultimately dependent on overcoming the temperature sensitivity of the LCFP etalon resonance peak wavelength, and use of a liquid crystal material with a higher transition temperature would reduce the temperature sensitivity, but it will not remove it. The developments of the LCFP etalon based Bragg grating sensor demultiplexing system proposed, using a second, narrower linewidth, LCFP etalon, and a fibre Fabry-Perot filter respectively, can then, in principle, be attempted. The most promising arrangement is therefore to use the most temperature-insensitive liquid crystal material available, house it in a box constructed from a material of high thermal capacity, as in 4.8.2.5, in order to minimise the temperature variation of its surround environment, and apply one of the compensation schemes discussed in 4.8.2.

5. True time delay control of phased array antennas

5.1 Introduction

As discussed in 1.3, the principles of a compact, potentially low cost approach to wavelength switched optical true time delay (TTD) control of phased array antennas based on in-fibre Bragg gratings have been proposed by *Lembo et al*[40]. The work which comprises this chapter recounts the initial demonstration of such a TTD scheme and the subsequent development of the first 3-bit fibre Bragg grating based optical TTD control element to be reported. Progression from the first 3-bit to the first 6-bit Bragg grating optical TTD element will then be presented.

In a phased array antenna controlled by optical TTD the RF excitation signal is impressed on an optical carrier as an intensity modulation. The optical signal is then transmitted, via an optical link, to a fibre Bragg grating true-time delay line, and then to the antenna element, where the RF electrical signal is recovered by a photodiode. The photodiode output is subsequently amplified and used to drive the microwave radiator. In the simplest antenna array control network the signal path to each antenna element contains a single TTD line.

A fibre Bragg grating delay line, Figure 5.1, comprises a single length of optical fibre with high reflectivity Bragg gratings, of different central wavelengths, fabricated along its length. The delay line is connected via optical fibre links, through a 3dB coupler, or an optical circulator, to the optical source at one end of the system and a photodetector at the other. By tuning the optical source to the appropriate wavelength the optical signal can be reflected from any of the Bragg gratings within the delay line, hence determining the optical path length traversed by the signal, and selecting the required time delay. The reflected

optical signal is separated from the incoming signal by the optical coupler, and then routed to the photodiode. The 3dB coupler will introduce a loss of 6dB into a basic 3-bit (8-element: 8 fibre Bragg gratings) delay line; approximately equal to the loss suffered by a typical 4-bit, non-wavelength-switched optical TTD device. One of the attractions of the fibre Bragg grating TTD approach is that the delay line could be expanded up to 6 or 7-bits without any increase in loss. The optical link system remains the same while the number of Bragg gratings in the delay line, and the tuning range of the optical carrier, is increased. Use of an optical circulator would, in principle, reduce the loss still further, to potentially less than 4dB, dependent on the insertion loss.

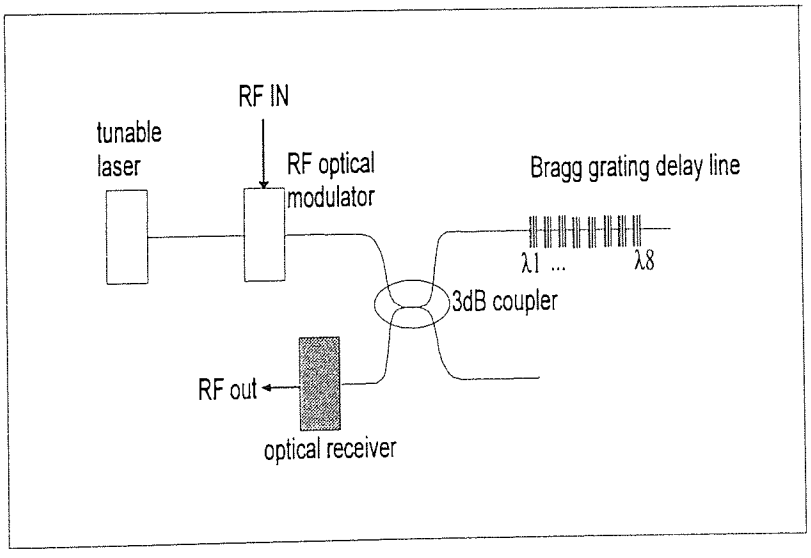

Figure 5.1 Basic 3-bit fibre Bragg grating delay line

The time delay acquired by the RF signal is determined indirectly through measurement of the phase delay which it acquires on reflection from the delay line. As described above, the RF signal is impressed on the optical carrier as an intensity modulation. The optical signal is launched down an optical link, via the 3dB coupler, to the optical TTD line, where it is reflected from the appropriate grating. The return signal is detected by a photodiode and the phase of the resulting electrical signal from the photodiode compared to that of

RF modulation signal. Any phase delay acquired by the signal is then converted to the equivalent time delay using the following expression:

$$\Delta\theta = 2\pi\Delta T f$$

Equation 5-1

where $\Delta\theta$ is the phase delay acquired by the signal, ΔT is the equivalent time delay, and f is the RF modulation frequency.

The phase of the RF signal rotates continuously as the optical carrier travels along the fibre link to the delay line. It is therefore necessary to define a phase reference point, close to the delay line, with respect to which the phase of the reflected signal can be compared, in order to determine how much extra phase is acquired by the signal as it travels further along the delay line. The phase of the signal returned from the first grating in the array was chosen as the reference phase, and the phase incurred by the signal on reflection from subsequent gratings in the array was compared to this value.

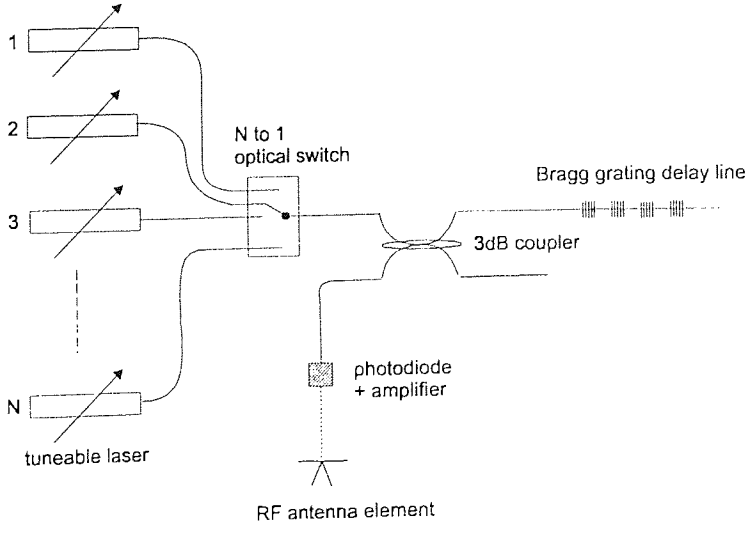

Figure 5.2 Wavelength multiplexing several tuneable lasers to increase the source bandwidth for a grating based true time delay line

5.2 Delay line fabrication

The maximum number of time delay elements that can be fabricated in each delay line is determined by the tuning range of the optical source and the optical bandwidth of each grating. The optical bandwidth, $\Delta\lambda$, of a Bragg grating is described by Equation 2-12 and determines the minimum possible wavelength spacing between adjacent gratings in the delay line and, hence, the maximum number of discrete time delay elements, N_{max}, which can be addressed by a single optical source:

$$N_{max} \approx \frac{\Delta\Lambda}{\Delta\lambda}$$

Equation 5-2

where $\Delta\Lambda$ is the tuning range of the optical source. The minimum achievable time delay, T_{min}, is given by

$$T_{min} = \frac{2nd_g}{c}$$

Equation 5-3

where d_g is the centre-to-centre spacing between gratings, n is the refractive index of the optical fibre and c is the free space speed of light.

The maximum number of Bragg gratings which can be written in a single TTD element can be increased by expanding the optical carrier tuning range. This can be achieved by wavelength-division-multiplexing several tuneable lasers of different optical bandwidths, such that as the limits of one tuning range are reached the adjoining laser is switched in as the optical source, Figure 5.2.

5.3 Measurement systems

5.3.1 500-900MHz frequency range

The prototype system, designed to verify that true-time delay measurement via phase delay measurement could be achieved, operated over the microwave frequency range 500MHz to 900MHz. Light from an external cavity, grating-tuned semiconductor laser (Photonetics Tunics 1550) was amplitude modulated at the RF signal frequency, provided by a signal generator, using a GaAs Mach-Zehnder optical modulator (GMMT LC1476), and coupled into the delay line under test via a 3dB coupler, Figure 5.3. The optical signal reflected from the delay line was detected with a standard large area photodetector, and the phase of the resulting electrical signal compared to that of the RF modulation signal using a vector voltmeter. For each RF frequency setting (500MHz, 600MHz, 700MHz, 800MHz and 900MHz) the wavelength of the optical carrier was manually tuned to the peak grating wavelengths in the array, and the phase delay recorded; both steps were performed manually and were the most significant sources of error within the system.

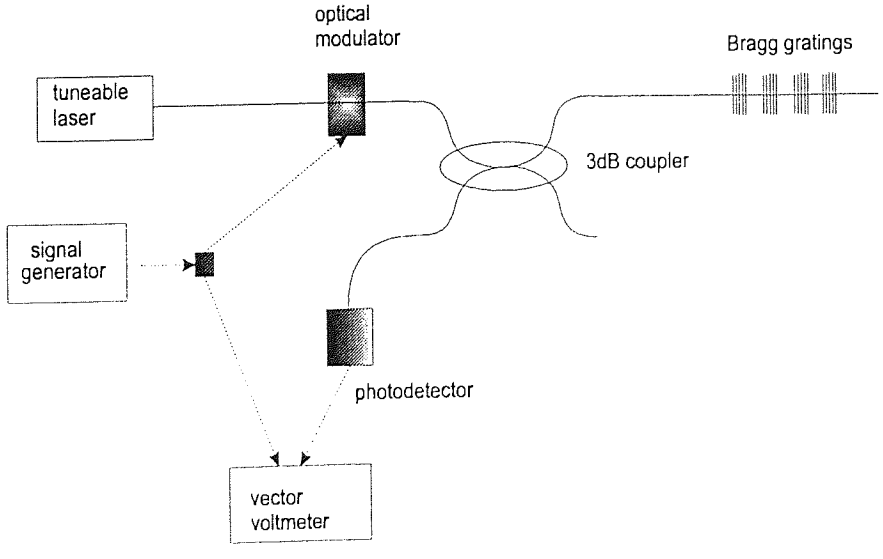

Figure 5.3 500MHz-900MHz measurement system

5.3.2 1GHz RF modulation frequency

Real phased array antennas require RF signal frequencies of the order of a few gigahertz. In order to more closely approximate true system requirements, a second measurement system, which operated at 1GHz, was built. The RF signal was generated by a frequency synthesiser, and used to drive the optical modulator and as the reference signal to the vector voltmeter (HP8508A) Figure 5.4. The optical carrier, an external grating, semiconductor tuneable laser (HP8168B), was amplitude modulated using a Lithium Niobate optical modulator (GMMT Y35893001). The optical signal reflected from the delay line was detected with a highspeed photodetector (Anritsu MA9301A & ML910A), and the phase of the resulting electrical signal compared to that of the RF modulation signal at the vector voltmeter; phase measurement resolution 0.1 degrees. The optical carrier wavelength was tuned in 0.02nm steps, under computer control, across the delay line spectral bandwidth. The vector voltmeter reading and the reflected signal intensity were recorded at each wavelength step. The delay line grating peaks were identified from the recorded reflected intensity information, enabling accurate determination of the grating peaks, and their respective phase delays read and converted to equivalent time delays.

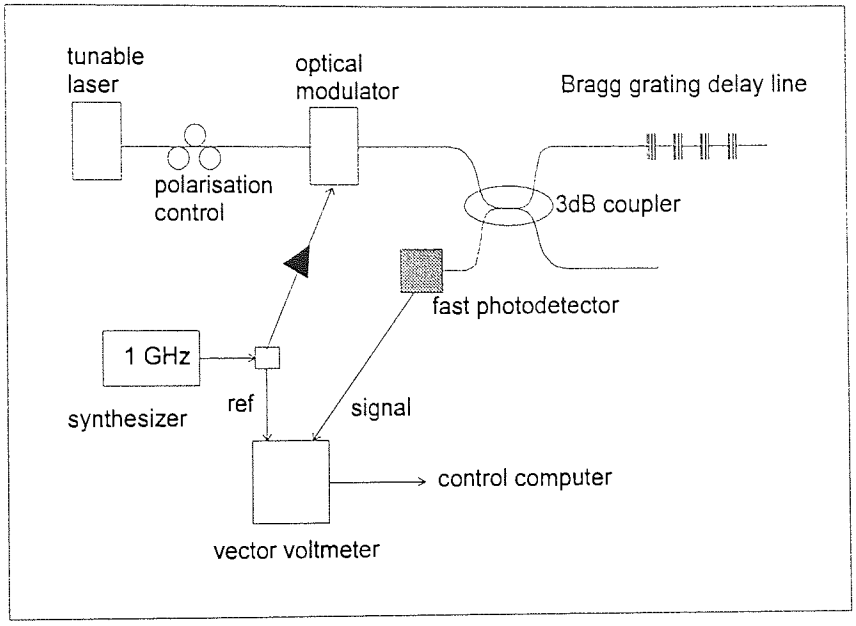

Figure 5.4 1GHz RF frequency measurement system

5.3.3 130MHz-20GHz modulation frequency

To facilitate independent verification of the 1GHz time delay results, and to simulate the effect of a signal pulse, containing a range of RF frequencies, being reflected from the delay line, the delay line measurements were repeated in a second measurement system. This operated over a broad range of RF frequencies, with a notably higher maximum RF signal frequency of 20GHz, and is illustrated in Figure 5.5. Light from an external cavity, grating-tuned semiconductor laser (Photonetics Tunics 1550), resolution 1pm, linewidth less than 0.01nm, was amplitude modulated using a GaAs Mach-Zehnder optical modulator (GECLC1376). The network analyser (HP8703A) combined the functions of the frequency synthesiser, photodetector and vector voltmeter, acting as the source of the swept RF signal, monitoring the optical signal reflected from the delay line, and comparing the reflected signal phase with that of the RF modulation signal; a full calibration was carried out before each period of work commenced.

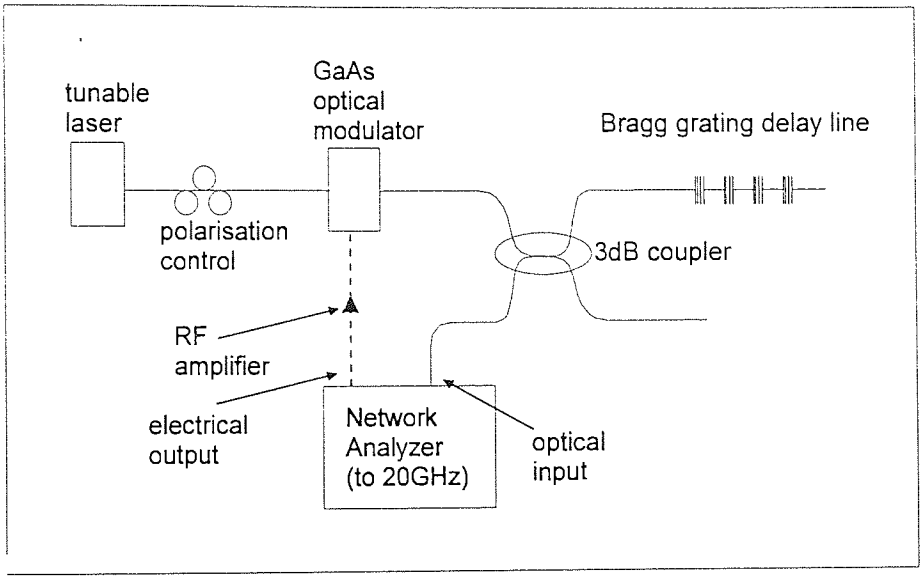

Figure 5.5 130-MHz-20GHz RF frequency measurement system

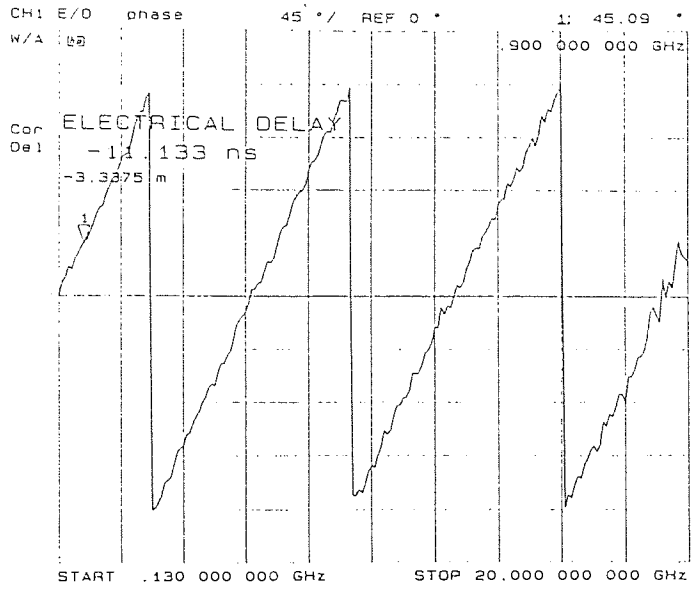

Figure 5.6 Phase difference between measurement and reference signals recorded at network analyser: phase as a function of RF frequency

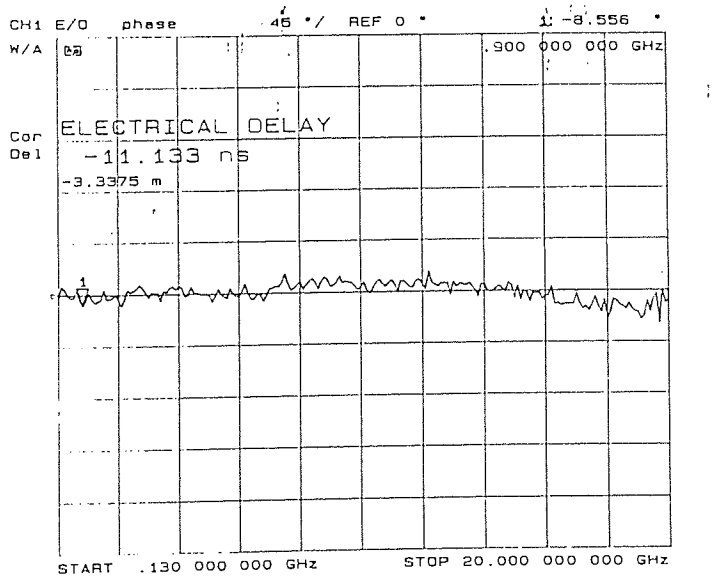

Figure 5.7 Phase difference between measurement and reference signals nulled by adding electrical delay to the reference signal path

The optical carrier wavelength was tuned to that of the first grating in the array, the reference grating, and the network analyser output recorded; for example, Figure 5.6. The phase difference between the reflected optical signal and the modulation signal was then nulled by adding electrical time delay to the modulation signal path, Figure 5.7. The time delay incurred by the signal on reflection from subsequent gratings in the array was then measured by tuning the carrier wavelength to the next grating wavelength and recording how much more electrical delay must be added to the modulation signal path to renull the phase difference. Both the optical carrier wavelength tuning and the addition of

electrical delay were performed manually, and hence formed the main sources of error in this measurement system.

5.4 Discrete grating arrays

5.4.1 Grating length 5mm, centre-to-centre separation 5mm

As reported in 3.2.2, an optical fibre delay line, comprising four Bragg gratings, was fabricated with a centre-to-centre spacing between adjacent gratings of 5.0mm, and had grating central wavelengths of 1542.27nm, 1545.13nm, 1547.65nm and 1553.86nm; optical spectrum Figure 3.4.

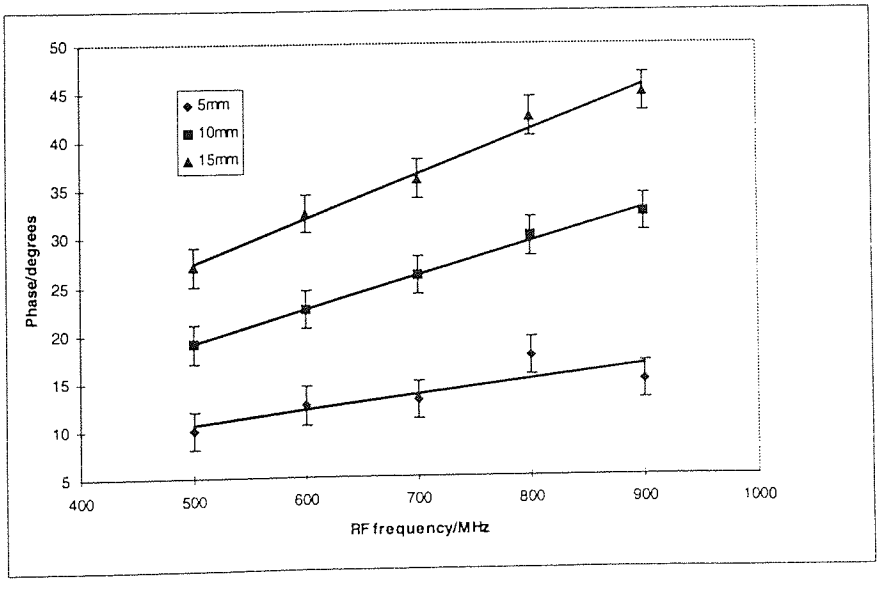

Figure 5.8 Phase delay as a function of frequency for grating delay line with 5mm separation; delay path lengths of 5mm, 10mm, and 15mm

The variation in phase delay acquired by the RF modulation signal as a function of frequency was recorded for each grating in the delay line[182], Figure 5.8. The gradients of the straight-line fits to the experimental data yield the equivalent time delays incurred by the signal on reflection from the gratings. An average

time delay step of 48.18ps was produced, which compared well with the value of 48.37ps predicted by Equation 5-1. This delay line is suitable for beamforming control at RF frequencies of up to 576MHz, with 10 degrees phase resolution; the operational system requirement for a phased array antenna radar.

5.4.2 Grating length 5mm, centre-to-centre separation 2.5mm

A second delay line containing four 5mm long gratings was fabricated with a grating separation of 2.5mm, and central wavelengths of 1547.24nm, 1549.72nm, 1553.48m, and 1557.86nm; optical spectrum Figure 3.5.

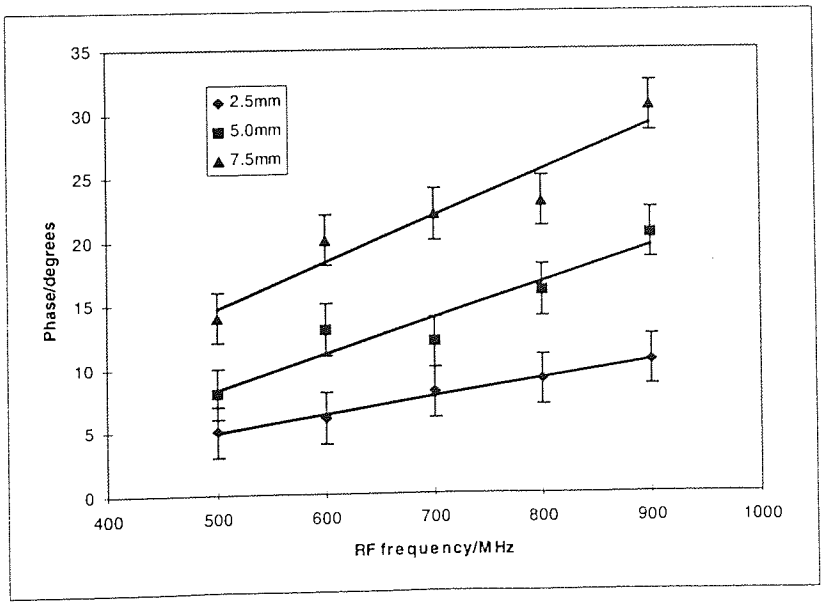

Figure 5.9 Phase delay as a function of RF frequency for grating delay line with 2.5mm separation: delay path lengths of 2.5mm, 5mm and 7.5mm

The variation of phase delay as a function of RF frequency[183] for each grating in the delay line can be found in Figure 5.9. The average minimum time delay created using this delay line was 30.88ps, compared to the theoretical prediction of 24.18ps. The discrepancy between the average experimentally

measured value and the theoretical value can be attributed to uncertainties in the precision of the positioning of the gratings during fabrication, and to system measurement error. RF beamforming control, with 10 degrees phase resolution, can be performed at frequencies of up to 896MHz using this delay line.

5.4.3 2mm long gratings, 2mm grating separation

The provision of 10 degrees phase resolution for antennas operating at higher RF signal frequencies requires the production of significantly smaller time delay steps. This demanded a decrease in the centre-to-centre separation between adjacent gratings within the delay line. For ease of fabrication this was implemented by reducing the width of the UV writing beams, enabling 2mm long gratings to be produced. A 2mm grating separation could then be achieved by fabricating gratings 'back-to-back' along the delay line. In parallel, improvements to the delay line fabrication rig design facilitated an increase in the number of gratings which could be written in a single delay line.

The optical spectrum of the fibre Bragg grating delay line containing eight gratings, with a 2mm centre-to-centre spacing between the gratings, and central wavelengths of 1530.80nm, 1536.55nm, 1539.35nm, 1542.55nm, 1544.55nm, 1549.30nm, 1555.70nm and 1560.00nm, is shown in Figure 3.6.

From Equation 5-3, a 2mm spacing between neighbouring gratings in a delay line corresponds to a minimum time delay of 19.35ps. To confirm this prediction, the minimum achievable time delay for the above delay line was measured using both the 1GHz and 130MHz-20GHz measurement systems[184].

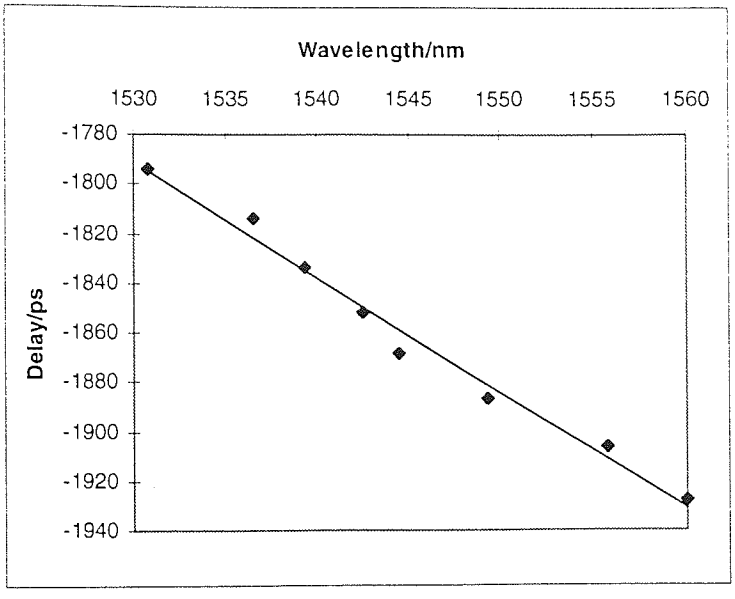

Figure 5.10 Time delay as a function of wavelength (position along delay line); 2mm separation array, 130Mhz-20GHz measurement system

5.4.3.1 130MHz-20GHz measurement system results

The measured absolute time delay, at wavelengths corresponding to each of the grating peaks, is plotted as a function of wavelength in Figure 5.10. The gratings lie on a dispersion of -4.66ps/nm, with a standard deviation of 0.26ps/nm; the time delay measurement resolution was less than 1.0ps. The small deviations of the experimentally measured values away from the straight-line fit can be attributed to uncertainties in the precision of the positioning of the Bragg gratings during the fabrication of the delay line, and to measurement system error in the determination of the amount of additional electrical time delay required to renull the network analyser output.

Wavelength/nm	delay/ps	delay step/ps
1530.8	-1794.4	
1536.55	-1813.5	-19.1
1539.35	-1833.4	-19.9
1542.55	-1851.7	-18.3
1544.55	-1868.2	-16.5
1549.3	-1886.8	-18.6
1555.7	-1905.9	-19.1
1560	1927.8	-21.9
gradient =	-4.65642	

Figure 5.11 Delay step size between gratings in delay line of 2mm long gratings with 2mm separation; 130MHz-20GHz measurement system

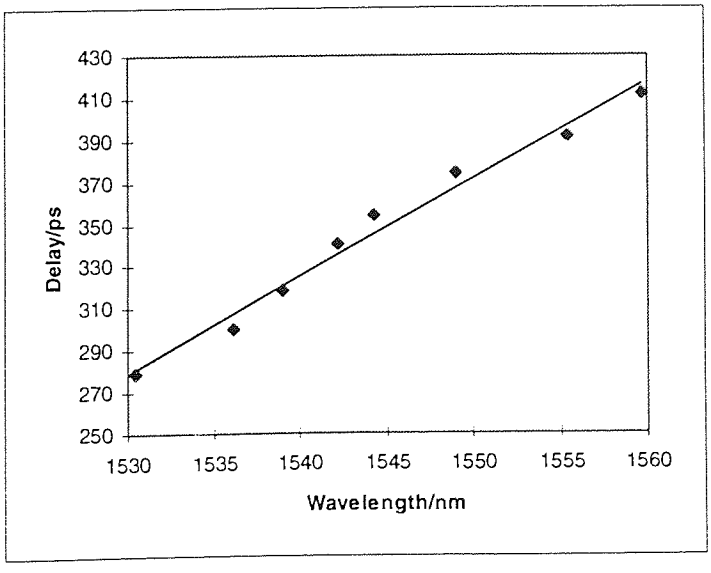

Figure 5.12 Time delay as a function of wavelength; delay line with 2mm long gratings and 2mm separation, 1GHz measurement system

Referencing from the first grating in the delay line, the additional time delay acquired by the optical signal on tuning the source wavelength from one grating peak to the next, is shown in Figure 5.11. The average delay step size is 19.06ps, with all the delay step sizes agreeing with the predicted value of 19.35ps to within 3ps; equivalent to a grating positioning error of <0.29mm.

Wavelength/nm	delay/ps	delay step/ps
1530.4	278.89	
1536.2	300.28	-19.1
1539.05	318.33	-19.9
1542.25	340.28	-18.3
1544.25	353.89	-16.5
1549.0	374.72	-18.6
1555.4	391.39	-19.1
1559.7	411.94	-21.9
gradient =	4.62926	

Figure 5.13 Delay steps between gratings in 2mm long, 2mm separation delay line; 1GHz measurement system

5.4.3.2 1GHz measurement

The measured absolute time delay as a function of wavelength is shown in Figure 5.12. The gratings lie on a dispersion of 4.63ps/nm, with a standard deviation of +/-0.29ps/nm; the time delay measurement resolution was less than 0.3ps. Referencing to the first grating in the delay line, the optical source was tuned to wavelengths corresponding to each subsequent grating peak, and the time delay steps between adjacent gratings measured, Figure 5.13. The average measured delay step size is 19.01ps, and all measurements agree with

the predicted value to within 3ps. This delay line is suitable for beamforming control at RF frequencies of up to ~1.44GHz, with 10 degrees phase resolution.

5.4.4 Grating length 2mm, centre-to-centre separation 1mm

To further increase the RF frequency at which 10 degrees phase resolution is available the grating separation was reduced to 1mm. This was achieved, using the 2mm UV writing beams, by fabricating adjacent gratings such that they physically overlapped by one half of their length. The spectral profile of the delay line is shown in Figure 3.7; the secondary peaks displayed by the grating spectra will be investigated further in 5.8. The minimum achievable time delay was measured using both the 130MHz-20GHz and 1GHz measurement systems[185]

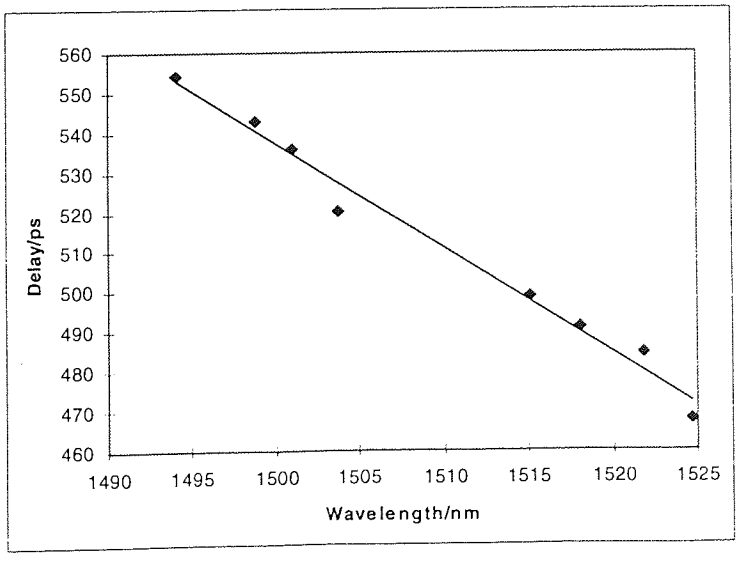

Figure 5.14 Time delay as a function of wavelength; 2mm long gratings array, 1mm separation; 130MHz-20GHz measurement system

5.4.4.1 130MHz-20GHz measurement system results

The measured absolute time delay as a function of wavelength is shown in Figure 5.14; the gratings lie on a dispersion of -2.65ps/nm, with a standard deviation of 0.15ps/nm. The average delay step size is 12.36ps.

5.4.4.2 1GHz measurement

Figure 5.15 shows the measured absolute time delay as a function of wavelength. The measurements lie on a dispersion of 2.04ps/nm, with a standard deviation of 0.22ps/nm, and the average delay step size is 9.09ps.

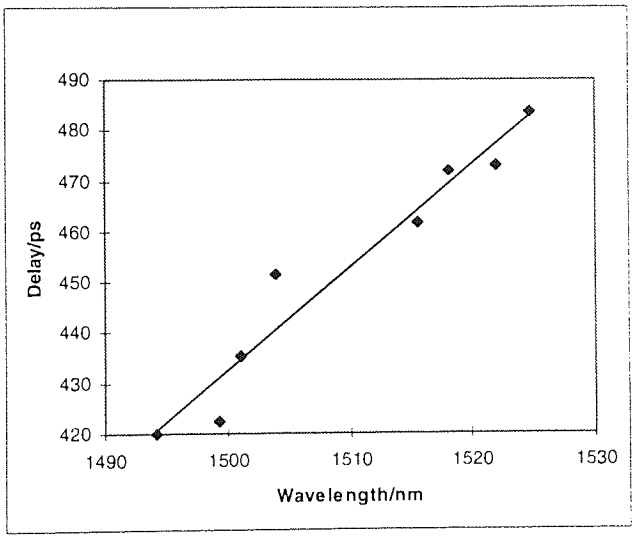

Figure 5.15 Time delay as a function of wavelength; 2mm long gratings array, 1mm separation; 130MHz-20GHz measurement system

The small deviations of the experimentally measured values away from the straight-line fits in both sets of measurements can be attributed to error in the precision of the positioning of the Bragg gratings during fabrication, and to their spectral characteristics; discussed further in 5.7 and 5.8. This fibre Bragg grating TTD delay line is capable of producing time delays of the order of 10ps, making it suitable for beamforming control, with 10 degrees phase resolution, at RF frequencies up to ~2.8GHz.

5.4.5 Discussion

The 9.09ps delay steps represent the practical lower limit on the time delay step size which can be produced through the use of delay lines comprising individually fabricated linear gratings. As discussed in Chapter 3, producing delay lines with grating separations of less than 1mm is prohibitively difficult due to the inability to know the exact position of the previously fabricated grating on the fibre. Using 2mm long gratings would also be a problem for shorter time delays as the number of gratings which could be written on the same length of fibre will be limited by the fibre photosensitivity. A move to the use of 1mm long gratings could be made, but such short gratings would have an increased optical bandwidth, hence reducing the number of gratings which could be written within the optical carrier bandwidth.

5.5 Chirped grating 'arrays'

5.5.1 Introduction

In order to produce time delay steps significantly smaller in duration than 10ps, a single chirped fibre Bragg grating can be used in place of the discrete grating array. Chirped grating delay elements enable production of continuously variable time delays, rather than discrete steps as in the grating arrays reported in 5.4. Tuning the optical source wavelength across the bandwidth of the grating results in the point of reflection within the grating 'sliding' along its length. The minimum time delay which can be created using a chirped grating 'array' delay line is determined by the optical carrier tuning step size and the optical bandwidth of the grating.

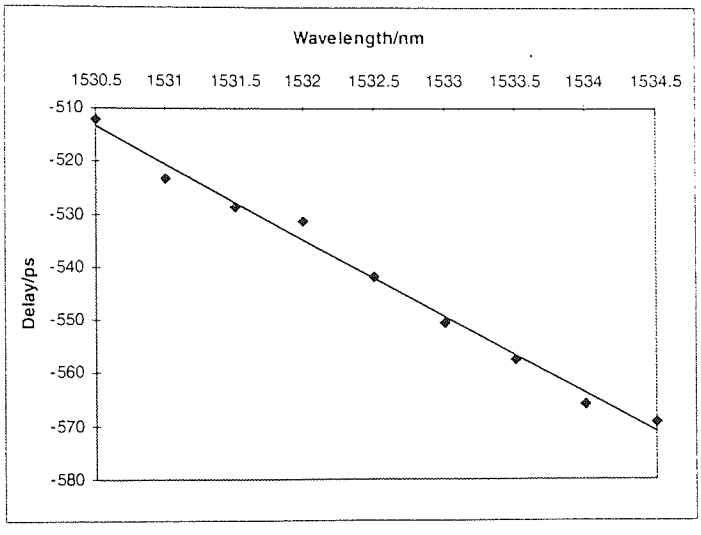

Figure 5.16 Time delay as a function of wavelength for 7nm chirped grating; 130Mhz-20GHz measurement system

As described in 3.3.2, the chirped gratings used here were fabricated, using the dissimilar-wavefront, holographic writing technique, and had FWHM bandwidths in the range 7nm to 30nm. The minimum achievable time delay for each grating was measured using both the 1GHz and 120MHz-20GHz measurement systems, and the individual spectral profiles recorded.

5.5.2 7nm chirp

The normalised spectral profile of the 7nm bandwidth grating is shown in Figure 3.15. In the 130MHz-20GHz measurement system the optical carrier wavelength was tuned in 0.175nm steps. The experimentally measured points lie on a dispersion of -14.442ps/nm, Figure 5.16, with a standard deviation of 0.563ps/nm; calculated using least-squares straight-line fit statistics on the experimental data. The optical carrier in the 1GHz measurement system was tuned in 0.02nm steps, under computer control. The 1GHz system experimental results, Figure 5.17, lie on a dispersion of -11.841ps/nm, with a standard deviation of 0.196ps/nm.

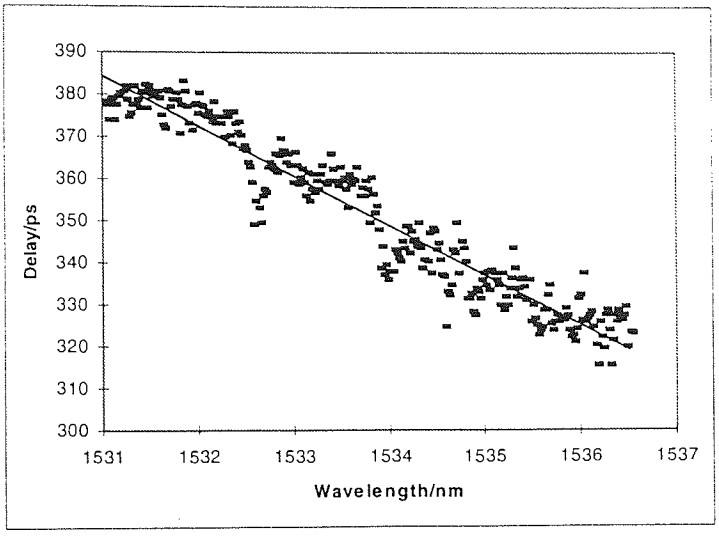

Figure 5.17 Time delay as a function of wavelength for 7nm chirped grating; 1GHz measurement system

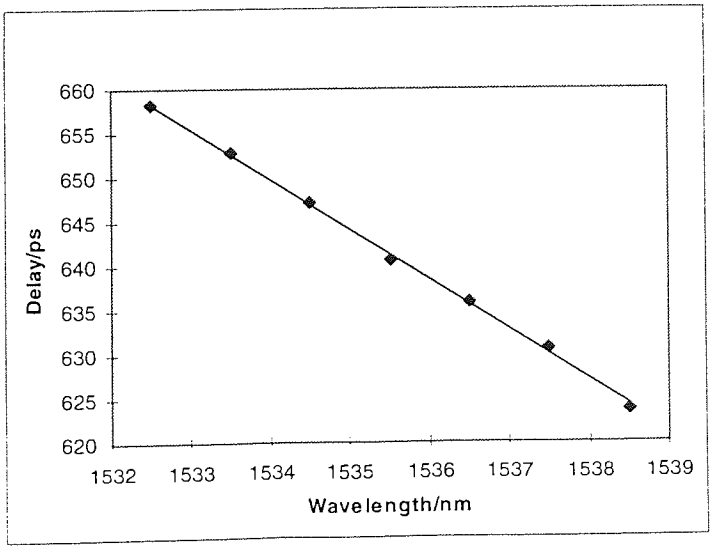

Figure 5.18 Time delay as a function of wavelength for 12nm chirped grating; 130MHz-20GHz measurement system

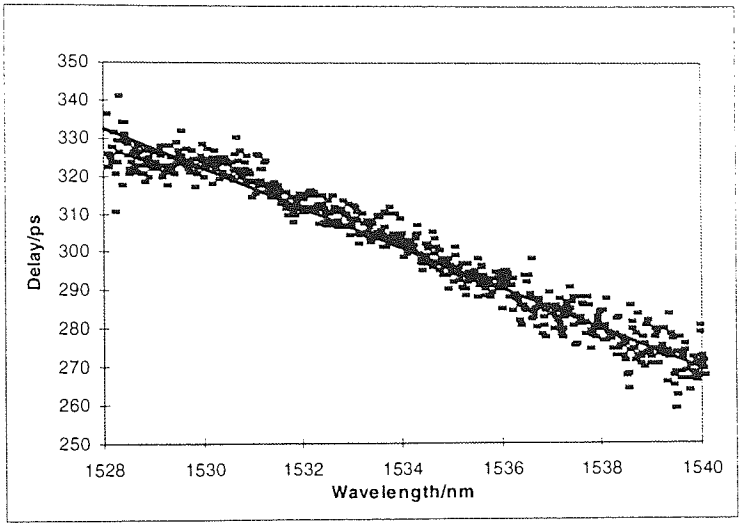

Figure 5.19 Time delay as a function of wavelength for 12nm chirped grating; 1GHz measurement system

5.5.3 12nm chirp

Figure 3.16 shows the normalised spectral profile of the 12nm chirped grating array. The 130MHz-20GHz system experimental results, Figure 5.18, lie on a dispersion of -5.681ps/nm, with a standard deviation of 0.096ps/nm. The 1GHz system experimental results, Figure 5.19, lie on a dispersion of -5.231ps/nm, with a standard deviation of 0.048ps/nm.

5.5.4 20nm chirp

The normalised spectral profile of the grating can be found in Figure 3.17. The 130MHz-20GHz system experimental measurements, Figure 5.20, lie on a dispersion of 2.497ps/nm, with a standard deviation of 0.04ps/nm. The 1GHz system experimental results Figure 5.21, lie on a dispersion of 2.169ps/nm, with a standard deviation of 0.044ps/nm.

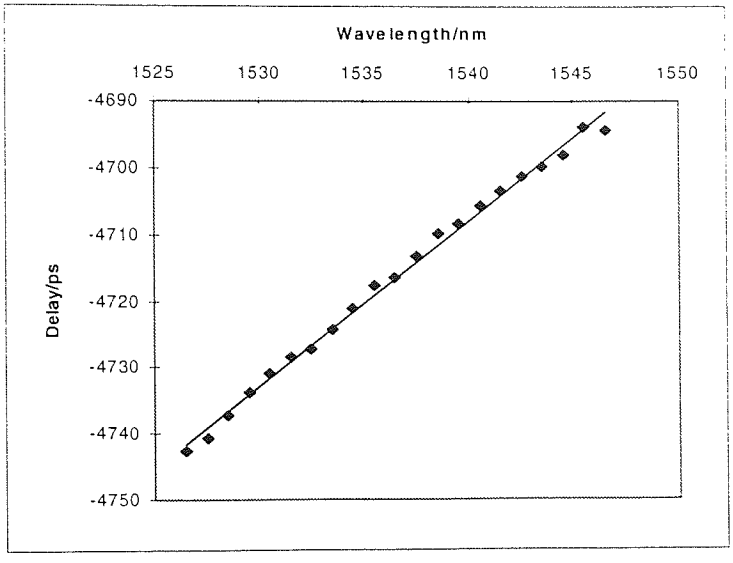

Figure 5.20 Time delay as a function of wavelength for 20nm chirped grating; 130MHz-20GHz measurement system

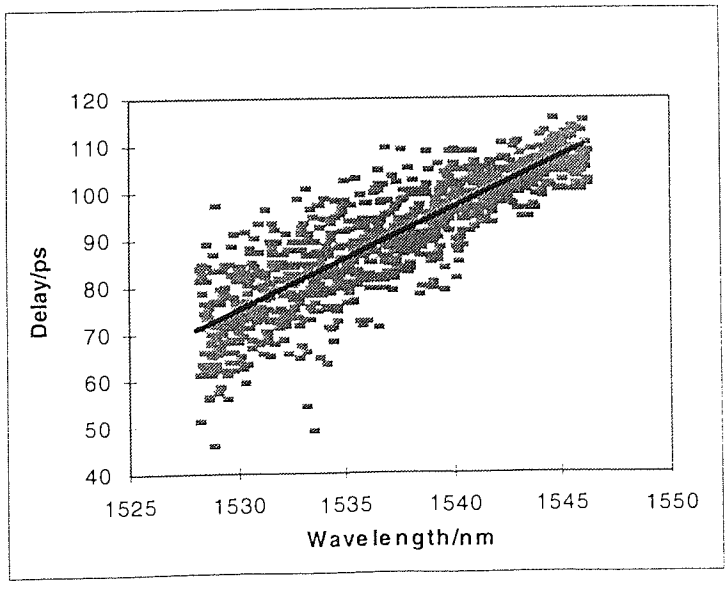

Figure 5.21 Time delay as a function of wavelength for 20nm chirped grating; 1GHz measurement system

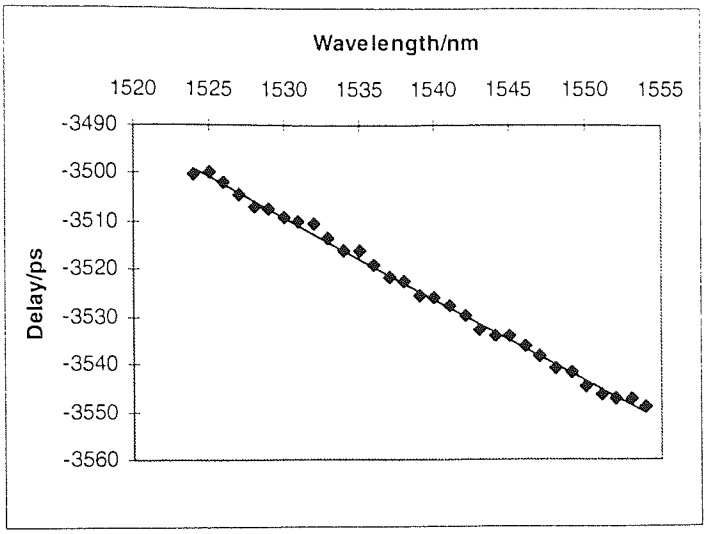

Figure 5.22 Time delay as a function of wavelength for 30nm chirped grating; 130MHz-20GHz measurement system

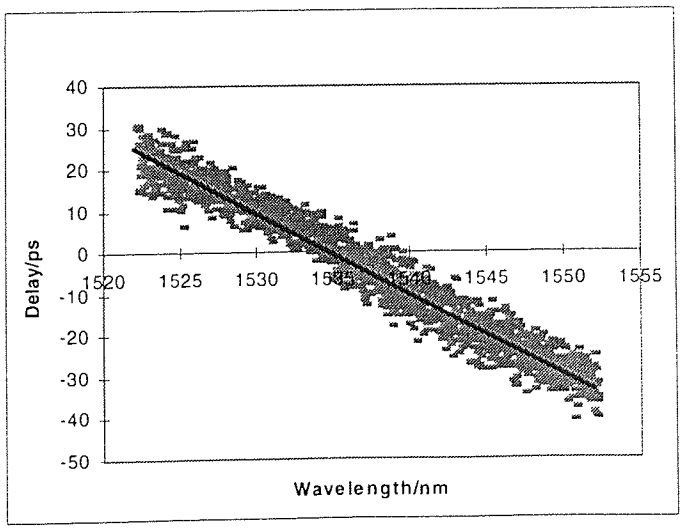

Figure 5.23 Time delay as a function of wavelength for 30nm chirped grating; 1GHz measurement system

5.5.5 30nm chirp

Figure 3.18 displays the normalised spectral profile of the grating. The 130MHz-20GHz system results, shown in Figure 5.22, lie on a dispersion of -1.713ps/nm, with a standard deviation of 0.019ps/nm. The 1GHz system

results[185], Figure 5.23, lie on a dispersion of -1.962ps/nm, with a standard deviation of 0.011ps/nm.

5.5.6 Discussion

In principle, the chirped grating delay lines above can be used to create time delays from as small as 40fs to as large as 59ps; the former being that available using the smallest wavelength tuning step size in the 1GHz measurement system and the 30nm grating; and the latter being that produced by tuning the wavelength across an entire grating bandwidth and hence utilising the full 4mm grating length. In practice, the smallest delay step size available here was approximately 0.6ps; determined by the 1GHz system characteristics and the optical linewidth broadening effect of modulating the optical carrier. This grating is therefore suitable for controlling an array at an RF frequency of up to ~48GHz, with 10 degrees phase resolution. In the case of the 30nm grating, in principle, use of 0.23nm wavelength tuning steps would produce 130 ~0.3ps time delay increments across the grating bandwidth, making it suitable for 7-bit (128 steps) time delay control. Similarly, wavelength steps of 0.14nm, 0.06nm and 0.03nm will produce 7-bits of 0.3ps delay with the 20nm, 12nm and 7nm gratings respectively. In practice, the ~0.6ps minimum time delay step size reduces the number of delay steps available to 6-bits.

The dissimilarity in the values of dispersion (straight-line fit gradient) measured with the two systems is created by the variance in the wavelength tuning step size; having the smaller wavelength tuning step size, the 1GHz system therefore has the higher measurement resolution.

5.6 RF frequency pulses

As discussed in 1.3, phased array radar systems are required to transmit beams which have a wide instantaneous signal bandwidth, of the order of a few hundred megahertz. Further, should a phased array antenna be required to

produce a pulsed RF beam an even wider RF signal bandwidth may be called for, depending on the temporal characteristics of the pulse; a 75ps pulse corresponds to a 16GHz bandwidth spectral envelope. It has been suggested[186] that modulating the optical carrier with an RF pulse signal would produce prohibitively large phase errors in the signals transmitted by the antenna elements because all of the different frequencies present in a pulse will experience different delays, through being reflected from different sections of the grating.

While it is true that modulating an optical signal with high frequency RF signals will result in linewidth broadening, to the scale of 0.018nm/GHz, the modulating frequency and chirp rate (nm/unit length) can be selected such that the required system phase resolution is not compromised. In the case of the 20nm chirp, 4mm long grating reported in 5.5.4, the laser linewidth (<0.01nm) would be broadened by 0.36nm on the application of a 20GHz RF modulation signal, resulting in a reflection point error of +/-36μm. This translates into a time delay error of +/-0.348ps, which is equivalent to a phase error of 2.5°. The insignificance of this error can be appreciated by comparing the measured phase response of the optical modulator, Figure 5.24, used in the 130MHz-20GHz experimental arrangement with the phase response over the same range of the 20nm chirped Bragg grating, Figure 5.25; both recorded with the (HP8703) network analyser.

The optical modulator, GaAs Mach-Zehnder (GMMT 9550Z), was specified for operation within the frequency range 2GHz-18GHz, and displayed the characteristic phase roll-off above 14GHz, with small phase oscillations present across the entire frequency bandwidth, and a significant phase excursion below 2GHz. The phase response of the chirped grating exhibited the same degree of roll-off at frequencies above 16GHz, and a similar response below 2GHz. In the frequency range 2GHz-5GHz the oscillations present in the modulator response appear amplified in the grating phase response, this is most probably caused by

a poor quality RF cable since it was not observed in all measurements. The effect cannot be due to the presence of the Bragg grating as it was not seen at the high frequency end of the response, where the linewidth broadening is most pronounced. Both traces are flat between 5GHz and 16GHz, apart from the small scale ripple caused by the modulator, from which it can be concluded that the various frequencies are not experiencing significantly different time delays; at 10GHz the phase error for the 20nm grating is +/-0.6°.

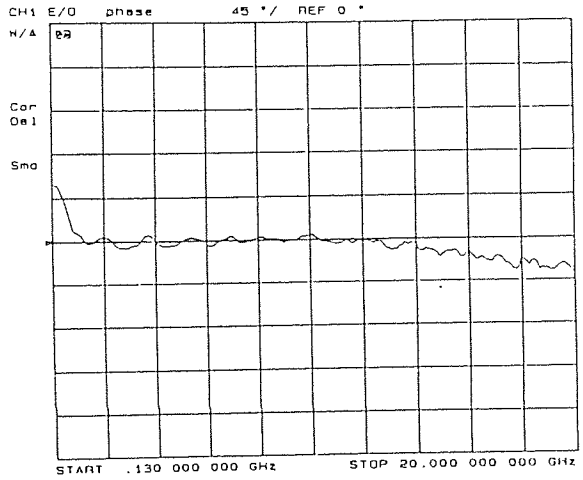

Figure 5.24 Phase response of GaAs Mach-Zehnder modulator (GMMT 9550Z) used in 130MHz-20GHz measurement system

The dispersion-induced pulse spreading for short pulses (75ps) travelling down even highly dispersive fibre has been derived by *Marcuse*[187], and found to be negligble, hence no phase errors will be incurred as a result of the optical carrier traversing long lengths of fibre optic link.

Bragg grating TTD elements are therefore suitable for use with both continuous wave RF signals and wide band RF signals if the chirp rate and maximum operating frequency are matched; the frequency should not exceed the value at which the phase response of the modulator starts to roll off. The noise at the lower modulation frequencies is a characteristic of this modulator only, devices with flatter phase responses over this range can be produced, but one was not available for this work.

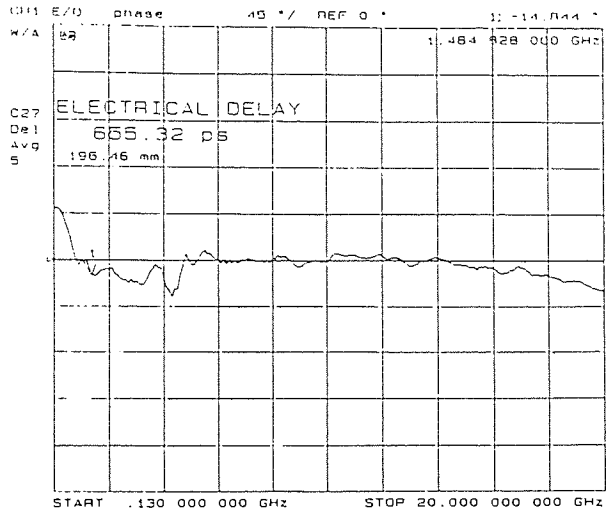

Figure 5.25 Phase response of 20nm chirped Bragg grating measured using 130MHz-20GHz measurement system

5.7 Individual grating profiles

5.7.1 Introduction

Each linear grating within the discrete grating delay lines has a unique time delay profile: the time delay incurred by a signal on reflection from a single grating varies depending on which wavelength within the grating bandwidth the optical carrier is tuned to. There are two sources of this time delay variation: the individual Bragg grating coupling coefficient profiles and changes to the average core refractive index produced by the physical overlapping of gratings within an array. A variable time delay across the individual grating bandwidths within an array can allow very sensitive time delay tuning across a small optical carrier wavelength range. However, when more coarse tuning is used this can lead to the production of dissimilar time delays for optical carrier wavelengths of nominally the same value; for example, should the tuneable laser wavelength drift away from its initial value, two different time delays may be created on reflection from the same grating within the delay line.

5.7.2 Grating profiles

Using the 1GHz experimental measurement system, the phase and intensity of the signals reflected by the 2mm grating delay lines were recorded for each optical carrier wavelength step across the delay line bandwidths, allowing the time delay profile of each grating within the arrays to be investigated.

The time delay profiles of the gratings in the delay line with a 1mm grating separation[184] can be seen in Figure 5.26, and those of the gratings in the delay line with 2mm grating separations[188] are shown in Figure 5.27. Comparing the two sets of graphs, one can see that the time delay profiles of the 2mm separation delay line gratings display less variation than the profiles of the 1mm separation delay line gratings. It may also be observed that the 1mm separation delay line grating profiles vary only at the extremes of the grating bandwidths.

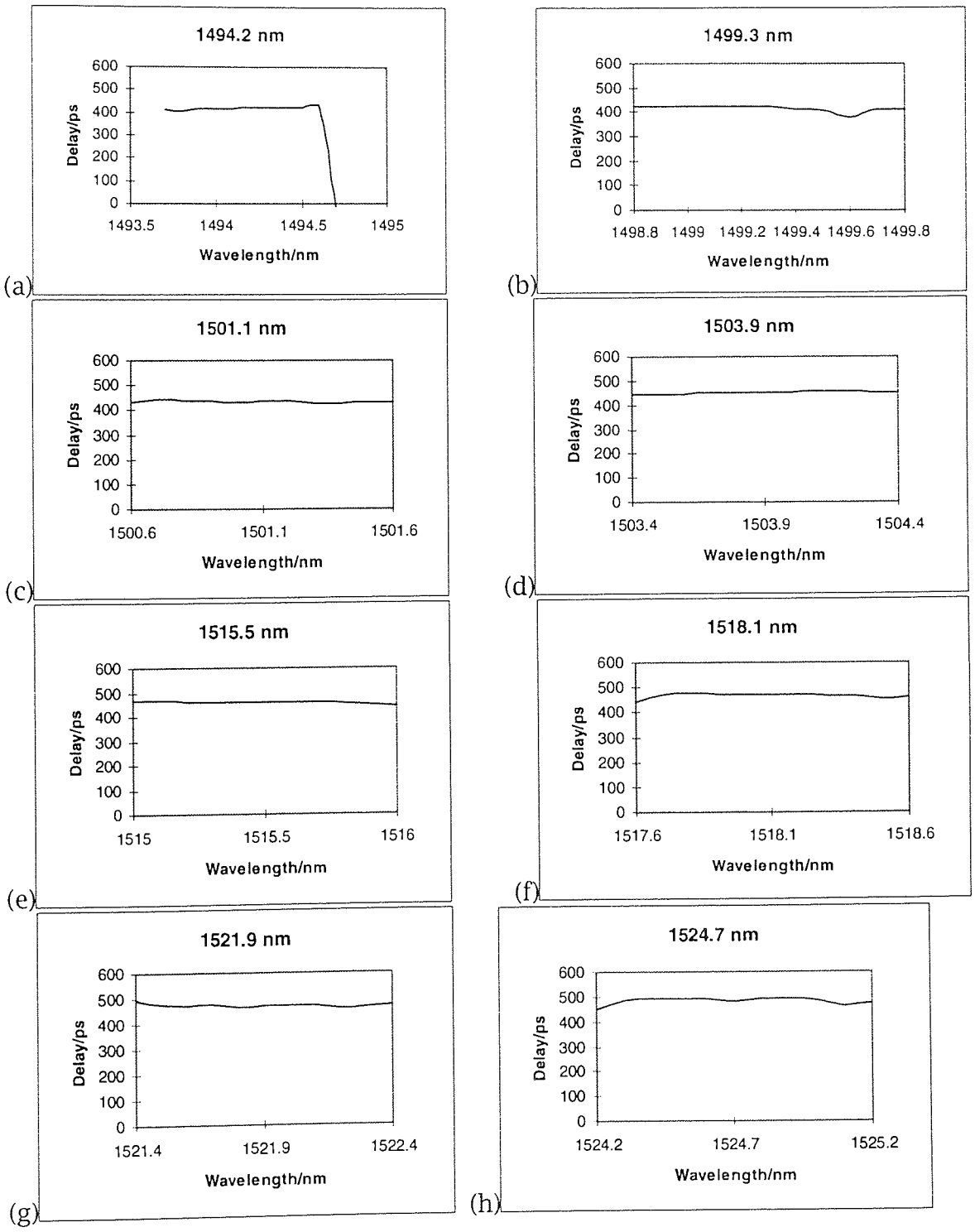

Figure 5.26 Individual time delay profiles of gratings in delay line of 2mm long gratings, with 1mm inter-grating separation

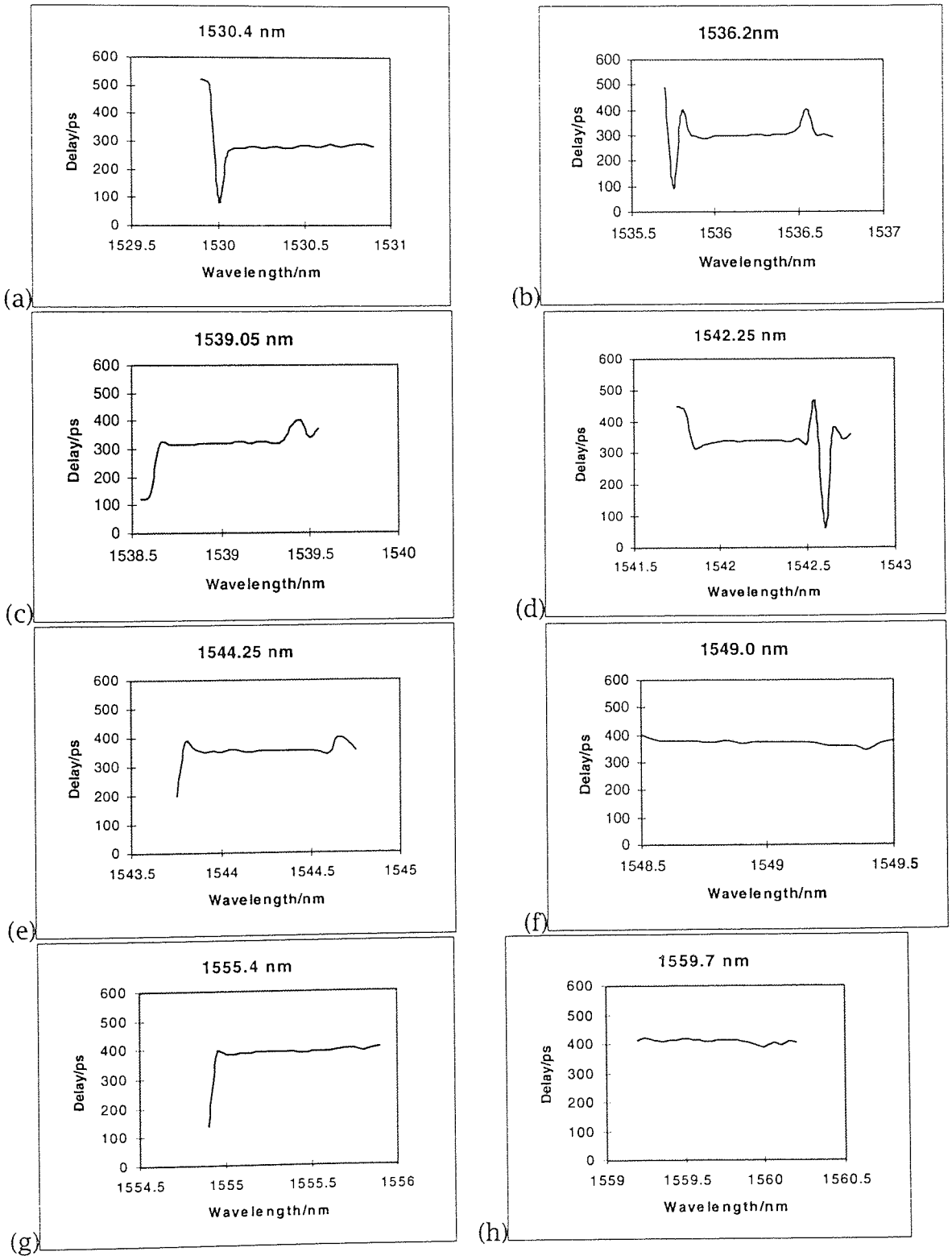

Figure 5.27 Individual time delay profiles for gratings in delay line of 2mm long gratings with 2mm inter-grating separation

The variation in the shapes of the profiles can be explained by the difference in the physical properties of the arrays. As described previously, adjacent gratings within the 1mm separation delay line physically overlap, whilst those in the 2mm separation delay line do not. Therefore, the 2mm separation array gratings will contain less average core refractive index variation than those in the 1mm separation delay line, and hence less variation in time delay along their length i.e. across their bandwidth.

The grating delay profiles were magnified in order to observe any fine detail which they might contain:

Figure 5.28 shows the central sections of the grating profiles of the 1mm grating separation delay line and Figure 5.29 shows the profiles of the gratings in the 2mm separation delay line. Time delay variations of the order of 10ps to 50ps can be seen on all of the graphs. These time delay fluctuations are real, and are a result of resonance effects within the individual gratings caused by their refractive index profiles. Time delay fluctuations occur in gratings with sharp edges to their refractive index profiles because the pronounced boundary between the core refractive index and that of the grating acts as a broadband reflector, which some fraction of the incoming light is reflected off. Gratings with shaded edges to their refractive index profile will not experience this effect, and will produce smooth time delay profiles. The individual Bragg grating coupling coefficient profiles used here did not contain much 'shading' or apodization due to the intensity profile of the interference pattern used to fabricate the gratings; see 3.2.1 and 3.2.2.

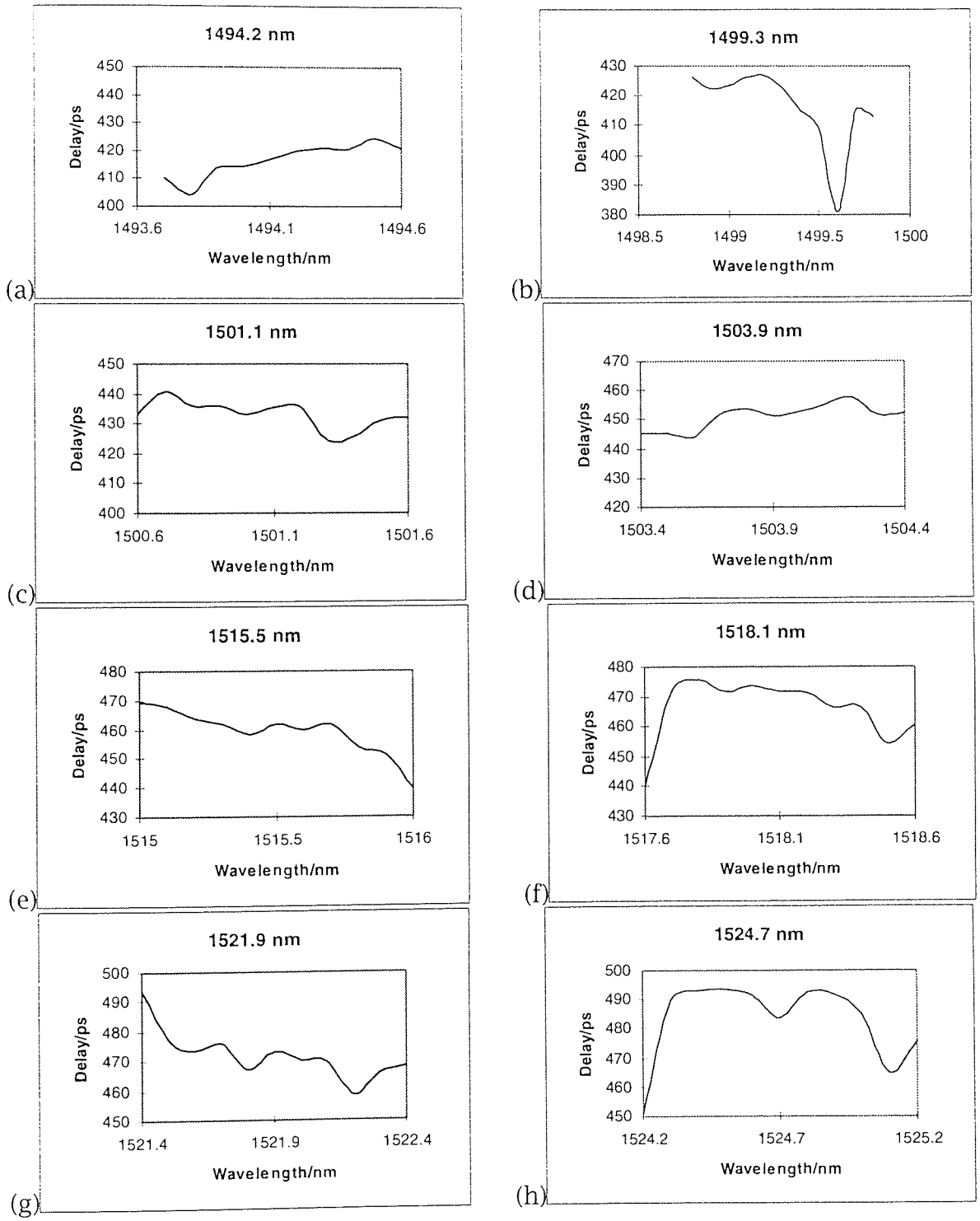

Figure 5.28 Magnified central sections of individual time delay profiles of gratings in array with 1mm grating separation

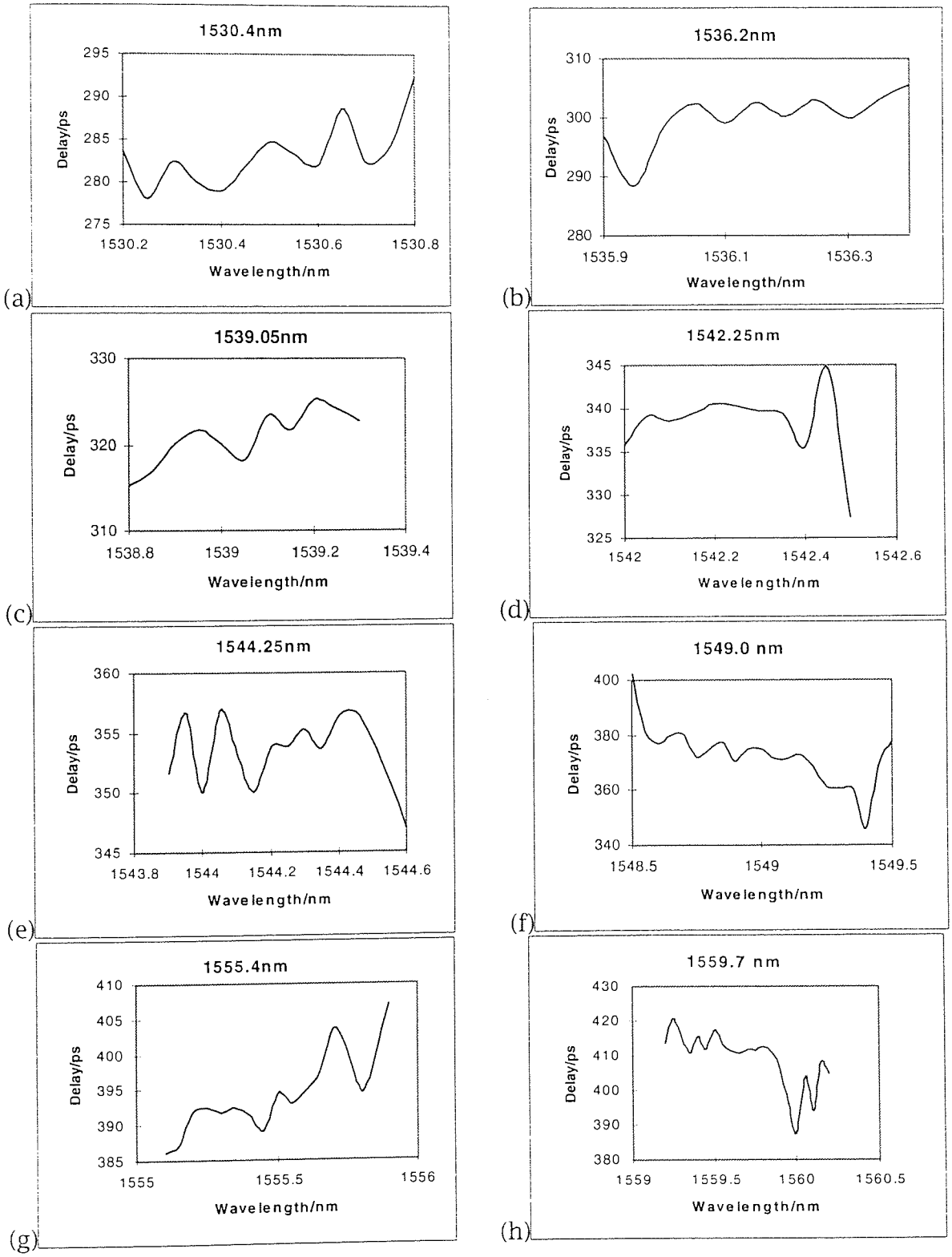

Figure 5.29 Magnified individual time delay profiles of gratings in array with 2mm grating separation

5.8 Delay line modelling

5.8.1 Introduction

The spectra of the gratings in the delay line constructed from 2mm long gratings with an inter-grating separation of 1mm displayed multiple reflection peaks, the probable cause of which are resonance effects occurring within the grating array. There are several factors which could contribute to this: grating separation, linewidth and strength, and average core refractive index.

In the fabrication of this delay line adjacent gratings were positioned so that they were physically overlapping. In the ideal case, this would lead to the production of a grating structure, for n gratings of length l, in which the first and last sections of the structure, length $l/2$, contained only one refractive index variation, and the main section comprised $(n-2)$ sections, of length $l/2$, each containing two superimposed refractive index variations of different periods. In practice, due to errors in the positioning of the gratings during fabrication, it is possible that individual lengths of fibre contained one, two, or even three, superimposed refractive index variations of different periodicity.

The process of writing a grating in a length of fibre raises the average index of the core, and writing a second grating on the same length of fibre will raise it further still. This would result in the ideal grating array containing two values of average core refractive index: the first and last sections of the array structure having one value of average index, assuming all gratings are of equal strength, and the central section being of a different, higher value. In the experimental array, the positioning errors and the variation in the grating reflectivities will have produced many distinct variations in the value of the average refractive index of the core along the length of the array structure.

In order to determine which of these factors are contributing to the multiple resonances in the grating spectra, and to ascertain the relative importance of

each factor, a mathematical model of the delay line was constructed on which they could be tested. The amplitude and phase response of the modelled structure were calculated using a program called 'tf', (thin film)[189] based on the transfer matrix formalism. The size of the effect of each factor on the grating spectra was measured through comparison of the calculated response with the experimentally recorded array spectrum. These effects are also thought to be causing the variations in the individual time delay profiles of the gratings. By varying the properties and the relative positions of the gratings within the array and analysing the reflection responses calculated by the tf program, further insight into the cause of the multiple resonances in the grating spectra and the nature of the individual grating delay profiles can be obtained.

5.8.2 tf analysis program

5.8.2.1 Introduction

Several different techniques can be used to calculate the response of a periodic waveguide structure such as an in-fibre Bragg grating. Analysis of purely periodic structures and nearly-periodic structures is generally carried out using numerical techniques. While either coupled-mode theory[190,191] or transfer matrix techniques[192,193] can be used to calculate the response of more general structures.

Under coupled-mode theory a pair of first-order coupled differential equations is used to approximately relate the amplitudes of the forward and backward travelling modes. A numerical solution can be reached by combining these equations to give a single, solvable, second-order Ricatti differential equation[194]. Coupled-mode theory provides a good description of the interaction of the fibre modes with the Bragg grating core-refractive-index perturbation in all but the strongest gratings; the approximations which are used break down when the induced refractive index modulation is greater than the refractive index difference across the core/cladding boundary. In the transfer matrix technique

the grating structure is 'sliced' into a large number of thin, homogeneous, rectangular sections, for which the optical field continuity conditions can be solved exactly to give a 2x2 transfer matrix. Multiplying the transfer matrices of all of the sections together gives the overall response of the structure.

Coupled mode theory and the transfer matrix technique are related, however as the transfer matrix technique is applicable to the analysis of both general waveguide structures and sequences of waveguide structures, it is this which is used in the tf program.

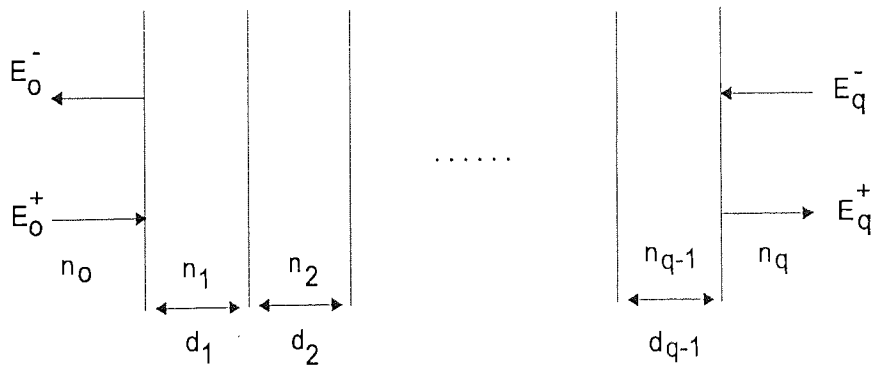

Figure 5.30 Electric fields, E, at each layer in the grating structure under transfer matrix analysis technique; refractive index n; thickness d.

5.8.2.2 Transfer matrix technique

At each layer in the grating structure the electric field is split into forward and backward travelling components E^+ and E^-, Figure 5.30, and, similarly, the magnetic field is split into components H^+ and H^-. Solving for the boundary conditions and the phase change across each layer gives a transfer matrix relating the electric field at one layer to the next as follows:

$$\begin{pmatrix} E_{j+1} \\ H_{j+1} \end{pmatrix} = \begin{pmatrix} \cos g_j & \frac{i}{U_j}\sin g_j \\ iU_j \sin g_j & \cos g_j \end{pmatrix} \begin{pmatrix} E_j \\ H_j \end{pmatrix} = M_j \begin{pmatrix} E_j \\ H_j \end{pmatrix}$$

Equation 5-4

where

$$g_j = (2\pi/\lambda) n_j d_j \cos\vartheta$$

Equation 5-5

is the change in phase across the j'th layer for an angle of incidence ϑ, d is the thickness of the layer, and U_j is the generalised refractive index for the polarisation components normal (s) and parallel (p) to the plane of incidence, given respectively by:

$$U_s = n\cos\vartheta$$

Equation 5-6

$$U_p = n/\cos\vartheta$$

Equation 5-7

The matrix is for one j'th film, and one polarisation. For a sequence of dielectric films, the iterative result is given by:

$$\begin{pmatrix} E_q \\ H_q \end{pmatrix} = M_1 M_2 \ldots M_{q-2} M_{q-1} \begin{pmatrix} E_1 \\ H_1 \end{pmatrix}$$

Equation 5-8

$$M = \begin{pmatrix} M_{11} & iM_{12} \\ iM_{21} & M_{22} \end{pmatrix}$$

Equation 5-9

The complex reflection and transmission coefficients are described by:

$$r = \frac{E_0^-}{E_0^+} = \frac{U_q M_{11} - U_0 M_{22} + i\left(U_q U_0 M_{12} - M_{21}\right)}{U_q M_{11} + U_0 M_{22} + i\left(U_q U_0 M_{12} - M_{21}\right)}$$

Equation 5-10

$$t = \frac{E_q^+}{E_0^+} = \frac{2U_q}{U_q M_{11} + U_0 M_{22} + i\left(U_q U_0 M_{12} + M_{21}\right)}$$

Equation 5-11

These equations apply for a general stack of planar dielectric films. For non-absorbing structures, having only real values of n, all terms $\mathbf{M}_{11}$ - -$\mathbf{M}_{22}$ are real. In optical fibre the light always strikes the dielectric structure at normal incidence, $\vartheta = 0$, so the polarisations, s and p, are degenerate. The coefficients r and t are the complex amplitude responses, therefore the reflectivity and transmissivity of the structure are given respectively by:

$$R = |r|^2$$

Equation 5-12

$$T = |t|^2$$

Equation 5-13

A structure with a continuously spatially varying refractive index *n(z)* is divided up into a large number of homogenous layers, and solved as above. To increase

the accuracy of the calculation the spacing between the slices can be decreased; in practice about 20 layers per sinusoidal period is sufficient.

5.8.3 Results

5.8.3.1 Introduction

The computer code modules relating to this section can be found in Appendix A; to aid the interested reader all the *functions* in the code are given in italics, and the variables are given in brackets, alongside the relevant text. In the thin film model, the grating array structure is defined as a series of *Shortgrating* sections, each Shortgrating has a *TopHat* intensity profile and a *Bragg* sinusoidal refractive index variation, whose periodicity ($period) must be defined. The length of the grating array structure (@z) must be defined, as must the length of the Shortgratings ($length), and the position of each Shortgrating within the array ($centre). In addition, values for the core refractive index ($n), Shortgrating spectral bandwidth ($stopband), array spectral bandwidth (@lambda), any chirp across the Shortgratings ($chirpfactor), the effect of the average refractive index change (env), and the grating reflectivity must be defined. For comparison, the reflection response of an ideal array of eight 2mm long linear gratings of equal strength, grating separation 2mm, was calculated, Figure 5.31.

5.8.3.2 Linear gratings

The first model of the grating array was constructed from eight linear gratings of length 2mm, with a 1mm centre-to-centre grating separation, Appendix A.1. Initially, the spectral response of an ideal array with perfect grating separations, was calculated, Figure 5.32. This displayed very clean grating spectra, with low intensity sidebands. In order to produce closer correspondence between the theoretical and experimental grating spectra, Figure 3.7, the grating separations used in model were changed from the ideal value. The spectrum of an array with grating separations which varied by up to 20% from the ideal case is

shown in Figure 5.33; little degradation of the individual grating spectra was observed.

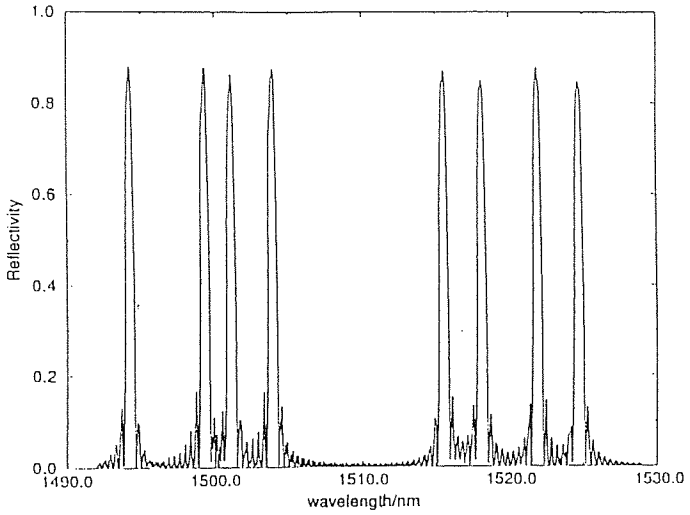

Figure 5.31 Calculated reflection response of an ideal grating array comprising eight equal strength, 2mm long gratings, separated by 2mm

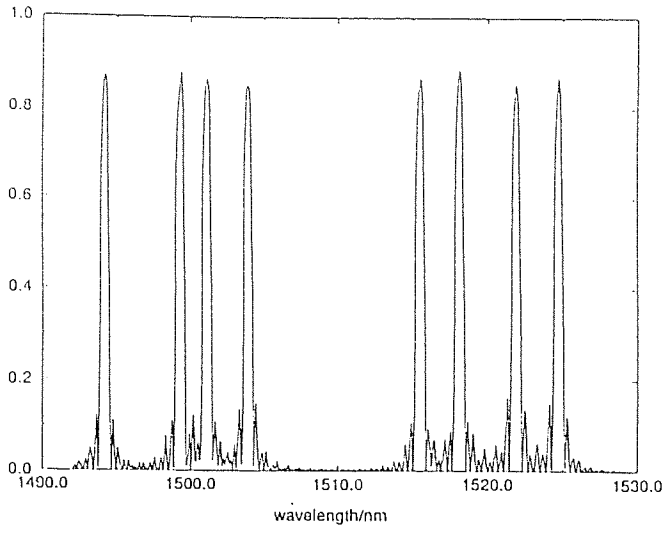

Figure 5.32 Calculated reflection response of array of eight 2mm long, equal strength gratings, separation 1mm

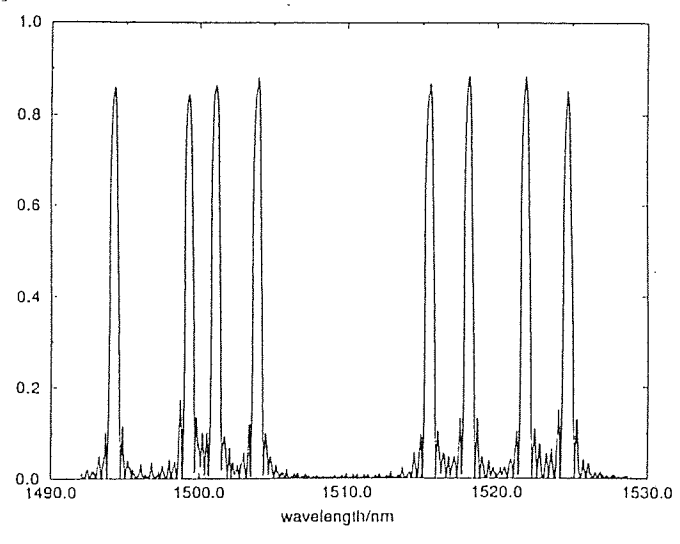

Figure 5.33 Calculated reflection response of array of eight 2mm long, equal strength gratings; grating separations varied by up to 20% from the 1mm ideal separation

5.8.3.3 Chirped gratings

In order to make the Shortgratings in the model more like the experimental gratings a small amount of wavelength chirp, *chirpfactor,* was designed into them, Appendix A.2. The response of an ideal array, with a 1nm chirpfactor, was calculated, Figure 5.34; compared to the spectra for the linear grating arrays, the bandwidth of the gratings has increased, and the grating spectra have developed small, secondary resonance peaks. The grating separations were then changed, producing an increase in the size of the secondary peaks in the grating spectra: grating spacings of 1mm, 1.5mm, 1mm, 1mm, 1.5mm, 1.5mm,

and 1mm, gave an array reflection response as shown in Figure 5.35 Increasing the chirpfactor to 2nm, while keeping the grating separations as before, resulted in a dramatic increase in the size of the secondary peaks and a decrease in the maximum reflectivity Figure 5.36.

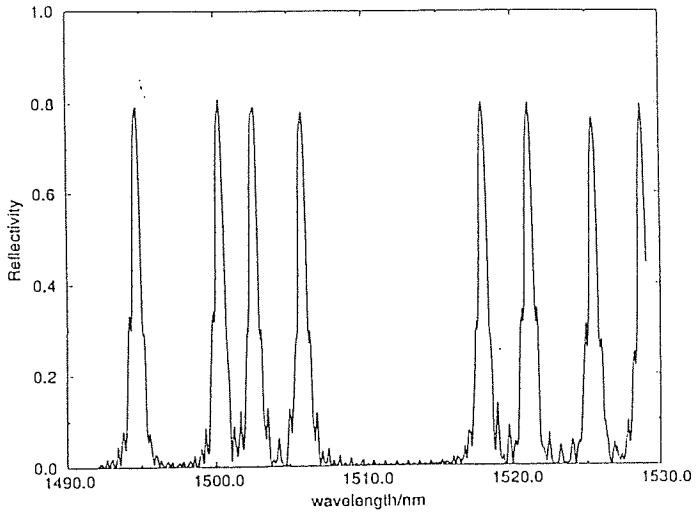

Figure 5.34 Calculated response of an ideal array of 2mm long, 1nm chirp, gratings, with a 1mm inter-grating separation

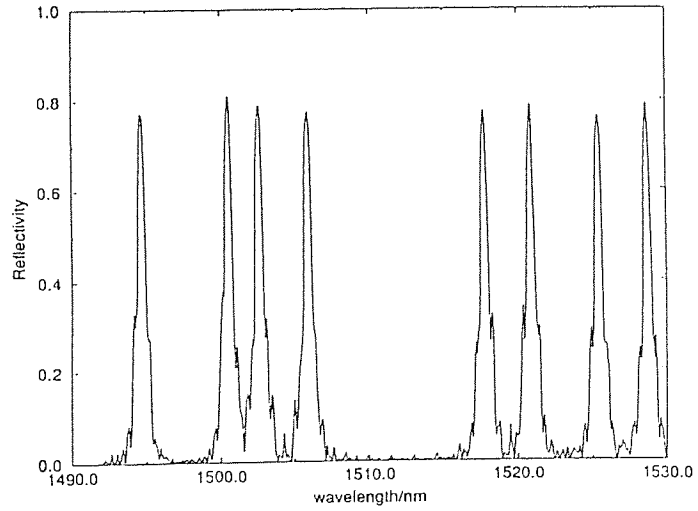

Figure 5.35 Calculated response of array of 2mm long, 1nm chirp gratings, in which the inter-grating separations of 1mm and 1.5mm

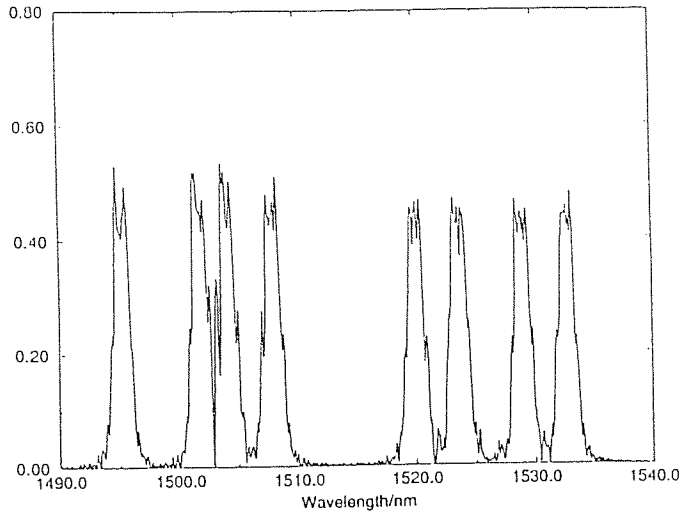

Figure 5.36 Calculated response of array of 2mm long, 2nm chirp gratings, in which the inter-grating separations of 1mm and 1.5mm

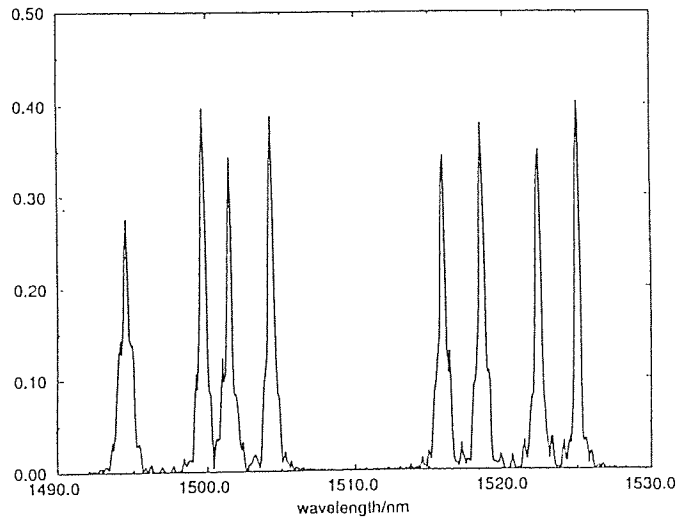

Figure 5.37 Calculated response of array of 2mm long, 1nm chirp gratings, with 1mm grating separation, including effect of change of average core refractive index on fabrication of a grating

5.8.3.4 Chirped gratings and average core refractive index change

The third model of the delay line, Appendix A.3, included the change in the average refractive index of the fibre core when a grating is fabricated in it. An array of perfectly spaced, 1nm chirpfactor, gratings produced the reflection response shown Figure 5.37; the reflectivity is reduced compared to the ideal array of 1nm chirped gratings in Figure 5.34, in which the effect of the average refractive index change was not included.

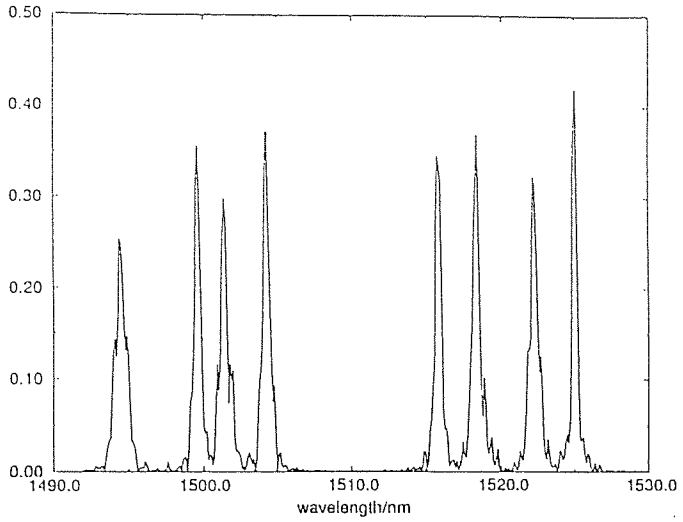

Figure 5.38 Calculated response of array of 2mm long, 1nm chirp gratings, with grating separations of 1mm and 1.5mm, and including effect of change of average core refractive index on fabrication of a grating

Various different grating spacings were subsequently built into the model, with the largest change to the grating spectra seen for an array where the third, sixth and seventh gratings are 50% away from their ideal positions; grating separations of 1mm, 1.5mm, 1mm, 1mm, 1.5mm, 1.5mm, and 1mm. The reflection response of this delay line is shown in Figure 5.38; the reflectivities of some of the gratings has decreased and the amplitude of the sidebands increased. The chirpfactor was then increased to 2nm, grating spacings as before, and a significant increase in the amplitude of the sidebands was observed, again with a reduction in the maximum reflectivity, Figure 5.39.

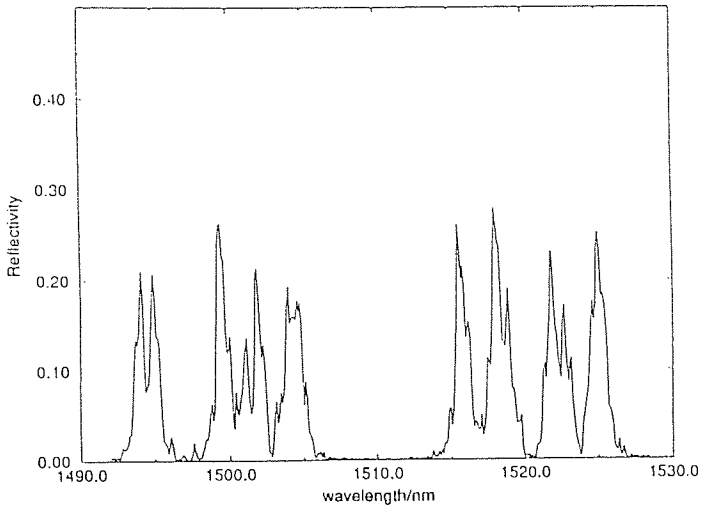

Figure 5.39 Calculated response of array of 2mm long, 2nm chirp gratings, with grating separations of 1mm and 1.5mm, and including effect of change of average core refractive index on fabrication of a grating

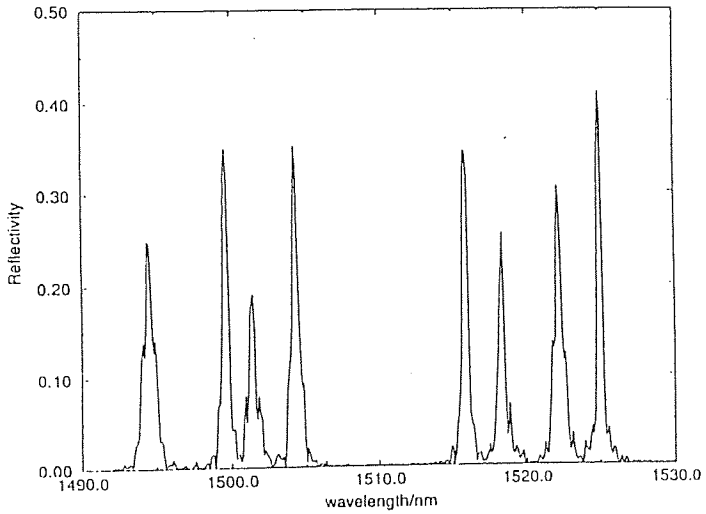

Figure 5.40, Calculated reflection response of an array of 2mm long, 1nm chirp factor gratings, inter-grating separations of 1mm and 1.5mm, and with the reflectivities of gratings 3 and 6 set to 0.8.

5.8.3.5 Chirped gratings, average core refractive index change and different reflectivities

Gratings in a non-ideal array will differ in strength, so some variation in grating reflectivity was included in the fourth model of the grating array, Appendix A.4. An array with grating spacings of 1mm, 1.5mm, 1mm, 1mm, 1.5mm, 1.5mm, and 1mm, 1nm chirp factor, and with the reflectivities of gratings 3 and 6 set to 0.8, produced the reflection response shown in Figure 5.40. The reflectivities of

some of the other gratings were affected by the reduced reflectivity of gratings 3 and 6, but the secondary resonances were unchanged.

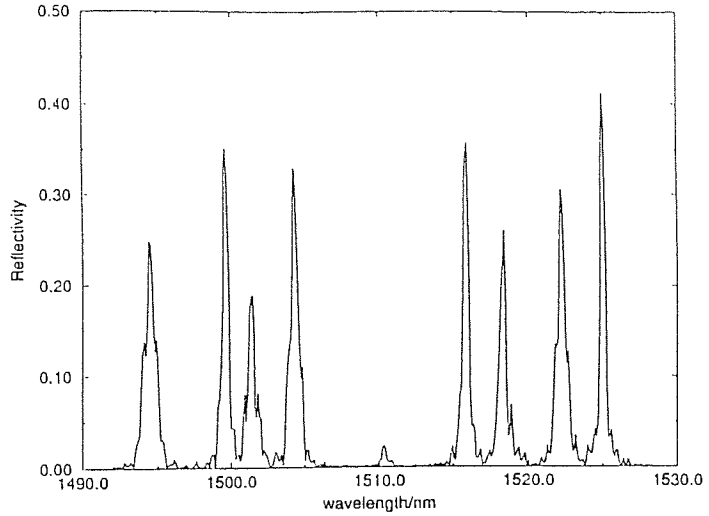

Figure 5.41 Calculated response of array as for Figure 5.40 but also including an extra grating with a reflectivity of 0.2, and a wavelength of ~1510nm, sharing same position as grating 5 (1515.2nm)

During fabrication of the experimental array a very weak grating was written in the grating number five (1515.2nm) position, at a wavelength of 1510nm, as can be seen in the experimental array spectrum, Figure 3.7. The fifth grating was then written on top of the weak grating. In order to investigate the effect of this grating on the array spectrum, an extra grating, with a reflectivity of 0.2, was included in an array like that used for Figure 5.40. Comparing this reflection response, Figure 5.41, to Figure 5.40, no change was observed, indicating that the extra grating was too weak to have any significant effect on the array characteristics.

Using the same separations and reflectivities as for Figure 5.40, the chirpfactor was increased to 2nm, Figure 5.42. As above, the increase in the size of the chirp across the gratings had a notable effect on the grating spectra.

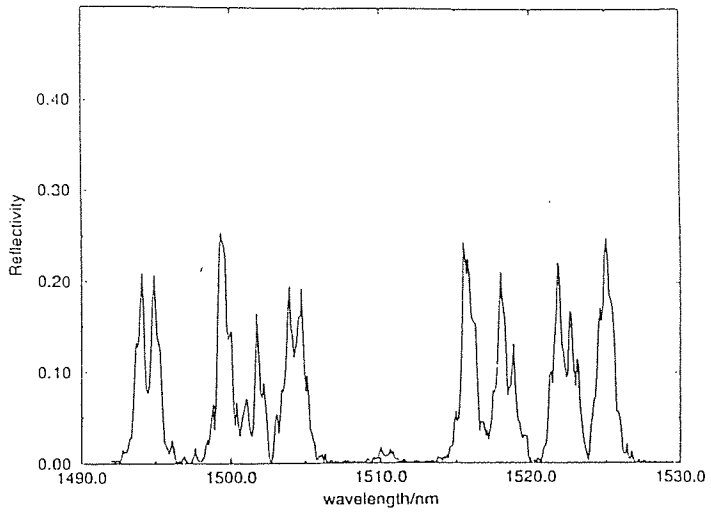

Figure 5.42 Calculated reflection response of an array of 2mm long, 2nm chirp factor gratings, inter-grating separations of 1mm and 1.5mm, and with the reflectivities of gratings 3 and 6 set to 0.8.

5.8.4 Discussion

From the delay line modelling results it is clear that an increase in the bandwidth of the individual gratings produced the most significant effect on the array spectrum, causing large secondary resonance peaks to appear in the grating spectra. It was also shown that non-ideal grating separations induce a similar, though smaller, degradation of the spectra, and inclusion of the change in average core index created during grating fabrication resulted in an overall reduction in grating reflectivity.

In the experimental array spectrum all of the grating spectra displayed multiple resonances, and were of different reflectivity. Several of the gratings displayed more pronounced secondary peaks, which the modelling results would suggest is due to these gratings having a larger chirp across them. Different linewidths would be produced if the lengths of the gratings were not the same, which could be caused, during the fabrication process, by the UV writing beams not overlapping by an equal amount each time; thus forming interference patterns of varying length. The dissimilarity in the grating reflectivities can be explained

by the variation in exposure times used for different gratings during fabrication, and the amount of error in their positioning.

For a real phased array antenna system it is important that the optical signals arriving at the output photodiodes, where the recovered RF signal is amplified to drive the microwave radiators, are all of approximately the same amplitude. If this is not the case different radiators will emit signals of different amplitude, and the RF beam will not have the desired profile, or may point in the wrong direction. This requires that the gratings within each delay line in the control architecture have the same reflectivity and that the grating profiles are of a constant shape, containing only one peak. The delay line modelling results indicate that this can be achieved through the use of gratings with a spectral-linewidth of ~1nm. It will also be necessary to fabricate the gratings with equal reflectivities, and to maintain the grating separation at a constant value. Another factor which can affect the grating reflection profiles, but which could not be included in the model, is fringe tilt. This is caused when the interference fringes used to write a grating are not perpendicular to the fibre axis, and leads to out-coupling of light at certain wavelengths.

5.9 Conclusion

Four discrete grating arrays have been fabricated in hydrogenated, standard single-mode fibre. The first comprised four 5mm long gratings, centre-to-centre separation 5mm, and the second four 5mm long gratings, grating separation 2.5mm. These delay lines were used to produce delays of 53.49ps and 30.88ps respectively. The third delay line contained eight 2mm long grating, with an inter-grating separation of 2mm, and yielded a minimum time delay of 19.01ps, while the fourth array consisted of eight 2mm long gratings separated by 2mm, and was used to create a minimum delay of 9.09ps. These delay lines are suitable for the control of phased array antennas, with 10 degrees phase

resolution, at frequencies of up to 519MHz, 896MHz, 1.44GHz and 3GHz respectively.

The 9.09ps time delay represented the lower limit available for delay lines fabricated as arrays of discrete gratings. In order to produce significantly smaller time delays the discrete grating array was replaced by a chirped Bragg grating. Four such arrays were fabricated in hydrogenated, boron-germania co-doped, single mode fibre, with bandwidths of 7nm, 12nm, 20nm and 30nm. A minimum time delay of 0.6ps was imposed by the 1GHz measurement system, while a maximum time delay of 59ps was available, and all of the gratings were capable of producing 6-bit time delay control.

The time delay profiles of the individual, 2mm long, gratings were recorded using the 1GHz measurement system, and were observed to contain some fluctuations. Two sources of these time delay variations were identified: the large scale fluctuations seen on the 1mm separation array were due to average index variations caused by the spatial overlapping of adjacent gratings; and the smaller scale fluctuations, of the order of 10ps to 50ps, originated in the Bragg grating coupling coefficient profiles, which did not contain much apodization.

A mathematical model of the delay line which comprised eight 2mm long gratings, with 1mm inter-grating separations, was constructed. Using the 'tf' program the reflection response of the array was calculated for various different values of grating separation, linewidth and reflectivity. The comparison of the mathematical model reflection spectra with that of the experimental array allowed the most important resonance effects occurring within the grating array to be identified. Changing the grating linewidth from 1nm to 2nm had the most significant effect on the array reflection response, producing the grating spectra which most closely resembled those in the experimental array.

The performance of the discrete grating array time delay lines could be enhanced in several ways. Some apodisation of the coupling profile of the gratings could be included through the use of the phase mask fabrication technique, or by applying the simple apodisation scheme reported by *Kashyap et al*[195], hence reducing the small scale fluctuation on the individual grating delay profiles. The larger scale variations in the time delay profiles, visible at the extremes of the profile, can be wholly or partially removed, depending on the relative grating length and separation, by reducing any positioning errors, to within a few percent of the grating length, through improvements to the grating fabrication rig positioning system. Ideally, the fibre movement and the UV beam alignment should be carried out under computer control, by a system designed to remember the exact position of the previous grating. The grating linewidth should be maintained at 1nm or less in order to produce grating spectra which do not contain secondary resonance peaks, as indicated in 5.8.3.4. However, the inverse relationship between grating linewidth and length will always result in some degree of trade off between these two properties. To assist in minimising any secondary resonances which do occur, the gratings should all be fabricated with the same reflectivity, to within a few percent.

Using gratings with apodized coupling coefficient profiles, where the sidebands in the grating spectra have been suppressed, will also reduce the required wavelength separation between gratings, hence allowing the fabrication of a larger number of gratings within the available optical bandwidth, and improving the system resolution.

Whether a discrete grating array or a chirped grating should be used is determined by the application for which the delay line is intended. If very small time delays, of less than 10ps, are required, then for ease of fabrication and to minimise RF signal amplitude fluctuations, chirped gratings should be chosen as the time delay elements. However, for larger time delays, particularly those

greater than 60ps, it is most appropriate to utilise discrete grating arrays. For delays which lie between ~10ps and ~60ps, a discrete grating array can be used to produce an incremental delay, whilst a chirped grating should be chosen if a continuously tuneable time delay is required. It has also been shown that the fibre Bragg grating TTD elements are suitable for use with wide instantaneous bandwidth RF signals, and with pulsed RF signals.

Any further work on these fibre Bragg grating true time delay lines must commence with the implementation of the improvements to the fabrication process described above. Having completed this the fabrication of delay lines with a larger number of time delay bits can be attempted, in order to progress towards real phased array antenna system requirements. Control of a phased array antenna by fibre Bragg grating based true time delay demands the fabrication of many delay lines comprising wavelength identical arrays of gratings, but with different, accurately known, grating separations. To produce significantly longer continuously variable time delays an array of chirped gratings can be fabricated back-to-back in both physical space and wavelength space.

Once arrays containing a large number of gratings have been successfully fabricated they can be arranged into a control architecture in a test-bed RF phased array antenna. Beam steering through wavelength tuning the optical carrier can then be attempted, and the accuracy of the beam steering can then be investigated to determine the quality of the delay lines.

6. Conclusions

The work reported in this thesis can be arranged into three main parts: fibre Bragg grating fabrication; the application of fibre Bragg gratings as strain sensors in smart materials, with the associated development of a sensor signal demultiplexing scheme; and the application of fibre Bragg gratings as true time delay elements for the control of phased array antennas. The results obtained have been fully discussed in chapters 3, 4 and 5 respectively, and may be summarised as follows:

- Several arrays of uniform period Bragg gratings were successfully fabricated using the transverse holographic exposure technique: two arrays of four 5mm long gratings were produced with centre-to-centre separations of 5mm and 2.5mm respectively; and two arrays of 2mm long gratings were fabricated, in which the inter-grating separation was set at 2mm and 1mm. The spectral response of each array was recorded.

- Chirped fibre Bragg gratings were produced using the fibre deformation fabrication method, the first reported production of gratings using this technique, and had a chirp which varied quadratically with distance along the grating structure. A series of four 5mm long gratings were written in fibres of increasing curvature, resulting in chirps of between 2.9nm and 17.3nm.

- The effect of hydrogenation on the post exposure evolution of the Bragg wavelength of gratings written in three types of optical fibre was characterised.

- Four chirped gratings were fabricated using the method of dissimilar wavefronts, and their spectral characteristics recorded. Each grating was of length 4mm, and peak reflectivity ~60%, with chirps of 7nm, 12nm, 20nm and 30nm selected from a range of values regularly produced.

- The application of fibre Bragg gratings as strain sensors embedded within a sheet of carbon composite material was investigated, with sensitivity to applied strain and compression measured for both embedded and surface

mounted gratings. Excellent agreement of the experimental and theoretical results was achieved for strain applied to a surface mounted Fabry-Perot filter grating.

- A fibre Bragg grating sensor demultiplexing scheme based on a liquid crystal filled Fabry-Perot (LCFP) etalon tuneable transmission filter, capable, in principle, of interrogating many grating sensors, was proposed, successfully constructed and fully characterised.

- The LCFP etalon filter was found to have several limitations to its performance which severely affected its potential use as a wavelength selective tuneable transmission filter. The most significant limitation was posed by the temperature dependence of the resonance peak wavelength; measured to be -2.77nm/°C. The optical power transmission was found to be a non-constant function of the voltage amplitude applied to the liquid crystal, and at certain values of applied voltage the LCFP filter transmitted at more than one wavelength. These characteristics greatly reduced the available wavelength tuning range of the filter.

- Several approaches for overcoming the temperature dependence of the LCFP etalon were investigated, including methods for compensating for the temperature sensitivity within the system's computer control programme, and a method of controlling the temperature of the surrounding environment of the device. Limited wavelength measurement success was achieved using these methods.

- It was concluded that LCFP etalons filled with the liquid crystal E7, as used here, are not suitable for use as wavelength demultiplexing filters in a Bragg grating sensor system.

- The arrays of uniform period Bragg gratings reported above were constructed for use as true time delay elements for the control of phased array antennas, and the minimum time delay available with each array was measured. No work had previously been reported on this application of Bragg grating arrays, hence the measurement of arrays of 5mm long gratings took

the form of a demonstration that they could be used in this manner. Success was achieved and the work carried forward.

- A minimum time delay of 30.88ps was created using the arrays of 5mm long uniform period gratings, making them suitable for controlling phased array antennas operating at RF frequencies of up to 896MHz, with 10° phase resolution

- The 2mm long grating arrays comprised eight Bragg gratings, and as such were the first reported 3-bit fibre Bragg grating true time delay elements. These arrays were used to produce minimum time delays of 19.02ps and 9.09ps, for the 2mm and 1mm separations respectively, making them suitable for the control of phased array antennas, with 10° phase resolution, at frequencies of up to 1.44GHz and 3GHz.

- The chirped Bragg gratings produced using the dissimilar wavefronts fabrication technique, as described above, were utilized to create time delays of significantly smaller step size. A minimum time delay of 0.6ps was measured, with a maximum delay of 59ps available. All of the gratings were capable of producing 6-bit time delay control, and as such were suitable for the control of phased array antennas at frequencies of many tens of gigahertz, with 10° phase resolution. This work forms the first report of 6-bit fibre Bragg grating true time delay elements.

- The time delay profiles of the individual gratings within the arrays of 2mm long gratings were recorded, and were observed to contain some fluctuations. A mathematical model of the array of 2mm long gratings of 1mm centre-to-centre separation was constructed and used to identify the most significant resonance effects occurring within the array structure.

The results recorded in the experiments investigating the application of fibre Bragg gratings as strain sensors embedded within a sheet of carbon composite material indicated that incomplete strain transfer was occurring between the sheet and the embedded gratings, most probably caused by slippage of the fibre within the sheet due to incomplete bonding between the optical fibre and the

composite material. This highlighted the need to apply care when selecting the composite material to be used in each application, ensuring that its elastic properties are compatible with the type of strain to which it will be exposed. The excellent agreement of the experimental and theoretical values for the surface mounted fibre Fabry-Perot filter grating under strain supported the bending theory which was being applied.

The significant temperature dependence of the LCFP etalon resonance, -2.77nm/°C, required that in order to be able to measure the wavelength of a sensor signal to the required 0.1nm accuracy the temperature of the etalon must be held stable to better than 0.04°C. Although several different methods for minimising the effects of the LCFP temperature sensitivity were fully tested, the required temperature stability, for its successful application as a wavelength selective filter in a Bragg grating sensor system, could not be achieved. The variation of the transmitted optical power level with the amplitude of the voltage applied to the liquid crystal, due to the tuning characteristics of the resonance peaks relative to the source, erbium fluorescence, bandwidth rendered one third of the applied voltage tuning range unusable. In addition, at certain values of applied voltage more than one resonance peak existed within the source bandwidth, hence more than one wavelength could be transmitted by the LCFP etalon. The available tuning range of each resonance peak was therefore reduced from ~85nm to between 61nm and 65nm in order to ensure that only one wavelength signal was transmitted at any one voltage. Together, these three characteristics of the E7 filled LCFP etalon make its use as a Bragg grating sensor demultiplexing element impracticable. Further developments of the LCFP etalon based Bragg grating sensor demultiplexing system were proposed, and some of the necessary elements built and characterised. However, the success of these schemes is dependent on overcoming the temperature sensitivity of the LCFP etalon.

Since the completion of this work a novel liquid crystal filled fibre Fabry-Perot etalon filter has been reported by *Bao et al*[196] which has a 12nm tuning range

centred about 1550nm, a linewidth of ~0.07nm, and which can be accurately temperature controlled due to its small size. The filter is filled with liquid crystal type BDH764E, and can tune over its full range in <33μs. This device appears to offer several advantages over the LCFP etalon used here, including fibre compatibility, the ability to be temperature controlled, and significantly narrower linewidth and faster tuning; the LCFP etalon used here required ~1ms to settle between each applied voltage increment. Placed in the optical switch and transmitting chirped Bragg grating arrangement of Figure 4.31 this filter could be applied to the demultiplexing of large numbers of Bragg grating sensors. Another recent development in the demultiplexing of grating sensors has been reported by *Davis et al*[197] which can interrogate five arrays of twelve gratings, making a system total of 60 grating sensors. A tuneable fibre Fabry-Perot filter with a 45nm free spectral range and a measurement resolution of 0.7pm was used to wavelength demultiplex the 12 gratings in each array, with spatial division multiplexing, via optical switches, applied to increase the number of gratings which the system could interrogate.

The total amount of time delay required for a phased array antenna, and the desired time delay resolution, determines which type of Bragg grating delay line should be used in each application. For ease of fabrication, and minimisation of RF signal amplitude fluctuations, chirped gratings should be used when a minimum time delay of less than 10ps is called for. When larger time delays are required, particularly when the delay is to be in excess of 60ps, it is more appropriate to utilise arrays of discrete Bragg gratings. If the delay lies between these values then either approach may be used: an incremental delay can be produced by using a discrete grating array; while a continuously tuneable delay can be achieved through the use of a chirped grating. Since the completion of this work an extremely long chirped grating has been fabricated by *Kashyap et al*[198], which can be used to produce 13.5ns of time delay over a reflection bandwidth of 10nm. Applying the smallest wavelength tuning step available with the 1GHz experimental measurement system reported in 5.4.3.2, this grating can, in principle, be used to create 13.5ns of time delay with 27ps time

resolution, and would therefore be suitable for 8-bit time delay control of phased array antennas operating at frequencies of up to 1.03GHz, with 10° phase resolution. Although this grating offers a high total delay, the bandwidth needs to be increased considerably to be able to offer the same time delay resolution that was achieved with the chirped gratings reported here: the bandwidth must be increase to >29nm in order to produce time delays of ~9ps, equivalent to the best available using the discrete grating arrays; while an unattainably large bandwidth of ~900nm would be needed to create the 0.3ps time delays available with the chirped gratings reported here.

7. Appendices

7.1 Appendix A: Array Modelling

7.1.1 Linear gratings

```
@z = (0, 9e-3, 400000);
@lambda = (1492e-9, 1529e-9, 0.04e-9);

sub ShortGrating {
        my ($z, $period, $center, $length, $phase) =@_;
        TopHat (($z-$center)/$length)*Bragg ($z, $period, $phase);
}

sub n {
        my $z = shift
        return 1.5+0.4e-3*(ShortGrating ($z, 4.98066666e-7, 1e-3, 2e-3)+
                        ShortGrating ($z, 4.99766666e-7, 2e-3, 2e-3)+
                        ShortGrating ($z, 5.00366666e-7, 3e-3, 2e-3)+
                        ShortGrating ($z, 5.013e-7, 4e-3, 2e-3)+
                        ShortGrating ($z, 5.05166666e-7, 5e-3, 2e-3)+
                        ShortGrating ($z, 5.06033333e-7, 6e-3, 2e-3)+
                        ShortGrating ($z, 5.073e-7, 7e-3, 2e-3)+
                        ShortGrating ($z, 5.08233333e-7, 8e-3, 2e-3));
}
```

7.1.2 Chirped gratings

```
@z = (0, 9e-3, 400000);
@lambda = (1492e-9, 1529e-9, 0.04e-9);
use Math::Envelopes;
use Grating::Functions;

sub ShortGrating {
        my ($z, $period, $center, $length, $chirpfactor) =@_;
        TopHat (($z-$center)/$length)*Bragg ($z, $period+($z-$center)*$chirpfactor);
```

```
}

my $stopband = 1e-9;
my $n = 1.5;
my $length = 2e-3;
$chirpfactor = $stopband/(4*$n*$length);

sub n {
        my $z = shift
        return $n+0.4e-3*(ShortGrating ($z, 4.98066666e-7, 1e-3, $length, $chirpfactor)+
                          ShortGrating ($z, 4.99766666e-7, 2e-3, $length, $chirpfactor)+
                          ShortGrating ($z, 5.00366666e-7, 3e-3, $length, $chirpfactor)+
                          ShortGrating ($z, 5.013e-7, 4e-3, $length, $chirpfactor)+
                          ShortGrating ($z, 5.05166666e-7, 5e-3, $length, $chirpfactor)+
                          ShortGrating ($z, 5.06033333e-7, 6e-3, $length, $chirpfactor)+
                          ShortGrating ($z, 5.073e-7, 7e-3, $length, $chirpfactor)+
                          ShortGrating ($z, 5.08233333e-7, 8e-3, $length, $chirpfactor));
}
```

7.1.3 Chirped gratings and average refractive index

```
@z = (0, 9.5e-3, 400000);
@lambda = (1492e-9, 1530e-9, 0.1e-9);
use Math::Envelopes;
use Grating::Functions;

sub ShortGrating {
        my ($z, $period, $center) =@_;
        $z- = $center;
        my $env = TopHat ($z/$length)/2;
        $env+$env*Bragg($z, $period+$z*$chirpfactor);
}

my $stopband = 1e-9;
my $n = 1.5;
$length = 2e-3;
$chirpfactor = $stopband/(4*$n*$length);
```

```
sub n {
        my $z = shift
        return $n+0.4e-3*(ShortGrating ($z, 4.98066666e-7, 1e-3)+
                          ShortGrating ($z, 4.99766666e-7, 2e-3)+
                          ShortGrating ($z, 5.00366666e-7, 3.5e-3)+
                          ShortGrating ($z, 5.013e-7, 4.5e-3)+
                          ShortGrating ($z, 5.05166666e-7, 5.5e-3)+
                          ShortGrating ($z, 5.06033333e-7, 6e-3)+
                          ShortGrating ($z, 5.073e-7, 7.5e-3)+
                          ShortGrating ($z, 5.08233333e-7, 8.5e-3));
}
```

7.1.4 Chirped gratings, average refractive index, and varying reflectivities

```
@z = (0, 10.5e-3, 200000);
@lambda = (1492e-9, 1530e-9, 0.1e-9);
use Math::Envelopes;
use Grating::Functions;

sub ShortGrating {
        my ($z, $period, $center) =@_;
        $z- = $center;
        my $env = TopHat ($z/$length)/2;
        $env+$env*Bragg($z, $period+$z*$chirpfactor);
}

my $stopband = 1e-9;
my $n = 1.5;
$length = 2e-3;
$chirpfactor = $stopband/(4*$n*$length);

sub n {
        my $z = shift
        return $n+0.4e-3*(ShortGrating ($z, 4.98066666e-7, 1e-3)+
                        ShortGrating ($z, 4.99766666e-7, 2e-3)+
                        0.9*ShortGrating ($z, 5.00366666e-7, 3.5e-3)+
                        ShortGrating ($z, 5.013e-7, 4.5e-3)+
                        0.05*ShortGrating ($z, 5.03333333e-7, 5.5e-3)+
                        ShortGrating ($z, 5.05166666e-7, 5.5e-3)+
                        0.7*ShortGrating ($z, 5.06033333e-7, 7e-3)+
                        0.7*ShortGrating ($z, 5.073e-7, 8.5e-3)+
                        0.7*ShortGrating ($z, 5.08233333e-7, 9.5e-3));
}
```

7.2 Appendix B: LCFP control program

7.2.1 . Form

The window viewed by the user is constructed in a 'form' which has code associated with it to run the various devices in the window, such as the START button, the STOP button and the PRINT TO FILE button. The variables used in these code 'subroutines' (Sub) must be defined, and this is done in the *General Declarations* section of the form for variables which are used by more than one subroutine within it. The *Form_Load* subroutine is initiated when the program is loaded and it is here that the AIAO board is configured. The *BtnSearch_Click* subroutine initiates the LCFP voltage scan driven by the *TmerRampPeriod* subroutine. When the LCFP voltage scan is completed the *Scan_Finished* subroutine is called which scales, converts and normalises the experimental data, and then calls the *GetPeaks* subroutine, B3. To stop the voltage scan at any time the STOP button can be selected and this activates the code in the *BtnStop_Click* subroutine. When the program has, the LCFP voltage and photodiode voltage values stored by the program can be printed to file, for viewing through spreadsheet software, by selecting the PRINT TO FILE button which runs the code in the *PrintFile_Click* subroutine.

General declarations

```
'Declare ramp start and stop voltages as doubles
  Dim Volts As Double
  Dim StartVolt As Double, StopVolt  As Double, Stepsize As Double
  Dim PhotodiodeVolts As Double
  'define array so can use throughout the form
  Dim C As Integer
  Dim X As Integer
  Dim wlnorm() As Double, vnorm() As Double
  Dim lcfp As LCFPData
  Dim Tvolts As Double
```

```
Sub Form_Load ()
   Dim fname As String
   fname = GetPrivateProfileStr("Normalization", "Filename", "lcfpnorm.txt", config_fname)
   TBoxfname.Text = fname
   Call ReadLCFPData(fname, lcfp)
   LCFP_VtoLConvert lcfp, wlnorm(), vnorm()

   'Configure the NIDAQ board
   frmSearch.TBoxErrorCode.Text = Str$(AO_Configure(1, 0, 1, 0, 0, 0)) 'lcfp1 Vout
   frmSearch.TBoxErrorCode.Text = Str$(AI_Configure(1, 0, 1, 10, 1, 0)) 'lcfp1 photodiode input
   frmSearch.TBoxErrorCode.Text = Str$(AI_Configure(1, 1, 1, 10, 1, 0)) 'lcfp1 thermometer input
End Sub


Sub btnSearch_Click ()
   'convert (2-5)V input in textbox on settings form
   'to (0-9)V using the ConvertVoltage function
   'these variables are global to this form only
   StartVolt = ConvertVoltage(Val(TBoxStartVoltage.Text))
   StopVolt = ConvertVoltage(Val(TBoxStopVoltage.Text))
   Stepsize = (Val(TBoxStepsize.Text) * .001)

   'redeclare Voltages array
   C = ((StopVolt - StartVolt) / Stepsize) - 1
   ReDim Vout(C), Vpd(C), Thermometer(C)
   Volts = StartVolt  'first output value
   x = 0  'put first results in array element 0

   TimerRampPeriod.Enabled = True  'ramp voltage in TimerRamp Sub
End Sub


Sub TimerRampPeriod_Timer ()
   Dim status As Integer
   'read pd voltage; to start LCFP volts =2V always, if controller switched on
```

```
status = AI_VRead(1, 0, 1, PhotodiodeVolts)
If (status <> 0) Then TBoxErrorCode.Text = Str$(status)
'output voltage to controller
status = AO_VWrite(1, 0, Volts)
If (status <> 0) Then TBoxErrorCode.Text = Str$(status)
'read temperature
status = AI_VRead(1, 1, 1, Tvolts) 'read in voltage from lcfp1 thermometer
If (status <> 0) Then TBoxErrorCode.Text = Str$(status)

If (x Mod 10) = 0 Then 'update display
   TBoxPhotodiode.Text = Str$(PhotodiodeVolts)
   TBoxBoardOutput.Text = Str$(Volts)
   TBoxCircuitOutput.Text = Str$(InvertConvertVoltage(Volts))
End If

'store Volts, PhotodiodeVolts and Tvolts in arrays
Vout(x) = Volts
Vpd(x) = PhotodiodeVolts
Thermometer(x) = Tvolts

'increment the voltage output
Volts = Volts + Stepsize
If x = C Then
   TimerRampPeriod.Enabled = False
   ScanFinished 'searches for peaks and displays results
End If
'move to next elements in arrays
x = x + 1
End Sub


Sub ScanFinished ()
'called at end of LCFP voltage scan
'scales and converts experimental data
'then normalises experimental data
'then finds peaks in experimental data
```

```
Dim LCFPTemp As Double, value As Currency, D As Double, T As Double, j As Integer, n As Integer
T = 0
For j = 0 To C
   T = T + Thermometer(j)
Next j
n = C + 1
D = (T / n)
LCFPTemp = (D * VtoT_m) + VtoT_c
value = LCFPTemp
TBoxLCFPTemp.Text = Str(value)

'construct, scale and convert exptl results
LCFPConstruct LCFPTemp, Vout(), Vpd(), lcfp  'read exptl data into d_exptl
Call SaveData("c:\tmp\exptlv2.txt", Vout(), Vpd())
LCFP_VtoLConvert lcfp, Vout(), Vpd()
Call SaveData("c:\tmp\exptll2.txt", Vout(), Vpd())

'scale and convert normalisation data to active temperature

Call SaveData("c:\tmp\norml2.txt", wlnorm(), vnorm())
Normalise wlnorm(), vnorm(), Vout(), Vpd()
Call SaveData("c:\tmp\exptln2.txt", Vout(), Vpd())

'peak search
Dim peaks() As Double, i As Integer
GetPeaks Vout(), Vpd(), peaks()
lstPeaks.Clear
For i = 0 To UBound(peaks)
   lstPeaks.AddItem Str$(peaks(i))
Next i
End Sub


Sub btnStop_Click ()
   TimerRampPeriod.Enabled = False
```

```
    frmSearch.TBoxErrorCode.Text = Str$(AO_VWrite(1, 0, 0))
    frmSearch.TBoxBoardOutput.Text = ""
    frmSearch.TBoxCircuitOutput.Text = ""
End Sub


Sub PrintFile_Click ()
    CMDialog.Flags = &H2&
    CMDialog.CancelError = True
    On Error GoTo Oops
    CMDialog.Action = 2
    Dim i As Integer
    Dim fnum As Integer
    fnum = FreeFile
    Dim fname As String
    fname = CMDialog.Filename
    Call SaveData(fname, Vout(), Vpd())
    GoTo Penultimate
Oops:
    Resume Penultimate:
Penultimate:
End Sub
```

7.2.2 . LCFPData code module

In the general declarations section of this code module the constants used by the program are defined and a 'user-defined-type', *LCFPData*, is declared which the experimental values are converted into for ease of processing by the program, and they are entered into an array called *dexptl* by the *LCFP_Construct* subroutine. The photodiode voltage values are converted to wavelength by the *VtoL_Convert* subroutine, before they are processed to find the peaks, and the normalisation data is read in with the *ReadLCFPData* subroutine.

General Declarations

```
'constants for T/V(recorded for l=1550nm) and V/l(recorded at T=23.43C) conversion equations
  Global Const temp_m = .2601
  Global Const temp_c = .616
  Global Const lambda_m = -10.532
  Global Const lambda_c = 1580
  Global Const ref_temp = 19.55
  Global Const ref_wavelength = 1550
  Global Const VtoT_m = 10.428
  Global Const VtoT_c = -.7737


' define user defined type for experimental data
Type LCFPData
  Temperature As Double
  N As Integer
  LCFPVariable(1023) As Double   'Vout or LCFPwavelength
  Vpd(1023) As Double
End Type


Sub LCFPConstruct (T As Double, Vout() As Double, Vpd() As Double, 'reads Vout, Vpd, Temp and
number_elements into d_exptl
d_exptl As LCFPData)
  d_exptl.Temperature = T
  d_exptl.N = UBound(Vout) + 1
  Dim i As Integer
    For i = 0 To d_exptl.N - 1
      d_exptl.LCFPVariable(i) = Vout(i)
      d_exptl.Vpd(i) = Vpd(i)
    Next i
End Sub


Sub LCFP_VtoLConvert (src As LCFPData, wl() As Double, sig() As Double)
```

```
'convert voltage data into wavelength at reference temp 19.55C
'src is voltage data, wl is wavelength converted data, sig is photodiode volts
ReDim wl(src.N - 1) As Double, sig(src.N - 1) As Double
Dim dv As Double
dv = Vshift(src.Temperature)
Dim i As Integer
For i = 0 To src.N - 1
   wl(i) = LCFP_VtoLFn(src.LCFPVariable(i) - dv)'LCFPVariable is wavelength here
   sig(i) = src.Vpd(i)
Next i
ReverseArray wl()
ReverseArray sig()
End Sub

Function LCFP_VtoLFn (d As Double) As Double
'voltage to wavelength conversion function
   LCFP_VtoLFn = (lambda_m * d) + lambda_c
End Function

Function LCFPConst (TempVolt As Double) As Double
'calculating constant in voltage/wavelength equation for given temperature
   LCFPConst = ref_wavelength + (-lambda_m * TempVolt)
End Function

Function LCFPTempVolt (d As LCFPData) As Double
'converting experimental data to same temperature scale as reference/equation data
   LCFPTempVolt = (temp_m * d.Temperature) + temp_c
End Function

Sub ReadLCFPData (fname As String, d_exptl As LCFPData)
   'to read in normalisation data
   Dim fh As Integer, i As Integer
```

```
  fh = FreeFile
  Open fname For Input As fh
  Input #fh, d_exptl.Temperature
  Input #fh, d_exptl.N
  For i = 0 To d_exptl.N - 1
     Input #fh, d_exptl.LCFPVariable(i), d_exptl.Vpd(i)
  Next i
  Close fh
End Sub
```

7.2.3 . Psearch.Bas code module

This code module contains the peak search subroutine *GetPeaks,* and the subroutine for normalising the photodiode voltages, *Normalise.* The subroutine *ReverseArray* which reverses the order of the elements in an array is also located in this module.

General declarations

```
Global Vout() As Double, Vpd() As Double, norm() As Double, Thermometer() As Double
Global Const config_fname = "lcfp.ini"
Const MaxNoPeaks = 20
Const thresh_low = .1
Const thresh_high = .2
```

```
Sub GetPeaks (x() As Double, y() As Double, xpeaks() As Double)
   'finds peaks in data
   ReDim xpeaks(MaxNoPeaks)
   Dim n As Integer, i As Integer, ymax As Double, ythresh As Double
   n = UBound(x)
   ymax = y(0)
   For i = 1 To n
      If y(i) > ymax Then ymax = y(i)
   Next i
   ythresh_low = thresh_low * ymax
   ythresh_high = thresh_high * ymax
```

```
  Dim ipeak As Integer, pmode As Integer, imax As Integer
  ipeak = 0
  pmode = False
  For i = 0 To n - 1
    If pmode Then ' Inside a peak
      If y(i) > ymax Then ' if a bigger value store it as peak
        imax = i
        ymax = y(imax)
      End If
      If y(i) > ythresh_high And y(i + 1) <= ythresh_high Then ' move to outside peak mode, storing the
peak
        pmode = False
        xpeaks(ipeak) = x(imax)
        Debug.Print "wl=", x(imax), "Vpd=", y(imax)
        ipeak = ipeak + 1
      End If
    Else 'outside a peak
      If y(i) <= ythresh_low And y(i + 1) > ythresh_low Then ' move to inside peak mode
        imax = i + 1
        ymax = y(imax)
        pmode = True
      End If
    End If
  Next I
End Sub


Sub Normalise (xnorm() As Double, ynorm() As Double, x() As Double, y() As Double)
'takes in norm data, xnorm() and ynorm(), and measurement data, x() and y()
'outputs normalised measurement data in x() and y()
  Dim i As Integer, inorm As Integer, n As Integer, nnorm As Integer
  Dim m As Double, z() As Double
  i = 0
  inorm = 0
  n = UBound(x)
  nnorm = UBound(xnorm)
```

```
' set all values of y() outside the normalisation data range to zero
While x(i) < xnorm(inorm)
   y(i) = 0
   i = i + 1
Wend
While x(n) > xnorm(nnorm)
   y(n) = 0
   n = n - 1
Wend

ReDim z(n) As Double
'z(i) is value of ynorm at x(i)
For i = 0 To n
   If (inorm < nnorm) Then
      While (x(i) > xnorm(inorm + 1))
         inorm = inorm + 1
      Wend
   End If
   m = (ynorm(inorm + 1) - ynorm(inorm)) / (xnorm(inorm + 1) - xnorm(inorm))
   z(i) = ynorm(inorm) + m * (x(i) - xnorm(inorm))
   y(i) = y(i) / z(i)
Next i
End Sub


Sub ReverseArray (a() As Double)
'reverses order of elements in array
   Dim n As Integer, i As Integer, dummy As Double
   n = UBound(a)
   For i = 0 To n / 2
      dummy = a(i)
      a(i) = a(n - i)
      a(n - i) = dummy
   Next i
End Sub
```

8. Publications

1. K.Sugden, I.Bennion, A.Molony, N.J.Copner, 'Chirped gratings produced in photosensitive optical fibre by fibre deformation during exposure', *Electron.Lett.*, **30**, 1994, pp.440-442

2. M.C.Farries, K.Sugden, D.C.J.Reid, I.Bennion, A.Molony, M.J.Goodwin, 'Very broad reflection bandwidth (44nm) chirped fibre gratings and narrow bandpass filters produced by the use of an amplitude mask', *Electron.Lett.*, **30**, 1994, pp. 891-892

3. K.Sugden, I.Bennion, A.Molony, M.C.Farries, D.C.J.Reid, M.J.Goodwin, 'Fabrication and properties of chirped fibre gratings with reflection bandwidths exceeding 50nm and narrow bandpass fibre grating filters', *CLEO Europe*, Amsterdam, Netherlands, 1994, Tech. Dig. CWF57

4. L.Zhang, K.Sugden, I.Bennion, A.Molony, 'Wide stopband chirped fibre Moire grating transmission filters', *Electron.Lett.*, **31**, 1995, pp. 477-479

5. A.Molony, I.Bennion, J.Fells, C.Edge, 'Fibre Bragg grating delay lines for the control of phased array antennas', Institute of Physics Meeting on *In-Fibre Bragg Gratings and Special Fibres*, London, 24 May 1995

6. A.Molony, C.Edge, I.Bennion, 'Fibre grating time delay element for phased array antennas', *Electron.Lett.*, **31**, 1995, pp. 1485-1486

7. A.Molony, L.Zhang, J.A.R.Williams, I.Bennion, C.Edge, J.Fells, 'Fibre Bragg grating time delay control of phased array antenna systems', *12th UK National Quantum Electronics Conf.*, Southampton, 4-8 September 1995, Tech. Dig., pp P3-34

8. A.Molony, L.Zhang, J.A.R.Williams, I.Bennion, C.Edge, J.Fells, 'Fibre Bragg grating time delay control of phased array antennae', *Journal of Modern Optics*, **43**, 1996, pp.1017-1024

9. A.Molony, L.Zhang, J.A.R.Williams, I.Bennion, C.Edge and J.Fells, 'Fibre Bragg grating networks for true time delay control of phased array antennas', *Canterbury Workshop on Microwave and Millimetre-Wave Optoelectronics,* Canterbury, 25th March 1996

10. A.Molony, L.Zhang, J.A.R.Williams, I.Bennion, C.Edge and J.Fells, 'Fibre Bragg grating networks for time-delay control of phased-array antennas', *Conf. Lasers and Electro-Optics,* Anaheim, U.S.A., 2-7 June 1996, Tech. Dig., pp. 244-245

11. A.Molony, L.Zhang, J.A.R.Williams, I.Bennion, C.Edge and J.Fells, 'Fibre Bragg grating True Time Delay control of Phased Array Antennas: discrete grating array 3-bit delay lines and chirped grating 6-bit delay lines', *IEEE Trans. Microwave Theory and Techniques: Microwave and Millimeter-Wave Photonics II,* submitted for publication August 1997.

9. References

[1] K.O.Hill, Y.Fujii, D.C.Johnson and B.S.Kawasaki, 'Photosensitivity in optical fibre waveguides: application to reflection filter fabrication', *Appl. Phys. Lett.*, **32**, 1978, pp.647-649

[2] W.W.Morey, G.Meltz and W.H.Glenn, 'Fiber optic Bragg grating sensors', *SPIE Fiber Optic and Laser Sensors VII*, **1169**, 1989, pp.98-107

[3] G.Meltz, W.W.Morey and W.H.Glenn, 'Formation of Bragg gratings in optical fibers by a transverse holographic method', *Opt. Lett.*, **14**, 1989, pp.823-825

[4] K.O.Hill, B.Malo, F.Bilodeau, D.C.Johnson and J.Albert, 'Bragg gratings fabricated in monomode photosensitive optical fibre by UV exposure through a phase mask', *Appl. Phys. Lett.*, **62**, 1993, 1035-1037

[5] I.Bennion, D.C.J.Reid, C.J.Rowe and W.J.Stewart, 'High-reflectivity monomode-fibre grating filters', *Electron. Lett.*, **22**, 1986, pp.341-343

[6] C.M.Ragdale, D.C.J.Reid and I.Bennion, 'Fiber grating devices', *SPIE Fiber laser Sources and Amplifiers*, **1171**, 1989, pp.148-156

[7] D.L.Williams, B.J.Ainslie, J.R.Armitage, R.Kashyap and R.Campbell, 'Enhanced UV photosensitivity in boron codoped germanosilicate optical fibres', *Electron. Lett.*, **29**, 1993, pp.45-47

[8] P.J.Lemaire, R.M.Atkins, V.Mizrahi and W.A.Reed, 'High pressure H_2 loading as a technique for achieving ultrahigh UV photosensitivity and thermal sensitivity in GeO_2 doped optical fibres', *Electron. Lett.*, **29**, 1993, pp.1191-1193

[9] M.C.Farries, C.M.Ragdale and D.C.J.Reid, 'Broadband chirped fibre Bragg filters for pump rejection and recycling in erbium doped fibre amplifiers', *Electron. Lett.*, **28**, 1992, 487-489

[10] Livanos,A.C., Katzir, A., and Yariv, A., 'Fabrication of grating structures with variable period', *Opt. Comms.*, **20**, 1977, pp.179-182

[11] K.C.Byron, K.Sugden, T.Bricheno and I.Bennion, 'Fabrication of chirped gratings written holographically in optical fibre tapers', *Electron. Lett.*, **29**, 1993, 1695-1660

[12] R.Kashyap, S.V.Chernikov, P.F.Mckee and J.R.Taylor, '30ps chromatic compensation of 400fs pulses at 100Gbit/s in optical fibre using an all fibre photoinduced chirped reflection grating', *Electron. Lett.*, **30**, 1994, 1078-1080

[13] M.C.Farries, K.Sugden, D.C.J.Reid, I.Bennion, A.Molony and M.J.Goodwin, 'Very broad reflection bandwidth (44nm) chirped fibre gratings and narrow bandpass filters produced by the use of an amplitude mask', *Electron. Lett.*, **30**, 1994, 891-892

[14] K.Sugden, 'Fabrication and applications of fibre Bragg gratings', 1996, PhD thesis, pp.67-82

[15] D.Garthe, R.E.Epworth, W.S.Lee, A.Hafjifotiou, C.P.Chew, T.Bricheno, A.Fielding, H.N.Rourke, S.R.Baker, K.C.Byron, R.S.Baulcomb, S.M.Ohja and S.Clements, 'Adjustable dispersion equaliser for 10 and 20Gbit/s over distances up to 160km', *Electron. Lett.*, **30**, 1994, pp.2159-2160

[16] M.LeBlanc, S.Y.Huang, M.M.Ohn and R.M.Measures, 'Tuneable chirping of a fibre Bragg grating using a tapered cantilever bed', *Electron. Lett.*, **30**, 1994, 2163-2165

[17] A.Seeds, 'Optical Technologies for phased array antennas', *IEICE Trans. Electron.*, **E76-C**, 1993, pp.198-206

[18] I.Frigyes and A.Seeds, 'Optically generated true-time delay in phased-array antennas', *IEEE Trans. Microwave Theory and Techniques*, **43**, 1995, pp.2378-2386

[19] A.P.Goutzoulis, D.K.Davies and J.M.Zomp, 'Prototype binary fiber optic delay line', *Opt. Eng.*,**28**, 1989, pp.1193-1202

[20] A.P.Goutzoulis and D.K.Davies, Hardware-compressive 2-D fiber optic delay line architecture for time steering of phased-array antennas, *Appl. Opt.*, 29,1990 , pp 5353-5359

[21] A.P.Goutzoulis, D.K.Davies andJ.M.Zomp, 'Hybrid electronic fiber optic wavelength-multiplexed system for true time-delay steering of phased array antennas', *Opt. Eng.*, 31, 1992, pp.2312-2322

[22] D.T.K.Tong and M.C.Wu, 'A novel multiwavelength optically controlled phased array antenna with a programmable dispersion matrix', *IEEE Photon. Technol. Lett.*, 8, 1996, pp.812-814

[23] W.Ng, A.Walston, G.Tangonan, I.Newberg, and J.J.Lee, 'Wideband fibre-optic delay network for phased array antenna steering', *Electron. Letts.*, 25, 1989, pp.1456-1457

[24] W.Ng, A.Walston, G.Tangonan, I.Newberg and J.J.Lee, 'Laser-switched wideband fiber optic delay network for phased array antenna steering', *Conf. Optical Fibre Communication*, 1990, Tech. Dig., pp.80-81

[25] W.Ng, A.Walston, G,Tangonan, J.J.Lee, and I.Newberg, 'Optical steering of dual band microwave phased array antenna using semiconductor laser switching', *Electron. Lett.*, 26, 1990, pp791-792

[26] W.Ng, A.A.Walston, G.L.Tangonan, J.J.Lee, I.L.Newberg, and N.Bernstein, 'The first demonstration of an optically steered microwave phased array antenna using true-time-delay', *J. Lightwave Technol.*, 9, 1991, pp 1124-1131

[27] W.Ng, A.Walston, G.Tangonan, J.J.Lee, and I.Newberg, 'Optical steering of dual band microwave phased array antenna using semiconductor laser switching', *Electron. Letts.*, 26, 1990, pp.791-793

[28] W.Ng, A.Walston, G.Tangonan, I.Newberg, and J.J.Lee, 'Laser-switched wideband fiber optic delay line for phased array antenna steering', *Conf. Optical Fibre Communication*, 1990, Tech. Dig., pp.80-81

[29] R.Y.Loo, G.L.Tangonan, H.W.Yen, J.J.Lee, V.L.Jones and J.Lewis, '5 bit photonic time shifter for wideband arrays', *Electron. Letts.*, 31, 1995, pp.1532-1533

[30] J.J.Lee, R.Y.Loo, S.Livingston, H.W.Yen and G.Tangonan, 'Conformal array controlled by photonics', *Electron. Letts.*, 31, 1995, pp.1620-1621

[31] R.D.Esman, M.J.Monsma, J.L.Dexter and D.G.Cooper, 'Microwave true time-delay modulator using fibre-optic dispersion', *Electron. Lett.*, 28,1992, pp1905-1907

[32] D.Norton, S.Johns, C.Keefer and R.Soref, 'Tunable microwave filtering using high dispersion fiber time delays', *Photon. Technol. Lett.*, 6, 1994, pp831-832

[33] R.D.Esman, M.Y.Frankel, J.L.Dexter, L.Goldberg, M.G.Parent, D.Stilwell, and D.G.Cooper, 'Fiber-optic prism true time-delay antenna feed', *Photon. Technol. Lett.*, 5, 1993, pp1347-1349

[34] M.Y.Frankel, R.D.Esman, and M.G.Parent, 'Array transmitter/receiver controlled by a true time-delay fiber-optic beamformer', *Photon. Technol. Lett.*, 7, 1995, pp.1216-1218

[35] M.Y.Frankel, R.D.Esman and M.G.Parent, 'Fiber-optic true-time-delay control of an array antenna', *Conf. Optical Fibre Communication*, 1995, Tech. Dig., pp.125-127

[36] M.Y.Frankel and R.D.Esman, 'True time-delay fiber-optic control of an ultrawide array transmitter/receiver with multibeam capability', *IEEE Trans. Microwave Theory and Techniques*, 43, 1995, pp. 2387-2394

[37] X.S.Yao and L.Maleki, 'A novel 2-D programmable photonic time-delay device for millimetre-wave signal processing applications', *Photon. Technol. Lett.*, 6, 1994, pp.1463-1465

[38] L.Eldada, R.Scarmozzino, R.M.Osgood, D.C.Scott, Y.Chang and H.R.Fetterman, 'Laser-Fabricated delay lines in GaAs for optically steered phased-array radar', *J.Lightwave Technol.*, 13, 1995, pp.2034-2039

[39] K.Horikawa, Y.Nagasuga and H.Ogawa, 'Self-Heterodyning optical waveguide beam forming and steering network integrated on Lithium Niobate substrate', IEEE Transactions on microwave theory and techniques, 43, 1995, 2395-2401

[40] L.J.Lembo, T.Holcomb, M.Wickham, P.Wisseman and J.C.Brock, 'Low-loss fiber optic time-delay element for phased-array antennas', *SPIE*, **2155**, 1994, pp.13-23

[41] F.Farahi and D.A.Jackson, 'Temperature and strain sensing using monomode optical fibre', *SPIE Fiber Optic Sensors: Engineering and Applications*, **1511**, 1991, pp.234-243

[42] P.Akhavan Leilabady, J.D.C.Jones and D.A.Jackson, 'Interferometric strain measurement using optical fibers', *SPIE-Int. Soc. Opt. Eng.*, **486**, pp.230, 1985

[43] P.G.Kazansky, P.St.J.Russell and C.N.Pannell, 'Optical fibre electrets and electro-acousto-optic transduction', *Conf. Optical Fibre Sensors*, 1994, Tech. Dig., pp.12-15

[44] F.Bucholtz, C.A.Villarruel, C.K.Kirkendall, D.M.Dagenais, J.A.McVicker, A.R.Davis, S.S.Partick, K.P.Koo, A.Dandridge, G.Wang, T.Lund and H.Valo, 'Eight element array for three-axis fiber optic magnetometers for undersea applications', *Conf. Optical Fibre Sensors*, 1994, Tech. Dig., pp.36-39

[45] Y.J.Rao and D.A.Jackson, 'Minitature fibre-optic-based interferometric medical pressure and temperature sensor system', *Conf. Optical Fibre Sensors*, 1994, Tech. Dig., pp.67-70

[46] I.P.West, R.Holmes and G.R.Jones, 'Optical fibre based pulse oximeter for monitoring in magnetic resonance scanners', *Conf. Optical Fibre Sensors*, 1994, Tech. Dig., pp.94-97

[47] W.W.Morey, J.R.Dunphy and G.Meltz, 'Muliplexing fibre Bragg grating sensors', *Fiber and Integrated Optics*, **10**, 1991, pp.351-360

[48] S.M.Melle, K. Liu, and R.M.Measures, 'Strain sensing using a fibre optic Bragg grating', *SPIE Fiber Optic Smart Structures and Skins IV*, **1588**, 1991, pp.255-263

[49] L.E.Giesler, J.R.Dunphy, W.W.Morey, G.Meltz and W.Glenn, 'Instrumentation concepts for multiplexed Bragg grating sensors', *SPIE Sensors and Sensor Integration*, **1480**, 1991, pp.138-141

[50] A.Dandridge and A.D.Kersey, 'Muliplexed interferometric fiber sensor arrays', *SPIE Distributed and Multiplexed Fiber Optic Sensors*, **1586**, 1991, pp.176-182

[51] A.D.Kersey and T.A.Berkoff, 'Interferometric signal processing for strain and vibration sensing using two-mode and Bragg grating fiber sensors', *SPIE Conf. Active Materials and Adaptive Structures*, 1992, Tech. Dig., pp.651-657

[52] R.S.Weis, A.D.Kersey and T.A.Berkoff, 'A four element fiber grating sensor array with phase-sensitive detection', *IEEE Photon. Technol. Lett.*, **6**, 1994, pp.1469-1472

[53] T.A.Berkoff and A.D.Kersey, 'Eight element time-division multiplexed fiber grating sensor array with integrated-optic wavelength discriminator', *Conf. Smart Structure and Materials*, 1994, Tech. Dig., pp.350-353

[54] M.A.Davis and A.D.Kersey, 'Fiber fourier transform spectrometer for decoding Bragg grating sensors', *Conf. Optical Fibre Sensors*, 1994, Tech. Dig., pp.167-170

[55] M.A.Davis and A.D.Kersey, 'Application of a fiber fourier transform spectrometer to the detection of wavelength-encoded signals from Bragg grating sensors', *J. Lightwave Technol.*, **13**, 1995, pp.1289-1295

[56] Y.J.Rao, K.Kalli, G.Brady, D.J.Webb, D.A.Jackson, L.Zhang and I,Bennion, 'Spatially-mulitplexed fibre-optic Bragg grating strain and temperature sensor system based on interferometric wavelength-shift detection', *Electron, Lett.*, **31**, 1995, pp.1009-1010

[57] Y.J.Rao, D.A.Jackson, L.Zhang and I.Bennion, 'Strain sensing of modern composite materials with a spatial/wavelength-division multiplexed fiber grating network', *Opt. Lett.*, **21**, 1996, pp.683-685

[58] Y.J.Rao and D.A.Jackson, 'Universal fiber-optic point sensor system for quasi-static absolute measurements of multiparameters exploiting low coherence interrogation', *J. Lightwave Technol.*, **14**, 1996, pp. 592-599

[59] S.M.Melle, K.Liu and R.M.Measures, 'A passive wavelength demodulation system for guided-wave Bragg grating sensors', *IEEE Photon. Technol. Lett.*, **4**, 1992, pp.516-518

[60] S.M.Melle, K. Liu, and R.M.Measures, 'Strain sensing using a fibre optic Bragg grating', *SPIE Fiber Optic Smart Structures and Skins IV*, **1588**, 1991, pp.255-263

[61] M.A.Davis and A.D.Kersey, 'All-fibre Bragg grating strain-sensor demodulation technique using a wavelength division coupler', *Electron. Lett.*, **30**, 1994, pp.75-77

[62] Q.Zhang, D.A.Brown, H.Kung, J.E.Townsend, M.Chenm L.J.Reinhart and T.F.Morse, 'Use of highly overcoupled couplers to detect shifts in Bragg wavelength', *Electron. Lett.*, **31**, pp.480-482

[63] A.B.Lobo Ribeiro, L.A.Ferreira, M.Tsvetkov and J.L Santos, 'All-fibre interrogation technique using a biconical fibre filter', *Electron. Lett.*, **32**, 1996, pp.382-383

[64] A.D.Kersey and W.W.Morey, 'Multiplexed Bragg grating fibre-laser strain-sensor system with mode-locked interrogation', *Electron. Lett.*, **29**, 1993, pp.112-114

[65] G.A.Ball, W.W.Morey and P.K.Cheo, 'Single- and Multipoint fiber-laser sensors', *IEEE Photon. Technol. Lett.*, **5**, 1993, pp.267-270

[66]K.P.Koo and A.D.Kersey, 'Bragg grating-based laser sensors systems with interferometric interrogation and wavelength division multiplexing', *J. Lightwave Technol.*, **13**, 1995, 1243-1249

[67] K.P.Koo and A.D.Kersey, 'Fibre laser sensor with ultrahigh strain resolution using interferometric interrogation', *Electron. Lett.*, **31**, 1995, pp.1180-1182

[68] K.P.Koo and A.D.Kersey, 'Fiber laser sensor system with interferometric read-out and wavelength multiplexing', *Conf. Optical Fibre Sensors*, 1994, Tech. Dig., pp.331-334

[69] G.A.Ball, W.W.Morey and P.K.Cheo, 'Fiberlaser source/analyzer for Bragg grating sensor array interrogation', *J.Lightwave Technol.*, **12**, 1994, pp.700-703

[70] M.G.Xu, H.Geiger, J.L.Archambault, L.Reekie and J.P.Dakin, 'Novel interrogating system for fibre Bragg grating sensors using an acousto-optic tunable filter', *Electron. Lett.*, **29**, 1993, pp.1510-1511

[71] H.Geiger, M.G.Xu, N.C.Eaton and J.P.Dakin, 'Electronic tracking system for multiplexed fibre grating sensors', *Electron. Lett.*, **31**, 1995, pp.1006-1007

[72] M.Volanthen, H.Geiger, M.G.Xu and J.P.Dakin, 'Simultaneous monitoring of multiple fibre gratings with a single acousto-optic tunable filter', *Electron. Lett.*, **32**, 1996, pp.1228-1229

[73] M.G. Xu, H.Geiger and J.P.Dakin, 'Modeling and performance analysis of a fiber Bragg grating interrogation system using an acousto-optic tunable filter', *J. Lightwave Technol.*, **14**, 1996, pp.391-396

[74] T.Coroy, P.J.Ellerbrock, R.M.Measures and J.H.Belk, 'Active wavelength demodulation of Bragg fibre-optic strain sensor using acousto-optic tunable filter', *Electron. Lett.*, **31**, 1995, pp.1602-1603

[75] D.A.Jackson, A.B.Lobo Ribeiro, L.Reekie and J.L Archambault, 'Simple multiplexing scheme for a fiber-optic grating sensor network', *Opt. Lett.*, **18**, 1993, pp.1192-1194

[76] M.A.Davis and A.D.Kersey, 'Matched-filter interrogation technique for fibre Bragg grating arrays', *Electron. Lett.*, **31**, 1995, pp.822-823

[77] A.D.Kersey, T.A.Berkoff and W.W.Morey, 'Multiplexed fiber Bragg grating strain-sensor system with a fiber Fabry-Perot wavelength filter', *Opt. Lett.*, **18**, 1993, pp.1370-1372

[78] K.Hirabayashi and T.Kurokawa, 'Tunable wavelength-selective demultiplexer using a liquid-crystal filter', *IEEE Photon. Technol. Lett.*, **4**, 1992, pp.737-740

[79] K.Hirabayashi, H.Tsuda and T.Kurokawa, 'Tunable liquid-crystal Fabry-Perot interferometer filter for wavelength-division multiplexing communication systems', *J.Lightwave Technol.*, **11**, 1993. pp.2033-2043

[80] R.M.Measures, 'Smart structures with nerves of glass', *Progress in Aerospace Sciences*, 26, 1989, pp.289-351.

[81] E.J.Friebele and A.D.Kersey, 'Fiberoptic sensors measure up for smart structures', *Laser Focus World*, May 1994, pp.165-212.

[82] B.Mason, D.Hogg and R.M.Measures, 'Fiber optic sensing for smart adaptive structures', *First European Conf. Smart Structures and Materials, Glasgow*, 1992, Tech. Dig., pp.135-138

[83] R.M.Measures, 'Advances toward fiber optic based smart structures', *Opt. Eng.*, 31. 1992, pp.34-47

[84] E.Udd, 'Fiber optic smart structures for aerospace applications', *First European Conf Smart Materials and Structures, Glasgow*, 1992, Tech. Dig., pp.7-12

[85] W.C.Michie, B.Culshaw, S.S.J.Roberts and R.Davidson, 'Fibre optic techniques for simutaneous measurement of strain and temperature variations in composite materials', SPIE Fiber Optic Smart Structures and Skins IV, 1588, 1991, pp.342-355

[86] H.D.Simonsen, R.Paetsch and J.R.Dunphy, 'Fiber Bragg grating sensor demonstration in glass-fiber reinforced polyester composite', *First European Conf. Smart Structures and Materials, Glasgow*, 1992, Tech. Dig., pp.73-76

[87] R.M.Measures, T.Alavie, R.Maaskant, S.Huang and M.LeBlanc, 'Bragg grating fiber optic sensing for bridges and other structures', *Second European Conf. Smart Structures and Materials, Glasgow*, 1994, Tech. Dig., pp.162-167

[88] I.Bennion, J.A.R.Williams, L.Zhang, K.Sugden and N.J.Doran, 'UV-written in-fibre Bragg gratings', *Opt. Quantum. Electron.*, **28**, 1996, pp.93-135

[89] D.K.Lam and B.K.Garside, 'Characterisation of single-mode optical fibre filters', *Appl. Opt.*, 20, 1991, pp.440-445

[90] G.P.Agrawal, *Nonlinear Guided Optics*, 2nd Ed., Academic Press, San Diego, 1995, pp.451-456

[91] K.O.Hill, 'Aperiodic distributed parameter waveguides for integrated optics', *Appl. Opt.*, 13, 1974, pp.1853-1856

[92] M.Matsuhara and K.O.Hill, 'Optical-waveguide band rejection filters: design', *Appl. Opt.*, 13, 1974, pp.2886-2888

[93] H.Kogelnik, 'Filter response of non-uniform almost-periodic structures', *Bell Syst. J.*, 55, 1976, pp.109-127

[94] W.W.Morey, G.Meltz and W.H.Glenn, 'Fiber optic Bragg grating sensors', *SPIE Fiber Optic and Laser Sensors VII*, **1169**, 1989, pp.98-107

[95] G.Meltz, W.W.Morey and W.H.Glenn, 'Formation of Bragg gratings in optical fibers by a transverse holographic method', *Opt. Lett.*, **14**, 1989, pp.823-825

[96] R.J.Campbell and R.Kashyap, 'Spectral profile and multiplexing of Bragg gratings in photosensitive fiber', *Opt. Lett.*, **16**, 1991, pp.898-900

[97] D.P.Hand and P.St.J.Russell, 'Photoinduced refractive-index changes in germanosilicate fibers', *Opt. Lett.*,**15**, 1990, pp.102-104

[98] P.S.Cross and H.Kogelnik, 'Sidelobe suppression in corrugated-waveguide filters', Opt. Lett., 1, 1977,pp.43-45

[99] A.C.Livanos, A.Katzir, and A.Yariv, 'Fabrication of grating structures with variable period', *Optics. Communications.*, 20, 1977, pp.179-182

[100] A.Katazir, C.Livanos, J.B.Shellan, and A.Yariv, 'Chirped gratings in integrated optics', *IEEE J.Quantum Electron.*, **QE-12**, 1977, pp.296-304

[101] K.D.Simmons, S.LaRochelle, V.Mizrahi, G.I.Stegeman and D.L.Griscom, 'Correlation of defect centres with a wavelength-dependent photosensitive response in germania-doped silca optical fibres', *Opt. Lett.*, **16**, 1991, pp.141-143

[102] D.L.Williams, S.T.Davey, R.Kashyap, J.R.Armitage, and B.J.Ainslie, 'Direct observation of UV induced bleaching of 240nm absorption band in photosensitive germanosilicate glass fibres', *Electron. Lett.*, **28**, 1992, pp.369-371

[103] T.E.Tsai, C.G.Atkins and E.J.Friebele, 'Photoinduced grating and intensity dependence of defect generation in Ge-doped silica optical fibre', *Appl. Phys. Lett.*, **61**, 1992, pp.390-392

[104] R.M.Atkins and V.Mizrahi, 'Observations of changes in UV absorption bands of single-mode germanosilicate core optical fibres on writing and thermally erasing refractive index gratings', *Electron. Lett.*, **28**, 1992, pp.1743-1744

[105] R.M.Atkins, V.Mizrahi and T.Erdogan, '248nm induced vacuum UV spectral changes in optical fibre preform cores: Support for a colour centre model of photosensitivity', *Electron. Lett.*, **29**, 1993, pp.385-387.

[106] B.Malo, J.Albert, D.C.Johnson, F.Bilodeau and K.O.Hill, 'Elimination of photoinduced absorption in Ge-doped silica fibres by annealing of ultraviolet colour centre', *Electron. Lett.*, **28**, 1992, pp.1598-1599

[107] W.X.Xie, P.Niay, P.Bernage, M.Douay, J.F.Bayon, T.Georges, M.Monerie and B.Poumellec, 'Experimental evidence of two types of photorefractive effects occurring during photoinscriptions of Bragg gratings within germanosilicate fibres', *Opt. Commun.*,**104**, 1993, pp.185-189

[108] P.Cordier, J.C.Doukhan, E.Fertein, P.Bernage, P.Niay, J.F.Bayon and T.Georges, 'TEM characterisation of structural changes in glass associated to Bragg grating inscription in a germanosilicate optica fibre preform', *Opt. Commun.*, **111**, 1994, pp.269-275

[109] P.Niay, P.Bernage, S.Legoubin, M.Douay, W.X.Xie, J.F.Bayon, T.Georges, M.Monerie and B.Poumellec, 'Behaviour of spectral transmissions of Bragg gratings written in germania-doped fibres: writing and erasing experiments using pulsed or cw uv exposure', *Opt. Commun.*, **113**, 1994, pp.176-192

[110] J.P.Bernadin and N.M.Lawandy, 'Dynamics of the formation of Bragg gratings in germanosilicate optical fibres', *Opt. Commun.*, **79**, 1990, 194-199

[111] K.S.Chiang, M.G.Sceats and D.Wong, 'Ultraviolet photolytic-induced changes in optical fibres: the thermal expansion coefficient', *Opt. Lett.*, **18**, 1993, pp.965-967

[112] P.A.Krug, R.Stolte, and R.Ulrich, 'Measurement of index modulation along an optical fiber Bragg grating', *Opt. Lett.* , **20**, 1995, pp.1767-1769

[113] P.A.Krug, R.Ulrich, and R.Stolte, 'Measurement of the axial distribution of refractive-index modulation along a fiber grating by Bragg reflection of an external probe beam', *Conf. Optical Fiber Communications, San Diego 1995* , Tech Dig. pp.136

[114] C.H.Kwak, K.H.Kim, J.S.Jeong, H.H.Suh, and E-H.Lee, 'Formation dynamics of Bragg phase gratings in photosensitive optical fibers', *IEEE Photon. Technol. Lett.*, **6**, 1994, pp.836-838

[115] D.K.W.Lam and B.K.Garside, 'Characterisation of single-mode optical fibers', *Appl. Opt.*, **20**, 1981, pp.440-445

[116] J.Albert, B.Malo, F.Bilodeau, D.C.Johnson, K.O.Hill, Y.Hibino and M.Kawachi, 'Photosensitivity in Ge-doped silica optical waveguides and fibers with 193-nm light from an ArF excimer laser', *Opt. Lett.*, **19**, 1994, pp.387-389

[117] D.L.Williams, B.J.Ainslie, J.R.Armitage, R.Kashyap and R.Campbell, 'Enhanced UV photosensitivity in boron codoped germanosilicate fibres', *Electron. Lett.*, **29**, 1993, pp.1191-1193

[118] P.J.Lemaire, R.M.Atkins, V.Mizrahi and W.A.Reed, 'High pressure H_2 loading as a technique for achieving ultrahigh UV photosensitivity and thermal sensitivity in GeO_2 doped optical fibres', *Electron. Lett.*, **29**, 1993, pp.1191-1193

[119] R.M.Atkins, P.J.Lemaire, T.Erdogan and V.Mizrahi, 'Mechanisms of enhanced UV photosensitivity via hydrogen loading in germanosilicate glasses', *Electron. Lett.*, **29**, 1993, 1234-1235

[120] P.J.Lemaire, A.M.Vengsarkar, W.A.Reed, V.Mizrahi and K.S.Kranz, 'Refractive index changes in optical fibres sensitised with molecular hydrogen', *Conf. Optical Fibre Communication, San Jose,* February 1994, Tech Dig. pp.47-48

[121] V.Mizrahi, P.J.Lemaire, T.Erdogan, W.A.Reed, D.J.DiGiovanni and R.M.Atkins, 'Ultraviolet laser fabrication of ultrastrong optical fibre gratings and of germania-doped channel waveguides', *Appl. Phys. Lett.*, **63**, 1993, pp.1727-1729

[122] B.Malo, J.Albert, K.O.Hill, F.Bilodeau and D.C.Johnson, 'Effective index drift from molecular hydrogen diffusion in hydrogen-loaded optical fibres and its effect on Bragg grating fabrication', *Electron.Lett.*, **30**, 1994, pp.442-444

[123] P.J.Lemaire, 'Enhanced UV photosensitivity in fibers and waveguides by high-pressure hydrogen loading', *Conf. Optical Fibre Communication* ,Tech. Dig. pp.162-163

[124] Shackleford, J.F., Studt, P.L., and Fulrath, R.M., 'Solubility of gases in glass. II. He, Ne, and H_2 in Fused Silica', *J.Appl.Phys.*, **43**, 1972, pp.1619-1625

[125] M.Douay, E.Fertein, W.X.Xie, P.Bernage, P.Niay, J.F.Bayon and T.Georges, 'Thermal hysteresis of Bragg wavelengths of intra-core fibre gratings', *IEEE Photon. Technol. Lett.*, 5, 1993, pp.1331-1334

[126] T.Erdogan, V.Mizrahi, P.J.Lemaire and D,Monroe, 'Decay of ultraviolet-induced Bragg gratings', *J. Appl. Phys.*, **76**, 1994, pp.73-80

[127] P.Niay, P.Bernage, M.Douay, E.Fertein, F.Lahoreau, J.F.Bayon, T.Georges, M.Monerie, P.Ferdinand, S.Rougeault and P.Cetier, 'Behaviour of Bragg gratings, written in germanosilicate fibers, against γ-ray exposure at low dose rate', *IEEE Photon. Technol. Lett.*, **6**, 1994, pp.1350-1352

[128] C.Huygens, 'Treatise on Light', 1690 (translated by S.P.Thompson, Dover, New York, 1962)].

[129] S.A.Schelkunoff, 'A mathematical theory of linear arrays', *Bell Syst. Techn. J.*, **22**, 1943, pp.80-107

[130] M.I.Skolnik, 'Radar Handbook', 1st Ed., New York: McGraw-Hill, 1970

[131] M.I.Skolnik, 'Introduction to Radar Systems', 2nd Ed., New York, McGraw-Hill, 1980

[132] R.J.Mailloux, 'Antenna Array Architecture', *Proc. IEEE*, **80**, 1992, pp.163-172

[133] I.Frigyes and A.J.Seeds, 'Optically generated true-time delay in phased-array antennas', *IEEE Transactions on Microwave Theory and Techniques*, **43**, 1995, pp.2378-2386

[134] S.Takahasi and S.Shibata, 'Thermal variation of attenuation for optical fibers', *Jour. Non-Crys. Solids*, **30**, 1979, pp.359-370

[135] G.W.Yoffe, P.A.Krug, F.Ouellette and D.Thorncraft, 'Temperature-compensated optical-fibre Bragg gratings', *Conf. Optical Fibre Communication*, 1995, Tech. Dig. pp.134-135

[136] S.M.Melle, K. Liu, and R.M.Measures, ' Strain sensing using a fibre optic Bragg grating', *SPIE Fiber Optic Smart Structures and Skins IV*, **1588**, 1991, pp.255-263

[137] S.M.Melle, A.T.Alavie, S.Karr, T.Coroy, K.Liu and R.M.Measures, 'A Bragg grating-tuned fiber laser strain sensor system', *IEEE Photon. Technol. Lett.*, 5, 1993, pp.263-266

[138] Mallinder, F.P. and Proctor, B.A., 'Elastic constants of fused silica as a function of large tensile strain', *Physics and Chemistry of Glasses*, 5, 1964, pp.91-103

[139] G.A.Ball and W.W.Morey, 'Compression-tuned single-frequency Bragg grating fiber laser', *Opt. Lett.*, 19, 1994, pp.1979-1981

[140] J.L.Cruz, L.Dong and L.Reekie, 'Improved thermal sensitivity of fibre Bragg gratings using a polymer overlayer', *Electron. Lett.*, 32, 1996, pp.385-387

[141] M.G.Xu, H.Geiger and J.P.Dakin, '*Electron. Lett.*, 32, 1996, pp.128-129

[142] G.W.Yoffe, P.A.Krug, F.Ouellette and D.Thorncraft, 'Temperature-compensated optical-fiber Bragg gratings', *Conf. Optical Fibre Communication*, 1995, Tech. Dig., pp.134-135

[143] M.G.Xu, L.Dong, L.Reekie, J.A.Tucknott and J.L.Cruz, 'Temperature-independent strain sensor using a chirped Bragg grating in a tapered optical fibre', *Electron. Lett.*, 31, 1995, pp.823-825

[144] M.G.Xu, J.L.Archambault, L.Reekie and J.P.Dakin, 'Simultaneous measurement of strain and temperature using fibre Bragg grating sensors', *Conf. Optical Fibre Sensors*, 1994, Tech. Dig., pp.191-194

[145] K.O Hill, F.Bilodeau, B.Malo and D.C.Johnson, 'Birefringent photosensitivity in monomode optical fibre: application to external writing of rocking filters', *Electron. Lett.*, 27, 1991, pp.1548-1550

[146] S.E.Kanellopoulos, V.A.Handerek and A.J.Rogers, 'Photoinduced polarisation couplers in elliptical core optical fibres written using 532 and 266nm sources', *Electron. Lett.*, 28, 1992, pp.1558-1560

[147] S.E.Kanellopoulos, V.A.Handerek and A.J.Rogers, 'Simultaneous strain and temperature sensing with photogenerated in-fiber gratings', *Opt. Lett.*, 20, 1995, pp333-335

[148] M.G.Xu, J.-L.Archambault, L.Reekie and J.P.Dakin, 'Discrimination between strain and temperature effects using dual-wavelength fibre grating sensors', *Electron. Lett.*, 30, 1994, pp.1085-1087

[149] R.J.Mailloux, 'Antenna array architecture', *Proc. IEEE*, 80, 1992, pp.163-172

[150] K.Sugden, I.Bennion, A.Molony and N.J.Copner, 'Chirped gratings produced in photosensitive optical fibres by fibre deformation during exposure', *Electron. Lett.*, 30, 1994, pp.440-442

[151] M.C.Farries, K.Sugden, D.C.J.Reid, I.Bennion, A.Molony and M.J.Goodwin, 'Very broad reflection bandwidth (44nm) chirped fibre gratings and narrow bandpass filters produced by the use of an amplitude mask', *Electron. Lett.*, 30, 1994, pp.891-892

[152] K.Sugden, L.Zhang, J.A.R.Williams and I.Bennion, 'Dissimilar wavefront technique for linear and quadratic chirps', *Photosensitivity and quadratic nonlinearity in glass waveguides: Fundamentals and applications, Portland, Oregon*, 1995, Tech. Dig., pp.136-139

[153] E.Hecht, 'Optics', 2nd Ed., Reading, Massachusetts, Addison-Wesley, 1987, pp.145-148

[154] K.O.Hill, B.Malo, F.Bilodeau, D.C.Johnson and J.Albert, 'Bragg gratings fabricated in monomode photosensitive optical fiber by UV exposure through a phase mask', *Appl. Phys. Lett.*, 82, 1993, pp.1035-1037

[155] R.Kashyap, J.R. Armitage, R.J.Campbell, D.L.Williams, G.D.Maxwell, B.J.Ainslie and C.A.Millar, 'Light-sensitive optical fibres and planar waveguides', *BT Technol. J.*, 11, 1993, pp.150-160

[156] H.N.Rourke, S.R.Baker, K.C.Byronm R.S.Baulcomb, S.M.Ojha and S.Clements, 'Fabrication and characterisation of long, narrowband fibre gratings by phase mask scanning', *Electron. Lett.*, 30, 1994, pp.1341-1342

[157] J.Martin and F.Ouellette, 'Novel writing technique of long and highly reflective in-fibre gratings', *Electron. Lett.*, 30, 1994, pp.811-812

[158] K.Sugden, 'Fabrication and applications of fibre Bragg gratings', *PhD Thesis, Aston University*, 1996, pp.91-97

[159] G.E.Town, K.Sugden, J.A.R.Williams, I.Bennion and S.B.Poole, 'Wide-band Fabry-Perot like filters in optical fibre', *IEEE Photon. Technol. Lett.*, **17**, 1994, pp.78-80

[160] Q.Zhang, D.A.Brown, L.J.Reinhart and T.F.Morse, 'Linearly and nonlinearly chirped Bragg gratings fabricated on curved fibres', *Opt. Lett.*, **20**, 1995, pp.1122-1124

[161] J.McD.Baxter Brown, 'Introductory Solid Mechanics', London, John Wiley and Sons, 1973, pp.155

[162] D.C.J.Reid, GEC-Marconi Material Technology, Caswell, Towcester, Northants., Log Book **2847**, serial number 201293: 1-5.

[163] D.C.J.Reid, GEC-Marconi Material Technology, Caswell, Towcester, Northants., Log Book **2847**, serial number 161193: 16

[164] GEC-Marconi Materials Technology, 9630 Ridgehaven Ct., San Diego, CA 92123, U.S.A., private communication

[165] Y.J.Rao, D.A.Jackson, L.Zhang and I.Bennion, 'Strain sensing of modern composite materials with a spatial/wavelength-division multiplexed fiber grating network', *Opt. Lett.*, **21**, 1996, pp.683-685

[166] C.M.Ragdale, GEC-Marconi Materials Technology, Caswell, Towcester, Northants., private communication.

[167] W.Gunning, J.Pasko and J.Tracy, 'A liquid crystal tunable spectral filter: Visible and infrared operation', *SPIE*, **268**, 1981, pp.190-194

[168] K.Hirabayashi, H.Tsuda and T.Kurokawa, 'Narrow-band tunable wavelength-selective filters of Fabry-Perot interferometer with a liquid crystal intracavity', *IEEE Photon. Technol. Lett.*, **3**, 1991, pp.213-215.

[169] M.W.Maeda, J.S.Patel, L.Chinlon, J.Horrobin and R.Spicer, 'Electrically tunable liquid-crystal etalon filter for high-density WDM systems', *IEEE Photon. Technol. Lett.*, **2**, 1990, pp.820-822

[170] K.Hirabayashi, H.Tsuda and T.Kurokawa, 'New structure of tunable wavelength-selective filters with a liquid crystal for FDM systems', *IEEE Photon. Technol. Lett.*, **3**, 1991, pp.741-743

[171] K.Hirabayashi, H.Tsuda and T.Kurokawa, 'Tunable wavelength-selective liquid crystal filters for 600-channel FDM system', *IEEE Photon. Technol. Lett.*, **4**, 1992, pp.597-599

[172] Merck Ltd, Merck House, Poole, Dorset, BH15 1TD

[173] Dr.S.Day, Electronic Engineering, University College London

[174] M.J.Guy. S.V.Chernikov, J.R.Taylor and R.Kashyap, 'Low-loss fibre Bragg grating transmission filter based on a fibre polarisation splitter', *Electron. Lett.*, **30**, 1994, pp.1512-1513

[175] F.Bilodeau, K.O.Hill, B.Malo, D.C.Johnson and J.Albert, 'High-return-loss narrowband all-fiber bandpass Bragg transmission filter', *IEEE Photon. Technol. Lett.*, **6**, 1994, pp.80-82

[176] K.O.Hill, D.C.Johnson, F.Bilodeau, and S.Faucher, 'Narrow-bandwidth optical waveguide transmission filters', *Electron. Lett.*, **23**, 1987, pp.465-466

[177] L.Zhang, K.Sugden, J.A.R.Williams, I.Bennion, D.C.J.Reid and C.M.Ragdale, 'Postfabrication exposure of gap-type bandpass filters in broadly chirped fiber gratings', *Opt. Letts.*, **20**, 1995, pp.1927-1929

[178] K.Sugden, I.Bennion, A.Molony, M.C.Farries, D.C.J.Reid and M.J.Goodwin, 'Fabrication and properties of chirped fibre gratings with reflection bandwidths exceeding 50nm and narrow bandpass fibre grating filters', *Conf. Lasers and Electro-Optics Europe*, Amsterdam, 1994, Tech. Dig.

[179] K.Sugden, 'Fabrication and applications of in-fibre Bragg gratings', *PhD thesis*, Aston University, 1996, pp.70

[180] T.A.Birks, D.O.Culverhouse, S.G.Farwell and P.St.J.Russell, '2x2 single-mode fiber routing switch', *Opt. Lett.*, **21**, 1996, 722-724

[181] GEC Marconi Materials Technology, Hirst Research, Borehamwood, Hertfordshire, England

[182] A.Molony, I.Bennion, J.Fells and C.Edge, 'Fibre Bragg gratings for the control of phased array antennas', *IOP Conf. In-Fibre Bragg gratings and Special Fibres, London*, 24th May 1995,

[183] A.Molony, C.Edge and I.Bennion, 'Fibre grating time delay element for phased array antennas', *Electron. Lett.*, **31**, 17, 17th August 1995, pp.1485-1486

[184] A.Molony, L.Zhang, J.A.R.Williams, I.Bennion, C.Edge and J.Fells, 'Fibre grating time delay control of phased array antennae', *J.Mod.Opt.*, **43**, 5, 1996, pp.1017-1024.

[185] A.Molony, L.Zhang, J.A.R.Williams, I.Bennion, C.Edge and J.Fells, 'Fibre grating networks for time-delay control of phased-array antennas', *Conf. Lasers and Electro-Optics, Anaheim*, 1996, pp.244-245

[186] Prof.P.R.Herczfeld, Director, Center for Microwave/Lightwave Engineering, Drexel University, Philadelphia, P.A., U.S.A., *Private communication at Conf. On Lasers and Electro-optics, Anaheim, C.A., U.S.A.*, 1996.

[187] D.Marcuse, 'Pulse distortion in single-mode fibres', *Appl. Opt.*, **19**, 1980, pp.1653-1660

[188] A.Molony, I.Bennion and C.Edge, 'Fibre Bragg grating time delay control of phased array antenna systems', *QE-12, Southampton*, 1995, P3-34

[189] J.A.R.Williams, Photonics Research Group, Electronic Engineering and Applied Physics, Aston University, Aston Triangle, Birmingham, B4 7ET

[190] K.O.Hill, 'Aperiodic distributed-parameter waveguides for integrated optics', *Appl. Opt.*, **13**, 1974, pp.1853-1856

[191] M.Matsuhara and K.O.Hill, 'Optical-waveguide band rejection filters: design', *Appl. Opt.* , **13**, 1974, pp.2886-2888

[192] J.Hong, W.Huang and T.Makino, 'On the transfer matrix method for distributed feedback waveguide devices', *J. Lightwave Technol.*, **10**, 1992, pp.1860-1868

[193] B-G.Kim and E.Garmire, 'Comparison between the matrix method and the coupled-wave method in the analysis of Bragg reflector structures', *J. Opt. Soc. Amer. A*, **9**, 1992, pp.132-136

[194] H.Kogelnik, 'Filter response of nonuniform almost-periodic structures', *Bell Syst. Techn. J.*,**55**, 1976, pp.109-126

[195] R.Kashyap, A.Swanton and D.J.Armes, 'Simple technique for apodising chirped and unchirped fibre Bragg gratings', *Electron. Lett.*, **32**, 1996, pp.1226-1228

[196] Y.Bao, A.Sneh, K.Hsu, K.M.Johnson, J.-Y.Liu, C.M.Miller, Y.Monta and M.B.McClain, 'High-speed liquid crystal fiber Fabry-Perot tunable filter', *IEEE Photon. Technol. Lett.*, **8**, 1996, pp.1190-1192

[197] M.A.Davis, D.G.Bellemore, M.A.Putnam and A.D.Kersey, 'Interrogation of 60 fibre Bragg grating sensors with microstrain resolution capability', *Electron. Lett.*, **32**, 1996, pp.1393-1394

[198] R.Kashyap, H.-G.Froehlich, A.Swanton and D.J.Arnes, '1.3m long super-step-chirped fibre Bragg grating with a continuous delay of 13.5ns and bandwidth 10nm for broadband dispersion compensation', *Electron. Lett.*, **32**, 1996, pp.1807-1809